A THEORETICAL AND PRACTICAL STUDY OF THE LORENZ-TYPE INDUCTOR-ALTERNATOR

a thesis submitted for the degree of
DOCTOR OF PHILOSOPHY

RODNEY KINTORE LAY
THE UNIVERSITY OF ASTON IN BIRMINGHAM

April 1967

Summary:

Throughout this work the emphasis is laid on developing the theory in a form which contributes directly to the design technique; each stage is verified experimentally.

Relevant literature falls into two distinct categories: one, classical in form, based on the permeance of assumed magnetic circuits: the second, presenting computed solutions to models of detailed field problems. This thesis extends the classical approach to bring its capacity for analysis closer to the level of detail offered by the model/solution concept.

After a full analysis of these theories, the experimental machine's design, manufacture and instrumentation are reported. Problems connected with 'damping undesirable flux variations' and 'accounting for anomalous loss mechanisms' formed the original investigation. Their solution is presented in the complete analysis of tooth and core flux distribution, which leads to a detailed description of the on-load flux density distribution across the surface of a rotor tooth.

The theory derived to solve these early problems is extended to form an alternative technique to existing practice in the complete solution of the loaded machine. The expressions combine the load current and voltage with the field current and, in addition, are dependent on the airgap geometry, the load circuit power factor and the leakage reactance. By expressing the parameters in two equations, one limited by the load conditions and the second dependent on the characteristics of the particular machine, successful predeterminations of field requirements for practical non-linear conditions are obtained.

A paper on the history and changing fortunes of this class of machine is included, demonstrating its unique character and contribution to technology. From a research viewpoint great potential lies in the

combination of medium frequency and an unusual airgap geometry; this has allowed the detection and analysis of characteristics which, in other types of machine, are individually unidentifiable.

C O N T E N T S

CHAPTER 5 Voltage generation

CHAPTER 6 Future work - some thoughts on starting points suggested by this thesis

CHAPTER 7 References and Acknowledgments

CHAPTER 8 Appendices

CHAPTER 1 An introduction to the machine and the theories

Summary

Chapter 1 introduces the machine, existing theory, and an extension to the theory which forms the basis for this work. The new analysis is derived from an expression for the airgap field; hence many aspects of design are involved.

To provide comparisons between this approach and previous work it is necessary to summarise the existing theory point by point. This introduces the machine in detail rather than in the general form which is already satisfactorily presented by Walker [2].

Papers by Walker and Erdelyi are considered to represent the major contributions to inductor-alternator theory and these form the basis for the summaries. It is convenient to include under each heading contributions both from other sources, and from the new analysis, with references to subsequent chapters.

In this way a detailed assessment of published work is combined with the findings of this thesis, presenting a comprehensive survey of design techniques for the Lorenz-type inductor-alternator.

1.1 Origins of the Lorenz-type Inductor-Alternator

In a paper, included as appendix 8.11, titled 'The History and changing fortunes of the inductor-alternator' the writer has traced the progress of the inductor-alternator class of machine from its inception in the late 1880's to the present day. The single phase heteropolar Lorenz-type inductor-alternator referred to by Dr. Walker in section 2.2.1 of reference 2 is the subject of this thesis.

The term 'Lorenz' would appear to be derived from the company of C. Lorenz at Berlin - Templehof. In 1914 this company patented [20] an alternator due to Dr. Schmidt which was later designated type S[21], fig 1.

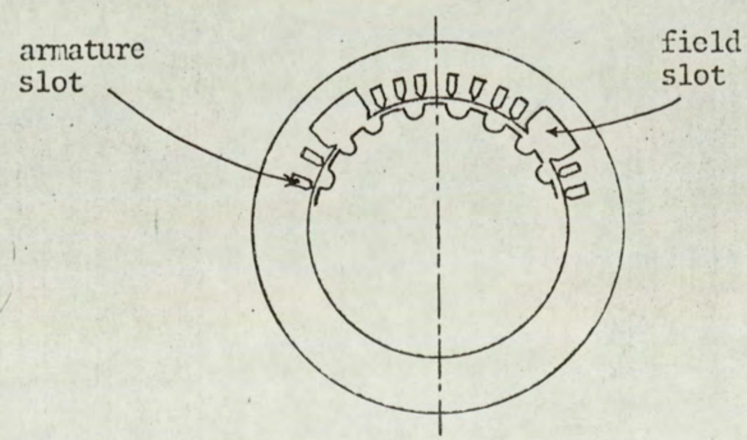

Fig 1: 100 Kw, 500c/s, 1500r.p.m. Type 'S'
from reference 21

The major contribution of the patent was the introduction of a winding layout wherein both field and armature coils were wound in the same plane. The earlier distinction between homopolar and heteropolar [23], which was solely concerned with the relative angular position of two rotor cores, had lapsed before the type S was manufactured. This made available the term 'heteropolar' to describe the new field system which had alternate directions of flux spaced around the airgap periphery [22]. From 1925 onwards the inductor-alternator was used to supply coreless induction furnaces for melting and smelting. This process required frequencies within the range 500 c/s to 5 Kc/s, which coincided with the efficient application of the Lorenz design. The action of 'skin effect' in limiting the penetration of eddy currents in the workpiece led to the technique of surface heat treatments by induction. This process required higher frequencies (of the order 8-12 kc/s) for which a design of the type patented by Guy [22] was suitable. The distinction between the Lorenz design and Guy's patent lay in the airgap surface geometry of the stators. The Lorenz design stator was that of an induction motor with a number of slots enlarged to take the field coils: in manufacturing terms this was its major advantage. The armature slot openings were 'semiclosed', consistent with winding techniques and acceptable leakage reactance. The field slots were sometimes enlarged without altering their opening but more often the advantages of pre-formed field coils led to 'open' slot designs. However, for the purposes of definition [22], the Lorenz design has 'semiclosed armature slots and an otherwise smooth stator-airgap surface between field slots'.

The essence of Guy's patent had been to arrange that several rotor tooth pitches (i.e. a.c. pole pairs), matched by identical inductors on the stator, should lie within one armature coil pitch. Thus the 'stator-airgap surface between field slots' for this design consisted of open unwound slots (i.e. inductors), fig 2.

The necessity to differentiate between the designs has produced a terminology [22] which, in the U.K., distinguishes these two main variations in stator slotting as Lorenz-type and Guy-type. On the continent 'Lorenz' remains a definition of 'heteropolar' as in the original 'type S'. In the writer's opinion the clearest description of a design is achieved by limiting the terms 'Lorenz' and 'Guy' to describing slotting while the terms 'homopolar' and 'heteropolar' describe field systems. Nevertheless it must be recognised that 'homopolar-Lorenz' is a contradiction in terms to some designers.

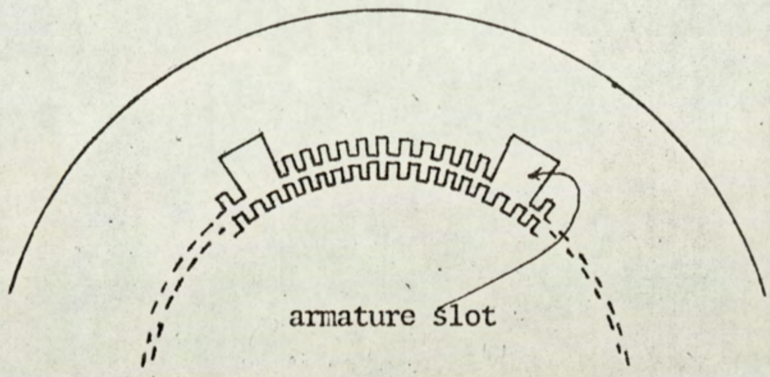

Fig 2: Guy slotting from reference 24

1.2 An appreciation of the major contributions to inductor-alternator theory

1.2.1 The two main types of theoretical approach

Relevant publications fall naturally into two categories which are characterised by the approach to, or model for, their respective theories. The broad definitions of these categories are:

(a) containing representation and analysis of 'total fluxes' (per pole, per tooth, etc.) from consideration of the m.m.f. imposed upon the magnetic circuit, assuming the flux paths are known.

(b) containing representation and analysis of the field throughout the machine by potential equations (Laplacian, two dimensional) limited by boundary conditions approximating to the iron and copper geometries.

Inductor-alternators as a class of machine are not unique in being the subject of two widely differing types of analysis: compared with most other machines there are, however, remarkably few publications in either group.

Undoubtedly a major work in group (a) is Walker's 1942 paper [1] on the 'Theory of the Inductor-alternator'. Very nearly every author in the field makes reference to this paper and often also to a second paper [2] by Walker in 1946. The first combines the contributions of references 3 to 9 to present a theory which is also a practical design technique. In his second paper Walker classifies single and polyphase, Guy and Lorenz-type designs, considers armature windings in detail, and identifies the positive and negative sequence components of armature-reaction flux. These two papers will be studied in detail in section 1.2.2.

Group (b) publications are the work of one man (et al); E.A.Erdelyi, at the University of Colorado. Since 1963 the U.S. Army Research and

Development Laboratories have supported the application of the analytical methods developed in reference 10. This is the parent paper to references 11 to 19 in which the partial differential field equations for a variety of design problems are established and solved. The solutions are numerical, involving 'over-relaxation of the potentials and permeabilities alternately'. These papers will be studied in section 1.2.3.

Therefore, to summarise the philosophies of these two approaches:

group (a) The m.m.f. is applied around a 'classic magnetic circuit', taking account of the complete machine's actual dimensions, thus deriving values for flux per pole or per teeth. This theory is unable to comment on flux density distribution within the core or teeth; it must calculate on-load field requirements by applying armature reaction m.m.f. to the same magnetic circuit. This restricts accurate calculation and understanding to operating conditions where the field and armature reaction m.m.f.s are coincident in space (i.e. ZPF). Further, the non-linear characteristics of the machine are only expressed by the iron manufacturer's B-H curve which does not account for non-uniform tooth and core flux-density distributions.

group (b) Elements of the machine, concentrating on the airgap region, are layed out on a grid so that the copper and iron geometries are described by groups of mesh points. These provide the potential and boundary conditions which lead to a solution for the complete field pattern expressed at each mesh point. This supplies the distribution detail lacking in group (a) and is possibly the only method applicable to very highly saturated conditions. Such a detailed analysis requires considerable computer facilities: to investigate core flux densities and overall machine characteristics by this approach would be to employ a process of far greater sensitivity than is necessary.

1.2.2 Survey and discussion of papers by J.H. Walker

In this section two papers by Walker [1,2] are considered in detail. Summaries on each point drawn directly from Walker are set into the page with a wider margin to distinguish them from the writers own comments and references to subsequent chapters. In this manner the inductor-alternator class of machine will be surveyed in detail: at the same time the relevance of the theoretical and experimental work of this thesis will be indicated.

Each section of the survey is numbered for ease of reference to those features which are investigated in later chapters.

The first summaries are from 'The theory of the inductor-alternator' (ref. 1) and run from (1) to (13) as follows:

(1) field systems
(2) airgap flux density pattern
(3) generation of e.m.f.
(4) flux utilisation factors
(5) e.m.f./flux equation
(6) comparison of unidirectional and bi-directional flux variation systems
(7) equipotential m.m.f. circles leading to ϕ_t and ϕ_s
(8) leakage paths
(9) open-circuit characteristic from $(\phi_t - \phi_s)$
(10) armature reaction m.m.f.
(11) damping of undesired pulsations in main flux
(12) calculation of field current on load
(13) losses

(1) Field systems

'The homopolar [3,22] fig. 3, and the heteropolar [4,22] fig. 4, are the two possible field systems shown here with their respective constructions.'

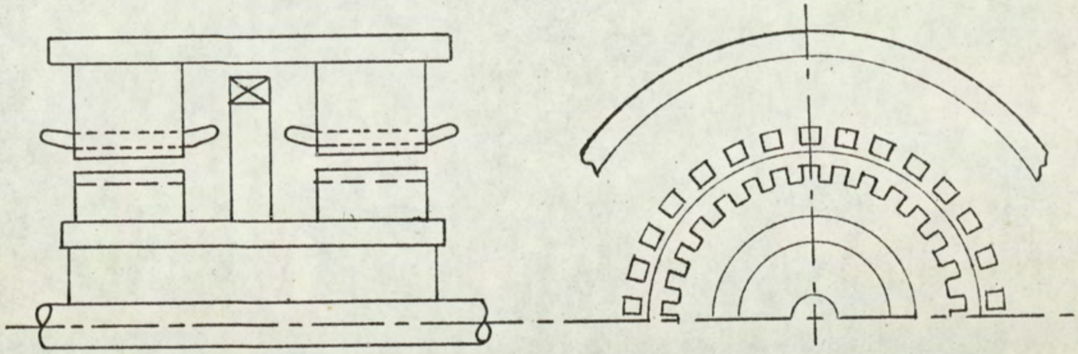

Fig 3: Homopolar inductor-alternator

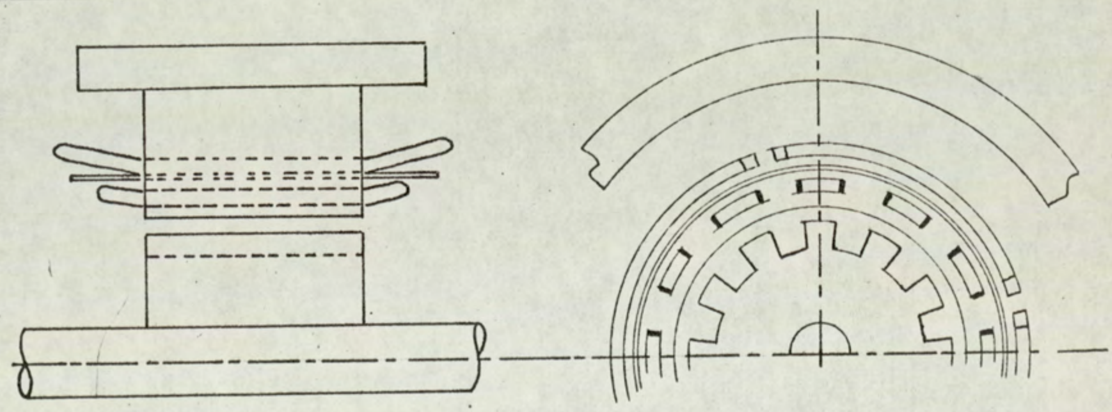

Fig 4: Heteropolar inductor-alternator

(2) Airgap flux density pattern

'The fundamental operational characteristic of this machine is flux modulation: the simplest physical element is a slot opposite a smooth surface, fig. 5.

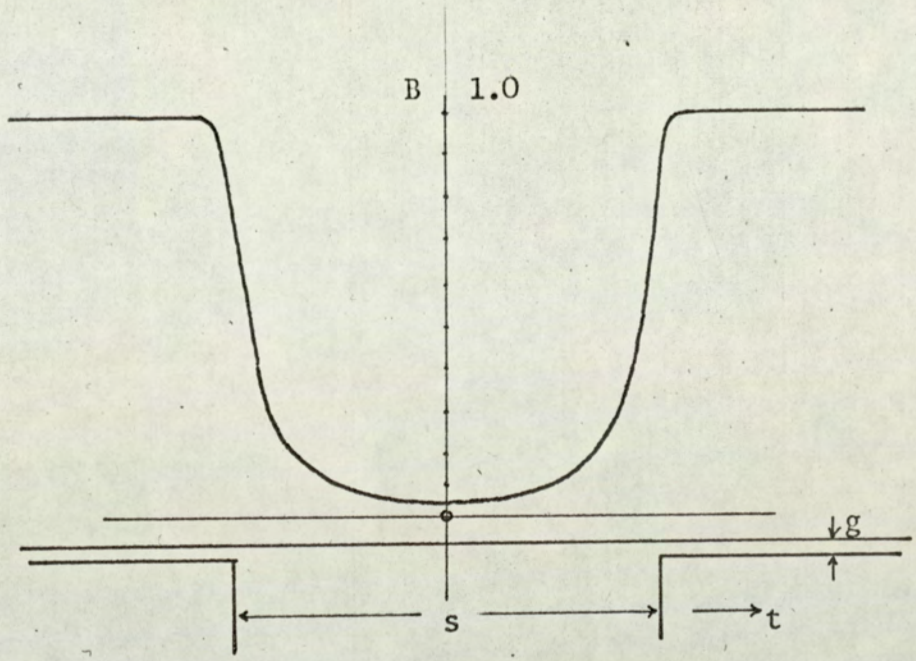

Fig 5: Space distribution curve of flux-density

The flux density in such an airgap is given by the equations:

$$B = B_{max} \frac{k + 1}{\sqrt{\left[\left\{ k + \left(\frac{\beta + \gamma}{2} \right) \right\} \left\{ k + \left(\frac{2}{\beta + \gamma} \right) \right\} \right]}} \quad \ldots\ldots\ldots\ldots 1A$$

$$\frac{x}{s} = \frac{g}{\pi s} \left\{ \text{arc cos h} \left(\frac{2k + \beta}{\gamma} \right) - \text{arc cos h} \left(\frac{2k^{-1} + \beta}{\gamma} \right) \right\} + \frac{1}{\pi} \text{ arc sin} \left\{ \delta \left(\frac{k - 1}{k + 1} \right) \right\} \quad \ldots\ldots\ldots\ldots 1B$$

where s = width of rotor slot
t = width of rotor tooth
g = length of airgap over rotor tooth
$\beta = (s/g)^2 + 2$

$$\gamma = \pm\, s/g \sqrt{\{(s/g)^2 + 4\}}$$
$$\delta = \pm \frac{s/g}{\sqrt{\{(s/g)^2 + 4\}}}$$

k = parameter corresponding to values of x

x = space co-ordinate measured along a rotor slot pitch from the axis of a slot ($0 \leq x < (s + t)/2$)

These equations are due to Carter [8]; they assume an infinitely deep parallel side slot. Coe and Taylor [9] show that the error is small if the depth is only 'slightly greater' than the width. Indeed, Carter comments that '... inasmuch as the field hardly penetrates beyond the mouth, this (the assumption of infinite slot depth) is of no consequence'. Carter further shows that the field between a smooth surface and a number of such slots is not significantly different from the pattern achieved by repeating the single slot analysis the desired number of times'.

The problem of obtaining and then expressing the flux density pattern in the airgap is central to any study of this type. Other than by testing, the three major methods of obtaining the distribution are a) Graphical b) Mathematical and c) Measurements on an analogue.

Stevenson and Park [25] collected and adapted the work of Rogowski, Lehmann and others to present a theory of field determination by graphical means. Weiseman [26] applied these techniques to the synchronous machine commenting that the '... mathematical solution' was often 'laborious and sometimes impossible'. However, Graphical techniques are by no means easy to apply accurately: they require expertise.

Mathematical methods are undoubtedly the most rigorous. Unfortunately, their application is limited by the very great increase in complexity caused by seemingly minor additions to the geometry. The problem of one slot opposite a smooth surface is comparatively simple because of its symmetry about the slot centreline. The required conformal transformation must describe two right angles and leads to a hyperbolic function. Gibbs[27] has considered this particular problem in detail including the method by which the flux density wave may be plotted. Transformations of geometries containing more than two right angles will lead to elliptic functions which may not be analytic. A technique for solving a Schwarz-Christoffel equation with five constants, by iteration and then numerical integration, is reported by Binns [28]: this requires considerable computer time.

Analogues for representing fields are many and varied. Some are purely descriptive on which accurate measurements are not practicable. Liebmann [29] has made the following summary of the most useful analogues:

'<u>Conducting paper</u>

Advantages - Cheap equipment, easy technique; applicable to complicated geometries.

Disadvantages - Limited accuracy (2 %), scale distortion, 2-dimensional only.

<u>Electrolytic tank</u>

Advantages - Applicable to complicated geometries.

Disadvantages - Limited accuracy, difficult measuring technique.

<u>Resistance network</u>

Advantages - High accuracy, easy technique, applicable to mathematically more complicated problems.

Disadvantages - Cumbersome when applied to complicated geometries.

<u>RC and LC networks</u>

Advantages - Applicable to transient conditions.

Disadvantages - Limited accuracy, specialised applications only, requires simple geometries.

<u>Computer</u>

Advantages - Applicable to complex problems of great variety.

Disadvantages - Expensive equipment, limited accuracy, requires simple geometries.'

The airgap flux density distribution may be obtained by which ever method suits the particular requirements of cost, time and accuracy. Patterns similar to fig. 5 are of direct use in calculating the overall airgap flux level and accounting for the effect of fringing into the slot sides (Carter's coefficient). More detailed investigations require a simple form of equation (1), or expressions for the patterns produced by graphical or analogue methods. A suitable form is achieved by fourier analysis of the patterns into infinite series. The series may be analysed component by component and the desired degree of accuracy simply controlled by the number of components that are considered. A further advantage lies in the series being a cyclic form: the total effect of several repetitions of the pattern is produced by considering the series between suitable limits. This is of special benefit when analysing a heteropolar field since complete field symmetry is about a field pitch, i.e. several rotor slot pitch patterns.

(3) <u>Generation of e.m.f.</u>

'E.m.f. is generated in each side of an armature coil as the flux density wave passes. Since the flux is unidirectional the e.m.f.s in each side of a full pitch coil will be 180^{o} out of phase so that when a rotor tooth axis coincides with the coil axis each coil side e.m.f. will be equal and opposite. Similarly, when a rotor slot axis coincides with the coil axis the net e.m.f. around the coil is zero. At all other positions one or other coil sides will lie in a greater flux density and the net e.m.f. will alternate through a complete cycle as the rotor moves through one rotor slot pitch. The frequency of this alternating e.m.f. is given by:

f = (number of rotor slots x rotor velocity (r.p.s.)) '

Fig. 6 is taken directly from ref. 1 showing the open-circuit e.m.f. produced in the manner described.

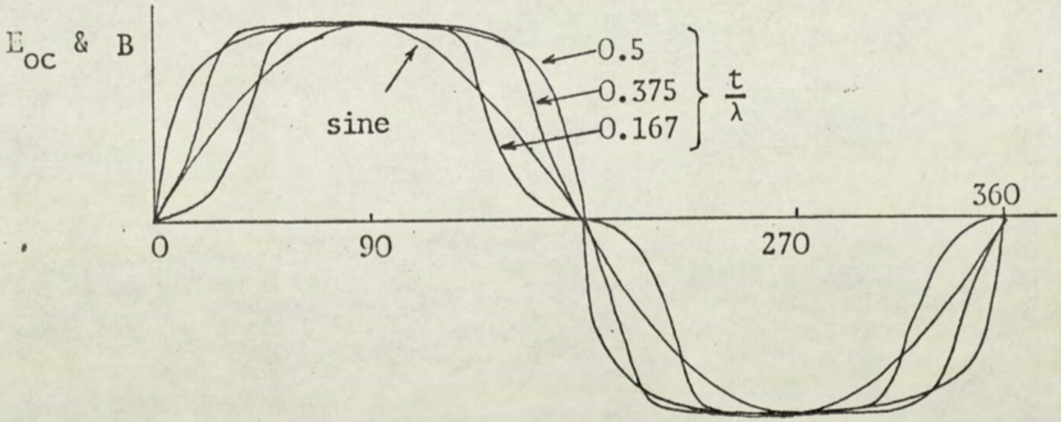

Fig 6: Waveforms of alternating flux, $\frac{s}{g}$ = 20, and open circuit e.m.f.

This process is investigated in Chapter 5 by differentiating the flux-linkages with the coil with regard to time. The flux-linkages are obtained by integrating the flux density distribution between suitable limits, at which point, the inability of a full pitch coil to sense even harmonic variations in flux is clearly demonstrated. Hence the 'B' referred to by Walker in fig. 6 is the flux density variation sensed by a full pitch winding, not the actual flux density existing in the airgap. ~~(except in the special case of t/λ = 0.5 , which will include no even harmonics)~~.

(4) <u>Flux utilisation factors</u>

'The desired alternating e.m.f. is sinusoidal: factors ε_1 and ε_2 are defined to relate the mean unidirectional and alternating flux levels together with the effective alternating flux. '

Walker's definition of ε_1 is used in this thesis, i.e.

$$\varepsilon_1 = \frac{\text{mean value of alternating flux density}}{\text{mean value of total unidirectional flux density crossing the gap}}$$

However, it has been the writer's practice to use a slightly different definition of ε_2 due to Davies and Pederson [30] i.e.

$$\varepsilon_2 = \frac{\text{mean value of fundamental component of flux density}}{\text{steady mean flux density}}$$

This definition replaces Walker's 'effective value of alternating flux' by the 'mean fundamental component'. The resulting advantage is detailed in the next section.

(5) E.m.f./flux equation

'The equation relating flux and generated e.m.f. is:

r.m.s. generated e.m.f. =

4 x frequency x effective turns x effective alternating flux. '

When the above definition for ε_2 is used the peak value of the fundamental component of flux (ϕ_{ac}) becomes available. If ϕ_{ac} replaces the 'effective alternating flux' in the e.m.f. equation the factor changes from 4 to 4.44, which brings the theory of the inductor-alternator into line with normal machine theory.

(6) Comparison of unidirectional and bi-directional flux variation systems

'For the ideal optimum case where the flux wave over a rotor tooth is rectangular and the flux over a rotor slot is zero, the mean unidirectional flux density = $\frac{1}{2}$ x maximum value of B_{DC}.
An excited rotor alternator (with conventional wound poles) will produce a rectangular flux wave with B_{DC} (mean) = B_{DC} (max).

This shows that for the same maximum density in the gap the excited-rotor machine will give double the output of an inductor machine. This comparison is made less unfavourable on relatively low frequency machines by the higher densities that the stator core - not being subjected to an alternating flux - can be worked on the inductor-alternator. '

Chapter 3 shows that, in fact, the core of a Lorenz-type inductor-alternator is subject to alternating flux. However, the comparison is still not justified unless the inductor-alternator is employed to generate frequencies, below 300c/s say, at which the wound-pole alternator is more suitable. Even if one considers the currently impractical concept of driving a 200 pole machine at 3000 r.p.m. (5000c/s) the limiting feature becomes one of heating due to losses. This in turn limits the alternating flux density to levels adequately supplied by the inductor principle, i.e. the maximum flux of the wound field can not be employed.

(7) <u>Equipotential m.m.f. circles leading to ϕ_t and ϕ_s</u>

'Referring to fig. 7, let the flux which takes path 'a' be denoted by ϕ_t and that which takes path 'b' by ϕ_s. '

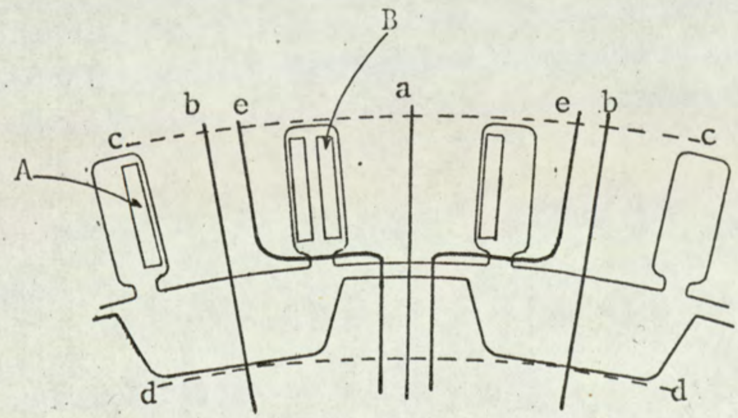

Fig 7: Flux paths between circles of equipotential m.m.f.

The total fluxes carried by the stator teeth under these two conditions (maximum and minimum) are the main design parameters for those whose approach section 1.1 termed group (a).

> 'Again in fig. 7 'cc' and 'dd' are equipotential circles, since the exciting m.m.f. is constant in magnitude round the stator core periphery. '

Here is the primary assumption upon which this approach rests. Large numbers of armature slots per d.c. pole pitch or deep armature slots with a shallow core section would produce an m.m.f. equipotential which was not circular. However, such comments on the limitations of this theory (not necessarily important limitations) will be considered in section 1.3, where the type of theory which naturally follows from this choice is discussed. (see also 1.2.2 (12)).

> 'The sum of the two fluxes ϕ_t and ϕ_s which passes into the rest of the magnetic circuit is the steady flux due to the field, ϕ. ϕ_t and ϕ_s may be expressed in terms of ϕ since
>
> $$\varepsilon_1 = \frac{\phi_t - \phi_s}{\phi_t + \phi_s} \quad \text{(ref. 1 and 30)}$$
>
> $$\text{i.e.} \quad \phi_t = \frac{\phi}{2}(1 + \varepsilon_1)$$
>
> $$\phi_s = \frac{\phi}{2}(1 - \varepsilon_1)$$
>
> For a given total flux the ampere-turns required to drive the rotor tooth flux from 'cc' to 'dd' along path 'a' must equal the ampere-turns required to drive the rotor slot flux from 'cc' to 'dd' along path 'b'. If the stator and rotor teeth are infinitely permeable the equations given above for ϕ_t and ϕ_s are correct. In practice appreciable m.m.f. is absorbed in driving ϕ_t through a saturated path 'a' whilst in path 'b' the stator teeth will require negligible m.m.f.

over the working range of the machine. Thus the m.m.f. acting across the gap between stator and rotor surfaces is not uniform, being a maximum over a rotor slot and a minimum over a rotor tooth. For a given exciting m.m.f. this will lead to a reduction in ϕ_t and an increase in ϕ_s, with a corresponding reduction in effective flux. '

Photographs, in Chapter 4 fig. 42, of an integrated rotor tooth-surface search-coil signal, i.e. displays which are proportional to airgap flux, show a reduction in flux as ϕ_t is established. This could in part be accounted for by a reduction in the peak value of ϕ_t described by Walker. The increase in ϕ_s however is as a ratio of the unidirectional flux at the airgap: while ϕ remains constant ϕ_s cannot increase unless new leakage fluxes appear.

(8) Leakage paths

'Leakage paths (such as e, fig. 7) will exist dependent on the slot permeance and armature conductor distribution within the slot. The level of leakage fluxes across armature slots and in core end regions are proportional to ϕ_t from which they must be subtracted. It follows that their calculation is iterative: the corrected value of ϕ_t must be calculated such that this reduced value plus its associated leakage level equals the original calculation which neglected leakage. A modified slot permeance which allows for the presence of armature conductors may be used to calculate 'linking' leakage fluxes: these are simply added to ϕ_s and subtracted from ϕ_t. '

These corrections to values for ϕ_s and ϕ_t are necessary if the process of evaluating ε_1 (in terms of $\frac{s}{g}$, $\frac{t}{\lambda}$ and $\frac{d}{g}$) made no provision for the field within the stator teeth and slots, and if a high degree of accuracy is required. Unpublished derivations of ε_1 and ε_2 have used conducting paper to represent the airgap region, thus producing general relationships assuming infinite iron permeability. In 3.1.2 a conducting paper analogue is described which accounts for the field distribution within stator core and teeth. Allowance is made for the variation in overall circuit reluctance due to the stator slot openings: accounting for the fringing and armature slot leakage paths would be a possible refinement. It is also possible to extend this technique to investigate the effects on ε_1 and ε_2 when saturated levels of ϕ_t exist.

(9) <u>Open-circuit characteristic from $(\phi_t - \phi_s)$</u>

'Combining the ampere-turns required to support the fluxes in the iron and air of both paths 'a' and 'b' leads to fig. 8(a), showing ϕ_s and ϕ_t plotted against total path m.m.f. The e.m.f. generated in a pair of adjacent coils (such as A and B fig. 7) is the difference of the e.m.f.s generated in the two individual coils [31]. The maximum flux linking a pair of adjacent coils will thus be the difference between the maximum flux (ϕ_t) which links the first and the minimum flux (ϕ_s) which links the second. Hence the maximum e.m.f. is proportional to $(\phi_t - \phi_s)$. The flux to be used in the flux/e.m.f. equation is $\frac{\varepsilon_2}{\varepsilon_1}(\phi_t - \phi_s)$, which allows the open-circuit voltage to be plotted against total exciting ampere-turns, fig. 8 (b). A major characteristic of the inductor principle is evident under saturated conditions: for increase in applied m.m.f. beyond a certain level the induced voltage decreases. This level is fixed by the relative gradients of ϕ_t and ϕ_s in fig. 8(a). If the gradient of ϕ_t becomes less than that of ϕ_s then for further increases in m.m.f. $(\phi_t - \phi_s)$ must decrease.'

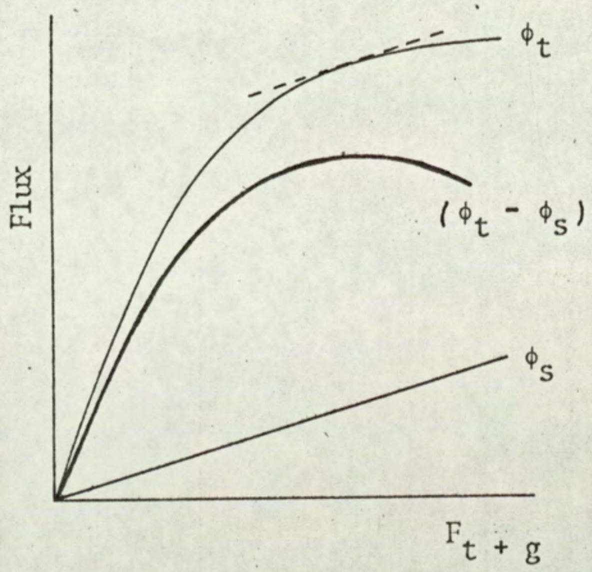

(a)

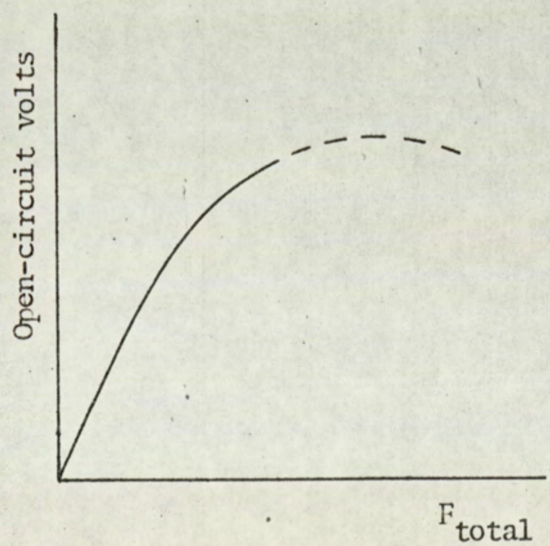

(b)

Fig 8: (a) Curves of ϕ_t and ϕ_s as functions of m.m.f.
(b) Open-circuit volts $\propto(\phi_t - \phi_s)$

(10) Armature reaction m.m.f.

'The armature reaction m.m.f. may be considered as the product of the turns distribution and the armature current. Fig. 9(b) shows the reaction m.m.f. due to the winding of fig. 9(a) in a homopolar field.

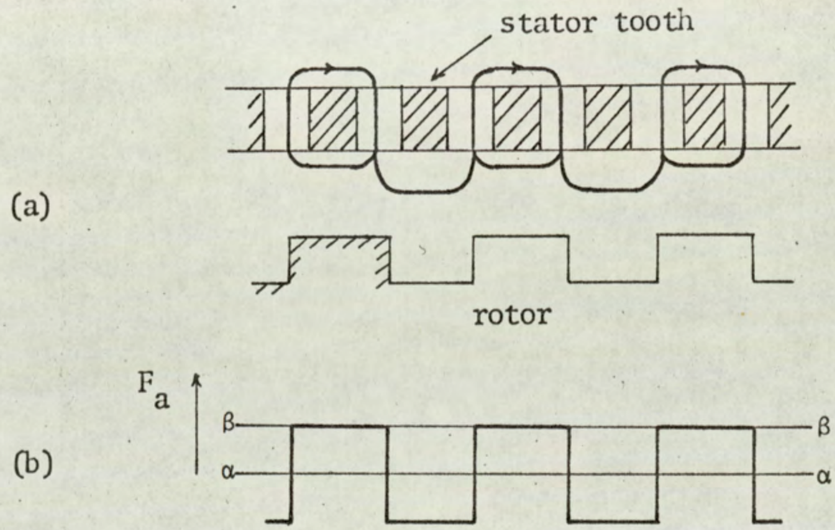

Fig 9: a) Armature winding
b) Armature reaction m.m.f.

Considering only the m.m.f. due to the conductors, the zero line of this pattern will be 'αα'. When the end windings between cores, fig. 10(a), are axially in line each discontinuous ring is equivalent to a continuous ring having half the number of effective turns of each armature coil, and the zero line will be shifted to 'ββ'.

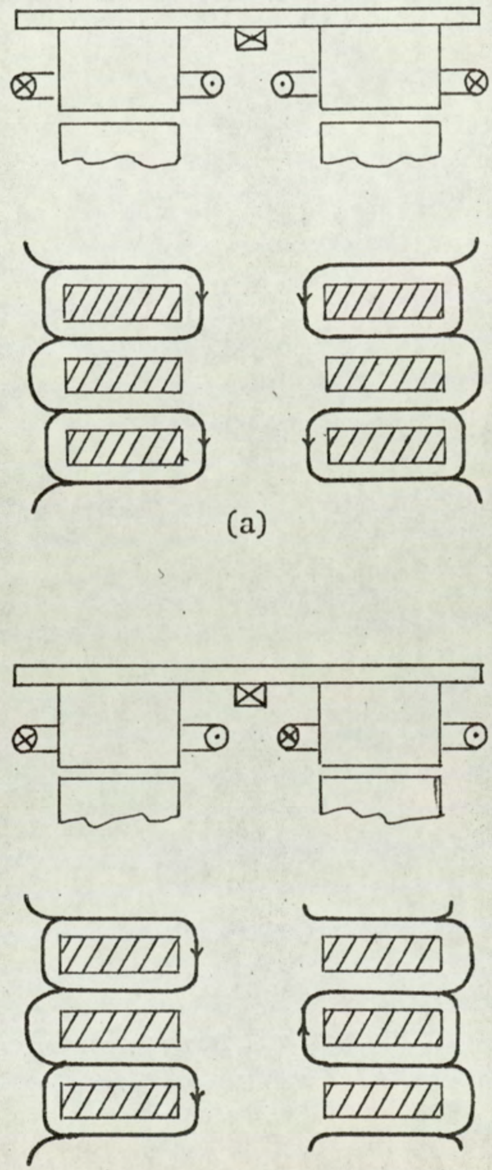

(a)

(b)

Fig 10: End windings between cores
(a) in line
(b) staggered

By staggering the coils in the two cores, fig. 10(b), this can be avoided without altering the effective number of conductors per slot. The fundamental of the full pitch distribution in fig. 9(b) about '$\alpha\alpha$' is expressed by

$$(N_a \cos \theta . \; I_a \cos \omega t)$$

where N_a = effective turns per armature coil
I_a = peak armature current
θ = space measurement around airgap from an armature coil centreline in electrical radians, $\lambda = 2\pi^c$

This can be written in the form

$$\frac{N_a I_a}{2} \left\{ \cos (\theta - \omega t) + \cos (\theta + \omega t) \right\}$$

The first term, $\cos (\theta - \omega t)$, rotates synchronously with the rotor, demagnetising the rotor tooth and magnetising the rotor slot if it be assumed that the load power factor is zero lagging. This reduces the difference between tooth and slot fluxes. The second term, $\cos (\theta + \omega t)$, may be considered as backward rotating at twice synchronous speed relative to the rotor. This will produce losses and require additional exciting current irrespective of load power-factor. '

Chapter 4 extends this theory by representing both the turns distribution and the armature current waveform by infinite series. The general expressions are derived: then the current waveform is restricted to its fundamental component and expressed with an arbitrary phase displacement from the open-circuit voltage. Thus the field patterns of the forward and backward components of armature reaction are expressed for all load power-factor values. The manner in which the forward component distorts the open-circuit rotor tooth flux-density distribution is computed: the resulting values compare (favourably) with measurements, fig. 50, 4.3.2.

Chapter 5 shows that both forward and backward components are responsible for inducing the 'reactive voltage of armature reaction'. This leads to a definition of load angle for single phase machines which is directly analogous to that existing for polyphase machines, but cannot be expressed in exactly similar terms.

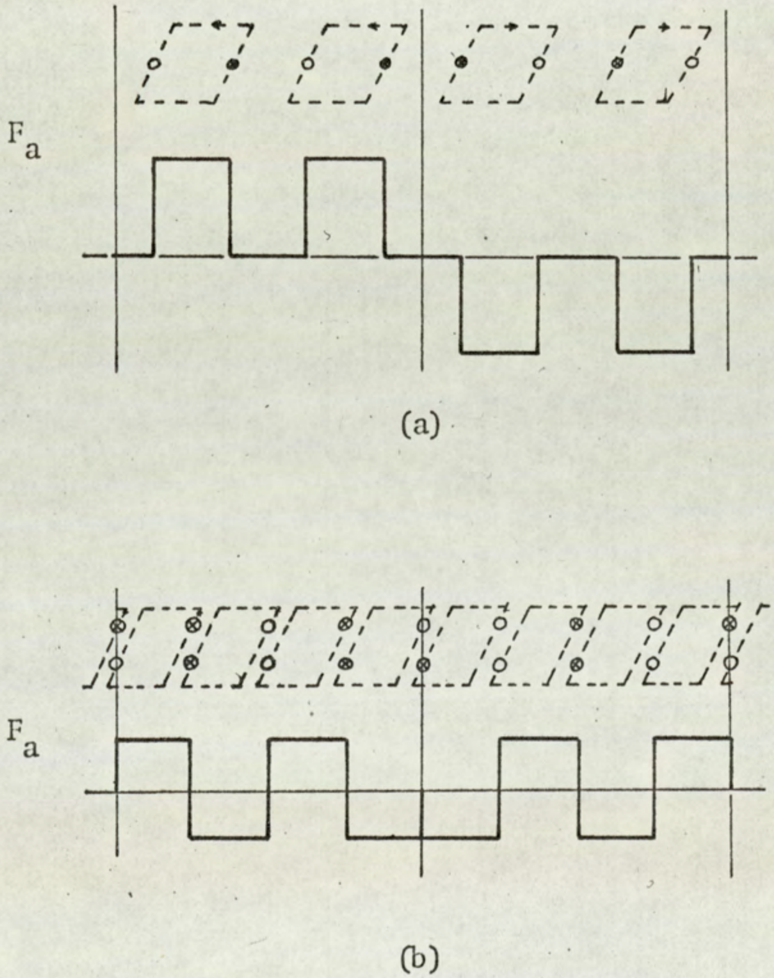

(a)

(b)

Fig 11: Reference 1
(a) fig 19 (b) fig 20

The end winding effects were described by Walker (as reported earlier in this section) by a shift of the armature m.m.f. zero line, fig. 9(b). The m.m.f. expression would then require a term to account for this displacement. When considering heteropolar designs Walker refers to figs. 19 and 20 of reference 1, here produced as figs. 11(a) and 11(b), and compares the two windings. Walker suggests that the armature reaction m.m.f. for the winding of fig. 11(a) requires a displacement term for its expression while the m.m.f. due to the winding of fig. 11(b) does not suffer this inconvenience. The writer finds these diagrams misleading, and the comparison unfounded, for the following reasons. Figs. 11(a) and 11(b) may be derived by the technique of 'summing ampere-conductors' around the airgap periphery. The zero line of such a pattern has meaning as the average of the m.m.f. variations over a complete cycle or a series of identical cycles. The cycle chosen may either have the pitch of a 'high-frequency' pole or of a field pole. Walker chooses the 'high-frequency' pole pitch for his equations, but in fig. 11(a) takes the zero line over a field pole pitch. In fig. 11(b) both cycles happen to have the same zero line and this leads to the suggestion that there is some fundamental difference between the two windings. In reality this 'difference' solely results from the lack of consistency in the choice of cycles.

Fig. 12 shows the m.m.f. patterns of each winding with zero lines drawn in as the mean level of variations with 'high-frequency' pole pitch. The zero lines for poles A and B are drawn in line simply because, in the absence of any other m.m.f.s, two isolated symmetrical systems will vary about the same mean level. The rotor is drawn in the position relative to the stator which corresponds to maximum armature current flowing in a ZPF load. At this instant, assuming the rotor slot reluctance to be very much greater than the airgap reluctance, the flux density distribution due solely to the armature ampere-turns is as shown in fig. 12. Chapter 3 investigates fluxes which link the field windings due to armature reaction flux density distributions such as both these windings exhibit. From this analysis

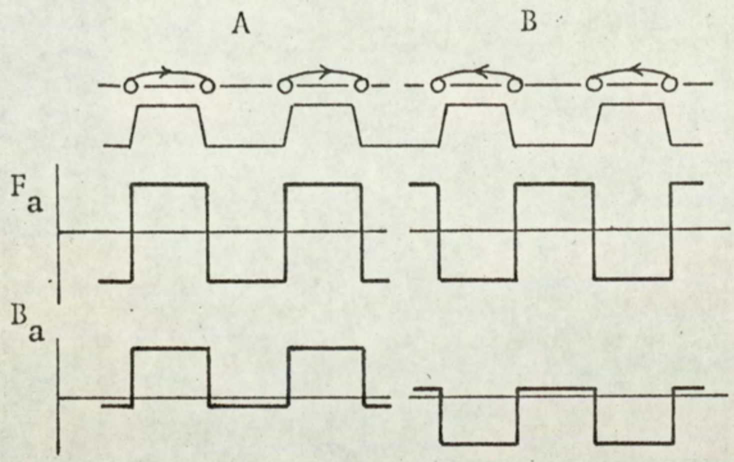

(a)

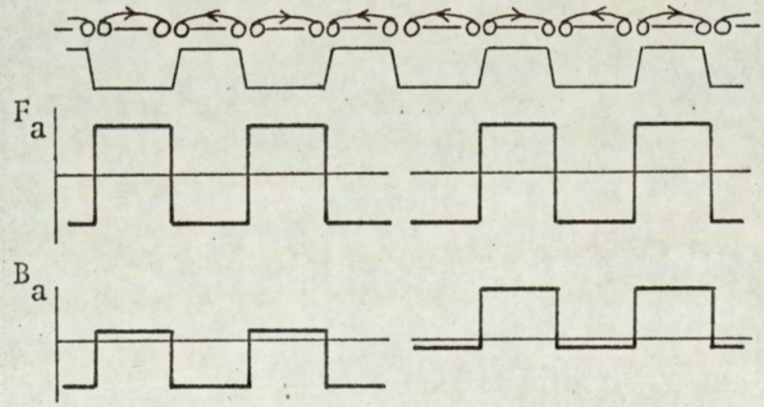

(b)

Fig 12: Peak reaction m.m.f.s and resulting flux-densities at ZPF (a) for fig 11(a) (b) for fig 11(b) neither winding scheme offers any advantage: both produce pulsations at twice line frequency linking subsequent field poles.

'With the elimination of the cos ωt (displacement term) and cos (θ + ωt) terms the armature reaction m.m.f. per pole is given by the expression

$$\left(\frac{I_a N_a}{2P_a} \right) \text{ per phase}$$

for a full pitch winding where P_a equals the number of 'high-frequency' poles (= 2 x rotor teeth). '

Walker presumes that the 'displacement' and 'backward rotating' components will be damped. The previous analysis has shown the 'displacement term' concept to be inconsistent in that it accounted for the field pole to pole fluxes of armature reaction in the winding of fig. 11(a) but not in the winding of fig. 11(b). Chapter 3 shows that, under practical load p.f. conditions, due to the airgap geometry and what appears to be a distortion of the theoretical field pattern, twice line frequency variations in flux exist but are very much reduced. It may even be unnecessary to damp them with short-circuited turns in the field slots. In Chapters 4 and 5 the backward rotating components are fully accounted for in a treatment of armature reaction which includes all combinations of 'turns distribution' and permeance harmonics which lead to fundamental variations in the reaction field pattern.

(11) <u>Damping of undesired pulsations in main flux</u>

'In the design of homopolar inductor-alternators all the undesired pulsations of main flux due to armature reaction m.m.f. may be damped by fitting copper wedges in the rotor slots which completely close the slot opening at the gap surface, the wedges being short circuited at each end. With rotors made of solid steel or iron there will be a degree of inherent damping.

With the fully laminated heteropolar design satisfactory damping is more difficult. Pulsations of main flux may be opposed by short circuited turns carried in the field slots. Any form of damping winding carried on the rotor will reduce the main field as it passes under consecutive poles. If the number of 'high-frequency' poles per exciting pole are high (> 6), copper wedges in the rotor slots (not short circuited to form a squirrel cage) will reduce pulsations in ϕ_s. '

Chapter 3 investigates the distribution of flux throughout the stator together with the factors controlling main and tooth flux pulsations. It is here convenient to introduce expressions for main flux, ϕ 1.2.2(7), due to Raby [36].

' The m.m.f. between equipotential circles, fig. 7, at any instant, is the algebraic sum of the field and the instantaneous armature ampere-turns: $(F_f + F_a \cos \omega t)$. If we assume sinusoidal permeance variations and iron of infinite permeability, we may write for the permeance at the same instant:

$$\Lambda . \{1 + \varepsilon_1 \cos (\omega t + \kappa) \}$$

where Λ depends upon the dimensions of the machine and on the unit of flux employed, and κ is the electrical angle representing the phase interval between the instants of peak current and peak permeance.

$$\begin{aligned} \text{Thus} \quad \phi &= (F_f + F_a \cos \omega t) \Lambda \{1 + \varepsilon_1 \cos (\omega t + \kappa) \} \\ &= \Lambda \Big[(F_f + \tfrac{1}{2}F_a\varepsilon_1 \cos \kappa) + \{F_f\varepsilon_1 \cos (\omega t + \kappa) + F_a \cos \omega t\} \\ &\quad + \{\tfrac{1}{2}F_a\varepsilon_1 \cos (2\omega t + \kappa) \} \Big] \end{aligned}$$

i.e. from a combination of fundamental armature reaction m.m.f. and fundamental permeance variation both fundamental and second harmonic pulsations are produced in the pole to pole flux, ϕ. '

Experiments designed to investigate these pulsations produced anomalous results, the explanations of which (chapter 3) required the analysis of component flux paths. This led naturally to an identification of those flux pulsations which can be damped and those which cannot.

(12) Calculation of field current on load

The calculation of field current on load is an area where the writer offers an alternative technique to that presented by Walker. In section 1.2.2(7), the 'primary assumption' of equipotential circles ('cc' and 'dd', fig. 7) was introduced. The comment was made that this assumption governed the type of theory, (specifically load theory) available to the designer. As previously, the Walker presentation will be summarised; followed by an introduction to the alternative process given in this thesis.

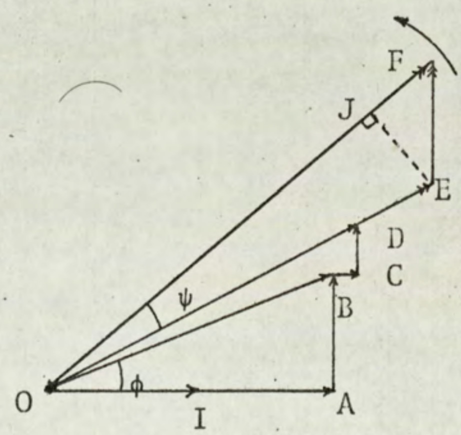

Fig 13

In fig. 13 the terminal voltage is represented by OB, and the load current by OI. The power factor of the load current is cos ϕ, and in the case shown the current lags on the terminal voltage. The resistance drop BC (in phase with OI) and the reactance drop CD (perpendicular to OI) added vectorially to the terminal voltage OB, give the internal e.m.f., OD. The ampere-turns required to produce this e.m.f. on open-circuit, 1.2.2(9), are represented by OE (in line with OD). The armature reaction ampere-turns, 1.2.2(10), to the same scale as OE, are represented by EF (perpendicular to OI). Then for a normal alternator, OF (the vector sum of OE and EF) would represent the total ampere-turns required on load. This is not the case with the inductor-alternator since the demagnetising effect of the armature reaction decreases the flux entering a rotor tooth and increases the flux entering a rotor slot. The demagnetising effect of the armature reaction is thus given by

$$(OF - OE \cos \psi) = JF$$

where ψ is the angle between OE and OF in fig. 13. This constant term is used to modify fig. 8(b) in the manner shown in fig. 14, shifting the origins of ϕ_t and ϕ_s to indicate their respective reduction and increase. The required field current is then obtained from that ampere-turn ordinate for which the difference between ϕ_t and ϕ_s corresponds to the terminal voltage. '

This analysis is true for ZPF conditions. For all other values of power-factor the fundamentals of open-circuit and armature reaction flux density will be out of phase; the field and armature reaction m.m.f.s will be acting across different airgap geometries. Walker's technique is to resolve OE onto OF, i.e. to consider the effect of both m.m.f.s acting along the direct axis of the complete field pattern and to modify the ϕ_t and ϕ_s curves as for ZPF conditions by the direct component of demagnetisation. Davies and Pedersen [30] extended this technique for polyphase machines by accounting for both the direct and quadrature components of armature reaction. They introduced the concept of direct

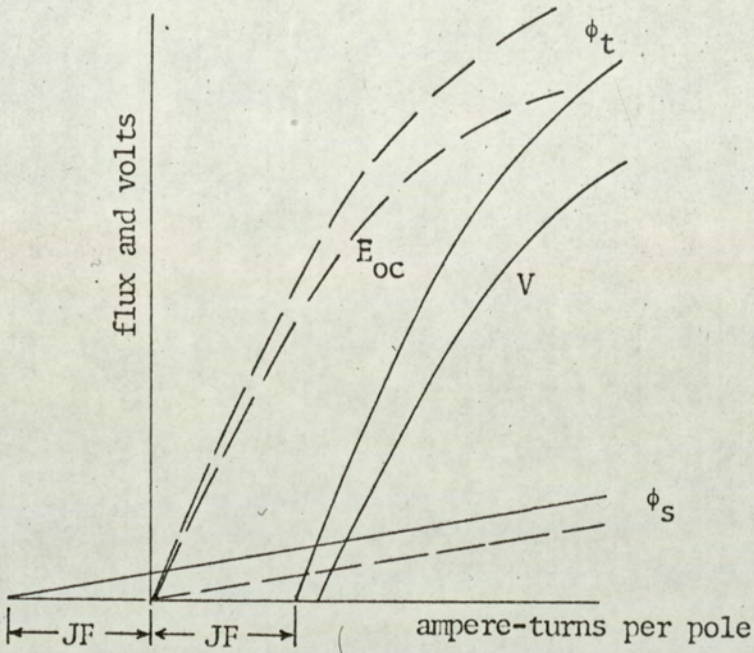

Fig 14: open-circuit -----------
on-load ———————

and quadrature-axis reactances calculated from analysis of the flux distribution in the airgap region. In fig. 15, IX_{aq} perpendicular to OI is added vectorially to OD giving OC as the axis of the rotor tooth. This agrees with normal two-axis theory and fig. 15 is a modification of the classical vector diagram for a salient pole machine. The internal voltage OD is resolved into two fictitious voltages OA and AD acting in the d- and q- axes, respectively. Now, the m.m.f. required to produce OA may be calculated by shifting the ϕ_t and ϕ_s curves through the distance F_{aq} since

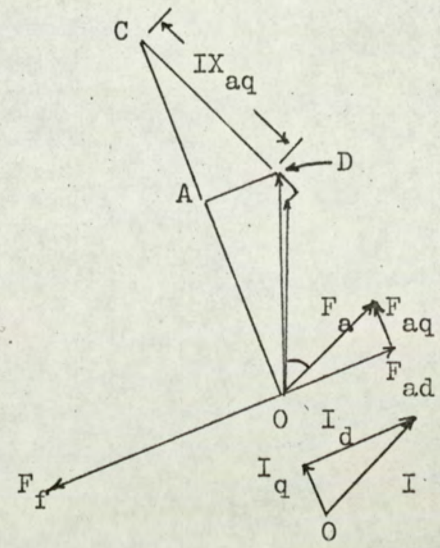

Fig 15: Vector diagram of polyphase inductor generator on-load, reference 30

this m.m.f. is directly demagnetising. The volt-drop AD, which has the magnitude I_qX_{aq} is proportional to F_{ad}. Thus, the total field m.m.f. which must be supplied is the sum of F_{ad} and the m.m.f. necessary to induce voltage OA. This theory has produced values of field current in good agreement with practice.

Additional problems arise in the treatment of single phase machines, however, which require an alternative analysis. As discussed in 1.2.2(10), the m.m.f. of armature reaction for a single phase machine has forward rotating components that may be represented on a vector diagram similar to fig. 15. There are also backward rotating components which cannot be included in such an analysis. In Chapter 5 an e.m.f. associated with the armature reaction m.m.f. alone is added vectorially to the open-circuit voltage induced by the field m.m.f. acting alone. Whereas the components of armature reaction m.m.f. may not appear on the same time vector diagram, the e.m.f. induced by this m.m.f. may be represented with the open-circuit voltage, their sum being the internal or generated e.m.f.

The on-load vector diagram is therefore 'built up' in the reverse order to the previous examples. Walker (et al) start with a desired terminal voltage and proceed to sum the component m.m.f.s required to support that terminal voltage. Due to the nature of single phase armature reaction, and as a logical extension of the theory developed in Chapters 3 and 4, the process introduced in Chapter 5 starts with the open-circuit voltage induced by the field m.m.f. and proceeds to the terminal voltage associated with a current drawn by a load at any arbitrary power-factor. The primary assumptions are not concerned with equipotentials but rather with superposition of fields and with the relationship of armature coil flux linkages to the airgap flux density distribution. This choice of assumptions has led to expressions for terminal voltage, not only in terms of load and field current as would be expected, but also in terms of the load power factor, the airgap geometry, the load angle and the leakage reactances.

(13) <u>Losses</u>

Walker assumes that all pulsations in the main flux can be eliminated and concludes that no variation in flux will occur in the stator core section.

> 'In the homopolar alternator the iron loss is set up in the stator teeth. In the heteropolar alternator additional losses exist in the rotor teeth and core due to their rotation in the heteropolar exciting field. The figure thus obtained must be multiplied by an empirical constant to allow for the effect of notching, imperfect insulation between laminations etc. This constant will usually be of the order of 2 to 3 and may be obtained from test results on similar machines'.

In the writer's experience, when manufacturing techniques which lead to breakdown in the interlamination insulation (such as machining the airgap surfaces) are avoided, the factor of '2 to 3' is reduced to one of '1.5 to 2'. The increased understanding of component flux paths (Chapter 3) and flux density distribution (Chapter 4) provide some explanations (Chapter 6) for the remaining discrepancy between calculated and measured iron losses.

Further to the volume limitations suggested by Walker the following assumptions are made in existing loss calculation procedures:

1) all tooth fluxes are radial, i.e. any 'circumferential' elements are neglected.

2) harmonic flux variations are neglected.

3) rotor flux variations are only considered at 'heteropolar frequencies, i.e. higher frequency variations due to armature reaction are neglected.

4) flux densities are calculated for open-circuit conditions, and assumed uniform across teeth cross-sections.

Since J.J. Thomson [32], a great volume of investigation has been carried out into the loss mechanism of iron subjected to varying magnetic fields. Recently Wilkins [33] (et al) has shown the degree of distortion within a batch of laminations, or even within one lamination, when the overall waveform appeared to be pure. Such problems of inhomogeneity complicate the loss calculation for simple volumes of iron. It is inevitable that a degree of 'expertise' must be applied, improved by feed-back from previous designs which have been tested, when the complex volumes of practical machines are considered.

Copper losses may be calculated in the usual manner and are normally negligible unless proper attention to armature conductor dimensions (if rectangular), and transposing [7], have been neglected. Excessive radial depth of copper or untransposed conductors will induce eddy currents and circulating currents respectively, resulting in considerable additional losses.

The second set of summaries are from 'High-frequency alternators' (ref. 2) and run from (14) to (22) as follows:

(14) comparison of salient pole and inductor type alternators

(15) comparison of homo- and heteropolar alternators

(16) single and double pitch coils

(17) classification of single and polyphase designs

(18) harmonic content of output voltage

(19) airgap length

(20) noise

(21) armature reaction m.m.f. (additions to 1.2.2(10))

(22) instruments for testing

(14) <u>Comparison of salient pole and inductor type alternators</u>

'With a maximum peripheral velocity of 40m/sec and a minimum pole pitch of 5cm the maximum frequency that may be generated by a salient-pole alternator (without using special rotor construction) will be in the region of 400c/s. The cylindrical rotor alternator may generate frequencies up to 1000c/s but compares uneconomically with the inductor alternator and is also less efficient. Due mainly to the simplicity of the rotor construction, the inductor-alternator has been used to the practical exclusion of all other types for generating frequencies above 400c/s for many years. With a minimum rotor tooth width of 0.11cm and a maximum peripheral velocity of 100m/sec the corresponding maximum frequency is 50,000c/s.'

In Great Britain the change-over from Lorenz slotting to Guy slotting occurs between 2000c/s and 5000c/s. Baffrey [34] reports the change-over in

French designs at about 10,000c/s and also quotes maximum peripheral velocities of 150m/sec.

(15) <u>Comparison of homo- and heteropolar alternators</u>

'In general, the homopolar design will be heavier and have a higher inertia providing a severe starting duty for its driving motor. The field losses may be less than for a heteropolar design due to the simpler field coil arrangement, however, this contributes to a much longer field time constant. Due to eddy currents in the solid homopolar yoke high transient voltages may persist for long enough to damage the insulation of either the alternator or the load circuit. The efficiency and output coefficients for similar ratings are substantially the same. Since the heteropolar design has a much shorter field time constant and is therefore the easier to control, and since it is also the cheaper to manufacture, this is the design used in most industrial applications.'

As solid state devices increase their power carrying capacity, oscillatory circuits are competing with the inductor-alternator for many industrial applications. The general advantages of rotating machinery, extended by the homopolar alternator's unique rotor construction, have made this type a choice for the extreme environment of spacecraft. The problems of high operating temperatures in vacuum, or corrosive metal vapour atmospheres, coupled with shock and radiation hazards, form a comprehensive design challenge.

(16) <u>Single and double-pitch armature coils</u>

'A full single-pitch coil, fig. 16(a), spans half of one rotor slot pitch. It will be seen that consecutive armature coils which lie within consecutive field coils carry currents of the same sense. Therefore they may be replaced by a single coil, fig. 16(b), with a reduction in copper, a gain in space in the field slot and no reduction in the induced e.m.f. for the total winding. Such a coil is referred to as 'double-pitch'. '

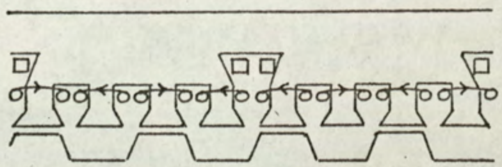

(a)

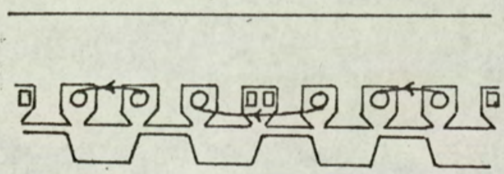

(b)

Fig 16: Armature coils

(a) single pitch)
(b) double pitch

The double-pitch coil is most commonly employed in designs using Guy slotting. M. Guy, in his patent [24] showed coils which are in fact double-pitch. It is not clear, however, that Guy attached any significance to this arrangement. The credit for recognising and analysing the potential of the double-pitch coil belongs to Dr. Walker who, together with E.C. Barwick, was granted a patent on the subject in 1941.

(17) Classification of single- and poly-phase designs

'This is a classification of heteropolar designs only; the categories depending upon slotting. Types I - III are single phase; IV - VI are polyphase.

Type I : Lorenz, one ac slot/dc pole

Type II : Guy, one ac slot/dc pole, several rotor slot pitches/dc pole, double-pitch coils

Type III : (Guy), one ac slot/dc pole, one rotor slot pitch = 2/3 stator slot pitch, double-pitch coils

Type IV : Lorenz, one ac slot/dc pole, one armature coil pitch = 3 field coil pitches

Type V : Guy, six ac coils/field coil

Type VI : (Guy), six ac coils/field coil, rotor slots equal stator slots $\pm$ 1

Types III and VI are less efficient than their alternatives. They are not Lorenz, nor are they really Guy since the unwound slots peculiar to the stator airgap geometry of Guy machines have been omitted. They have the advantage, however, of being designed for frequencies up to 12,000c/s without the stator slot pitch falling below 1.27cm. They also offer the advantages of requiring simple notching dies and the 'open' slots make for ease of winding on small frame sizes.'

Diagrams for these types are given in ref. 2. A combination slotting has been developed known as Guy-Lorenz. This employs the high-frequency generating potential of Guy slotting with the more economic armature coil to field coil ratios of Lorenz arrangements. An example is given in fig. 17

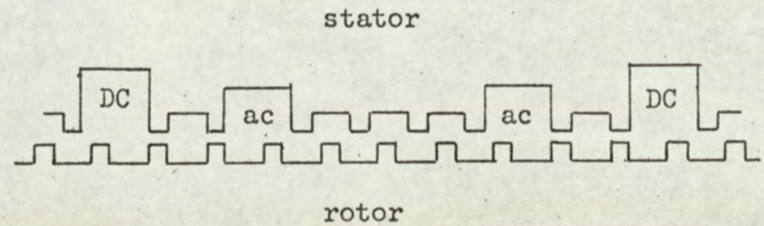

Fig 17: An example of Guy-Lorenz slotting

(18) <u>Harmonic content of output voltage</u>

In general the open-circuit e.m.f. waveform will be identical to a summation of all the odd harmonic components of the open-circuit airgap flux density pattern: the even harmonic components having been eliminated by the full pitch armature coil.

> 'The most important factor is the ratio of the width of rotor tooth to the rotor slot pitch; if this ratio is made large, i.e. 0.5, the waveform will be flat topped; if too small, i.e. 0.3, it will be peaked, each wave thus containing a substantial third harmonic. For a homopolar design, the elimination of a particular harmonic (and the incidental reduction of others including the fundamental) can be simply carried out by displacing the two halves of the rotor core with respect to each other, by the appropriate electrical angle, i.e. 60^{o}E for the third harmonic. Skewing the rotor is a similar technique for reducing higher harmonics (ripples). The importance attached to a pure waveform must be balanced against the

extent to which the machine size must be increased to compensate for the reduction in fundamental e.m.f. '

On load the voltage waveform is modified by the odd harmonic components of flux density due to the m.m.f. of armature reaction. Chapter 5 shows that, while the magnitude of these components is of consequence, the most important factor is the load angle at which the alternator is operating: this in turn is determined by the relative values of field and armature reaction m.m.f.s together with the power-factor of the load circuit. If the rotor slot opening to slot pitch ratio is chosen carefully, the next most efficient control over voltage waveform on load is the correct choice of 'working-point' (i.e. load angle) for the rated full-load conditions. This is discussed further in section 6.4.

(19) Airgap length

'In order to obtain the maximum output from an inductor-alternator the radial airgap should be made as small as is consistent with reasonable mechanical clearance between rotor and stator bore. It is necessary to use ball and roller bearings, to observe fine tolerances, and to machine the rotor and stator airgap surfaces. '

With Guy slotting for the higher ranges of frequencies, the flux utilisation factors fall to 0.2. The unwound slot openings become very small and a large percentage of the flux crosses the gap in the slot regions. In an attempt to increase ε, very short airgaps have been employed with all the associated manufacturing costs and problems. The outputs of the higher frequency machines, however, are usually limited by losses and not by flux density, see section 1.2.2(6). The writer has had some success with designs which sacrified airgap length in order to avoid machining the bore surfaces. The reduction in losses due to the full retention of inter-lamination insulation more than compensated for the increased field and/or reduced airgap flux density. This exercise has not been applied to Lorenz designs since the decrease in losses is unlikely to balance the necessary increase in field. However, experience of excessive rotor and stator bore temperatures, coupled with the conclusions of Chapter 6 on surface loss mechanisms, may well be suitable grounds for investigation.

(20) Noise

'Inductor-alternators rated at approximately 100KVA at 3000 r.p.m. or more, are liable to set up more windage noise than other industrial electrical machines of comparable physical dimensions. The relatively low mean gap densities coupled with stiff stator teeth practically eliminate magnetic vibrations as a source of noise.'

In small alternators (5KVA 500-1500c/s), magnetic noise has, in one instance, caused customers to change to solid state circuitory. The excessive vibrations were analysed by considering the stator as a dynamically loaded beam [33]. The existing deep field slots produced weak points which in turn governed the natural frequency of the stator core. In practice the machines were redesigned with wider field slots of the same depth as the armature slots (thus avoiding the 'weak points') with a dramatic reduction in noise level. Hence, although the stator teeth may be designed for stiffness and the densities not excessive, care must be taken that the natural frequency of stator, or shaft and rotor, lies well outside the range of frequencies to be generated.

(21) Armature reaction m.m.f.

'Further to section 1.2.2(10), the effect on the armature reaction of saturation in the magnetic circuit is allowed for a) by considering the m.m.f. responsible for the positive sequence component and b) by modifying the negative sequence component with a factor. Typical values for this factor are given in fig. 18 (fig. 19 of ref. 2).

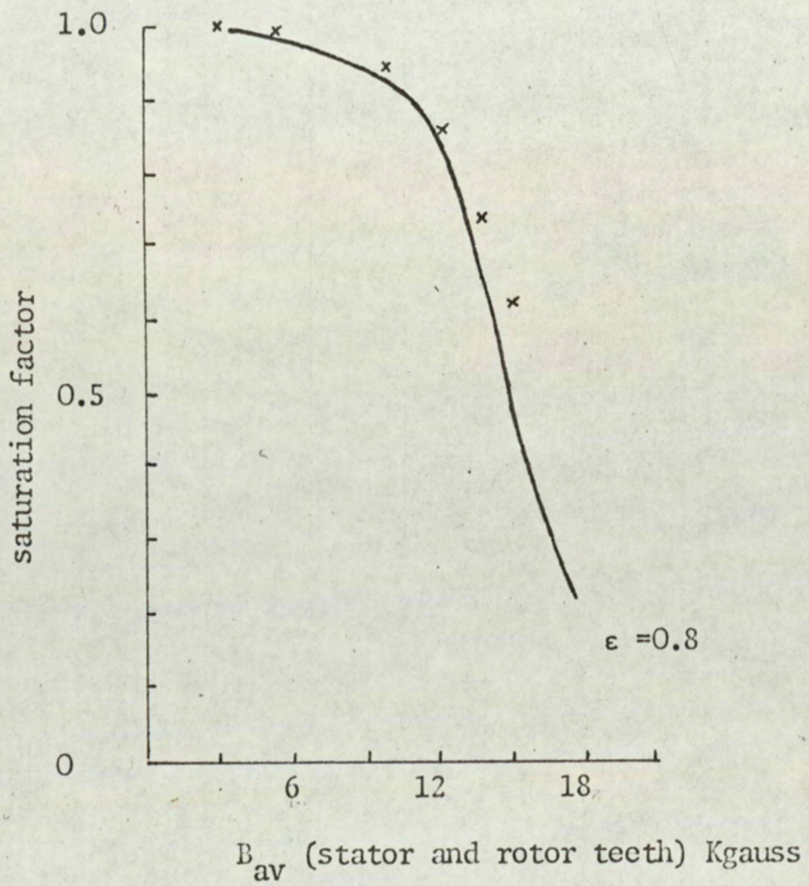

Fig 18: Walker saturation factor ——
k/k', 5.2.4 x x

In the procedure for calculating terminal on-load voltage presented in Chapter 5 a similar factor arises. This is applied to all the reactive voltages due to leakage and reaction. Points for this factor (k/k') are include in fig. 18 for comparison.

(22) <u>Instruments for testing</u>

'In testing high-frequency alternators it is most important that the voltmeters and ammeters used should have been calibrated at the frequency concerned. If the waveform deviates appreciably from a sine wave this will also introduce errors. '

Valve voltmeters are suitable for any frequency an inductor-alternator may generate. Ammeters suitable for measuring several hundred amps at 10kc/s, however, are not easily manufactured or calibrated. Galvanometers used with thermo-junctions have been successful after calibration by the N.P.L. The placing of the thermo-junction on the shunt is an empirical operation since the variation of current distribution through the shunt is a very complex function of density and frequency. Recent experiments with a linear-coupler such as is used for transmission line imbalance detection have showed promise. The linear-coupler is an air cored toroid wound in such a manner that an e.m.f. appears across its terminals in response to changes in field within the ring: it is insensitive to external fields. If the current carrying conductor is passed through the linear-coupler (similar to the manner of using a current transformer) and the output e.m.f. is integrated, the resulting signal very closely follows, and is proportional at all times to, the high-frequency current. The two e.m.f.s, one proportional to current and the other derived from the terminal voltage may possibly be multiplied by suitable amplifiers (such as form the elements of an analogue computer) to give a signal proportional to instantaneous power regardless of power-factor. This is under investigation because the conventional watt meter is presently capable of handling power at 2000c/s only if specially constructed. Instrument makers are unwilling to specify accuracies much above this frequency.

1.2.3 Surveys and discussion of papers by E.A. Erdelyi

The papers by Erdelyi (et al), referred to in section 1.2.1 as 'group (b)', are now considered in more detail. Excerpts from the introduction to ref. 18 serve to indicate the general concept and subsequent problems of this approach.

> 'Until recently, hand flux-plotting methods have been used to find the magnetic airgap induction of electrical machines. About forty years ago such a method was explained by Stevenson and Park [25]. The classical paper by Wieseman [26] using hand flux-plotting for synchronous machines, is still a useful tool of many designers. However, this method demands great skill, is very time consuming and can generally not take care of non-linear applications. For many years effort has been exerted to replace flux-plotting by hand for rotating machines by a computational method. Mamak and Laithwaite [37] have developed a method based on the magnetic vector-potential, to find the magnetic induction in the air space of heteropolar machines, under the assumption that the magnetic materials are infinitely permeable. In a former paper [38] the same concept has been used for high-speed aerospace synchronous machines, abandoning the assumption of infinite or of constant permeabilities. The method given there, a first try of this very complicated problem, has used a relaxation method that converged only slowly. '

In reference 18 Ahamed and Erdelyi changed from Froelich's formula [11] which had been used to describe the non-linear dependence of the permeability μ on the magnetic field intensity $\overline{H}$, to an alternative formulation, which involves reluctivity as a function of the flux density, '.... suggested among others by King' [39]. The quality of this type of analysis rests upon two questions. Firstly, the degree to which the analogue represents the real machine, and secondly, the accuracy of which a practical solution to the model is capable.

The second question is answered in the development of group (b). Subsequent papers evolve techniques to speed up the rate of convergence. This allows, in the same computer time, either greater accuracy per se or the use of a finer mesh. For example, from ref 11:

> '.... the solutions were checked in regard to boundary conditions. These have been satisfied and the maximum error was well below 8%, ... In order to save computer time, the total number of iterations selected was 300 per solution. The accuracy would be increased further by increasing the number of iterations and the number of mesh points. '

The first question, which would be answered by correlating measurements, has unfortunately received only minimal attention.

Ref 11 : 'At present it is rather difficult to estimate the accuracy of the solutions'.

Ref 17 : 'An exact comparison (between tests and calculations) cannot as yet be made because no accurate experimental measurements are available.

Ref 18 : 'Oscillograms of flux-distributions on a similar alternator show that the computed curves have the same shape as the experimental ones'. 'The calculated no-load characteristic of the alternator (agrees well with) a statistical average no-load characteristic of alternators of the same design...'

At each stage it has been possible to check the theory developed in this thesis by measurements, with the result that parts have been justified, and others have required further investigation. If the findings of papers 10 - 19 were substantiated at each step by actual measurement, this approach would be proved to be a very powerful design tool. Increasing computer speeds coupled with developing mathematical ability to produce iterative solutions with high convergence factors, will reduce the disadvantages associated with computed analogues even further. The designer, however, must also be satisfied that the model, whose solution has attracted so much attention, is valid for his purposes.

Many of the investigations in references 10 - 19, which involve airgap flux density distributions, describe for the homopolar alternator the same characteristics which are here studied for the heteropolar machine. A specific example, with measurements which led to 're-thinking' of theory, is given in 3.1.4 during comparisons between fundamental and second harmonic main flux pulsations. Whereas measurements substantiated the theoretical explanation for fundamental pulsations, the same theory was totally inadequate when applied to second harmonic variations. It had been assumed that the space distribution of flux density associated with the rotor, when moving at uniform speed past the stator, would produce uniform time variations in flux density at a point on the stator airgap surface. Further investigations showed that due to the stator slot openings, the field pattern was locally distorted. This had a negligible effect on fundamental, but considerable effect on second harmonic mechanisms.

In reference 14, Surti and Erdelyi introduce an 'approximate boundary condition' to represent the slot openings 'which accelerates the rate of convergence of the solution but ..... has to be used judiciously'. The authors satisfy the 'second question', referred to earlier, by checking that the model solutions with 'exact' and with 'approximate' boundary conditions are 'very similar'. The final link with practice is missing however: it is a matter for conjecture whether tests would justify their modifications or indicate a similar theoretical weakness to that described in 3.1.4.

In general the conclusions of this group are valuable in that they indicate the parameters which are expected to affect the airgap flux density distribution; they have been helpful during the work reported in this thesis. In this analysis the conditions in practice are dependent on a multitude of factors and variables; the greatest progress has been made when theory and measurement have interacted. Theory has indicated the most suitable measurements and then, often, measurements have led to improved theory as assumptions have been recognised as invalid or perhaps unnecessary.

Finally, it must be restated that group (b) has potentially the most powerful approach, especially for extremes of magnetic or electric loading. The "Sons of Martha' are well advised, however, to satisfy themselves that the elegance of the solution does not hide deficiencies in the model.

1.3 The relationship of this thesis to existing studies

The two major contributions to inductor-alternator theory considered in section 1.2 are wholly unconnected. On the one hand, group (a) papers may be described as classical in their treatment of the class of machines on a broad front. Comments on construction and application are given a similar amount of attention as the analysis of wave shape and leakage reactance. On the other hand, group (b) papers concentrate on detailed problems of field pattern and their solutions.

The contributions of both groups are directly dependent on the nature of their approach. The classical papers give a feeling for the machine as a type, and lead to a design technique which is somewhat empirical and restricted but nevertheless successful. The lack of detail as to flux distribution within the iron, the load angle, and the factors governing on-load voltage waveform, arise because the theory is expressed in overall terms of 'flux per tooth' or 'ampere-turns for gap and teeth'.

The detail papers of group (b) give no overall feeling for the class of machine. No immediate contributions to actual design procedure are forthcoming. They supply instead, complete information on the field pattern in iron and air, which allows the designer to work with more certainty as to the effects of saturation and the higher harmonics of field variations.

This thesis is the result of investigations in the region of theory and practice between the concepts of groups (a) and (b). It seemed desirable to try and extend the accepted theory of the classical approach to a level where the distribution and on-load problems might be investigated: thus avoiding the need for 'models' and iterative solutions for linear or near-linear conditions.

Similarly, experimental investigation to discover the distribution of flux in the airgap and within the iron was desirable on several counts. Firstly, it was hoped that the theory would be demonstrated as a useful representation of the real conditions. In fact as outlined towards the end of section 1.2.3 the interaction of tests and theory was of mutual benefit. Secondly, the inductor-alternator's airgap geometry and frequency make it inherently an interesting research 'vehicle'. Both aspects tend to magnify distortions, losses, and reactances, to a level where complicated instrumentation (described in Chapter 2) becomes worthwhile. Further, where a distortion or loss is due to several factors, it is possible to separate the origins: this is not always feasible in other classes of machine. Finally, in the context of an expanding machines research programme, the experience gained in the techniques of instrumentation would be valuable.

Therefore, the 'relationship' to earlier work has been one of extending the classical approach to bring its capacity for analysis closer to the level of detail offered by the model/solution approach. The emphasis has been laid on developing the theory in the form of a design procedure; testing the various stages by experiment, and using the greater analysis detail to understand the on-load mechanisms.

1.4 The main characteristics of theory in this thesis

The classical approach to analysis of flux distribution has been governed by the equation:

$$\text{Flux} = \text{m.m.f.} \times \text{permeance}$$

This relationship must be applied to a 'flux path' and involves the cross sectional area, thus not lending itself simply to the expression of a continuous function such as a distribution. For the distribution which is required is one of flux-density across individual teeth and sections of the core, not the overall expressions ϕ_t and ϕ_s.

Flux density has the property of a vector, having magnitude and direction and being expressed at a point. The distribution of flux density in the airgap was considered in section 1.2.2(2) together with techniques for deriving it in series form.

The basis for the theory is a general expression for the open-circuit airgap flux density in series form as a function of angular distance around the airgap. (The stator and rotor airgap surfaces are considered to have the same radii).

The airgap flux density distribution due to armature-reaction m.m.f. has been expressed in terms of the open-circuit distribution qualified by the ratio of field and armature m.m.f.s. This expressing of the load field pattern in terms of the open-circuit conditions was a simplification requiring careful application since it is invalid for the slot opening region. However, the corroboration of theory and test in Chapter 4 justifies the procedure.

This ability to describe the complete on-load airgap field pattern in terms of the open-circuit conditions leads on to a technique for calculating the field requirements on-load, which is offered in Chapter 5 as an alternative to the classical procedure. It is claimed that this approach is applicable to any condition of load, and tests have demonstrated its ability to represent non-linear conditions, not heavily saturated, but non-linear to the extent expected in an industrial design. The strength of the technique lies in its dependence on such parameters as, load angle, load power-factor, airgap geometry and leakage reactance. By attention to these factors the optimum balance between magnetic and electric loading for the desired working point may be investigated, 6.3. Any process which attempts to describe this many complex factors and the manner in which they interact as the machine settles to a working point, will be limited by assumptions which may be violated under extreme conditions. Within practical working regions this process has shown promise although it involves more parameters than the classical approach and still remains relatively simple in structure.

Another area in which this work has been concerned in some detail is that of negative sequence components of armature reaction. The demand for polyphase inductor-alternators is small and to have concentrated on this simpler version would have been to neglect a most important facet of the study. Some forward rotating components travel synchronously with the rotor distorting the pattern which existed on open-circuit. This pattern was computed from theory and measurements made to check the calculations. Neither the readings nor the calculations could be made until the negative sequence components were analysed and eliminated.

The concept of 'load-angle' for a single phase machine is analogous to that in the polyphase system but cannot be defined in identical terms because the field due to armature reaction is pulsating rather than rotating. Again, understanding of the difference came from the negative sequence analysis.

Therefore, the main characteristics of this theoretical approach are; flexibility, stemming from the use of the continuous flux density function in general terms;, and breadth, in that it involves all the parameters in one complete expression.

CHAPTER 2 The Experimental Machine

Summary

This chapter describes the design, building and instrumentation of the 30KW model of a 300KW industrial Lorenz-type inductor-alternator.

Sixty-six search conductors were located on the stator and a further twenty on the rotor airgap surface. On either member any two conductors may be selected to form a search coil: thus the distribution of flux in the airgap and throughout the teeth and stator core may be investigated.

The flux waveforms are obtained by integrating the search coil signals. The circuit which both integrates and measures the signals is described, together with the design of the load circuit, and a report on the driving motor.

2.1 The design of the experimental machine

In line with the policy of a Technological University, it was desirable that any theoretical advances be in terms applicable to engineering design. The smallest standard commercial generator in regular production is 300kW; this is much too big for university-laboratory use. Therefore, a 30kW model to the industrial unit was designed.

Dimensionally the model is closely equivalent on a reduced scale dictated by the output coefficient, except for the armature slots. The leakage reactance was arranged to be identical although the slots differed, but the p.u. armature resistance of the model was 0.017, against 0.008p.u. for the normal machine.

There follows a comparison of general dimensions and parameters:

dimension or parameter	model	industrial unit
frequency	1000c/s	1000c/s
speed	3000r.p.m.	3000r.p.m.
output	33kVA	333kVA
voltage	300/150 volts	1200/600 volts
current	111/222 amps	278/556 amps
power-factor limits	0.9 lead/lag	0.9 lead/lag
stator o.d.	40.0cm	76.2cm
stator i.d.	29.85cm	58.42cm
airgap (g)	0.28mm	0.76mm
core length (ℓ)	13.97cm	38.1cm
rotor slot pitch (λ)	4.69cm	9.17cm
rotor slot depth	1.02cm	1.14cm
rotor tooth width (t)	1.59cm	3.23cm
slope of tooth sides	20^{0}	20^{0}

dimension or parameter	model	industrial unit
stator slot opening	0.30cm	0.41cm
stator slot bridge	0.10cm	0.20cm
leakage reactance (x_ℓ)	0.32p.u.	0.32p.u.
ε_1	0.84	0.84
ε_2	0.83	0.83
ampere-turns/pole @ rated o.c. voltage	288	600

Fig. 19 shows the manufacturer's design sheet for the model which includes more detailed information on winding sizes and calculated load field requirements. No manufacturer's test data exists because the machine was delivered unwound. This enabled the machine to be completed in the laboratory to an experimental specification described in the next section.

Date 15.7.63 Ds. No.

CUSTOMER University of Aston **SYNCHRONOUS** AHS 6322 – 1000c/s – 3000 r.p.m.

Ex/Q A.C. Req. No. S.O. No. 65328J No. off

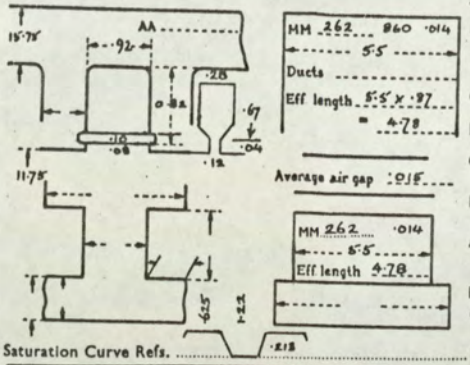

Saturation Curve Refs.

	Section	Density	AT/in	Length	AT
Stator Core	9·56 5·17	20·4	53		
Stator Teeth A.C. B max Bmin	3·4 3·12	31 74·5			
Air Gap C 2·478 kδ Leff. 5·53	4·12		61·4	·015	288
Rotor Teeth	3·31	70			
Pole Body	17·0		30		
Spider					

AT_{SI} = α = 1·08 SCR = AT_o

	AT	A	V	kW
N.L. 150 Volts	297	1·1	95	
FL(PF = ·9) LAG	666	2·47	214	·53
1 xFL(PF = 1)	478	1·77	154	·27
xFL(PF = ·9) LEAD	389	1·44	125	
xFL(PF =)				

LOSSES	Cos φ = F.L.	1 X.F.L. 0·9 LAG	1 X.F.L. U.P.F.	1 X.F.L. 0·9 LEAD
Windage Bearing		1·6	1·6	1·6
Core –		1·51	1·10	0·81
I^2R Stator 75° C		·57	·46	·57
Eddy Load		1·71	1·45	1·71
I^2R Field 75° C			·27	
Exciter –				
Total –		5·39	4·88	4·69
Output –			30	
Input –			34·88	
% Efficiency –			86	
Guarantee/Offer				

Specn. Enclosure

Drive Fans

kVA 33·3 Connection S P P. Speed 9230

Cos φ 0·9 Volts per phase 150 Pole Pitch 4·62

kW h.p. 30·0 Amp. per phase 222 Pole Arc = %

G = G_1 = Leakage Co-eff. Eff. P.A. = %

$$\text{Flux} = \frac{150 \times 10^8}{4{\cdot}44 \times 32 \times 1000} = {\cdot}1056 \text{ mgl.}$$ Field Flux = mgl.

$$AT_{AR} = \frac{\sqrt{2} \times 222}{2} \times \frac{4}{2} = 314$$ per inch

$\frac{kVA}{D^2L.N.}$ = 1·46 × 10^{-3} B. mean = 19·9 A.C. per slot

$\mathcal{E}_1$: ·838 $\mathcal{E}_2$: ·834 φ : 0·255 A.C. per inch

STATOR WINDING ϕ_t : 0·232 FIELD WINDING

Cond. Insn. I.S.	Turn Insn. Ter. T. SW. 62027	
Type of Winding	CHAIN	CHAIN
No. of Slots 2 // ckts — Total	40 = 32	+ 8
per phase		
Eff. per ph.	16	8
Conductors per Slot — Total	4	540
Effec.	4	540
d. bare	·24 × ·090	·028
d. insul.	·245 × ·095	·0312
"mf Cr. Secn.	·0212	·000616
Insulation — Sides		
T. and B.		
Total Copper Secn.	2·71	·266
Current Density	5240	4000
Mean L. of Turn	18·5	30
Turns in Series/ph.	32	2160
Res./ph. at 75°C	0·0115	= %
" " " 20°C	0·0095	= %

Ext. Turns I.S.	Turn Insn. F.F.
Type of Winding	
No. of Poles	8 DC 40 AC
Poles in parallel	20 slots
Turns per pole	270
d. bare	
d. Insul.	
Cross Secn.	
Current Density	
Mean L. of Turn	
Total cu. Secn.	
Ind. Volts per layer	
Res. at 75°C	86·7
" " 20°C	71·4

SQUIRREL CAGE WINDING

Bars ·045 × ·875 × 7·5 □"

Rings/Segs ·06 × ·55 × 45·5

λr 1·845 λs $\frac{\lambda r}{\lambda s}$ =

$$P_s = \frac{{\cdot}36}{3 \times 2{\cdot}3} + \frac{{\cdot}114}{{\cdot}28} + \frac{{\cdot}021}{{\cdot}16}\, \ln \frac{{\cdot}28}{{\cdot}12} + \frac{{\cdot}04}{{\cdot}12} + {\cdot}113$$

$$x_1 = 2\pi\, 10^3 .3{\cdot}2 .32{\cdot}4 [5{\cdot}5 .1{\cdot}393 + 0{\cdot}4\sqrt{1} .7{\cdot}5] .10^{8} = \left\{ \begin{array}{l} 0{\cdot}217\ \omega \\ 32\ \% \end{array} \right.$$

Iron Losses { Core 14 / Teeth 19·4 } 4·78 { 1·0 / 2·2 } { ·067 = / ·204 = ·271 }

Surface Loss R. ~~teeth~~ 2·66 / Loss R. core 39 } 478 { 1·05 / 1·75 } { ·21 } = { ·023 = / ·069 = ·092 }

S/g = 81·3 $\frac{t}{\lambda}$ = b/λ = 0·339 Total = ·363

POLE DIES	WINDING HEATING
Face Clip	Stator Watts/sq. in. Slot T. Drop °C
Piercing	Field Surface Watts/Sq. in.
Blanking	
Base Clip	K " ,,(mod.) (at °C) °C (res)

REGULATION, etc.	WEIGHTS, etc.
At F.L. (PF =) = %	S. Copper
" " (PF =) = %	R. Copper
Max. Output = × h.p.	Sq. C. Bars
P_o at PF = × kVA	Sq. C. Rings
WR^2 Rotor	
WR^2 Flywheel	
Nat. Frequency	

Des. by EB/JM RKL/EJD Appd. by

Fig 19

2.2 Building the experimental machine

2.2.1 Reasons for building in the laboratory

The machine was delivered unwound for two reasons: a) the instrumentation would involve search conductors within the iron circuit: it was necessary therefore to break down the stator core. b) with the intention of studying loss mechanisms during the research it was necessary to ensure that the inter-lamination insulation was satisfactory.

Winding the machine in the laboratory offered the further advantage that the layout could be designed for easy dismantling in the event of failure or the need for additional instrumentation.

2.2.2 Preparing and assembling the core laminations

During manufacture the rotor and stator cores had been built up, skimmed, and the whole assembled in order that the airgap dimension might be checked. The process of 'skimming', although carefully supervised, tended to destroy the inter-lamination insulation at the airgap surface. Each punching was individually inspected and all instances of 'burring over' carefully removed. As a final precaution all the laminations were then 'burr-rolled' and revarnished. Small changes in dimensions due to this process were not sufficient to produce any difficulties in re-assembly, or marked deterioration in the airgap surfaces. The stacking factor fell from .88 to .875.

To accommodate the search conductors a special stator-core packet, 1.27cm long, was fastened together using rivets situated away from the varying fluxes. This was then drilled as shown, fig. 20(a)(b), with 0.025cm diameter holes. The packet was securely clamped to minimise burrs. It was not possible to anneal after drilling, because the punchings were already varnished. The effect of drilling on the magnetic characteristics was discussed with a metallurgist and a physicist who in the absence of

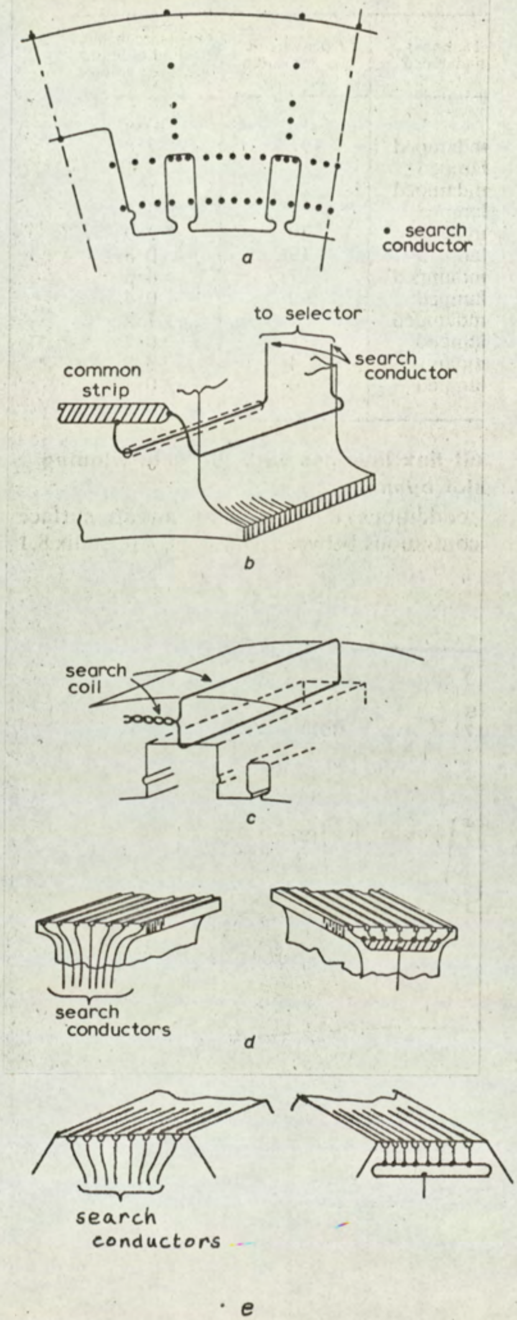

Fig 20: Details of search conductors

(a) Position of search conductors in a test stack punching
(b) Test stack with search conductors showing common strip
(c) Search coil for sensing flux passing behind field slot
(d) Surface search conductors on stator teeth seen from both ends of the core
(e) Surface search conductors on rotor teeth from both ends of core

published data, felt that the error from this source would be small. The laminations on either side of the packet were cut away to allow the introduction of the search wires.

Early attempts to locate search conductors on the surface of the stator and rotor teeth with Araldite, were short lived under operating conditions. It was necessary to machine channels 0.025cm wide and 0.02cm deep along the surface of the teeth using a slotting saw, fig. 20(d)(e). The conductors were then safely set in Araldite so that no part projected into the air space.

2.2.3 Windings

Three windings were required; for armature, field and damping.

The a.c. coils were formed from rectangular copper (6.1mm x 2.3mm) bent on edge as push-through hairpin coils. To allow the winding to be dismantled without difficulty, special links were devised to complete the coils at the connection end, fig 21(a). 32 a.c. slots each contained four conductors. Two parallel circuits were wound in alternate pairs of poles, i.e. poles 1, 2, 5 and 6 and poles 3, 4, 7 and 8, giving 32 effective turns in series. The 'copper content' of the slots is low, fig 21(b), in order that slot leakage characteristics might be analysed by varying the separation between conductors.

Each of the eight field coils comprised 270 turns of 0.71mm diameter wire. The coils were series connected and wound with consecutive coils having opposite directions. The internal connection between coils 1 and 2 was tapped and brought out to enable measurements to be made on one field coil alone.

The damping windings were in the form of a cage of copper strips lying at the bottom of each field slot. At one end, all the strips were connected to a common end ring. From the other ends individual leads, all of the

(a)

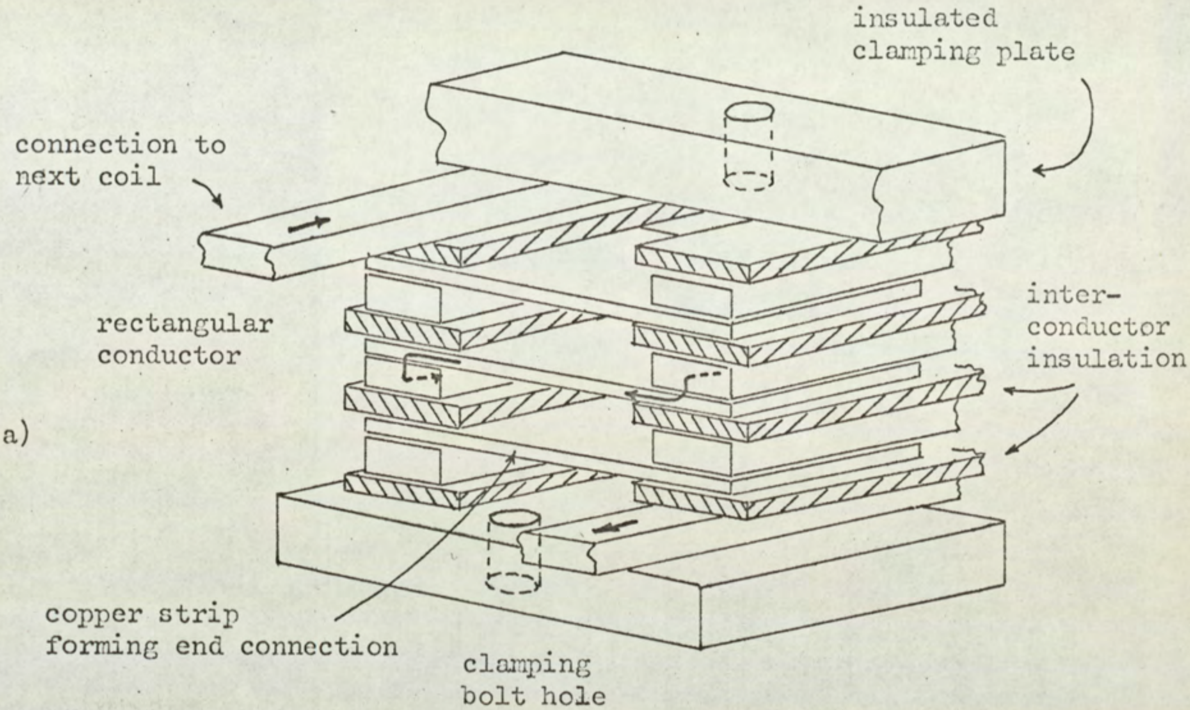

(b)

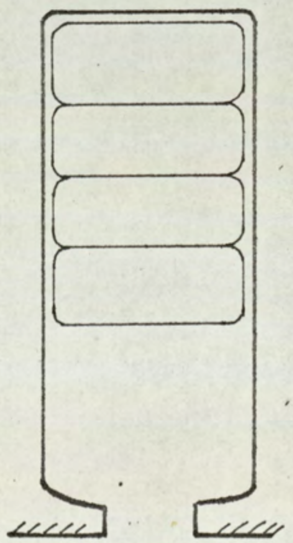

Fig 21: armature winding

(a) end winding connections for one armature coil

(b) slot copper content

the same length, were brought out to a special terminal block at which any number could be connected together.

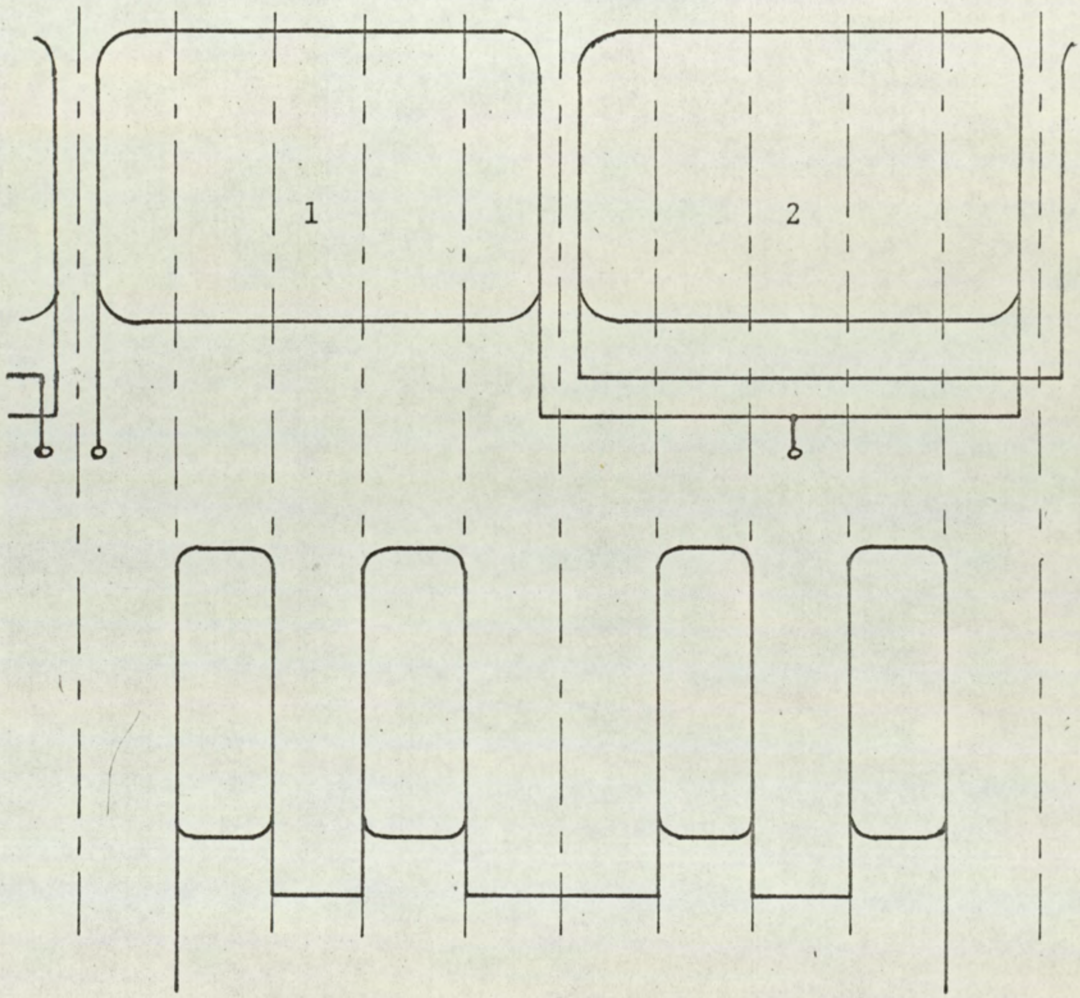

Fig. 22: Winding diagram for field poles 1 and 2

2.3 Instrumenting the experimental machine

To investigate the flux density distributions within the iron, which were the subject of the theoretical analysis, required a mesh of search coils. The drilling of suitable holes was described in 2.2.2, and fig 20 shows examples of the different locations and constructions employed. Plots using conducting paper (section 3.1.2) had established the desirability of at least six coils within a main tooth cross section. To avoid removing more than 10% of the iron cross section by drilling, it was necessary to use drills not greater than .025cm in diameter. If each small area was to be covered by a search coil, each hole must carry two coil sides, which fixed the preferred wire size at .076mm. A trial winding demonstrated just how delicate an operation producing such a system would be, and how limited an operating life must be expected. Further, the failure of one coil would mean the complete loss of any measurements from that area.

Working on the assumption that the inter-lamination planes were field equipotentials, i.e. that flux crossing this space was negligible, it appeared possible to use a common connection to all wires at one end of the 'packet' without introducing stray signals. The immediate advantages would be

1) half the number of wires
2) half the number of external connections
3) an increase in wire size

A pilot scheme was wound and not only proved successful but also demonstrated the very great potential of the resulting mesh. Any two search conductors might be externally chosen to form a search coil; for n conductors there were $\frac{n}{2}(n-1)$ possible search coils. Further, if one conductor failed the mesh 'pitch' in that area would increase, but a measurement might still be made.

These coils were supplemented by larger coils

a) around the stator core behind the field coil, fig 20(c)
b) in the surface of the stator and rotor teeth, fig 20(d) and (e)

These coils were run the whole length of the machine, thus embracing the total flux passing through that section. In hindsight this was a mistake because the stator surface coils and coil (a) above could not then be incorporated into the mesh. The decision was taken before it was certain that the small 'packet coils' would produce signals suitable for amplification and analysis. Since the airgap region was of primary importance it was decided to extend the surface coils the complete core length and be sure of useful signals.

Immediately each side of the instrumented packet the laminations were cut out to accommodate the common connection system, and the wires being led out radially. The stator surface wires were led, suitably twisted, around the back of the core. Both groups emerged through a ventilation port in the frame and were terminated at a double pole multi-way selector switch.

As the programme has developed, considered theoretical analysis has been corroborated using the existing search coils, For further study of the circumferential components of flux in the tooth surface regions it will be necessary to rewind the surface coils to include the 'packet' length only, and then link the surface common connection to the existing system.

The twenty rotor surface search conductors were led to a connection board on the rotor end-plate, from which heavier protected wires were run through a channel in the shaft under the bearing, out across a nylon universal coupling, to the slip ring assembly.

The assembly contained eight slip rings whose terminals were carried on an insulated annulus mounted on the shaft. From the slip ring terminals eight short wander-leads with plugs were connected to any eight of twenty sockets, carried on a board also mounted on the annulus, which represented the terminals of the rotor surface search coils. The brush terminals, mounted on the assembly frame, for any eight socket selections made before the machine was run up, represented twenty-eight possible search coils.

Three thermocouples were buried in the windings to monitor the working temperatures; two in the armature winding, one in the bottom slot and one in the end winding, and the third in the bottom field slot.

2.4 Supporting apparatus for the experimental machine

2.4.1 The driving motor

The driving motor had the following description.

T.E.F.C. Squirrel Cage induction motor No. 172863

Power	45 h.p.
Full load current	57 amps
Supply voltage	400 V. 3 phase 50c/s
Speed	2,940 r.p.m.
Rating	Continuous B.S.S. 168-1936
Manufacturer	Electric Construction Co. Ltd.

The motor output and efficiency were accurately calibrated at the Witton Laboratories of the General Electric Co. using a 60 h.p. precision dynamometer.

The motor and the experimental machine were flexibly coupled and mounted on a bed plate. The motor supply circuit is given in 8.2

2.4.2 The load

Several methods for dissipating the alternator output were investigated. The ideal specification would be a pure resistance, infinitely variable from 15Ω to 0.5Ω (10 amps to 300 amps).

Fan cooled load resistors (8.1 item 17) were variable but limited to 10 amps each. Expanded metal cages were capable of dissipating the load but suffered from being bulky and difficult to adjust.

The eventual solution was a nickel helix resistor on a ceramic core. This was small (3" diameter x 14" long) 3Ω maximum, variable by adjusting terminal clamps to any point on the helix, and cheap. Suspended in water which could be continuously changed, this device was capable of dissipating 50kW. Fortunately, the power-factor of this 'load' was effectively unity at 1000c/s. Only when the resistance was reduced to a low value, say $\frac{1}{2}\Omega$, and the reactance of the main leads became comparable (although they were kept as short as possible), did the power-factor of the load circuit change appreciably.

2.4.3 <u>Signal integration and measuring circuit</u>

The e.m.f. signals supplied by each search coil were proportional to the rate of change of flux (w.r.t. time) linking the coil area. In order to display and analyse the linking flux waveform, each signal was integrated using an operational amplifier (8.1 item 2). The mean level of the flux waveform, when displayed on an oscilloscope (8.1 item 1), may be arranged to lie on a given graticule by adjusting the oscilloscope controls. It may also be moved by injecting a d.c. voltage with the signal. In this manner the trace may be 'biassed', from peak to peak, or over any other desired dimension of the waveform. By amplifying the trace, and measuring the required bias d.c. input using a digital voltmeter, measurements may be repeated with an accuracy of better than 0.5%. The diagram of the circuit which was used it given in fig. 23.

A general list of other supporting instruments is given in 8.1

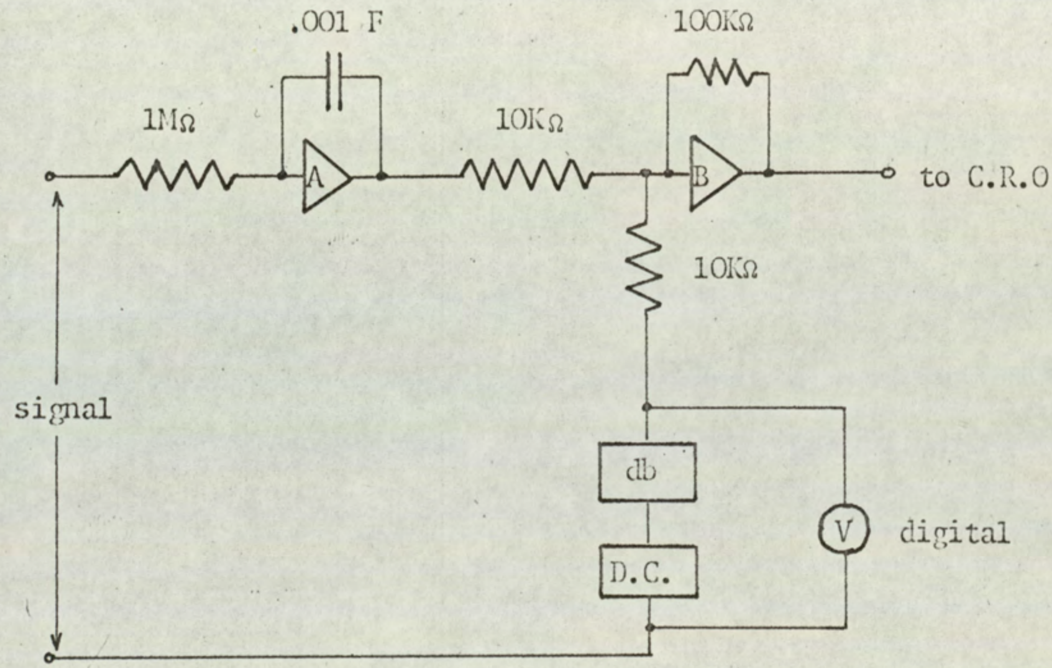

Fig 23

CHAPTER 3 Distribution of flux within the stator

Summary

In this chapter the manner in which flux levels vary throughout the stator iron is studied. The variations fall into the following categories

(a) variations due to design; those that are intended and which would exist in an ideal machine.

(b) variations, and modifications to (a), which exist because slots in the stator iron dictate the paths and magnitude of the flux components.

(c) variations under load conditions which are inherent in the design but which serve no useful purpose.

The differences between the actual and the ideal geometry of a machine are analysed using a conducting paper analogue. The results are given in the form of flux distributions within each tooth during a cycle; these are further analysed in terms of the harmonic content of the resulting flux density waves. The search coils are next used to establish the magnitude and phase relationship of flux components in various sections of the core and teeth, from which it is recognised that the airgap tooth widths control the overall pattern. A theory is derived to express the effect of armature slot opening dimensions. This suggests an open-circuit flux distribution throughout the teeth and core which is corroborated by measurements for fundamental variations. Second-harmonic variations are adequately described as to distribution and a distortion in the field close to the armature slot openings is shown to account for the difference between measured and calculated values.

The theory is extended to describe the flux distribution due to armature-reaction. Variations at twice line frequency due to the combination of the fundamental reaction m.m.f. and permeance variation are expressed in terms of the armature slot opening and an angle proportional

to the load angle. The measured effect of these additional components on load was small compared with theoretical values, and difficult to isolate in order to establish an explanation (presumably similar in kind to that accounting for the reduced open-circuit second-harmonic components). Therefore, the load theory was corroborated from a different approach which is reported in Chapter 4.

Finally, the greater understanding of flux distribution, and the voltages induced in the field coils, shows that damping turns are an unnecessary waste of field slot space in this particular machine. The losses will be redistributed rather than reduced and the peak induced voltages in the field windings are not excessive.

3.1 Distribution of stator fluxes under open-circuit conditions

3.1.1 Introduction

According to 'group (a)' theory, 1.2.2(4-9), variations in flux level are confined to the teeth and the section of core immediately behind the armature slots. On open-circuit no variations are expected in the main field pole to pole flux. Movement of the rotor past a stator tooth is designed to vary the flux carried by that tooth between a maximum of ϕ_t and a minimum of ϕ_s. The pattern of change from ϕ_t to ϕ_s is presumed to bear a linear relationship to the change in permeance of the airgap space facing the stator tooth, since the rotor speed is constant.

This theory was based on an element of the airgap geometry covering one rotor slot pitch. Two possible causes of variations not accounted for by this approach are

1) the 'half-teeth'
2) the overall change in circuit permeance from a maximum when a rotor tooth faces a stator tooth to a minimum when a rotor tooth faces a stator slot.

The conducting paper analogue, 1.2.2(2), offered a comparatively simple technique for a preliminary investigation as to whether the 'practical geometry' differed from the theoretical 'element' in its response. Not only were the tooth fluxes, as functions of time, found to contain substantial harmonic components; but the distribution of flux density within the teeth, and the differences between teeth, were indicated

These findings also suggested the most useful positions for search conductors in the experimental machine. From the search coil e.m.f.s, values were obtained for flux variations throughout the iron. Analysis of the voltages induced in a single field coil added to the knowledge of flux distribution, but also produced some anomalies.

As a result it was clearly necessary to investigate the nature of each tooth's 'contribution' to the core fluxes. Since the information already to hand was not consistent with the concept of equipotential m.m.f. circles, 1.2.2(7), a theory based on the airgap flux density distributions was employed. If the tooth distributions were to be analysed, the theory which lumped teeth and gap together had to be abandoned in favour of one which allowed separate, but interdependent, treatment of gap and teeth regions.

This leads to explanations for the anomalies and descriptions of the modifications to the 'ideal' theory required by individual airgap geometries.

3.1.2 <u>The conducting paper analogue</u>

The theory of conducting paper analogues is well documented [29]. In the majority of applications the paper represents the airgap space, with the iron boundaries as electrodes between which the voltage (analogous to m.m.f.) is applied.

The smallest segment of the stator bounded by radial equipotentials was a full field pole pitch, as shown in fig. 24. Although this area is symmetrical about the middle tooth centre-line, the permeances of each 'half field pole pitch airgap space' varies; for only two positions of the rotor are they equal. It is unlikely that the flux density along the field slot centre line will be uniform. However, since the gradient is unknown, and its representation complex enough to detract from the essential simplicity of the analogue, uniform density distribution is assumed. Any inaccuracies are unlikely to seriously affect the tooth field patterns.

Therefore, the current is fed in on two electrodes along the field slot centre lines and led out across the tooth airgap boundaries. Each tooth boundary is divided into ten tabs. To the same scale the armature

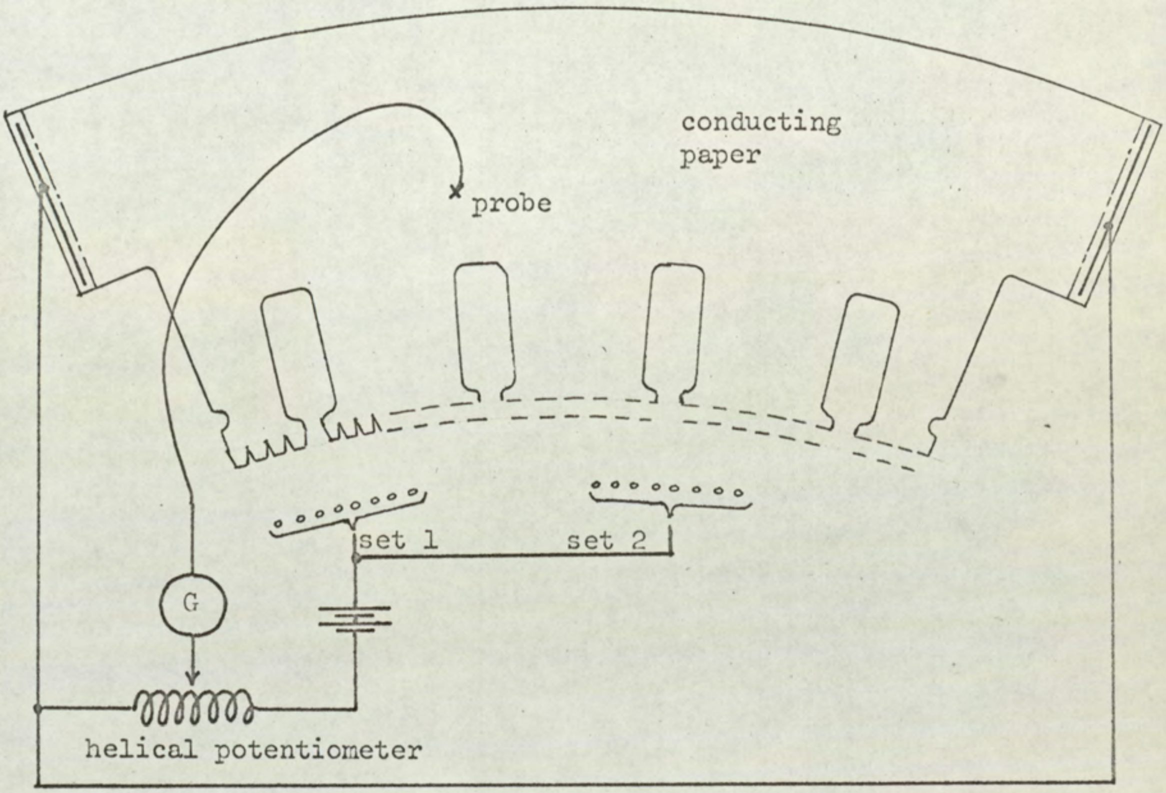

Fig 24: Full d.c. pole pitch conducting paper analogue and circuit for details of tab connections, see Fig 25.

slot opening is approximately 2 'tabs' width and the rotor tooth, 8 'tabs' width.

Leading the current out through the eight central tabs on a stator tooth boundary simulates a rotor tooth in line with a stator tooth. Similarly leading the current out through the three tabs on either side of a slot opening, fig 25, simulates a rotor tooth opposite a stator slot.

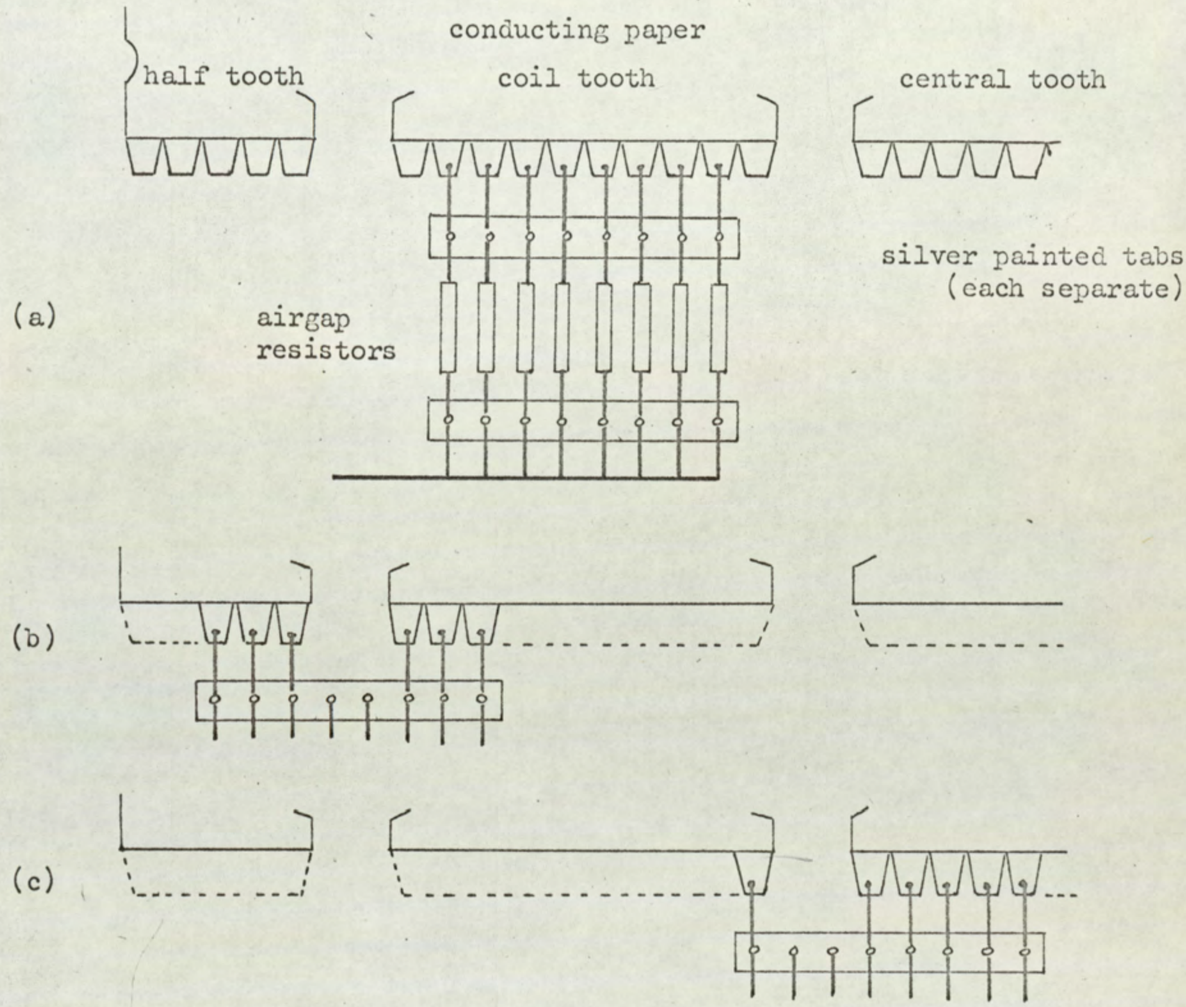

Fig 25: Detail of airgap surface 'tabs' on conducting paper analogue fed by resistors representing the airgap

(a) position 1, set 1 (b) position 19, set 2

(c) position 9, set 1 .

The circuit is completed through parallel resistors, one for each tab in operation, which represent the airgap. Thus for 'rotor tooth opposite stator slot' the number of parallel resistors is reduced from eight to six, increasing the total resistance of the circuit and therefore representing a decrease in permeance. The value of each resistor is calculated so that $\frac{\rho \text{ gap}}{\rho \text{ iron}} = \mu_r$; the value for μ_r is a function of tooth flux density.

Hence, by moving two sets of eight connections across the stator boundary 'tabs', the field pattern was investigated for several rotor positions, fig 26. The equipotential lines were plotted by selecting a ratio (with the helical potentiometer) and tracing the locus of points which gave no galvanometer deflection. This is a standard technique: the field density is proportional to the proximity of the equipotentials.

Conversely the potentials at two points may be measured. The average potential gradient between the two points is proportional to the mean field density along a line joining the two points. Hence, by subtracting the potentiometer reading at the first point from that at the second point, for different 'rotor positions', a cycle of readings proportional to the variation of flux density was obtained. The choice of 'points' governed the region within the teeth and the direction of the component which was investigated. Fig 26 shows the variation in field direction close to the airgap boundary. Readings there were taken as 'radial' and 'circumferential' components and used to investigate surface loss mechanisms, 6.1. Through the root of the teeth the field direction was close to radial throughout a cycle.

Variations of density in the main and half teeth roots were fourier analysed. Fig 27 shows the respective plots and table 1 the harmonic content of these variations.

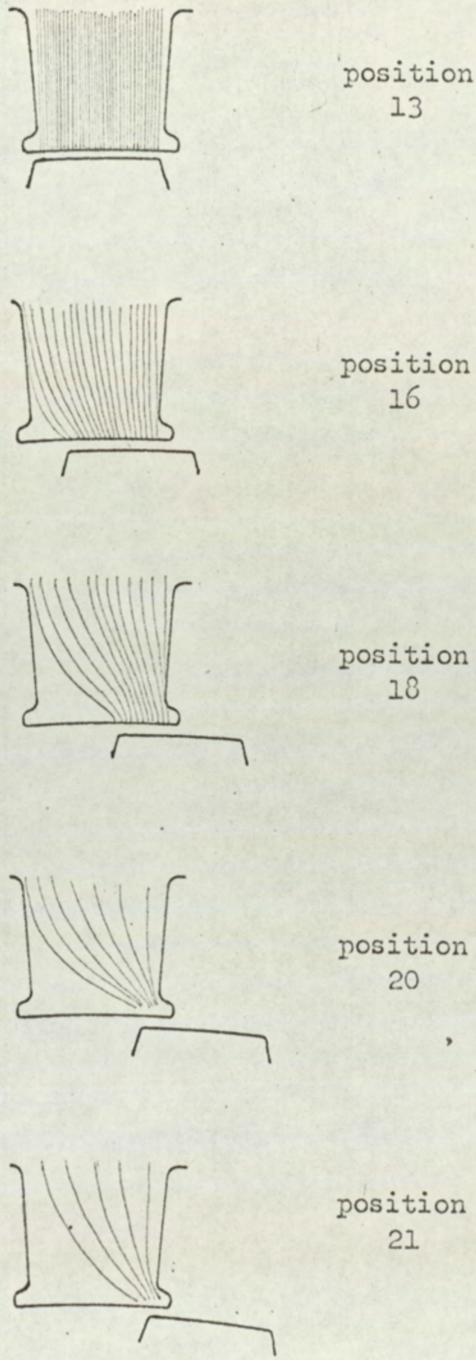

Fig 26: Orthogonal sketches from central tooth of conducting paper analogue

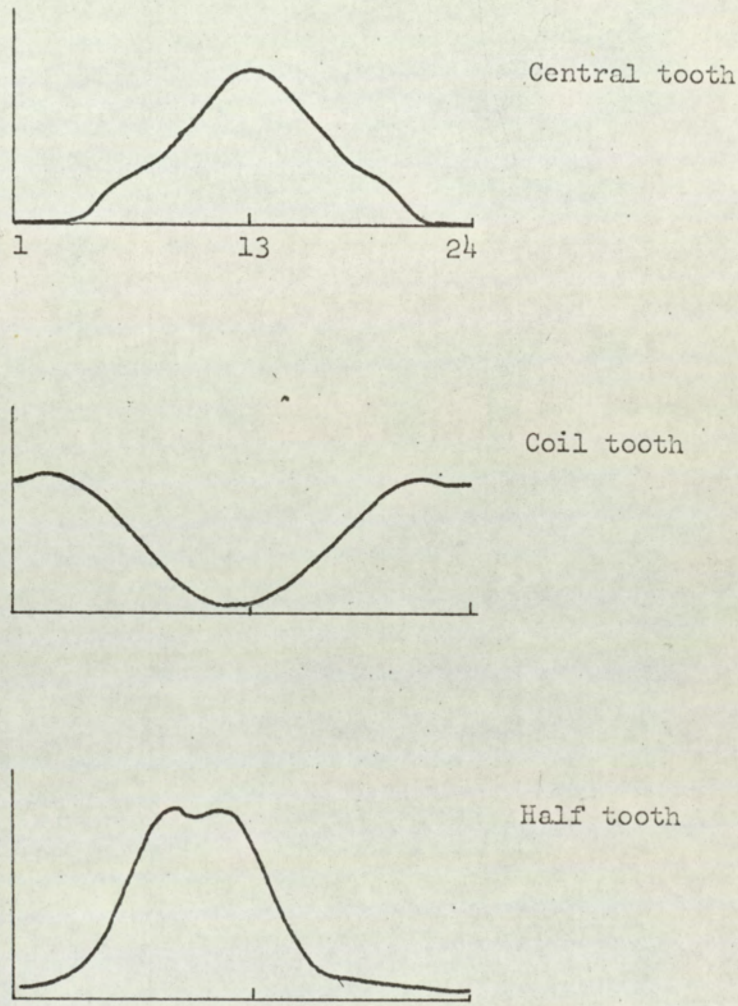

Fig 27: Cycles of variation in B ($\propto V/\ell$) at centre of each tooth root from conducting paper analogue, see Table 1 for analysis.

Table 1: Harmonic content (%) of cyclic variations in flux density at the stator teeth roots from measurements on a conducting paper analogue

harmonic order	half tooth	coil tooth	central tooth
fund.	100	100	100
2nd	38	14	14
3rd	2	2	4
4th	5	5	8
5th	2	5	3

The conducting paper analogue showed in a qualitative fashion, and a relatively short time, the nature of the field pattern within the stator teeth. This was invaluable, both for the placing of search conductors, and in the interpretation of readings subsequently taken on the experimental machine.

3.1.3 Investigation of the flux distribution by measurements

In the design of the conducting paper analogue it was assumed that the flux passing behind the field slots did not vary in time. To investigate the conditions in fact, a search coil was wound, fig 20(b), and the field winding was tapped in order that one coil might be used as a large 'field slot to slot' search coil. Fig 28 shows the harmonic analysis of the voltage induced in this single field coil under open-circuit conditions. Each harmonic was measured with and without the damping circuit connected.

When the harmonic fluxes passing behind the field slot were measured, for similar conditions, and compared with the fluxes linking the field coil, unexpected flux/voltage relationships appeared.

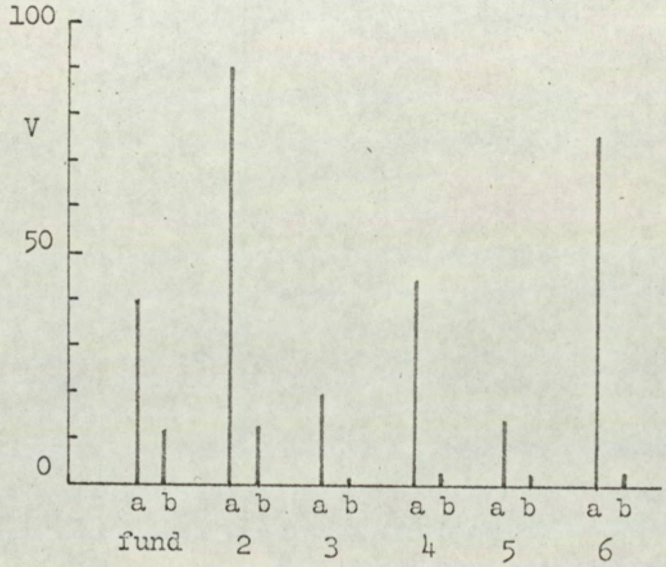

Fig 28: Harmonic voltage modulations present in a single field coil on rated open circuit (V_{rms})

(a) undamped

(b) damped

Note: Sum of all modulations across whole field winding < 1.0 volt

Table 2: Comparison of harmonic fluxes measured behind the field slot with those calculated from the voltages induced in the field coil.

harmonic	damped/ undamped	open-circuit flux measured μWb	open-circuit flux required to induce measured voltage μWb
1	undamped	191	7.8
	damped	189	3.1
2	undamped	15	19
	damped	2.6	2.5
3	undamped	20	2.9
	damped	19	0.3
4	undamped	7.7	4.6
	damped	0.7	0.4
5	undamped	4.6	1.2
	damped	2.3	0.2
6	undamped	4.4	3.9
	damped	0.3	0.2

Table 2 shows clearly that

a) the even-harmonic fluxes agree reasonably with the voltages they induce. They are substantially reduced by damping.

b) the odd-harmonic fluxes have much greater magnitudes than are required to induce the voltages found in the field coil. The fundamental and third harmonics are almost unaffected by damping, suggesting that the vector sum of the two fluxes behind adjacent field slots does not vary within the damping winding of that pole.

It was evident that odd and even harmonic flux components are distributed throughout the stator iron in separate and distinct patterns. A first attempt to learn more about these differences by measurements using the 'packet' search conductors is tabulated in fig 29.

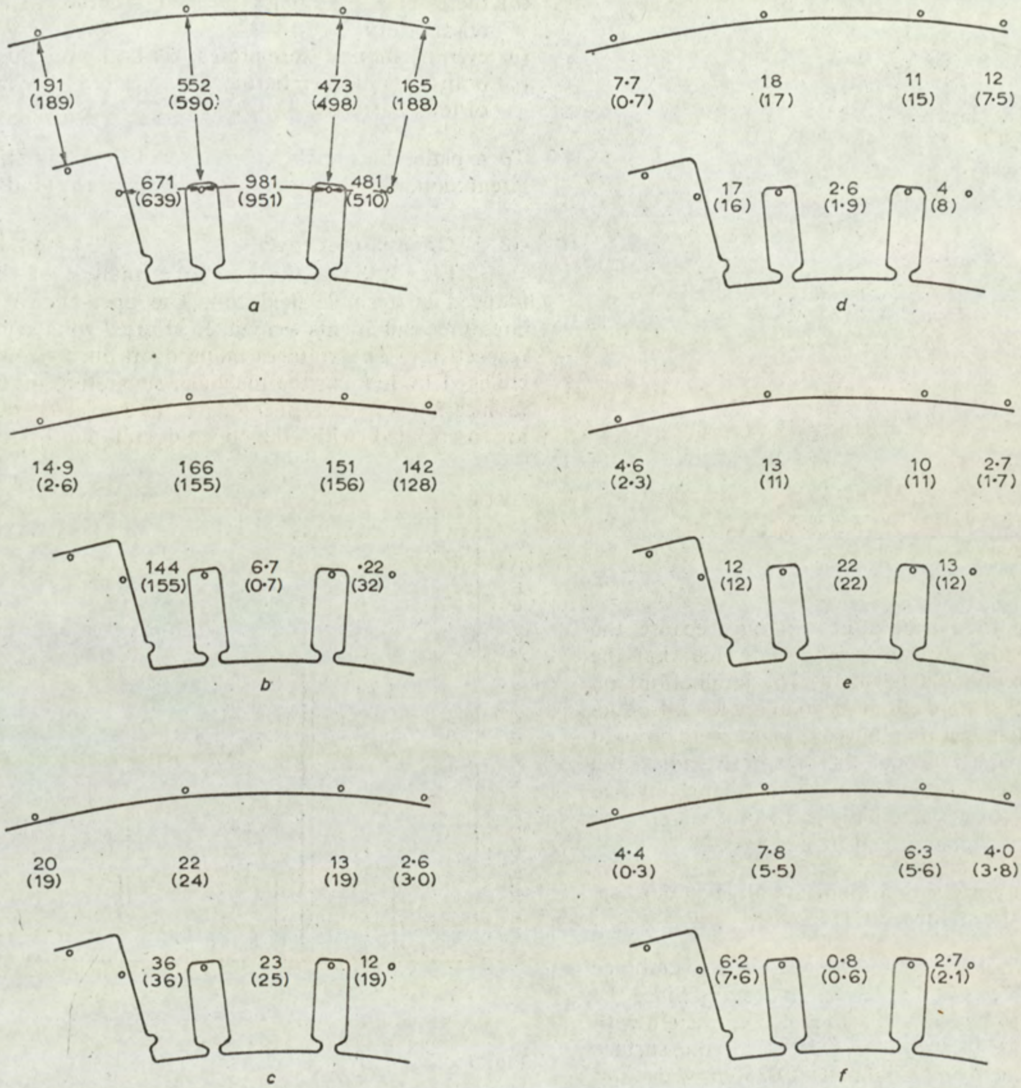

Fig 29: Harmonic components of peak flux, in μWb, in core and teeth at rated open circuit voltage

(a) Fundamental (b) Second (c) Third (d) Fourth
(e) Fifth (f) Sixth

Bracketed values refer to damped conditions

The following facts emerged:

a) odd-harmonic components behind the field slots are of the same order as components crossing the central tooth centre-line. Even components behind the field slots are in general smaller than those crossing the pole.

b) odd-harmonic components passing through the half tooth and 'half of the central tooth' roots, are approximately half the magnitude of components passing through the 'coil' tooth root. Even components from the half tooth are much greater than from other teeth.

The second stage measurements concentrated on fundamental and second harmonic components in smaller regions; they are tabulated in fig 30(a)(b). The values indicate the peak flux variations sensed by each coil. Since these variations are not necessarily in phase they do not, in themselves, add to the information on overall distribution. Coupled with the readings in fig 29, however, they suggest the following:

c) the fundamental time variations of flux in all parts of each tooth are in phase. The components crossing the pole and passing behind the field slot are not in phase with the tooth variations.

d) the second-harmonic time variations of flux in different parts of the 'coil' and 'central' teeth are not in phase, whereas in all parts of the 'half' tooth the flux variations are in phase.

This led to the recognition that the distribution of a certain harmonic component is related to the ratio of the tooth width to the space distribution of that harmonic in the airgap. The fundamental variations are uniformly distributed within the 'coil' and 'central' teeth, whose width equals half the fundamental space wavelength. The second-harmonic variations are uniformly distributed within the 'half' tooth, whose width equals half the second-harmonic space wavelength.

More evidence was obtained by comparing the waveforms of flux variations crossing behind the armature slots, fig 31.

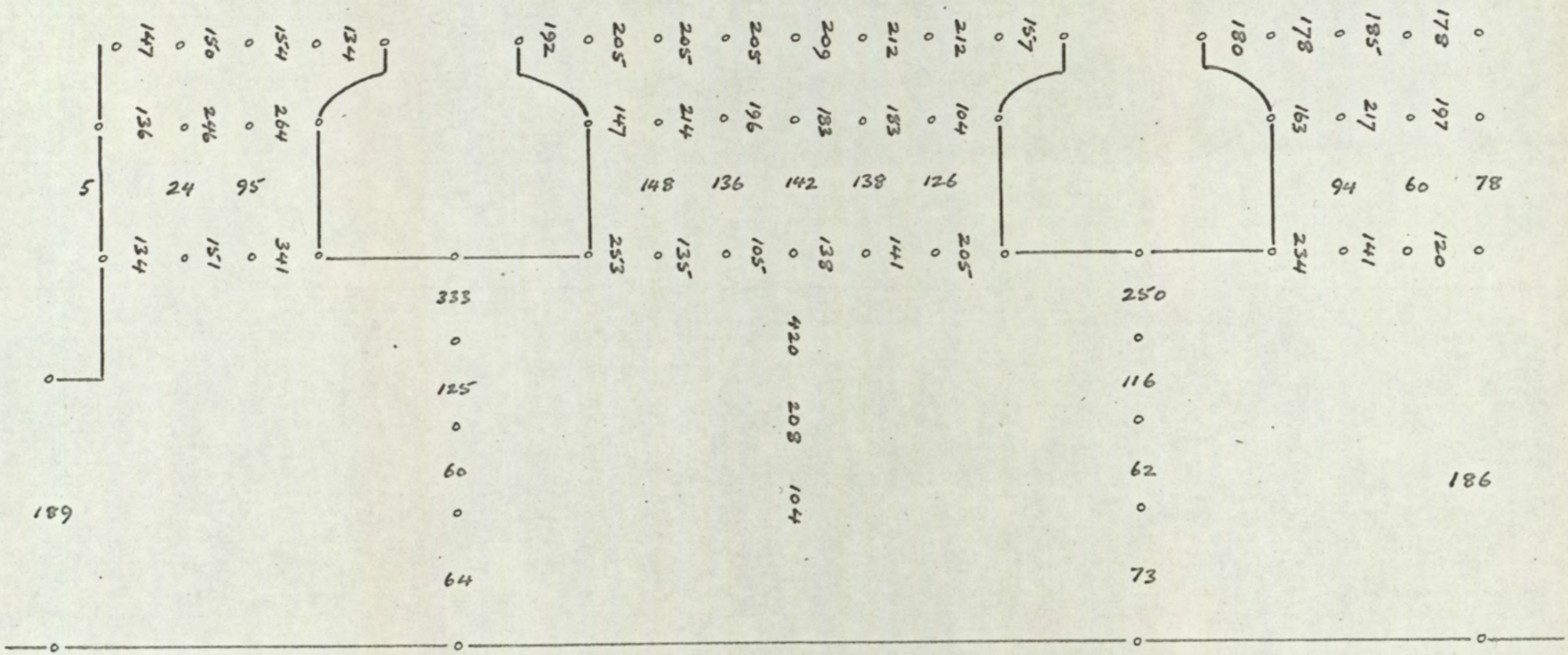

Fig 30(a): Fundamental fluxes o.c., μWb
Packet coil readings x 11 to represent complete core length
Effect of damping: negligible

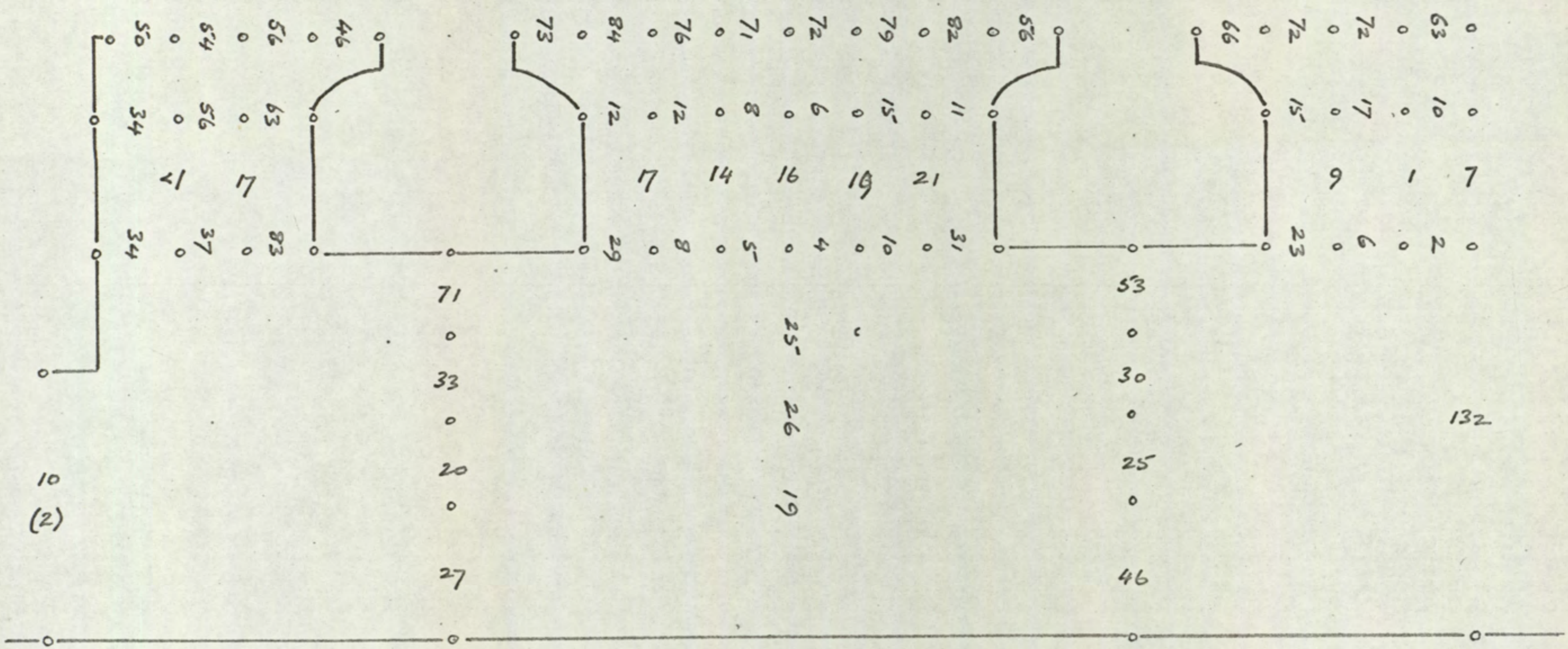

Fig 30(b): Second harmonic fluxes o.c., μWb
Packet coil readings x 11 to represent complete core length
Effect of damping: negligible except behind field slot

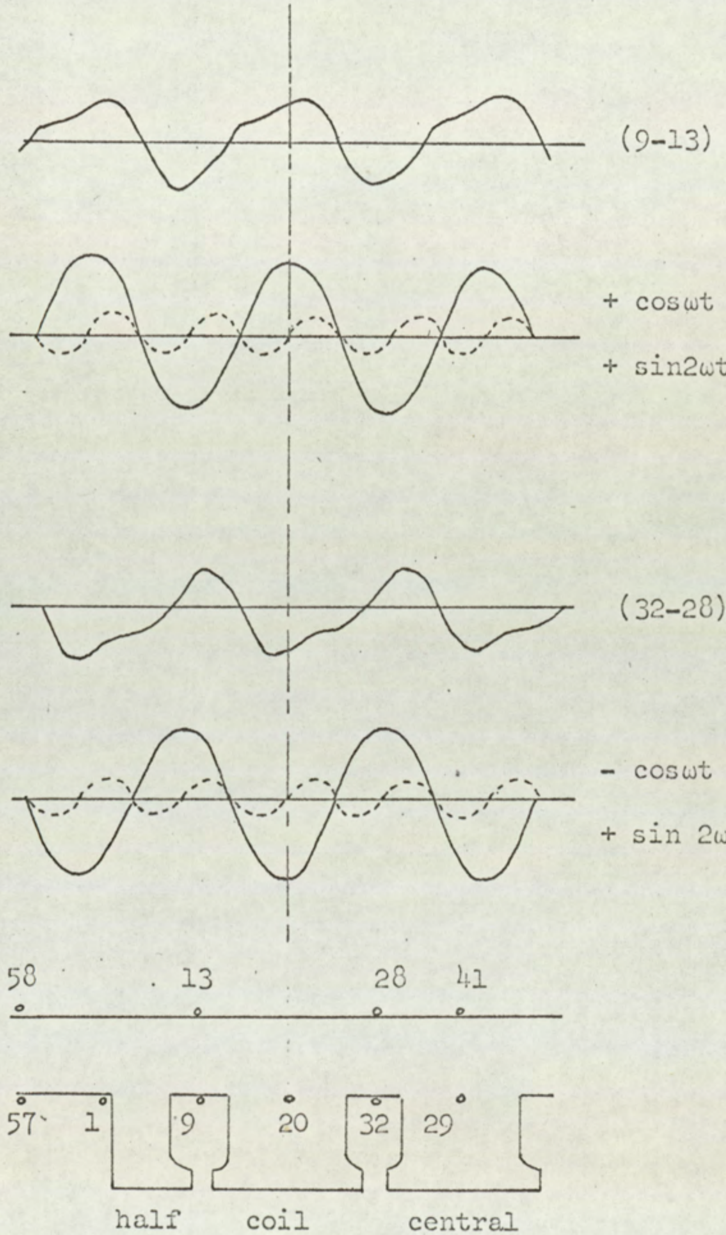

Fig 31: Comparison of flux waveforms behind consecutive armature slots

These waveforms were predominately composed of fundamental and second-harmonic; fig 29 shows the remaining components to be small. The numbering of the search conductors is shown in fig 31.

The previous findings were correlated as follows:

1) the fundamental components for each half of the coil tooth (20-32) and (9-20) are in phase as suggested in (c), whilst the dissymmetry in these waveforms, i.e. the second-harmonic, is out of phase. Similarly comparison of (1-9) and (9-20) shows the 'half' and 'coil' tooth variations to be out of phase.

2) comparison of (9-13) and (32-28) shows the fundamental components to be 180° out of phase, suggesting that the flux paths from each tooth split, passing behind the armature slots in opposite directions. The dissymmetry in (9-13) and (32-28) suggests that the second-harmonic components are shifted 90° from the fundamental but in phase with each other. If the fundamental is in terms of 'cos ωt' then the second-harmonic will be in terms of 'sin 2ωt' and, at any instant, the directions of these second-harmonic components behind the armature slots will be the same.

At this point in the investigation the pattern of paths taken by various components was becoming clearer in a qualitative fashion. However, the complex of odd and even, inphase and out-of-phase, cosine and sine components had not indicated a common mechanism which might be responsible for their existence.

3.1.4 Theoretical investigation of the flux distribution

The pattern of the fluxes contributed by each tooth to the core indicated a dependence on the relationship between tooth width and the space distribution of the airgap field. The flux variations at the stator airgap surface were caused by the modulation of a constant m.m.f. by a variable-reluctance pattern. Fig 32(a) shows the rotor and airgap which produced the

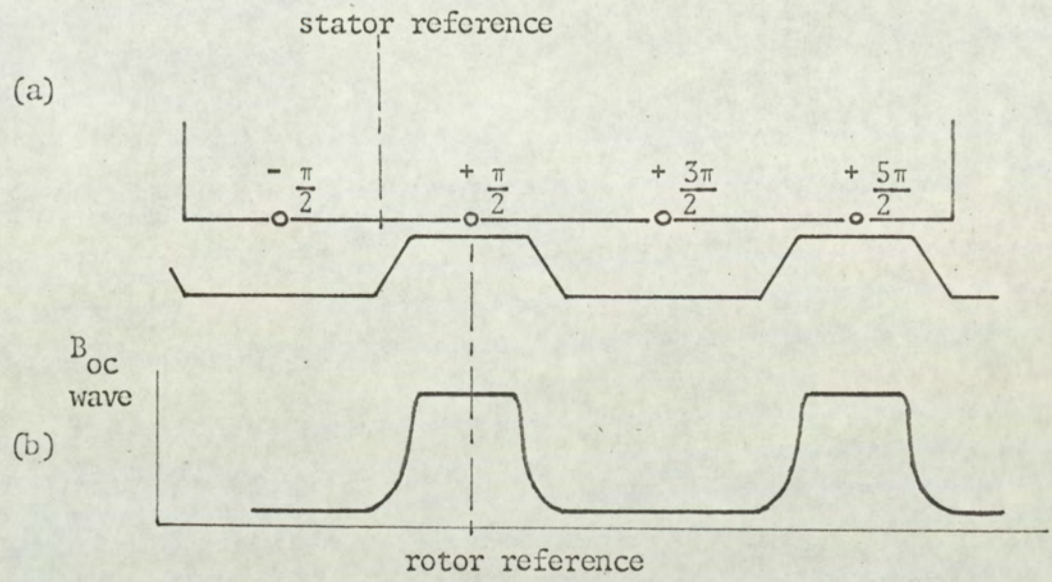

Fig 32: Ideal stator and rotor geometry with open-circuit flux-density wave.
Reference axes showing position of rotor reference relative to stator reference at time t = 0

variable-reluctance. If constant excitation is applied to this airgap, and stator slotting is neglected, the flux density pattern shown in fig 32(b) results. This can be analysed into a steady flux density on which is superimposed a fundamental, of wavelength equal to the rotor slot pitch, and its harmonics. The flux density wave shown in fig 32(b) moves with the rotor. If the stator slots are negligibly small and the active pole width an exact number of rotor pitches, it is seen that the total flux entering the pole on open-circuit will be constant, irrespective of rotor position. There will be flux density variations in the iron at all the frequencies present in the original flux density wave, but there will be no change of flux linkages with the field.

With these 'ideal' conditions, i.e. a continuous stator airgap surface between field slots, the open circuit airgap flux density distribution relative to the stator reference axis, is given by

$$\overline{B}_{oc} = \sum_{m=0.1.2...}^{\infty} B_m \cos m\,(\theta - \omega t - \pi/2) \text{ ....} (2)$$

The total flux linked by a coil having conductors at θ_1 and θ_2 of active length ℓ would be

$$\phi_{\theta_1}^{\theta_2} = \frac{\ell\lambda}{2\pi}\int_{\theta_1}^{\theta_2} \overline{B}_{oc} d\,\theta$$

Integrating between $-\pi$ and 3π gives the net flux that will link the field winding, ignoring field-slot leakage:

$$\phi_{-\pi}^{3\pi} = \frac{\ell\lambda}{2\pi}\int_{-\pi}^{3\pi} B_{oc} d\,\theta = \sum_{m=0}^{\infty} \frac{\ell\lambda}{2\pi}\left\{ \frac{B_m}{m} \sin m\,(\theta - \omega t - \frac{\pi}{2}\,\right\}_{-\pi}^{3\pi}$$

$$= \sum_{m=0}^{\infty} \frac{\ell\lambda}{2\pi}\,\frac{B_m}{m}\left\{ \cos m\,\omega t(2 \sin 2m\pi \cos m\,\frac{\pi}{2}) + \sin m\,\omega t(2 \sin 2m\pi \sin m\,\frac{\pi}{2}) \right\}$$

$= 0$ for m odd or even

For m =0, B_{oc} is constant. Therefore no time-varying flux linkages with the field coil can exist if

a) the stator airgap surface between field slots is smooth and continuous,

and b) the field pole pitch at the airgap is an even multiple of π electrical rad.

In the practical machine, the stator a.c. slotting is a major divergence from this ideal. This interrupts the stator surface between field slots and forces the fundamental and harmonic pole fluxes to close by different paths from the natural ones. This is especially true of the odd harmonics, which would have to take different paths even if the a.c. slots were very narrow. It also applies to the even harmonics, since normal tooth widths are less than an integral number of harmonic pole pitches. Tables 3 and 4 summarise the contributions of individual teeth to the core flux at fundamental and second-harmonic frequencies, respectively, in terms of the stator-slot opening σ (electrical rad). The tooth numbering is shown in fig 33(a) and the expressions are derived in detail in Appendix 8.3.1. These expressions led to explanations for the anomalies and to methods for calculating the various components of flux which had been measured.

Table 3: Summary of fundamental frequency contributions to core flux, (open-circuit).

Tooth	fundamental frequency contribution in units of $\frac{\ell\lambda B_1}{2\pi}$
1	$\cos\sigma/2 \sin\omega t - (1 - \sin\sigma/2)\cos\omega t$
2	$-2\cos\sigma/2 \sin\omega t$
3	$2\cos\sigma/2 \sin\omega t$
4	$-2\cos\sigma/2 \sin\omega t$
5	$\cos\sigma/2 \sin\omega t + (1 - \sin\sigma/2)\cos\omega t$
6	$\cos\sigma/2 \sin\omega t - (1 - \sin\sigma/2)\cos\omega t$

The sum of the terms in 'sin ωt' (table 3) over one d.c. pole pitch, i.e. teeth 1-5, is zero. The second term, cos ωt, for tooth 5 can be balanced by contributions from either tooth 1 (passing across the d.c. pole) or tooth 6 (passing behind the field slot), fig 33(b). The relative flux levels depend upon path reluctances and will be further studied in 3.1.6, but, as there is symmetry in successive poles, the net flux entering a pole is zero. This explains how there can be fundamental flux passing behind the field slot with the machine on open circuit without voltages being induced, either in the damping winding or in the field coil, by these fluxes. These remarks are true even if σ is very small; only the complete elimination of slotting will give the ideal conditions previously analysed.

Table 4: Summary of second-harmonic frequency contributions to core flux, (open-circuit).

Tooth	second-harmonic contribution in units of $\frac{\ell\lambda B_2}{4\pi}$
1	$-\sin\sigma\cos 2\omega t - (1+\cos\sigma)\sin 2\omega t$
2	$-2\sin\sigma\cos 2\omega t$
3	$-2\sin\sigma\cos 2\omega t$
4	$-2\sin\sigma\cos 2\omega t$
5	$-\sin\sigma\cos 2\omega t + (1+\cos\sigma)\sin 2\omega t$
6	$\sin\sigma\cos 2\omega t + (1+\cos\sigma)\sin 2\omega t$

Table 4 shows that the terms in $\cos 2\omega t$ are additive; their paths from pole to pole can only be completed by passing behind the field slot, fig 33(c). This explains the correct relationship noted between measured fluxes and voltages and the reduction in this flux due to damping (table 2). These terms are critically dependent on the angle σ, tending to zero as σ itself goes to zero. Table 4 also shows that the $\sin 2\omega t$ terms of teeth 1 and 5 sum to zero, and that those of teeth 5 and 6 are of the same sign. Hence, these second-harmonic fluxes are closed within a d.c. pole, and do not pass from pole to pole. Further, they are not eliminated by making σ small; only complete removal of the slotting will eliminate them. These fluxes cause losses, but do not induce voltages in the field or damper windings.

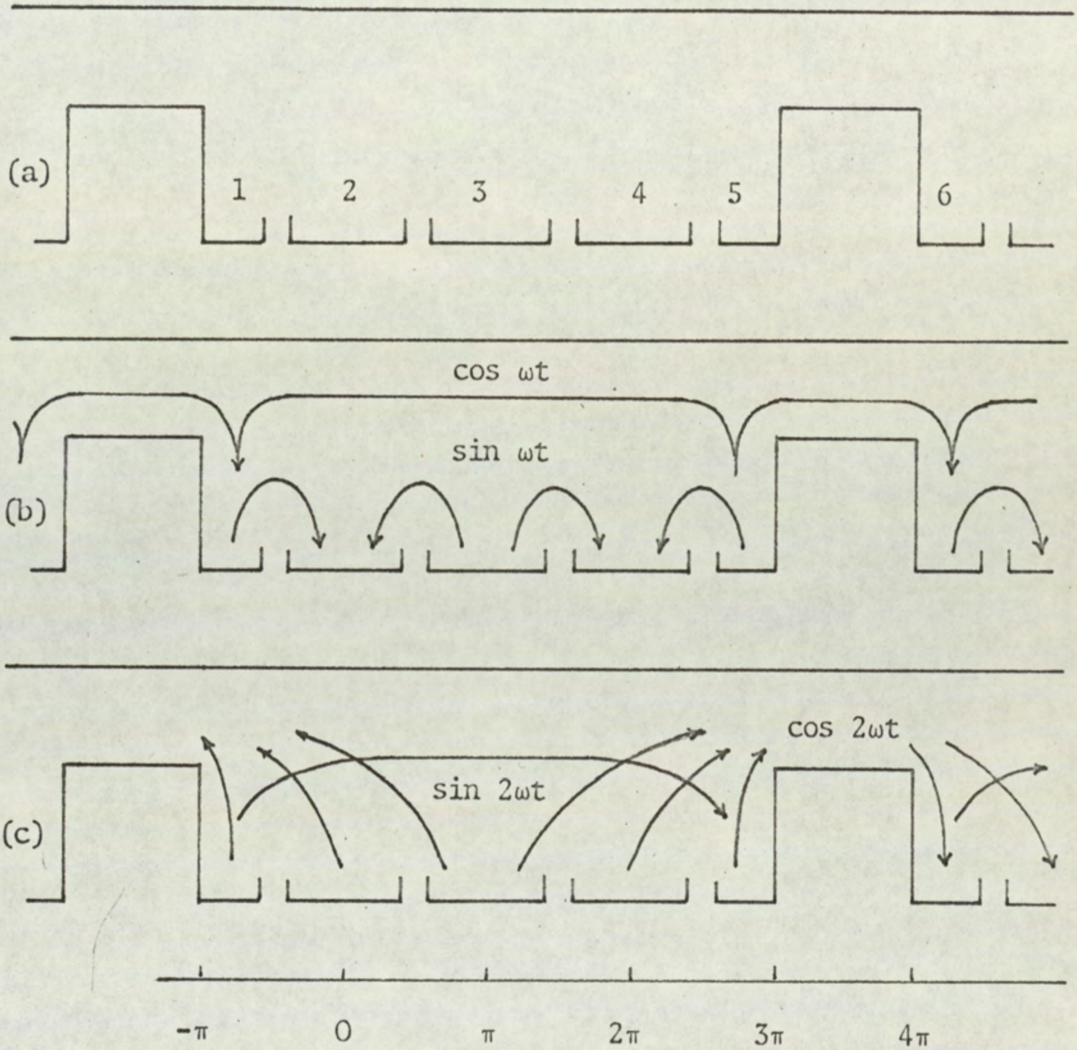

Fig 33: Distribution of open-circuit flux variations (even a.c. slots per d.c. pole)

(a) numbering system

(b) paths of fundamental components

(c) paths of second-harmonic components

3.1.5 Comparison of investigations by theory and measurement

Table 3 gives the theoretical fundamental contributions from teeth 2, 3 and 4 as having magnitude $\frac{\ell\lambda B_1}{\pi}\cos\frac{\sigma}{2}\sin\omega t$.

For the experimental machine the relevant design values are

$$B_1 = 0.55 \text{ Wb/m}^2$$

$$\ell = \text{(active core length) x (stacking factor)} = 12.22 \text{ cm}$$

$$\lambda = 4.69 \text{ cm}$$

$$\sigma = 0.46 \text{ electrical rad (26.35 electrical deg)}$$

If ϕ_{xy} denotes the peak xth harmonic component of flux contributed to the core by tooth y,

$$\phi_{12} = -\phi_{13} = \phi_{14} = -977\ \mu\text{Wb}$$

$$\text{and } \phi_{11} = \frac{\ell\lambda B_1}{2\pi}\left\{\cos\frac{\sigma}{2}\sin\omega t - \left(1 - \sin\frac{\sigma}{2}\right)\cos\omega t\right\}$$

$$= \text{vector sum of } 488 \sin\omega t \text{ and } 387 \cos\omega t$$

$$= 623\ \mu\text{Wb}$$

Assuming that the cos ωt component of ϕ_{11} is split equally between the two possible circuits, fig 33 (b), then 'flux behind field slot' = 'flux across pole pitch' = 193 μWb.

Table 4 gives the theoretical second-harmonic contributions from teeth 2, 3 and 4 as having magnitude $\frac{\ell\lambda B_2}{2\pi}\sin\sigma\cos 2\omega t$

$$B_2 = 0.39B_1 \text{ (see 8.4 Table 17 and note Table 1)}$$

$$= 0.21 \text{ Wb/m}^2$$

$$\text{then } -\phi_{22} = -\phi_{23} = -\phi_{24} = 84\ \mu\text{Wb}$$

$$\text{and } -\phi_{21} = \frac{\ell\lambda B_2}{4\pi}\left\{\sin\sigma\cos 2\omega t + (\cos\sigma + 1)\sin 2\omega t\right\}$$

$$= \text{vector sum of } 42 \cos 2\omega t \text{ and } 180 \sin 2\omega t$$

$$= 185\ \mu\text{Wb}$$

The value of $B_1 = 0.55\ Wb/m^2$ is the design value for rated open circuit voltage, 150V. With the field adjusted for $B_1 = 0.55\ Wb/m^2$ the actual voltage is 151V. For this field setting the flux from teeth 1 and 2 was measured together with the flux crossing the pole and passing behind the field slot. Table 5 compares the calculated and measured values for these regions.

Table 5: Core flux (μWb), field set for designed open-circuit fundamental flux density.

	Fundamental		Second-harmonic	
	Calculated	Measured	Calculated	Measured
From tooth 1	623	645	180	152
From tooth 2	977	990	84	4
Behind field slot	193	189	168	10
Across pole pitch	193	189	185	159

The fundamental measured and calculated values show good agreement, suggesting that the distributions discussed in 3.1.4 are soundly based. Equally, the values of second-harmonic contributions from tooth 1, which theory suggests cross the pole pitch to tooth 5, are corroborated. However, the contribution from tooth 2 is clearly affected by another mechanism. Since the flux measured behind the field slot is approximately twice that contributed by tooth 2, the path suggested in 3.1.4 seems correct; it is the magnitude which has to be investigated.

Fig 34(a) shows measured second-harmonic flux levels in tooth 2 and fig 34(b) the flux which links an array of search coils along the airgap surface of tooth 2, at rated open-circuit voltage. The average surface search coil flux is 74 μWb. Correcting for pitch this establishes the presence of 187 μWb of second-harmonic flux in the airgap. (This agrees with the theory of 3.1.4, since for $\sigma = \pi/2$, i.e.

(a)

(b)

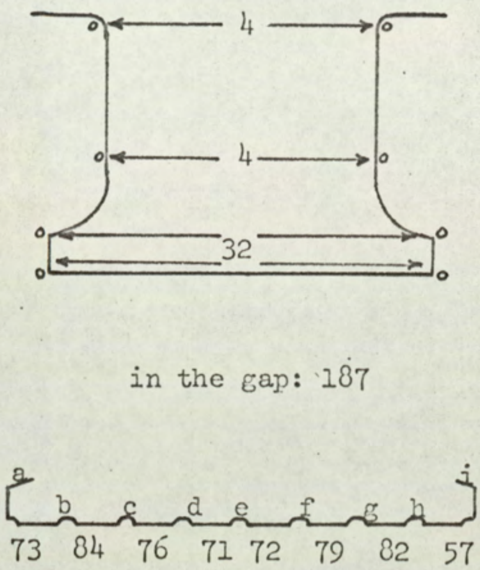

Fig 34: Detail of fluxes measured in tooth 2

(a) Second-harmonic fluxes, in μWb, in the airgap and at various cross-sections

(b) Lettering system for surface conductors with second-harmonic fluxes, in μWb, measured by coils made up from adjacent pairs tooth width equal to half a second-harmonic wavelength, $\phi_{22} = 190\mu Wb$). However, for the experimental machine the theory leads to a value of $84\mu Wb$ (Table 5) where only $32\mu Wb$ is measured. Further, the assumption that whatever flux penetrates the tooth surface will be contributed to the core without loss is shown to be unacceptable; only $4\mu Wb$ is in fact contributed. The theory of 3.1.4 depends upon the basic assumption that sinusoidal time variations of flux density in the stator teeth are the result of the uniform motion of the rotor with its associated sinusoidal space distribution of flux density. Since the second-harmonic flux per pole and the pitch of the tooth-surface coils are known, measurement of second-harmonic voltage in these coils can be compared with calculated values, using the known flux, to show any flux distortion that is present. Table 6 shows the actual pitch and the expected voltage, together with the measured voltage and the pitch that will correspond to those measurements.

Table 6: Calculated and measured second-harmonic voltages with corresponding values of pitch for the tooth-surface search coils, fig 34(b)

	de	df	ae	af	ag	bh	ah	ai
Calculated voltage	0.49	0.95	1.53	1.61	1.53	1.53	1.30	0.95
Actual pitch	0.1	0.2	0.4	0.5	0.6	0.6	0.7	0.8
Measured voltage	0.5	0.95	1.62	1.48	1.05	0.95	0.55	0.25
Corresponding pitch	0.1	0.2	0.5	0.63	0.77	0.8	0.89	0.95

Since the difference between actual and 'measured' pitch increases for coils covering the tooth tip region, distortion is suspected in this area. It is presumed that more of the second-harmonic flux distribution is able to complete its path within the tooth surface than is expected, reducing the contribution to the tooth proper from 84μWb to 32μWb. The flux not finding a path from one harmonic pole to the next within a tooth width is, by the theory of 3.1.4 proportional to the slot opening. The distortion of the flux distribution has effectively reduced the slot opening to a quarter its actual dimension (coil ai, 0.95 instead of 0.8).

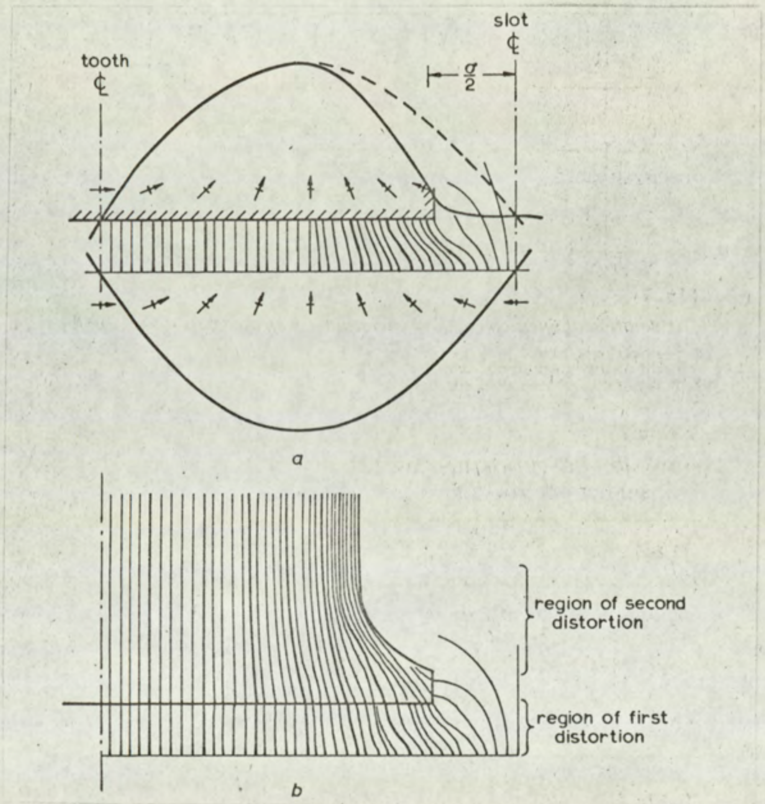

Fig 35: Postulated distortion of second-harmonic flux in tooth 2

(a) Flux entering tooth surface
undistorted flux ------
distorted flux ———
lower curve is spatial second-harmonic component of airgap flux

(b) Assumed distribution of flux within tooth

Fig 35(a) shows the spatial distortion of the second-harmonic component of airgap flux density at the tooth surface, with the associated redistribution of time-varying flux denoted by the vector arrows. The constriction of the teeth, due to the slotting, distorts the flux pattern at the sides of the teeth even further, fig 35(b). The combination of these postulated distortions at the gap surface and in the tooth make the assumed linearity invalid and allow the flux within the tooth to complete more of its pole-to-pole path, reducing the contribution to the core below that expected from theory.

3.1.6 Comparison of fundamental fluxes passing behind the field slot and across the pole pitch

In Table 5 measured values of fundamental flux passing behind the field slot and across the pole pitch are recorded as 189μWb and 186μWb respectively. The permeance coefficients for the two paths are very similar and therefore, with the evidence of the measurements, it seems valid to divide the 'cos ωt' component from tooth 1 by two and use these values for comparison.

However, when it is recognised that the path behind the field slot carries the field flux while ϕ_{11} is the only component crossing the pole, the equality of the two measurements becomes more of a curiosity than something to be expected.

Fig 36 shows the manner in which the fluxes vary for a range of field settings. The flux passing behind the core (57-58) reaches a peak for approximately open-circuit rated field conditions. The flux passing across the pole (41-39) continues to increase in value as the field current is increased. These two curves cross at approximately rated open-circuit field conditions; this explains the equality of the measurements recorded in Table 5.

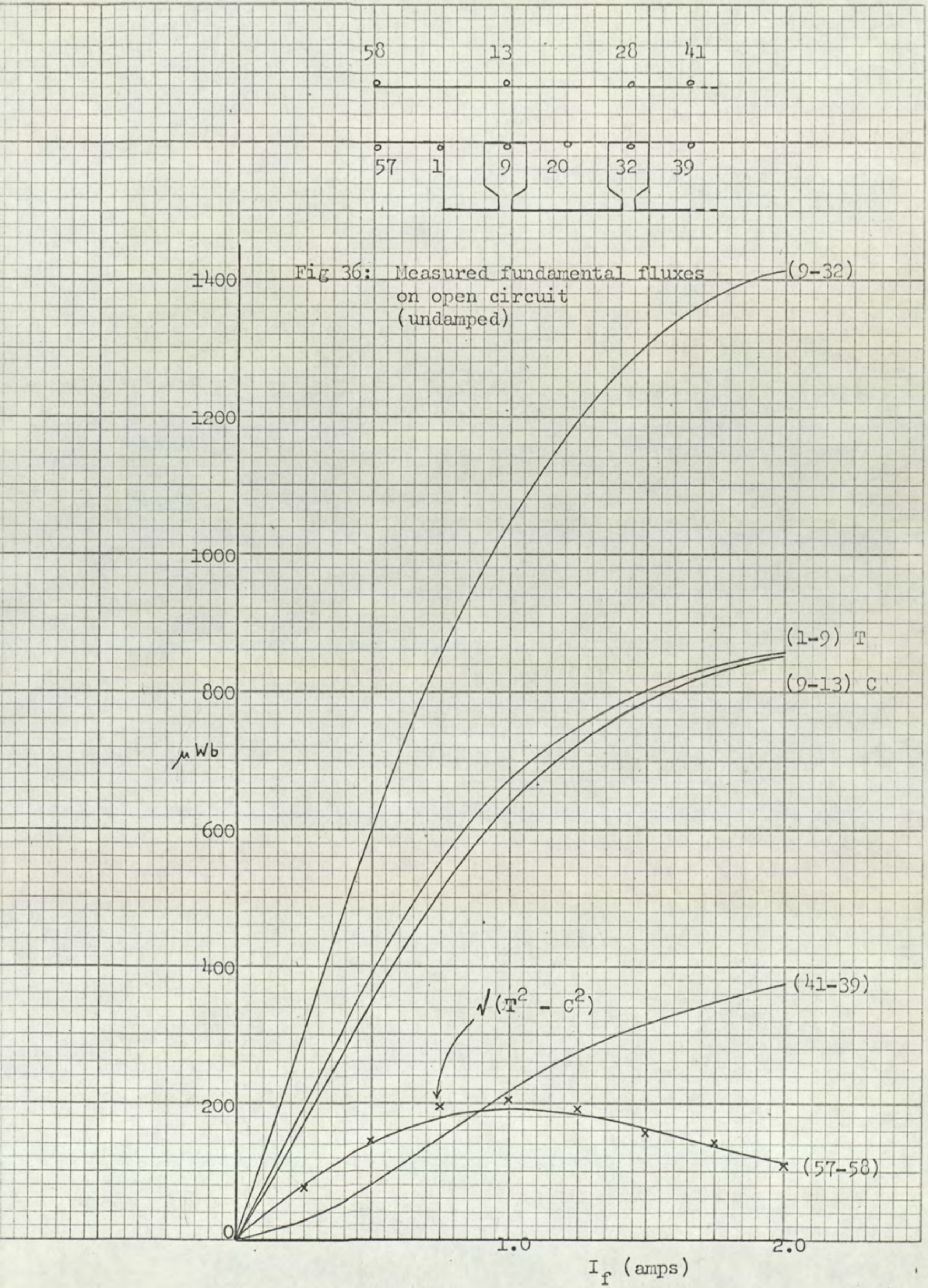

Fig 36: Measured fundamental fluxes on open circuit (undamped)

Since the major component of ϕ_{11} is in terms of 'sin ωt' while the split path components are in terms of 'cos ωt', the vector difference of flux from tooth 1 (1 - 9) and flux passing behind the adjacent armature slot (9 - 13) is calculated and included in fig 36. The fact that these calculated values agree closely with measurements of flux passing behind the field slot (57-58) is further demonstration that the theoretical distributions, fig 33(b) are correct.

Because the path behind the field slot carries the d.c. field flux, the component of ϕ_{11} taking this route varies about a high mean level. The path across the pole is comparatively lightly loaded magnetically; at the pole centre line the ϕ_{11} component is the only flux present. Thus the path behind the field slot experiences a reduction in incremental permeance as the overall flux level increases. This accounts for the reduction in flux sensed by (57 - 58) and more of ϕ_{11} (cos ωt) passing (41 - 39) as the field is increased. Fig 37 shows the good agreement between the calculated value of ϕ_{11} (cos ωt) and the sum of measurements made by coils (57 - 58) and (39 - 41).

Fig 38 shows the fundamental voltage induced in one field coil as the field is increased. Similar to the flux recorded in fig 37, the voltage induced in an undamped coil reaches a peak for approximately rated open-circuit conditions. When the coil is damped the peak induced volts are reduced to a third of their undamped value. However, due to the redistribution of flux at higher overall densities, the undamped values of induced volts falls below the damped value for approximately rated full-load field conditions. This and other factors influencing the decision to use damping coils are discussed in 3.3. The fundamental voltage of fig 38 is not accounted for by the theory. It is due to a small flux (calculated in Table 2) possibly arising from assymetrical conditions such as are considered in 8.5.

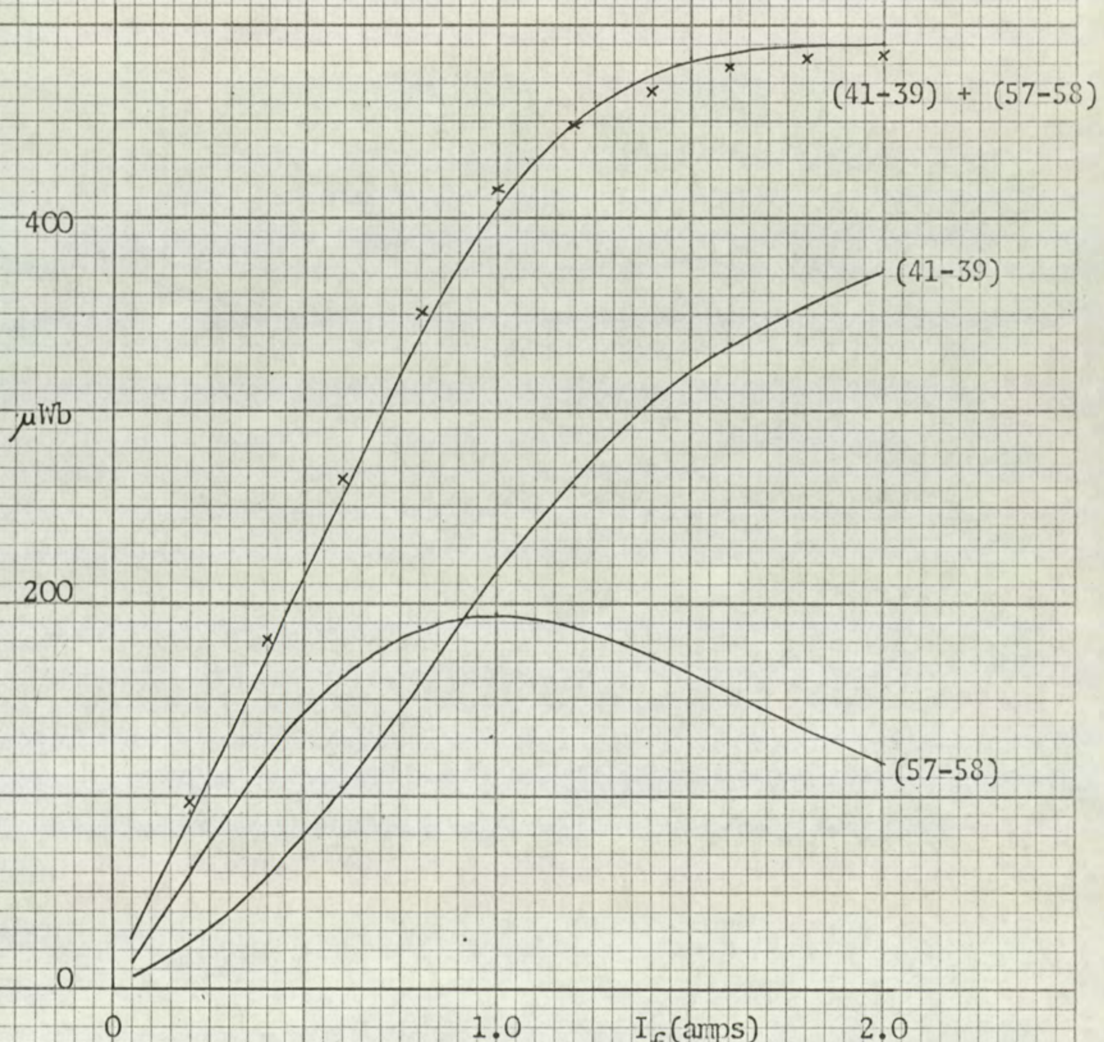

Fig 37: Fundamental fluxes, open-circuit, undamped.

Measured ————

Calculated x x

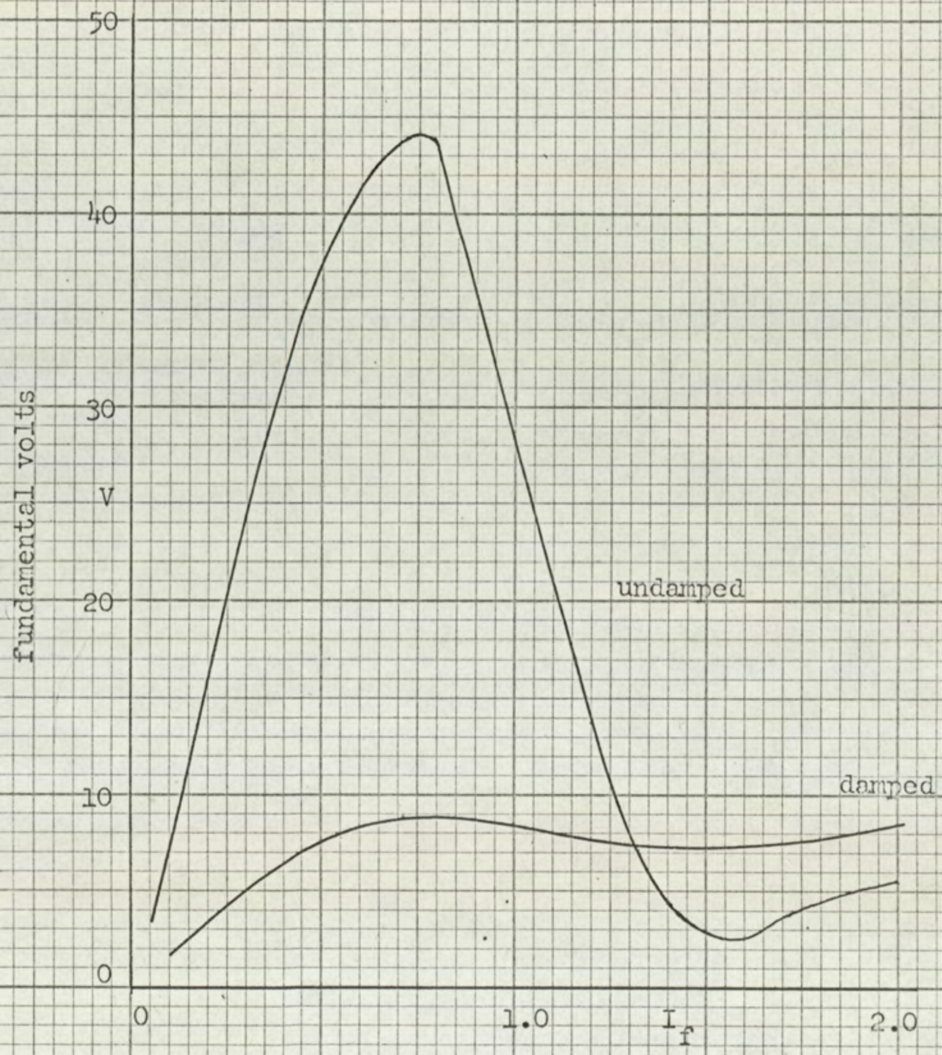

Fig 38: Fundamental voltage induced in a single field coil against field current

3.2 Distribution of flux in the stator due to armature reaction m.m.f.

3.2.1 Introduction

As in other machines, the problem of load behaviour is concerned with the interaction of the armature reaction m.m.f. (produced by the stator windings) and the airgap permeance, superimposed on existing o.c. conditions. In the Lorenz machine the problem is complicated by the use of a single phase, 1 slot/pole/phase stator winding, so that the armature reaction m.m.f. produced by an ideal winding concentrated at discrete points, ignoring slots, will be a square wave fixed in space with magnitude varying sinusoidally in time phase with the variation of the load current. In a practical machine, the armature reaction wave is not square but trapezoidal, because the windings are spread over the width of a stator a.c. slot. The mathematical treatment using a trapezoidal wave becomes unwieldy; however, the fact that in practice the distribution is trapezoidal and not square allows the following theory, based on square waves, to be applied across several stator slot pitches. This is covered more fully in 3.2.3.

3.2.2 Theoretical description of the airgap flux density distribution due to armature reaction

If θ is measured from the coil axis, fig 32, the distribution of armature turns is expressed by .

$$\left(\frac{4}{\pi} \sum_{n=\text{odd}}^{\infty} \frac{1}{n} \sin\frac{n\pi}{2} \quad \cos n\theta \right) \text{per turn}$$

being a unit full-pitch square wave. If the armature current reaches its peak value at time $t = (\delta/\omega)$, the m.m.f. due to armature reaction (F_a) is expressed by

$$\frac{4N_a I_a}{\pi} \sum_{n:odd}^{\infty} \frac{1}{n} \sin \frac{n\pi}{2} \cos n\theta \cos(\omega t-\delta) \quad \ldots\ldots\ldots\ldots\ldots\ldots\ldots\ldots(3)$$

where δ is the time phase angle by which peak open-circuit voltage leads the peak armature current.

When an m.m.f. F_1 is applied to the airgap of a rotating electrical machine, the distribution of the resulting flux density may be expressed as B_1. Both F_1 and B_1 may be functions of (θ, t). A second m.m.f. F_2 will produce a flux density wave B_2. F_1 and F_2 may have different magnitudes and time-dependence but providing they have identical space distributions acting on the same permeance:

$$\frac{F_1}{F_2} = \frac{B_1}{B_2}$$

Thus, if B_{oc} results from F_f and B_a from F_a, then

$$B_a = \left(\frac{F_a}{F_f}\right) B_{oc} \quad \ldots\ldots\ldots\ldots\ldots\ldots\ldots\ldots(4)$$

Combining equations (3) and (2) in (4)

$$\overline{B}_a = \frac{4N_a I_a}{\pi F_f} \sum_{\substack{m=0.1.2\ldots \\ n=odd}}^{\infty} \frac{B_m}{n} \sin \frac{n\pi}{2} \cos n\theta \cos(\omega t-\delta) \cos m(\theta-\pi/2-\omega t) \quad \ldots(5)$$

Equation (5) is analysed in detail in 8.3.2 where it is shown that for conditions of (n + m) even, time varying flux components link the field winding even though the pole iron is an integral number of rotor slot pitches in width. The major components are the result of the fundamental space distribution of armature m.m.f. (pulsating at fundamental frequency) combining with the fundamental variation in permeance (represented by B_1). The analysis of 3.1.4 and 8.3.1 is repeated in 8.3.2, i.e. the slot opening is described by σ (electrical rad), with the added complication of δ affecting the results.

Tables 7 and 8 summarise the expressions for two simple values of δ.

Table 7: Summary of tooth contributions to core flux due to armature reaction m.m.f., $\delta = +\pi/2$ i.e. ZPF lagging

Tooth	Components for $n = m = 1$ in units of $\frac{CB_1 \ell\lambda}{2\pi}$
1	$\frac{1}{2}(\sin\sigma + \sigma - \pi)(1 - \cos 2\omega t) - (1 + \cos\sigma)\sin 2\omega t$
2	$(\sin\sigma + \sigma - \pi)(1 - \cos 2\omega t)$
3	$(\sin\sigma + \sigma - \pi)(1 - \cos 2\omega t)$
4	$(\sin\sigma + \sigma - \pi)(1 - \cos 2\omega t)$
5	$\frac{1}{2}(\sin\sigma + \sigma - \pi)(1 - \cos 2\omega t) - (1 + \cos\sigma)\sin 2\omega t$

Table 8: Summary of tooth contributions to core flux due to armature reaction m.m.f. $\delta = 0$ i.e. a leading power factor

Tooth	Components for $n = m = 1$ in units of $\frac{CB_1 \ell\lambda}{2\pi}$
1	$\frac{1}{2}(\sin\sigma + \sigma - \pi)\sin 2\omega t - (1 + \cos\sigma)(\cos 2\omega t + 1)$
2	$(\sin\sigma + \sigma - \pi)\sin 2\omega t$
3	$(\sin\sigma + \sigma - \pi)\sin 2\omega t$
4	$(\sin\sigma + \sigma - \pi)\sin 2\omega t$
5	$\frac{1}{2}(\sin\sigma + \sigma - \pi)\sin 2\omega t - (1 + \cos\sigma)(\cos 2\omega t + 1)$

The significance of δ is discussed in more detail in chapters 4 and 5. Whereas the values $\delta = \pm\pi/2$ can only represent ZPF conditions, $\delta = 0$ applies to a leading power factor condition which in turn is determined by the balance of field and armature reaction m.m.f.s together with the leakage reactance. $(C = \frac{N_a I_a}{\pi F_f})$.

For n = m = 1, Tables 7 and 8 record the twice line frequency components from each tooth. This mechanism for the Lorenz machine is similar to that reported by Raby [36], 1.2.2(11), for the Guy machine. Since all the components have the same sense under one pole, they must link the field coil and induce twice line frequency voltages.

For ZPF load conditions the flux varies from zero to $8(\sin\sigma + \sigma - \pi)\dfrac{CB_1\ell\lambda}{2\pi}$ with a period of $(\frac{\pi}{2\omega})$. For $\delta = 0$ the flux varies between $\pm 4(\sin\sigma + \sigma - \pi)\dfrac{CB_1\ell\lambda}{2\pi}$ with the same period, $(\frac{\pi}{2\omega})$. These are the maximum variations that must be allowed for, since, at load conditions when $\delta = \pi/4$ the pole to pole flux alternates between zero and $4\sqrt{2}(\sin\sigma + \sigma - \pi)\dfrac{CB_1\ell\lambda}{2\pi}$, a reduction of 30%. As with the open circuit conditions, components also pass across the pole from 'half tooth' to 'half tooth'; these do not link the field winding since there is no alternative path behind the field slot open to them.

Combinations of m = 0 and 2 with n = 1 will produce fundamental and third-harmonic time varying components which theoretically may sum to zero within any pole similar to the '$\sin\omega t$' terms in fig 33(b). However, the components from 'half teeth' either side of a field slot are 180^0 out of phase, i.e. the flux from such a 'half tooth' may pass behind either the field or the armature slot. This accounts for additional odd harmonic voltages appearing in the analysis of voltages induced in a field coil under short-circuit ($\delta = +\frac{\pi}{2}$) conditions, fig 39. As with the open circuit analysis, the even harmonic components of the combined fluxes are considerably reduced by damping. The odd-harmonic components are slightly increased: no clear explanation for this has been discovered. Possibly the overall reduction in the major (even) variations and the consequent lower peak flux densities is responsible.

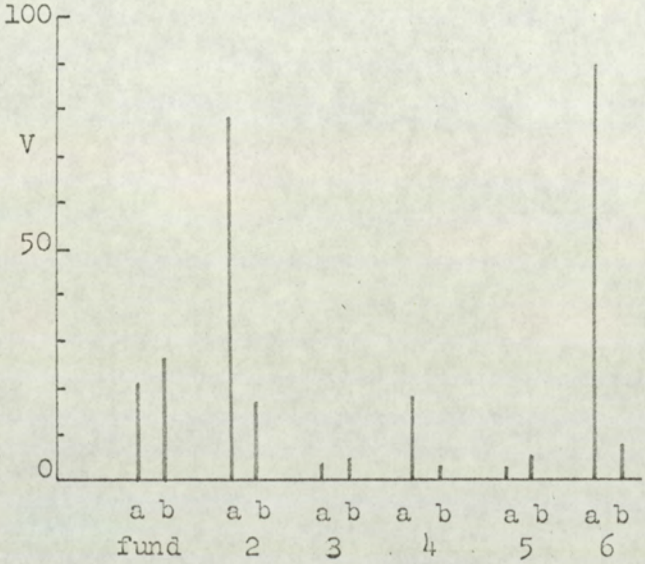

Fig 39: Harmonic voltage modulations present in a single field coil on rated short-circuit (V_{rms})

(a) undamped (b) damped

Note - sum of all modulations across whole field winding < 1.0 volt

3.2.3 Justification for applying equation (4) to several armature slots

The armature reaction m.m.f. (F_a) is constant at any instant in time across an armature coil pitch. The rectangular representation of the previous section assumes an instantaneous change in the sense of F_a at slot centre lines, which if applied rigorously, leads to incompatible field boundaries for consecutive coil pitches. Fortunately, the actual distribution of F_a at the stator airgap surface more closely resembles a trapezoid since the armature slot openings interrupt the field and the coils occupy a finite width. This allows the transition from peak values under one coil to the opposite peak values to occupy a finite time as distinct from occurring instantaneously. A trapezoidal distribution of F_a allows equation (4) to be applied to several armature coil pitches since no boundary incompatibilities exist.

The terms providing the 'instantaneous change of sense' in the rectangular series are small and of very high harmonic order. In any quantitative work using the series, they would probably be neglected. The time field pattern in the slot opening is not completely described by the theory, however, due to the low density of this region (itself the result of the slot opening permeance) any discrepancies are small.

3.3 Damping windings

3.3.1 Introduction

In the writer's experience it is established practice to use damping coils, or to fit damping resistors, in the field circuits of most inductor alternators. Walker [1] and Raby [36] have shown the theoretical existence of twice line frequency pole-to-pole fluxes when the machine is loaded. Designers have also been aware, from measurements, that alternating voltages are induced in individual field coils. Although the vector sum of these voltages as seen at the field terminals is small, evidence suggests that across each coil damaging potentials are quite possible.

Therefore short circuited turns are wound in the field slots to reduce the voltages by damping the responsible flux linkages. The established technique for calculating iron losses presumes that all components of flux passing behind the field slots are eliminated by these coils. The next two sections summarise the limitations of short circuited turns wound in the field slots.

3.3.2 Summary of alternating voltages induced in a field coil and the effect of a short circuited damping turn

Even harmonic voltages were expected on-load [1,36]. With rated short circuit armature current, 80V second harmonic and 90V sixth harmonic were measured, fig 39. These were the major components making up the peak value of the composite induced voltage waveform given in fig 40(b).

Odd harmonic voltages were not expected on load; those measured were due to the same fluxes which induced odd harmonic voltages in the field coil when the alternator was open circuit. The net linking fluxes required to support the odd harmonic voltages were small, Table 2, and presumed to originate from asymmetrical permeance variations of which leakage into the field slot, 8.5, is one example. Even harmonic voltages on open circuit were explained theoretically in 3.1.5, although the calculated values did not agree with measurements this was accounted for in fig 35.

All voltages induced in a field coil are reduced by a short circuited damping turn since the voltages are due to flux linkages, from whatever source, with both the field coil and the damping turn. The important consideration is to what peak value undamped voltages will rise, not considering harmonic by harmonic, but as a composite waveform. Fig 40(a)(b) gives these values for open circuit and short circuit conditions over a range of field and load currents. Neither maximum 'peak value' is likely to cause an insulation breakdown. With the damping turn at the bottom of the slot (away from the airgap) the induced volts are reduced to approximately a third of their undamped value. In this particular machine the space taken up by the damping turn would have been more usefully filled with field copper.

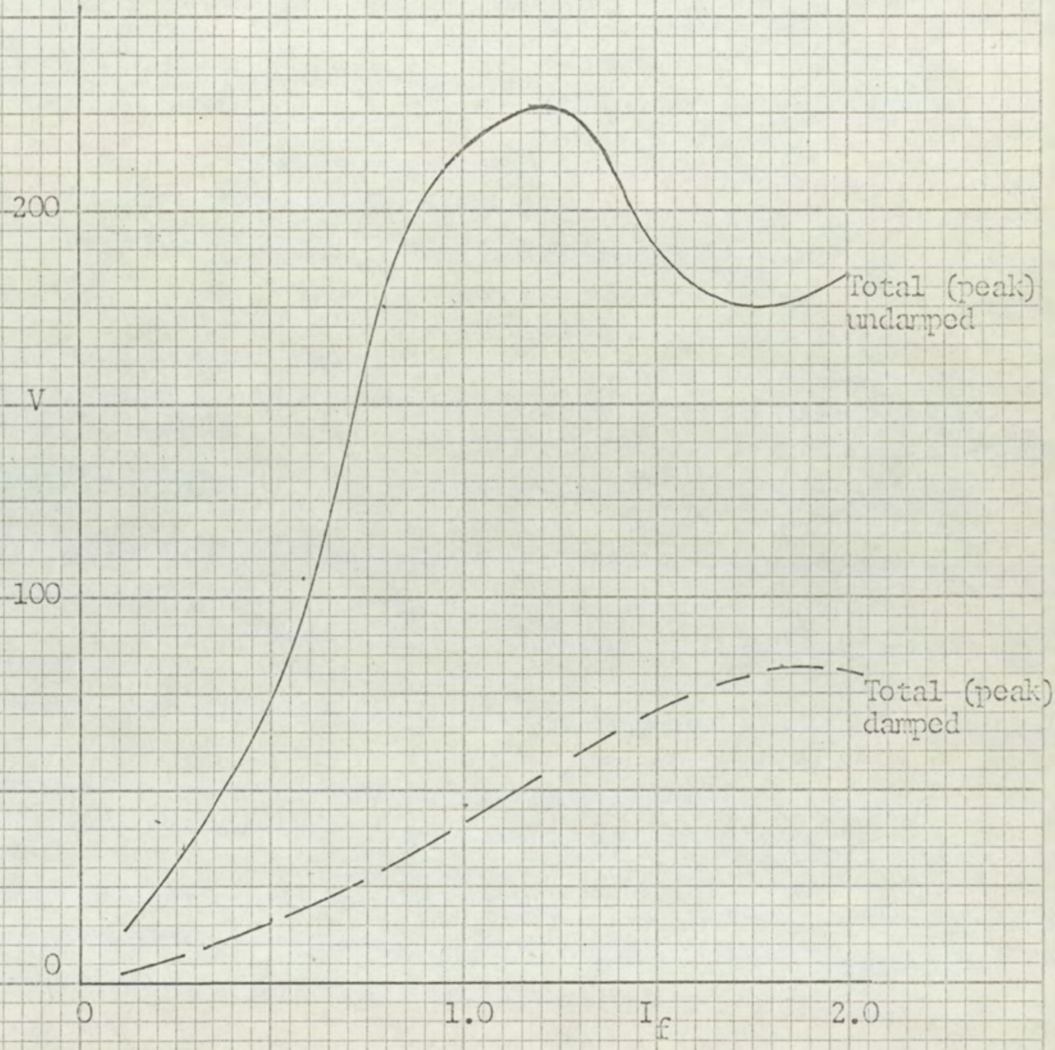

Fig 40(a): Peak voltage induced in a single field coil on open circuit, damped and undamped

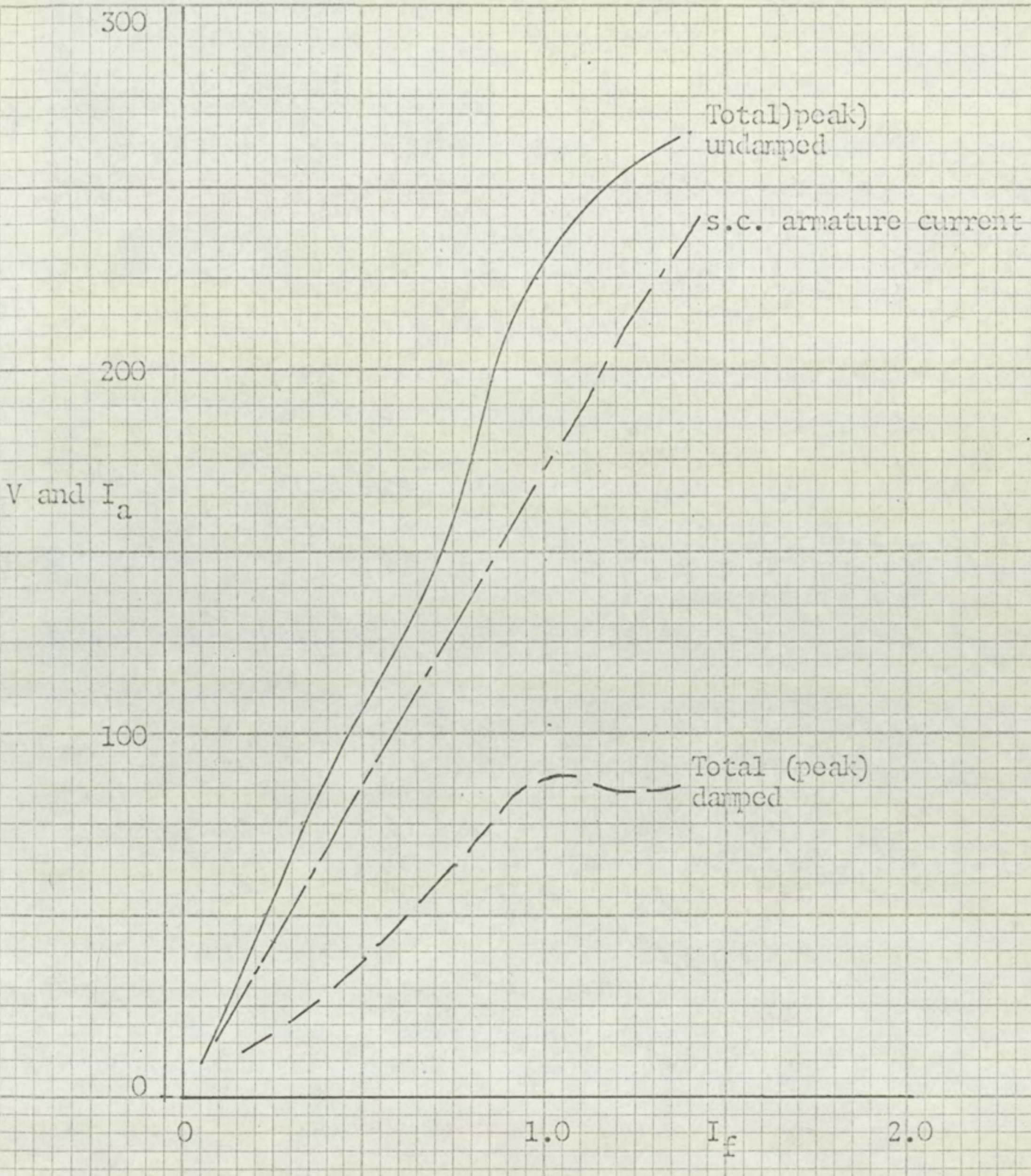

Fig 40(b): Peak voltage induced in a single field coil for short circuit conditions, damped and undamped

3.3.3 Summary of alternating fluxes in the stator core and the effect of a short circuited field damping turn

The peak induced voltages give information as to the peak 'linking' fluxes. Since the field coil contained 270 turns, only a comparatively small flux was required to induce large voltages, especially if the voltage harmonic order was high. Thus the large second- and sixth-harmonic voltages were not the result of the major alternating flux components. The twice line frequency fluxes due to armature reaction, whose theoretical recognition was the main reason for using damping coils, were found to add little to the general pattern of alternating core fluxes present on open circuit. Distortion in the armature slot-opening-region considerably reduces this potential problem, 3.1.5, and since the slot-openings on the experimental machine are unusually wide (tooth contribution to core only 5% of the airgap second harmonic level), in a normal design the core flux variations from this origin will be negligible.

With a short-circuited turn wound in the field slots the even harmonic components were reduced; the odd components were unaffected because those passing behind consecutive field slots were 180° out of phase. The odd components will be diverted from this path by short-circuited turns wound, as search coil (57-58), radially from field slot to the stator outside diameter. However these fluxes do not induce large voltages and the redistribution across the pole pitch will not reduce the losses.

If the peak voltages can be reliably calculated a simple decision on whether to use damping coils may be made on that basis, since only small advantages in core loss are in fact forthcoming. Unfortunately, the peak voltages are dependent upon asymmetric pole permeance, incremental permeability, and distortion; all impossible to calculate with accuracy; all, however, contriving to reduce the peak voltage values.

CHAPTER 4 Rotor surface flux density distribution

Summary

This chapter considers the theoretical distribution of flux density in the airgap and compares this with the measured flux density across a rotor tooth surface.

Rotor surface search coil signals are integrated and displayed using a process which allows accurate and consistent measurements. These are calibrated against flux meter readings taken with the rotor stationary and also compared with calculations based on the signals as 'e.m.f.s in short pitched coils'.

Each reading is adjusted to allow for variations in the coil areas so that the mean flux density over each coil gives one point on an open circuit flux density distribution curve. On-load, the readings require careful interpretation since the search coils are also linked by flux patterns travelling forward and backward relative to the rotor i.e. at assynchronous speeds. The components which move with the rotor are selected from the theoretical expressions and summed using a computer. The resulting distributions are corroborated by measurements taken in a form suggested by the theoretical analysis. The close agreement between tests and calculations gives confidence in the ability of the theory to describe the airgap field under load conditions.

4.1 Flux density distribution across a rotor tooth airgap surface under open circuit conditions

4.1.1 Theory

This section is not so much a 'derived theory' as a statement of the origins of the theoretical approach employed throughout this thesis. As discussed in 1.2.2(2) and specified in 3.1.4, the open circuit airgap flux density, $\overline{B}_{oc}$, , is expressed thus

$$\overline{B}_{oc} = B_1 \sum_{m=0.1.2...}^{\infty} b_m \cos m\,(\theta - \pi/2 - \omega t)$$

This series is relative to the stator reference axis, fig 32, and differs from equation (2) only in the introduction of a p.u. representation of the coefficients (b_m) based on the fundamental coefficient B_1 as 1 p.u.

When considering this expression relative to the rotor it is convenient, for future theory which involves the armature turns distribution, to take as rotor reference axis the location of the stator axis projected onto the rotor as time t = 0.

$$\text{i.e. } \overline{B}'_{oc} = B_1 \sum_{m=0.1.2...}^{\infty} b_m \cos m\,(\theta - \pi/2)$$

4.1.2 Displaying the flux density at the rotor tooth surface

The flux linkages with rotor surface search coils, fig 30(e), change as the rotor tooth passes from pole to pole. If a coil is chosen, say two adjacent conductors, which is comparable to the armature slot opening in width, changes in flux linking the coil also occur as it passes from one stator tooth to the next. The e.m.f. signal from such a coil is shown in fig.41. With the circuit of fig 23 this e.m.f. signal was

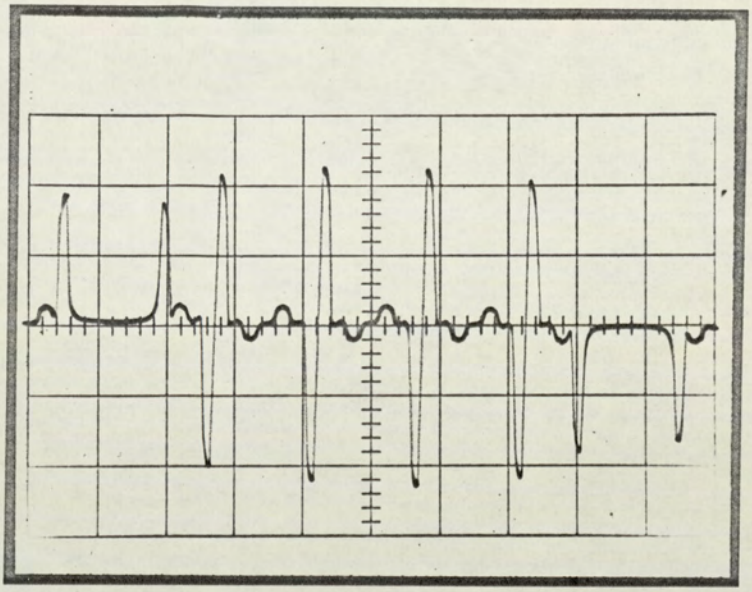

Fig 41

integrated, giving a display proportional to the flux linkages changing in time as shown in fig 42(a). If the search coil is formed from conductors at each side of the rotor tooth surface, the coil is no longer so sensitive to armature slot openings and the resulting display is proportional to the heteropolar flux-density wave, fig 42(b).

With adjacent conductors, fig 42(a), the effect of each tooth is distinct even to the dip in flux as the coil passes the centre line of a stator tooth. This is presumably due to a variation in the overall permeance of the complete magnetic circuit; a similar pattern was produced by the conducting paper analogue, fig 27.

Fig 42

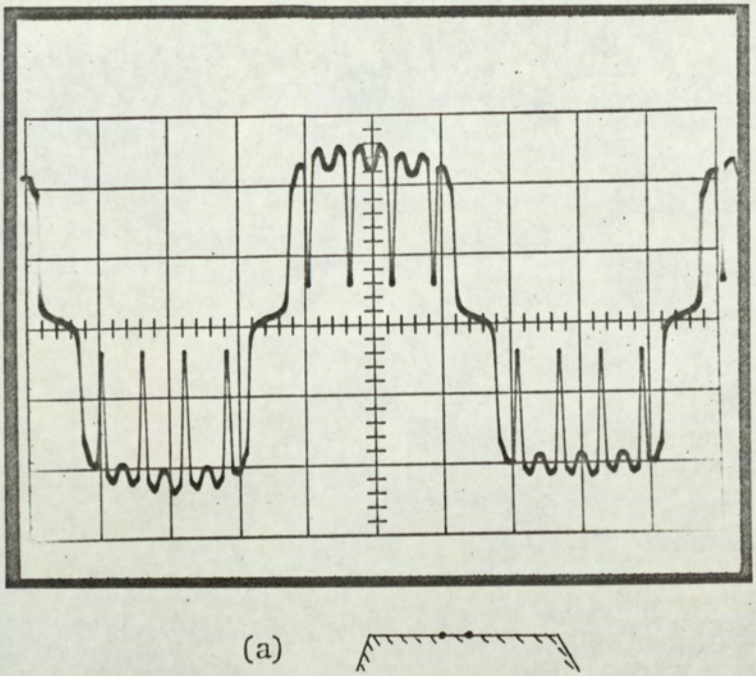

(a)

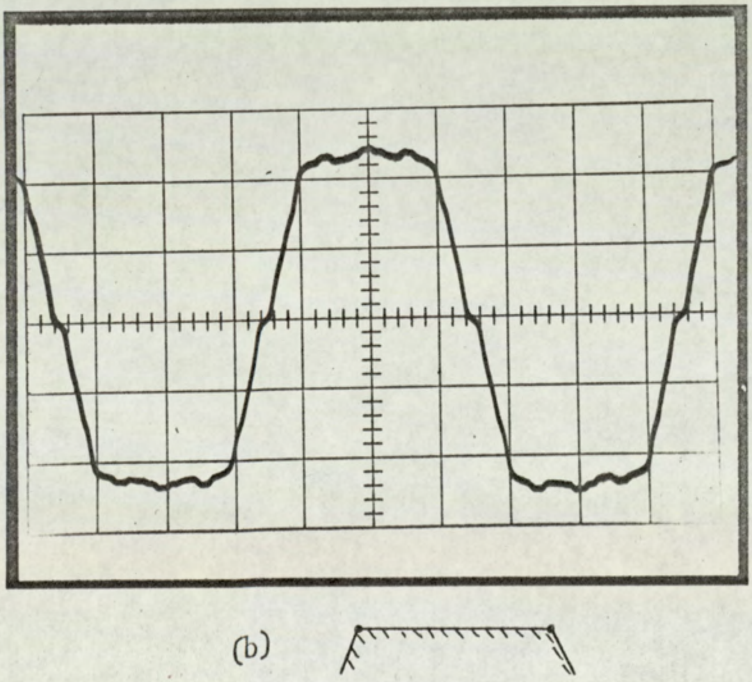

(b)

The gradual, rather than abrupt, changes in flux linkages sensed by a small search coil passing across a field slot opening indicate leakage paths from field slot sides to rotor teeth. Since rotor teeth are not opposite consecutive field slots simultaneously this asymmetrical leakage is a source of odd harmonic flux variations in the main flux. This is analysed and investigated further in 8.5.

4.1.3 Measurement of the open circuit airgap flux density distribution across a rotor tooth surface

Taking the rotor tooth surface search conductors in adjacent pairs to form seven search coils, each signal was integrated and displayed, fig 42(a), and measured from peak-to-peak, for a field current I_f. These measurements, taken with the machine running, were calibrated against readings of flux linking the same search coils during a stationary test for a reversal of field current from + I_f to - I_f. This calibration was linear over the available range of field current.

Each coil, however, required a correction for area in order that the signals might be directly compared. Both rotational and stationary tests produced individual 'open circuit curves' for each coil. Assuming the airgap to be uniform and working at flux densities such that the distribution across the rotor tooth was uniform, the gradient of each 'flux plotted against field current' is proportional to the area of that coil. Thus each area could be corrected to one seventh of the total tooth surface area. The stationary test was the more fundamental of the two since readings were taken using a flux meter. However, the peak-to-peak measurements of flux display were more sensitive and consistent. The d.c. voltage required to bias the display across the oscilloscope graticule was measured by a digital voltmeter, 2.4. Using the oscilloscope amplifiers to magnify the display and a three decimal place digital voltmeter, enabled considerable consistency to be achieved. Table 9 shows the correction factors obtained from each method. The second places of the stationary factors are due to readings of parts of a division on the flux meter scale whilst the digital voltmeter reading has been rounded to two decimal places. The similarity between these test results is taken as further proof of the accurate response of the integrating circuit to the search coil signals.

Table 9: Area correction factors for rotor surface coils from Stationary and Rotating tests.

Search conductors (fig 43)	5-6	6-7	7-8	8-9	9-10	10-11	11-12
Stationary (flux meter)	.88	1.09	.97	1.0	.97	.98	.89
Rotating (peak to peak)	.88	1.02	.98	1.00	1.00	.98	.89

As a further comparison between stationary and rotating conditions, the signal from search coil (8-9), see fig 43, was analysed at heteropolar frequency. The r.m.s. signal voltage was divided by the search coil pitch factor to give the fundamental pitch voltage: this led to the peak a.c. fundamental flux. This peak value was converted into the rectangular wave from which flux per tooth and thus flux per coil, during rotation, was calculated. Table 10 shows the comparison between flux measured with a flux meter during the stationary test and the calculate value of flux from the coil signal during rotation.

Table 10: Stationary (flux meter) and Rotating (calculated from coil signal) measurements of a.c. flux = μWb, coil (8-9)

Field current	0.2	0.4	0.6	0.8	1.0
Flux meter	71	149	220	288	350
Calculated	73	148	219	285	336

Whereas the analysis of the search coil signal is also a more fundamental approach to measuring flux than calibrating the integrated signal, greater consistent accuracy is possible with the second technique. The search coil pitch factor is .0297. Small changes in pitch factors of this size greatly affect the value of calculated flux. Wave analysers must be calibrated over the expected signal range since typical accuracies are not better than ± 1 db.

Hence the open circuit flux density distributions for a range of field current from 0.2 to 2.0 amps, given in fig 43, are derived from calibrated measurements. Coil (8-9) has been analysed at field currents from 0.2 to 1.0 amps; these values of flux density are included as a check.

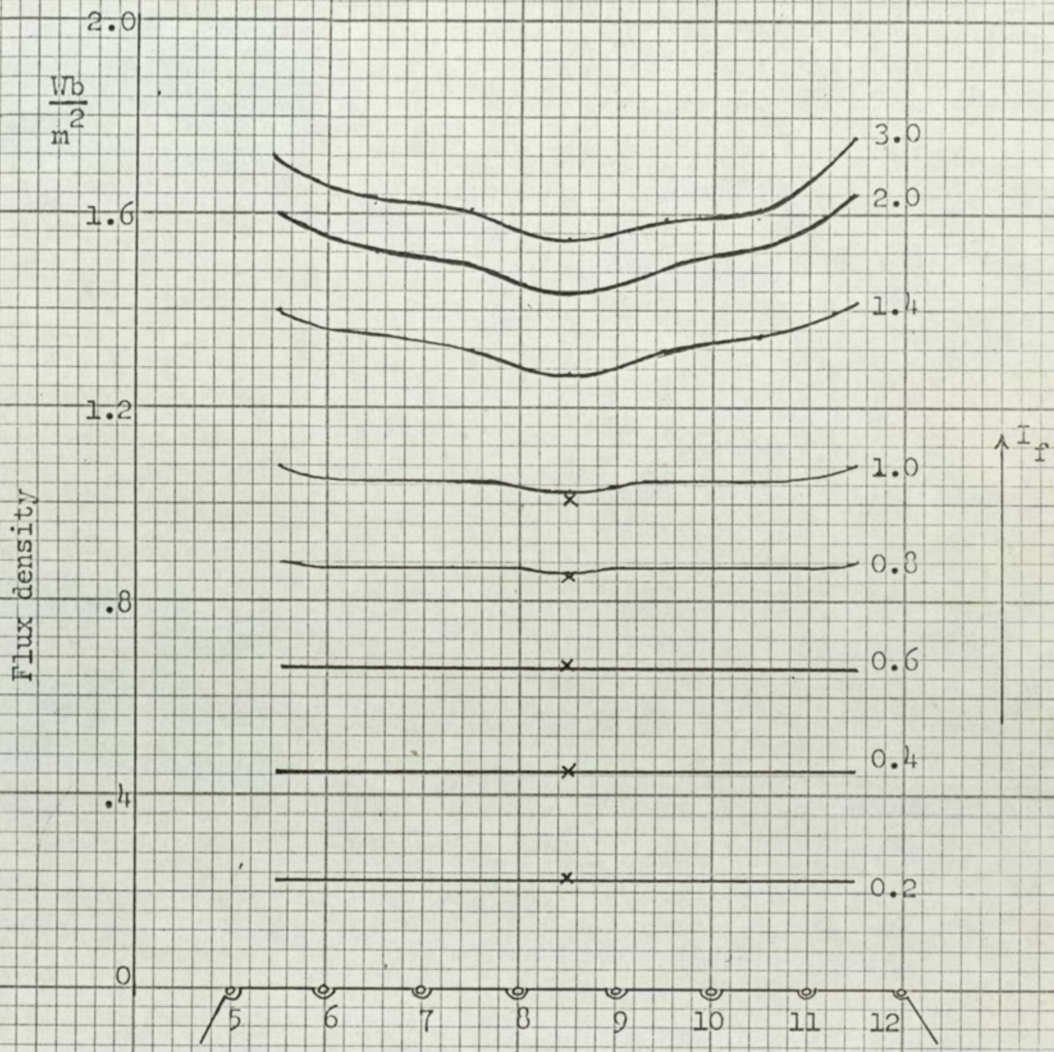

Fig 43: Distribution of flux density across rotor tooth surface - open circuit

calculated x x

measured ————

4.2 Flux density distribution across a rotor tooth airgap surface under loaded conditions

4.2.1 Theory

The completed airgap flux density distribution on load is expressed by

$$\overline{B} = \overline{B}_{oc}\left(1 + \frac{F_a}{F_f}\right) \quad \ldots\ldots\ldots\ldots\ldots\ldots\ldots\ldots(6)$$

assuming superposition of the distributions due to field and armature reaction m.m.f.s relative to the stator.

The open circuit distribution relative to the rotor has been expressed in 4.1.1. Equation (5), 3.2.2, represented the complete flux density pattern due to the armature reaction when the armature current is restricted to its fundamental component. The full general expression is

$$\overline{B}_a = \frac{4N_a I_a}{\pi F_f} \sum_{\substack{m:0.1.2..\\ n:odd}}^{\infty} \frac{B_m}{n} \sin\frac{n\pi}{2} \cos n\theta \cos(\omega t - \delta) \cos m(\theta - \pi/2 - \omega t)$$

To select the terms which describe the density distribution relative to the rotor will require two operations,

(i) select terms in $n(\theta - \omega t)$ only,

(ii) remove from this expression all 'ωt' components,

this refers the expression to the rotor, i.e. giving the space distribution relative to the rotor.

Equation (5), 3.2.2, is expanded in 8.6, expressing the forward rotating fundamental component of the flux density distribution across the rotor tooth surface due to armature reaction as

$$\frac{N_a I_a B_1}{\pi F_f}\left\{ 2b_o \cos(\theta + \delta) - b_2 \cos(\theta - \delta)\right\}$$

To obtain the complete loaded distribution this must be superimposed on the fundamental of the B_{oc} wave relative to the rotor: $B_1 \sin\theta$

i.e. the complete distribution is expressed by

$$B_1 \left[\sin\theta + \frac{N_a I_a}{\pi F_f} \left\{ 2b_o \cos(\theta + \delta) - b_2 \cos(\theta - \delta) \right\} \right] \quad ..(7)$$

In section 3.2.2 (δ/ω) was defined as the time at which the armature current reached its peak value. At time t = 0 the rotor position was chosen such that the voltage induced by ϕ_{oc} was at its peak value. Hence the angle δ describes the phase shift in time by which the armature current lags or leads the open circuit voltage for the chosen field conditions.

Thus δ is dependent on the power factor and the load angle associated with the load. By reference to fig 44 with the assumption that the vector difference between open circuit volts and terminal volts lies perpendicular to a vector describing the armature current, a simple expression for δ at any load is obtained

$$\cos\delta = \frac{V_T \cos\phi}{V_f}$$

where V_T = terminal volts for field F_f
V_f = open circuit volts for field F_f
ϕ = power factor of load circuit

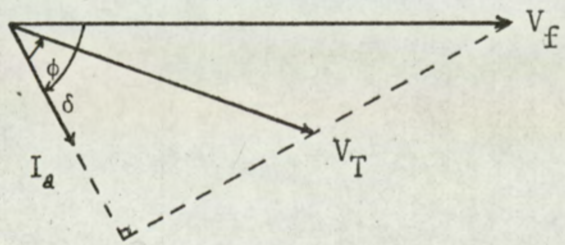

Fig 44

4.2.2 Interpretation of the on-load signal displays

Fig 45 compares the e.m.f. signal from a rotor search coil on open circuit and on load. On open circuit, the effect of armature slot openings is symmetrical, allowing analysis of the heteropolar frequency, 4.1.3. On load, the unequal flux density either side of an armature slot opening produces a signal whose fundamental is not solely due to the heteropolar characteristics. Thus the direct approach to measuring flux, using signal e.m.f.s and an harmonic analyser, is impracticable.

It is therefore necessary to examine carefully the actual nature of the flux that links a rotor search coil under load conditions and to use this knowledge to approximate to the steady load flux which moves with the rotor. There are four main components of the total flux linking a rotor search coil, fig 46.

(i) the 'steady' component caused by field excitation. This is constant across a d.c. pole but reverses at each pole, so that a signal of heteropolar frequency appears in the search coil.

(ii) the 'steady' component caused by the forward synchronous component of armature reaction: this also varies at heteropolar frequency.

(i) and (ii) are the required signals.

(iii) dips in the steady components which occur at the stator a.c. slot openings. These occur regularly at easily recognised intervals and can be used as timing marks to define the instantaneous position of the search coil.

(iv) all the non-synchronous components of armature reaction which form harmonic poles of various wavelengths moving at different speeds with respect to the rotor search coil. These are studied in detail in 8.7.1.

Fig 45: e.m.f. from 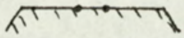

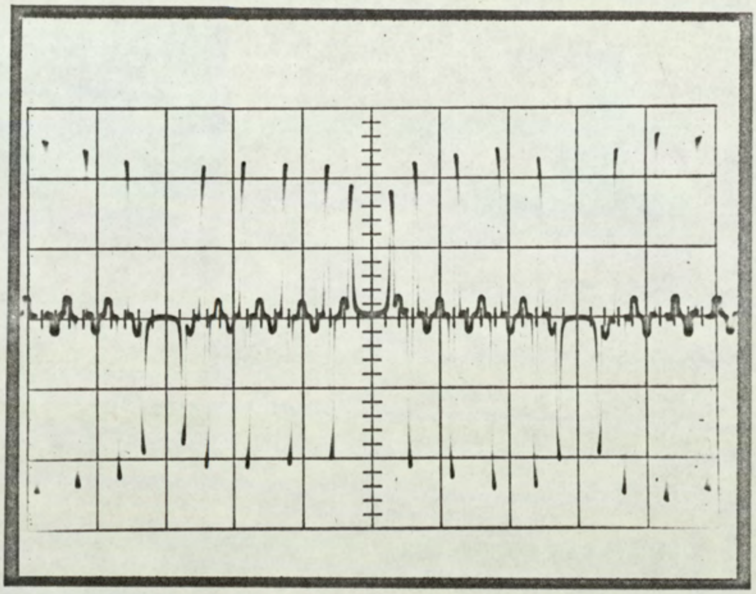

(a) open circuit

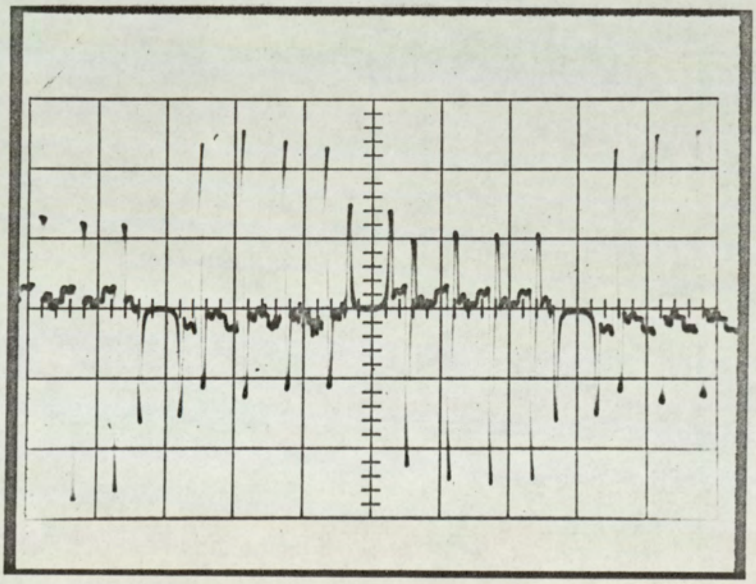

(b) on load

Fig 46: Integrated signal from
(on load)

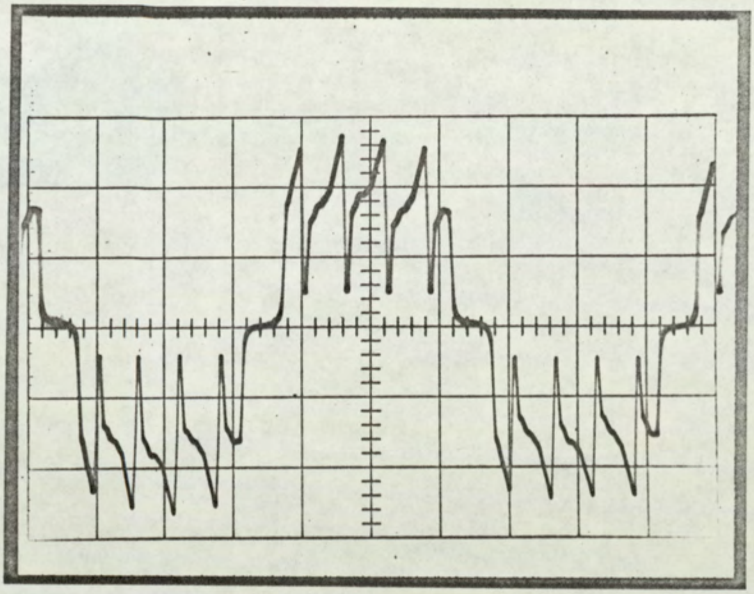

(a)

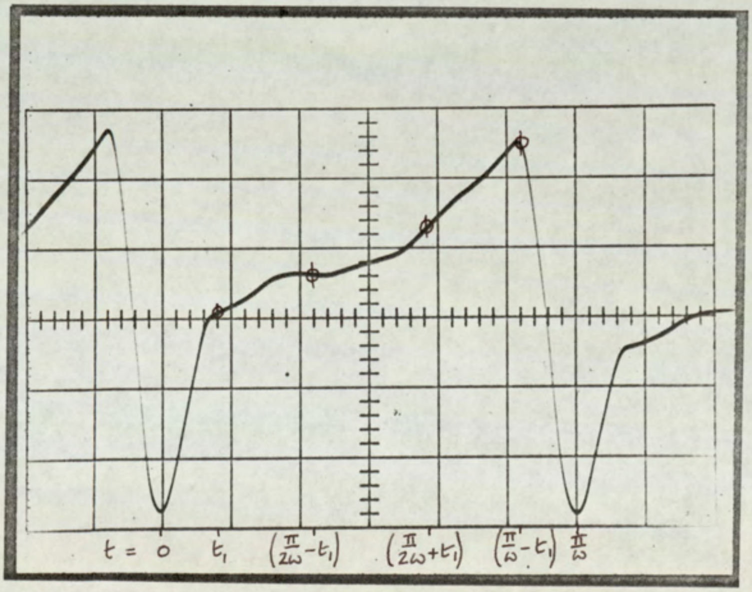

(b)

The output signal from each rotor search coil is the time rate-of-change of the total flux linking the coil from all four sources. Thus, from fig 46, components (i) and (ii) must be extracted taking account of the existence of components (iii) and (iv). Fig 46(b) is an enlargement of fig 46(a) during the time taken to pass from the centre line of one armature slot to the next; the instants of passing these two centre lines may be arbitrarily defined as $t = 0$ and $t = (\pi/\omega)$. The time at which the search coil links maximum flux, having moved across the slot opening and come fully under the influence of the stator tooth, is taken as t_1, as shown: the corresponding time when the coil leaves the same stator tooth is $(\frac{\pi}{\omega} - t_1)$. Similarly points may be defined t_1 either side of the 'centre line time' at $(\frac{\pi}{2\omega} \pm t_1)$.

In section 8.7.2, it is shown that the general term for time varying flux through a search coil, when sampled at these four points, sums to zero for the 2nd, 6th, 10th etc. time harmonics, which includes the most important terms. This is an extension of the identity.

$$\sin n(\theta + \alpha) + \sin n(\theta + \pi - \alpha) + \sin n(\theta + \tfrac{\pi}{2} + \alpha) + \sin n(\theta + \tfrac{\pi}{2} - \alpha) = 0$$

for $n = 2, 6, 10$ etc.

4.2.3 Measurements of peak flux density across the rotor tooth surface

To eliminate the major terms of type (iv), 4.2.2, in order that the readings should be proportional to the flux density distribution moving with the rotor, four peak-to-peak measurements of the integrated signal were taken at the points shown in fig 46(b) and averaged. As each pole flux, indeed each tooth flux, is not identical due to manufacturing and material tolerances, the readings were taken consistently on certain teeth on certain poles; these were chosen because their measurements were found to agree closely with the average of all the peak-to-peak readings between all possible combinations, for selected examples.

As with the presentation of the open circuit flux density distribution across a rotor tooth surface, the values of 'steady' flux linkages for each corrected coil area were converted into values of mean flux density for each coil, thus giving seven points across the tooth surface. Fig 47 shows the points measured by using the above methods on test results under two conditions of loading with different power factors, and with the alternator short-circuited. It shows clearly the distortion of the no-load flux pattern due to armature reaction and the direct demagnetization at ZPF lagging.

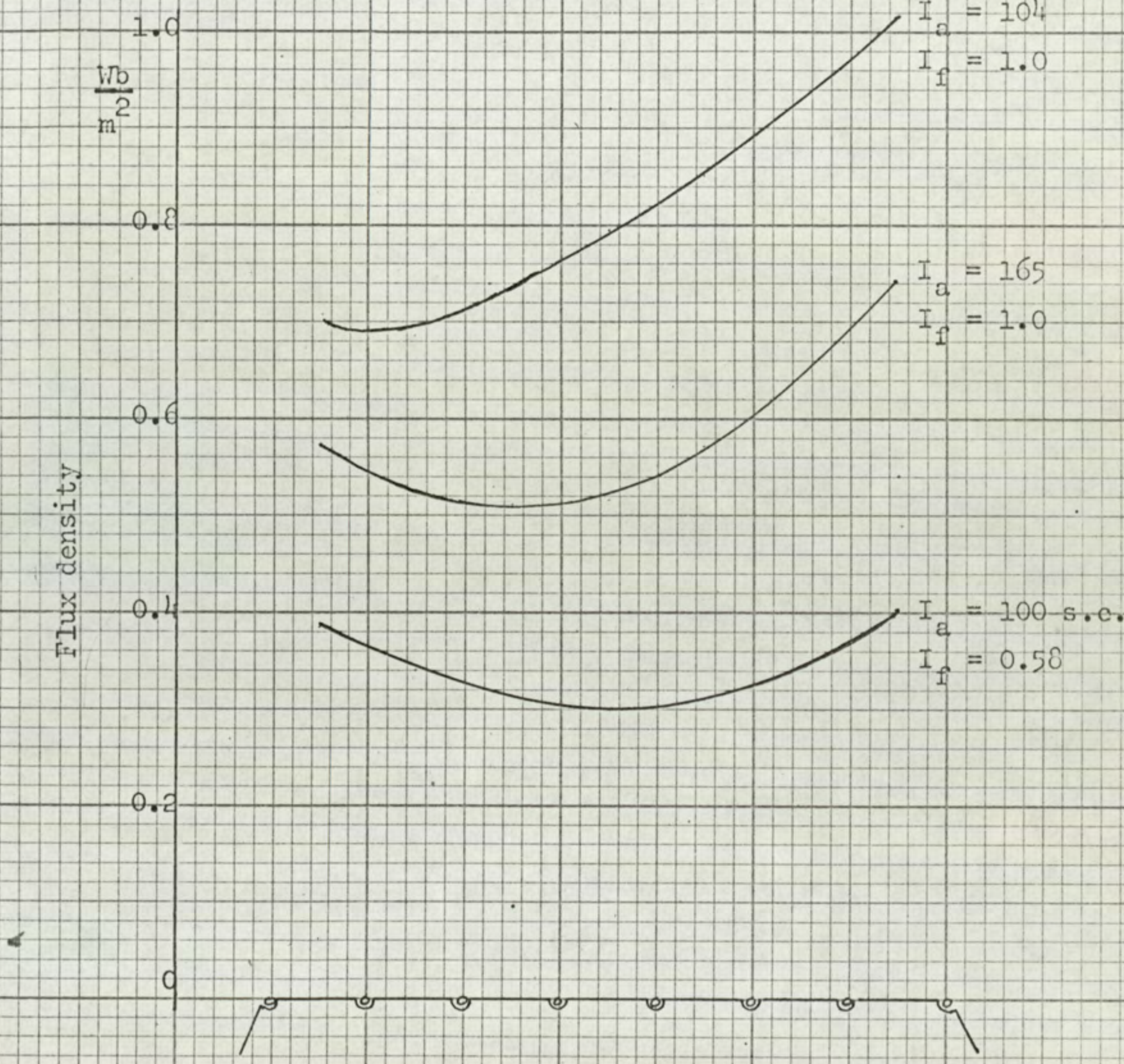

Fig 47: Measured on-load flux density distribution across rotor tooth surface

4.3 Comparison of the experimental results with the computed theoretical distribution

4.3.1 The computer programme to calculate $\overline{B}'_{oc} + \overline{B}'_a$

Selected components of equations (2) and (5) relative to the rotor, of which equation (7) is the fundamental component, are given in 8.8.1 to the 10th harmonic of θ. The summation of this series for the complete airgap flux density distribution on load, as a function of θ and δ, was programmed using Algol, 8.8.2, and run on an Elliott 803 digital computer. The series is in p.u. form and the data for a particular machine consists of values of δ, F_a, F_f and b_m for m = 0 to m = 11. For the experimental machine values for b_m were obtained by Fourier analysis of the open circuit wave (also computed, using a library programme), which in turn was derived from flux plots using a conducting paper analogue, 8.4

The programme was run for a range of values of F_a and F_f. For each value of δ the results were printed in the form of p.u. values of flux density (b_1 = 1 p.u.) at twenty points during a complete cycle of θ, i.e. every 18 electrical degrees.

All the components due to B'_a have a common factor C ($= \frac{F_a}{\pi F_f}$). By arranging the 'print-out' to supply open circuit and armature reaction components separately each combination of F_a and F_a need not be computed: a standard set of results for several values of δ and say rated full-load armature and field current may be scaled $\propto$C to describe any load condition.

If results for the required value of δ have not been computed they may be derived in p.u. form from the curves in fig 48. For each 'computed point' across the rotor tooth surface the 'standard' value of B_a has been plotted as a ratio of B_1 against a range of δ.

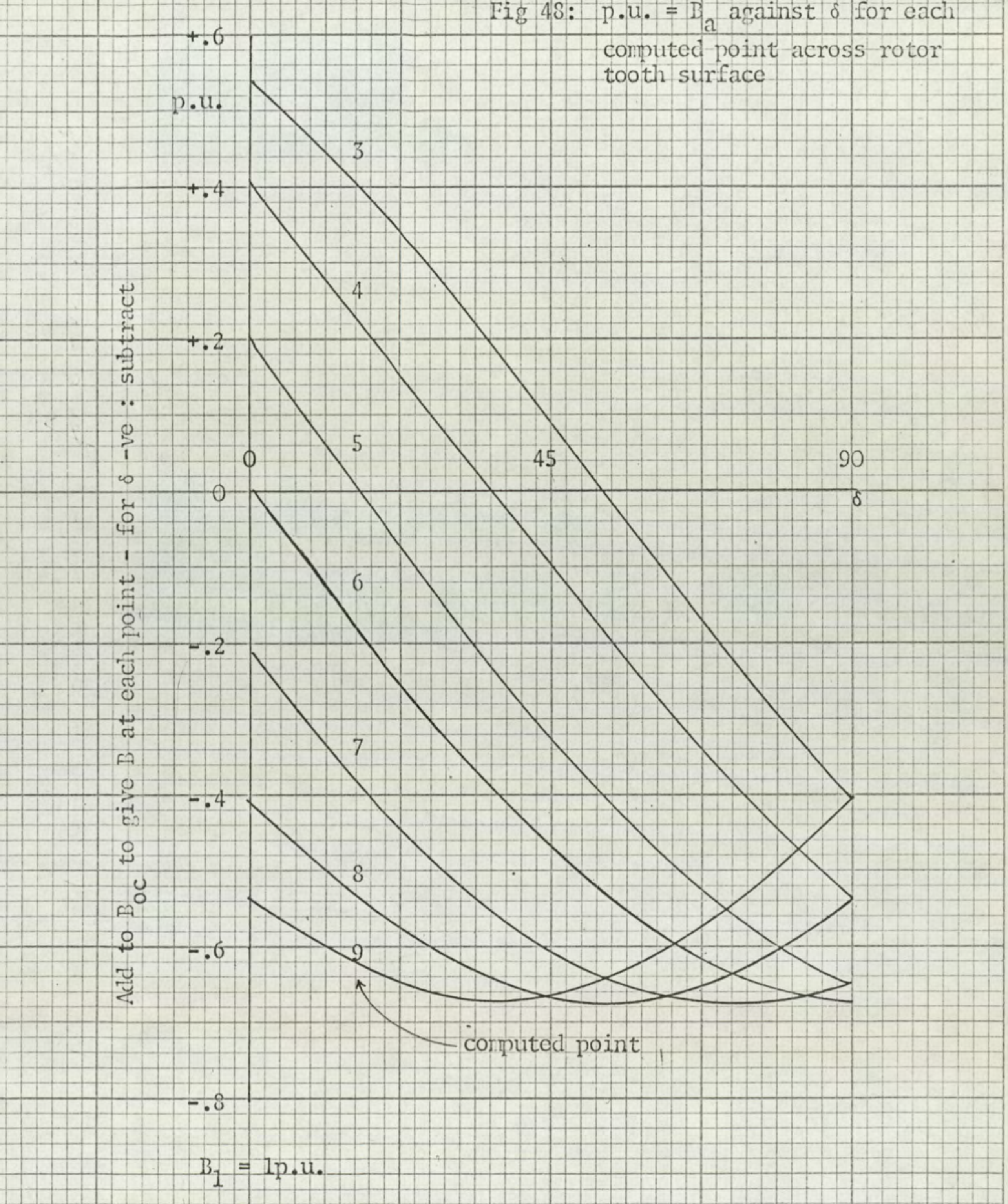

Fig 48: p.u. = B_a against δ for each computed point across rotor tooth surface

The curves formed by these points provide intermediate p.u. values of the B_a distribution.

With the knowledge of B_1/I_f from tests or calculations, the computed distribution may be plotted directly in Wb/m^2: fig 49 shows the 'standard set'.

4.3.2 Comparison of experimental and theoretical results

Table 11 shows the load conditions at which the comparison was made. Armature current, voltage and power were measured on a test set accurate at 1000c/s. The load, 2.4, was resistive; for high currents, however, the load resistor had to be reduced to a level where lead reactance affected the impedance presented to the alternator. Knowing the open circuit voltage at each field current, δ was calculated using the expression of section 4.2.1. $\delta = 45^o$ and 90^o were computed points; for $\delta = 77^o$ fig 48 was required.

The close agreement between test and calculated flux densities under load conditions give confidence both in the assumptions involved in superimposing the fields due to F_f and F_a and in the method employed to measure the flux density distribution which rotates with the rotor of this single phase alternator.

Table 11: Measured values of load current, voltage, power factor and field current, together with derived values of δ, 4.2.1. Flux density distributions at these loads are compared in fig 50 (a) and (b)

Load	I_a	V	p.f.	I_f	δ
Resistive	104	122	1.0	1.0	45^o
Impedance	165	39	.94	1.0	77^o
Short circuit	100	6	0	0.58	90^o

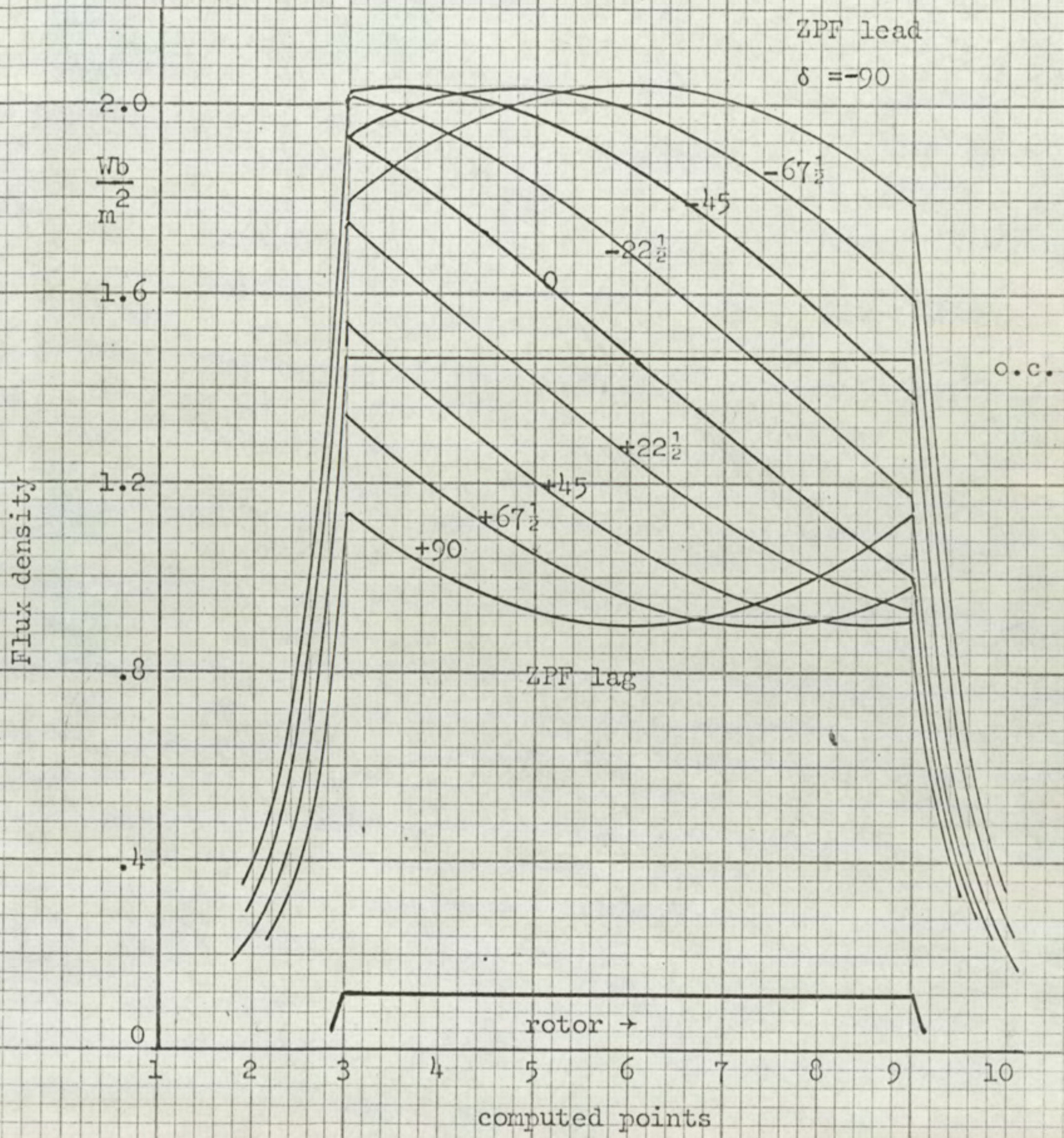

Fig 49: Flux density across a rotor tooth surface
Standard computed distributions at full load

I_a = 200A I_f = 1.76A

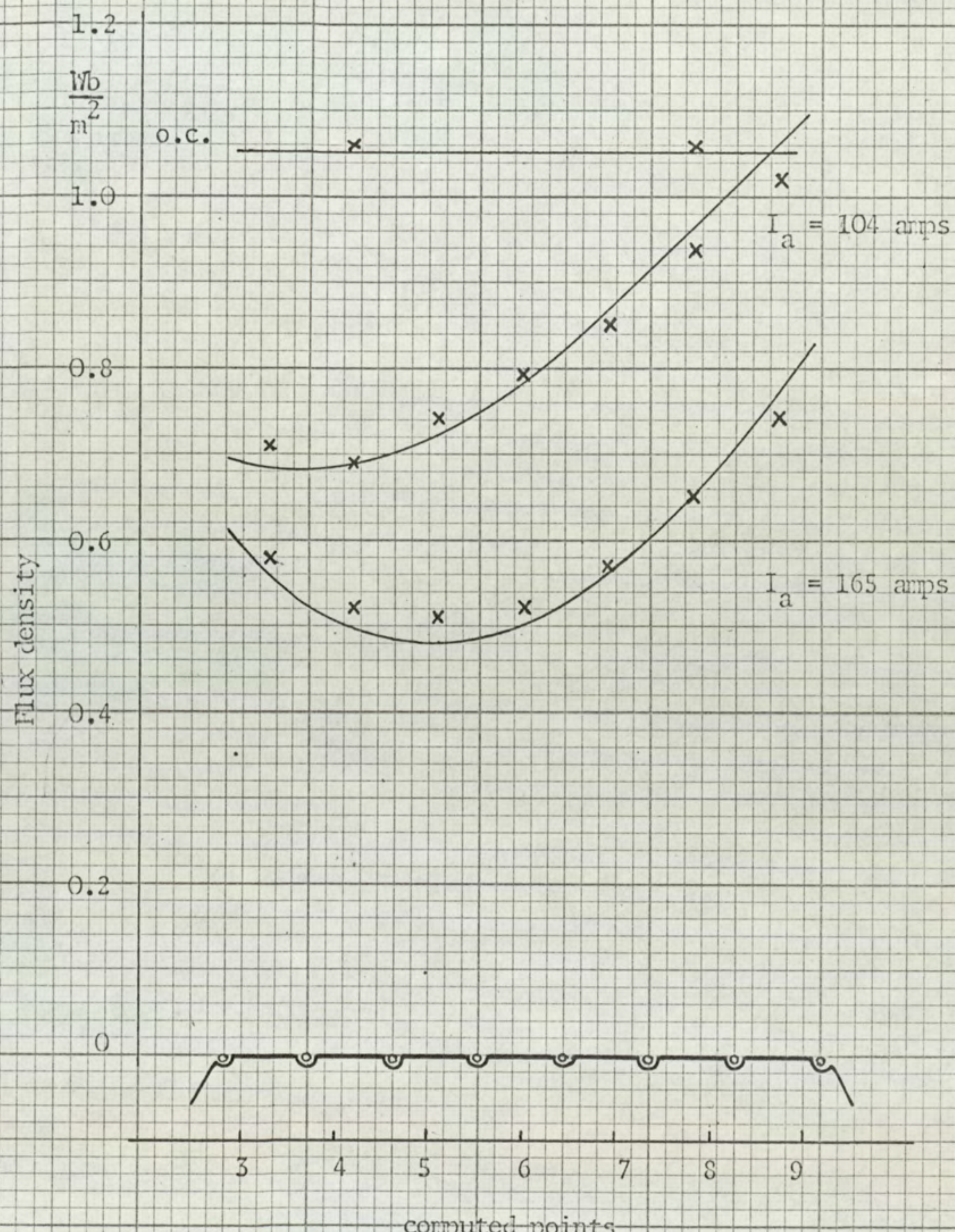

Fig 50(a): Flux density distribution across a rotor tooth surface on open-circuit and load, I_f = 1.0A see Table 11
computed ———— , measured x x

Fig 50(b): Flux density distribution across a rotor tooth surface on open- and short-circuit $I_f = 0.58A$ see Table 11

computer ———— , measured x x

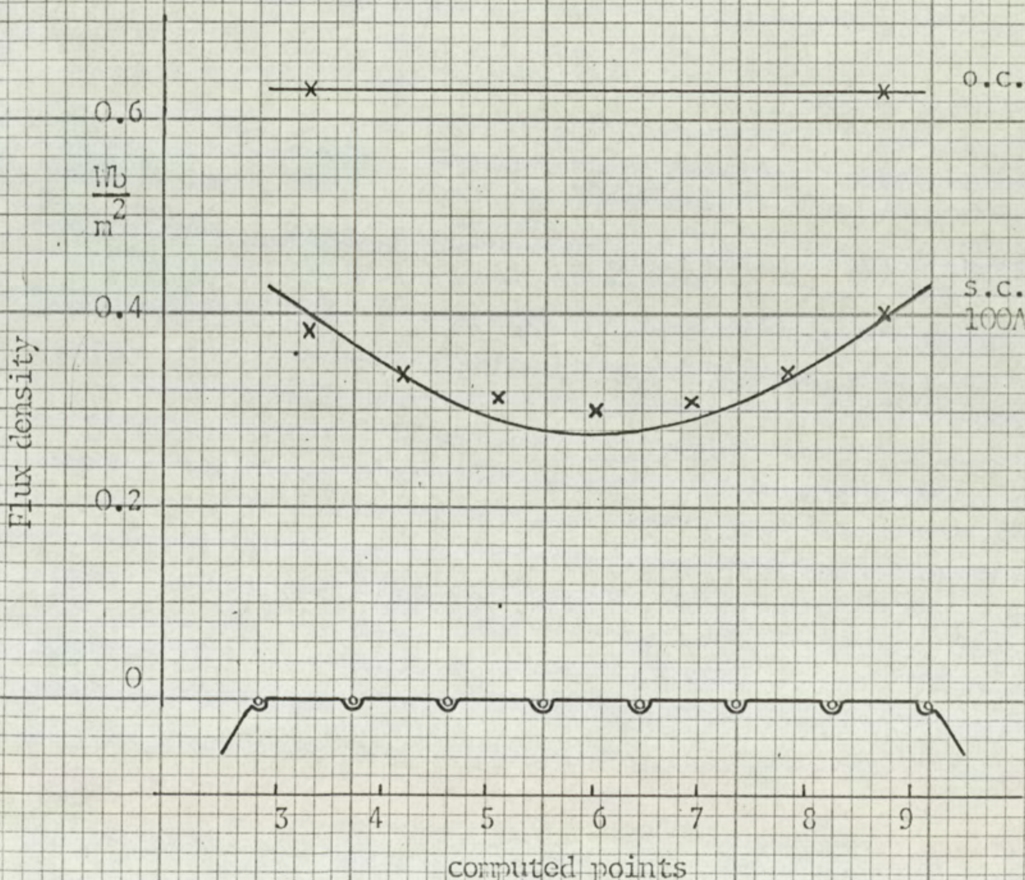

CHAPTER 5 Voltage generation

Summary

In this chapter the equations for airgap flux density are used to express the voltages induced in the armature windings due to the permeance variations combined with the armature reaction effects.

After the open circuit expressions have been corroborated by measurements and their form related to the normal flux/e.m.f. equation, the voltage that would be induced if B_a acted alone is expressed in terms of the open circuit voltage. Vector combination leads to expressions for the internal generated voltage which in turn is combined with a reactive voltage due to leakage effects to give an expression for the terminal voltage.

During the process of writing the expressions in p.u. form, factors are presented to account for the non linear relation between the voltage and field current p.u. systems, and to express the ratio of field and armature reaction m.m.f.s which has appeared previously in the theory. These are related but not identical to factors developed by previous writers.

For a particular load the alternator 'settles' to a working point which is a balance between the characteristics of the machine and the restrictions of the load. The 'characteristics' and the 'restrictions' are expressed by two simultaneous equations in terms of the 'non linear' factors whose solution presents the field requirements on load.

Examples are given which correlate the theoretical expressions with measurements on the experimental machine. Finally, the on load field requirements of the industrial unit (on which the experimental machine was modelled) are accurately 'pre-determined'. The corroborating test values were supplied by the manufacturer, which gives confidence in the technique being a useful design tool.

5.1 The generation of open circuit voltage

5.1.1 The theoretical derivation of an expression for open circuit voltage

The open circuit airgap flux density distribution in series form is given in equation (2), 3.1.4 and 4.1.1, as

$$B_{oc} = \sum_{m=0.1.2...}^{\infty} B_m \cos m(\theta - \pi/2 - \omega t)$$

The integration of this equation with regard to θ gives an expression for the total flux linking the area (between the limits of integration, per unit length) as a function of time t. Differentiation of this flux with regard to time leads to an expression for the voltage per turn resulting from B_{oc} which would be induced in a coil situated at the limits of the previous integration.

This assumes that the coil sides are concentrated at points or that all the airgap flux theoretically linking these points on the airgap surface also links the coil. In Chapter 3, Table 3, the fundamental flux contributed by a 'coil tooth' was modified by the term $(\cos \frac{\sigma}{2})$. In section 3.1.5 it was further demonstrated that the slot opening field distortion was equivalent to reducing the opening width to a quarter of its actual dimension for the purpose of calculating flux entering the tooth. Hence, the time varying value of flux linkages will be modified by the term $(\cos \frac{\sigma}{8})$.

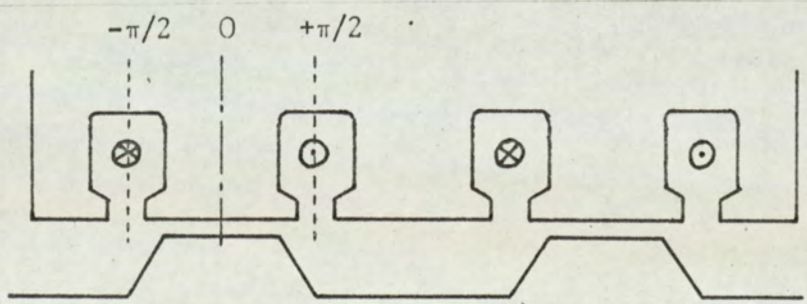

Fig 51: Basic inductor alternator airgap geometry with armature coil sense and rotor positioned for peak ZPF armature current condition

Typical armature coil side centre lines lie at $\theta = \pm \pi/2$, fig 51, and the total flux linking this coil is

$$\bar{\phi}_{oc}\Big|_{-\pi/2}^{+\pi/2} = \frac{\ell\lambda}{2\pi} \cos\frac{\sigma}{8} \sum_{m=0.1.2...}^{\infty} \int_{-\pi/2}^{+\pi/2} B_m \cos m(\theta - \pi/2 - \omega t)d\theta$$

$$= \frac{\ell\lambda}{2\pi} \cos\frac{\sigma}{8} \sum_{m=0.1.2...}^{\infty} \frac{B_m}{m}\left[\sin m(-\omega t) + \sin m(\pi + \omega t)\right]$$

$$= -\frac{\ell\lambda}{\pi m} \cos\frac{\sigma}{8} \sin m\omega t \; B_m \quad \text{for } m = 1,3,5 \text{ etc.}$$

$$= 0 \qquad \text{for } m = 0,2,4 \text{ etc.}$$

Therefore, the open circuit generated voltage $\bar{E}_{oc}$, is expressed by

$$-N_a \frac{\partial}{\partial t} \left(-\sum_{m=1.3.5...}^{\infty} \frac{\ell\lambda}{m\pi} B_m \cos\frac{\sigma}{8} \sin m\omega t\right)$$

$$\bar{E}_{oc} = \sum_{m=1.3.5...}^{\infty} N_a \frac{\ell\lambda}{\pi}\omega \; B_m \cos\frac{\sigma}{8} \cos m\omega t$$

from which the fundamental r.m.s. open circuit voltage is expressed as

$$E_{oc} = \sqrt{2}\, N_a \, \ell\lambda f B_1 \cos\frac{\sigma}{8}$$

since $\sigma = 26.35^{o}$ (electrical), $\cos\frac{\sigma}{8} = .997$; this is considered to be a negligible modification.

Comparing the expression above with the standard e.m.f/peak a.c. flux equation

$$E_{oc} = \sqrt{2}\, \pi N_a \, f \, \phi_{ac}$$

the flux ($\ell\lambda B_1$) is equivalent to $\pi\phi_{ac}$, i.e. the flux over a coil area

$(\frac{\ell\lambda}{2} B_1) = (\frac{\pi}{2} \phi_{ac})$ which shows that the derived expression is in terms of the mean of the peak alternating flux.

It is interesting to compare the designed value of ϕ, (.00256Wb, 2.1, fig 19), and the value obtained from this analysis, not solely to show that they are identical, but also to establish the group of parameters relating the two approaches.

$$E_{oc} = \sqrt{2}\, N_a \ell\lambda f \frac{c}{\ell\lambda} \phi_1 \qquad \text{from the theory above}$$

$$= c\sqrt{2}\, N_a f \phi_1$$

where c is Carters coefficient as used in the design.

$$\text{since } \phi_{ac} = \phi \frac{\varepsilon_2}{2} \quad \text{from 1.2.2(4) definition for } \varepsilon_2$$

$$E_{oc} = \frac{\varepsilon_2 \pi}{\sqrt{2}} N_a f \phi$$

$$\text{and } \phi = (\frac{2c}{\varepsilon_2 \pi}) \phi_1 \qquad \text{or } \phi_{ac} = \frac{c}{\pi} \phi_1$$

$$\left[\begin{aligned} \text{i.e. from this analysis } \phi_1 &= (\frac{\text{rated fundamental o.c. volts}}{c \sqrt{2} N_a f}) \\ &= .00134 \text{ Wb} \\ \text{and } \phi &= \frac{2c}{\varepsilon_2 \pi} (.00134) = .00253 \text{ Wb} \end{aligned} \right]$$

5.1.2 Comparison of calculated and measured values of open circuit voltage

The calculation of open circuit voltage is primarily dependent on the calculation of airgap flux density. The designed value of airgap flux density, 2.1, is 61.4Klines per in^2 at 1.1 amps field current for a gap of .015". The actual gap dimension of the experimental machine, averaged over several readings, was .013". Thus the 'corrected' designed value was 70.8Klines per in^2 or 1.09 Wb/m^2.

In section 8.4 the Fourier analysis of the analogue flux plot gives the ratio of the fundamental coefficient to the maximum level of the complete pattern as 1:1.79. Hence the fundamental flux density wave at I_f = 1.1 amp has a peak value $\frac{1.09}{1.79} = .609$ Wb/m^2.

For I_f = 1.0 amp the corresponding value is .554 Wb/m^2.

The airgap flux density was measured, 4.2.3, as 1.06 Wb/m^2 for I_f = 1.0amp. The fundamental equivalent sine distribution of this 'short pitched' square wave will have a peak value $B_1 = \frac{2}{\pi} B_{max} \sin\left(\frac{t}{\lambda}\pi\right)$ where $\frac{t}{\lambda} = 0.33$.

Hence $B_1 = \left(\frac{2 \times 1.06}{\pi} \frac{\sqrt{3}}{2}\right) = 0.584$ Wb/m^2

The favourable comparison between 'designed' and measured values was expected, but nevertheless had to be established, before any theoretical expression for voltage employing B_1 might be tested against measurements. Having shown good agreement the measured value (B_1 = .584 Wb/m^2) is used to calculate E_{oc} $(\doteqdot \sqrt{2}\, N_a \ell \lambda f B_1)$

$$= (\sqrt{2} \times 32 \times 0.14 \times 0.047 \times 10^3 \times 0.584) = 174 \text{ volts}$$

E_{oc} was defined as the fundamental r.m.s. component of the open circuit voltage. This was analysed and measured at I_f = 1.0 amp to be 175 volts.

Since the calculated value for voltage is directly proportional to flux density, comparison of one value is sufficient to demonstrate the claim of the theory to describe open circuit conditions. To calculate the open circuit characteristic into the region of non linearity requires a knowledge of the flux density under saturated conditions. This restriction applies to all expressions for voltage. The open circuit characteristic (E_{oc}/I_f) is a source of information as to the non-linear characteristics of that particular machine; this will be used to express on load field requirements in 5.3.2. There exist successful techniques for calculating this characteristic.

5.2 The terminal voltage on load

5.2.1 Introduction

Section 5.1 has described an expression for the open circuit voltage, $\overline{E}_{oc}$, derived from the open circuit airgap flux density pattern. Similarly a voltage, $\overline{E}_a$, may be derived from the airgap flux density distribution due to armature reaction. The vector combination, fig 52(a), of $\overline{E}_{oc}$ and $\overline{E}_a$ will produce $\overline{E}$, the internal generated voltage on load, assuming superposition. A relationship between $\overline{E}$ and the terminal voltage, dependent upon power factor and leakage reactance, leads to an expression for terminal voltage in p.u. terms of load and field currents, the load power factor, and the leakage reactance.

The base values chosen for the p.u. systems are:

Terminal voltage : rated r.m.s. open circuit voltage : V_o

i.e. $V = vV_o$

Armature current : rated peak full load current : I_{ao}

i.e. $I_a = iI_{ao}$

Impedance : ratio of rated voltage and current : $\frac{V_o\sqrt{2}}{I_{ao}}$

Field current : that current required to establish V_o : I_{fo}

where the subscript 'o' indicates a 'rated' value.

At a given excitation $E_{oc} = kV_o$

$$I_f = k'I_{fo}$$

the combination of the two factors k and k' is a point by point representation of the open circuit characteristic and the ratio k/k' is the non linear factor relating the two p.u. systems, when calculating working points in the region where the iron circuit ampere-turns are no longer negligible.

Fig 52

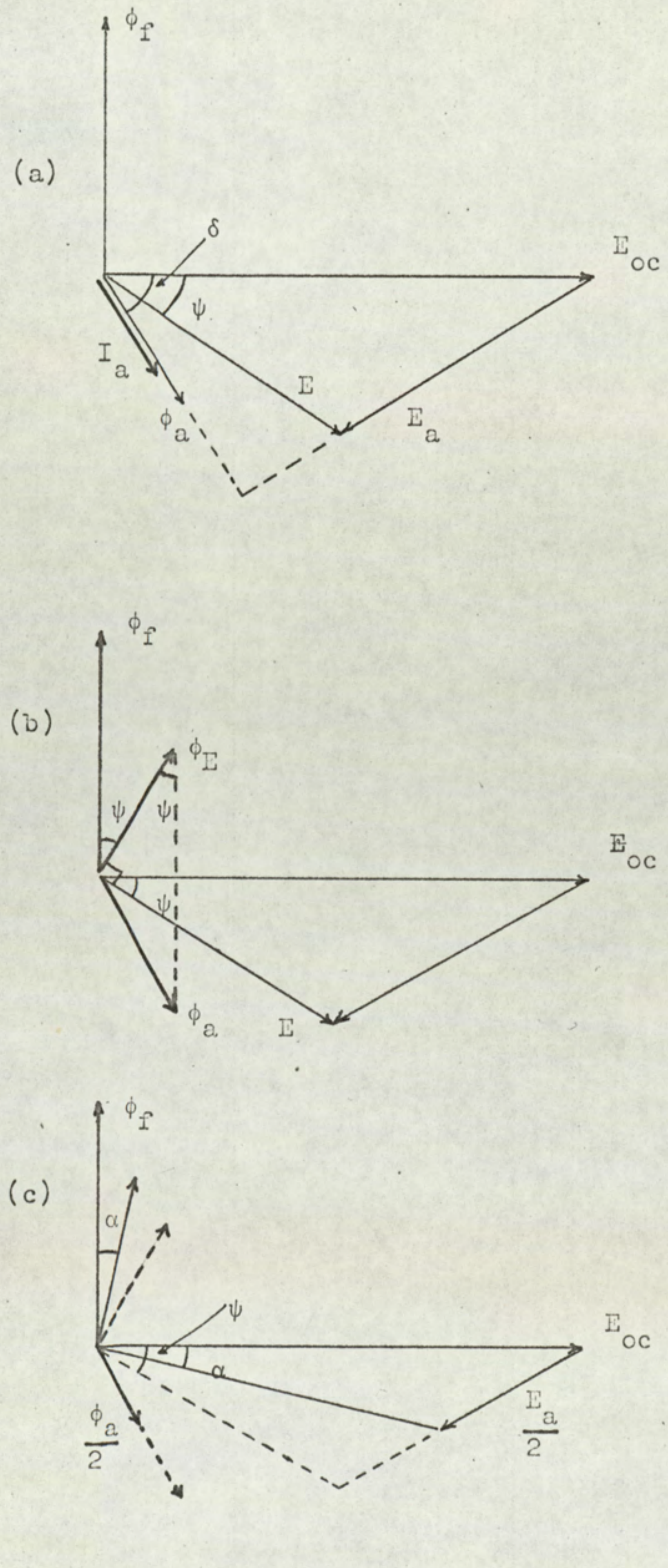

(a)
ϕ_f
δ
E_{oc}
ψ
I_a
E
ϕ_a
E_a
(b)
ϕ_f
ϕ_E
ψ
ψ
E_{oc}
ψ
ϕ_a
E
(c)
ϕ_f
α
ψ
E_{oc}
α
$\frac{\phi_a}{2}$
$\frac{E_a}{2}$

5.2.2 Theoretical derivation of $\overline{E}_a$ (voltage generated by armature reaction m.m.f.)

Equation (5), 3.2.2, for the airgap flux density distribution due to armature reaction may be expanded:

$$\overline{B}_a = CB_1 \sum_{\substack{m=0.1.2\ldots\\ n=odd}}^{\infty} \frac{b_m}{n} \sin\frac{n\pi}{2} \begin{bmatrix} \cos\{(m+n)\theta - (m-1)\omega t - \delta - n\frac{\pi}{2}\} \\ + \cos\{(m+n)\theta - (m+1)\omega t + \delta - m\frac{\pi}{2}\} \\ + \cos\{(m-n)\theta - (m-1)\omega t - \delta - m\frac{\pi}{2}\} \\ + \cos\{(m-n)\theta - (m+1)\omega t + \delta - m\frac{\pi}{2}\} \end{bmatrix}$$

The terms in θ represent the space distribution: the terms in ωt give the frequency at a given point in space. If we restrict the solution to effects that are fundamental in time, only terms in ωt are needed i.e. $m = 0$ or 2, giving an expression for the fundamental component of $\overline{B}_a$,

$$B_a = CB_1 \sum_{n=odd}^{\infty} \frac{1}{n} \sin n\frac{\pi}{2} \left[\begin{array}{ll} b_o & \{\cos(n\theta + \omega t - \delta) + \cos(n\theta - \omega t + \delta) \\ & +\cos(n\theta - \omega t + \delta) + \cos(n\theta + \omega t - \delta)\} \\ +b_2 & \{\cos(\overline{n+2}.\theta - \omega t - \delta - \pi) \\ & +\cos(\overline{2-n}.\theta - \omega t - \delta - \pi)\} \end{array} \right.$$

$$= CB_1 \sum_{n=odd}^{\infty} \frac{1}{n} \sin n\frac{\pi}{2} \quad 2\cos n\theta\{2b_o \cos(\omega t - \delta) - b_2 \cos(2\theta - \omega t - \delta)\}$$

The fundamental frequency flux linking an armature coil due to B_a will be similar to that due to B_{oc} (but qualified by the ratio of the mean armature reaction ampere turns to the field ampere turns), i.e. the integration of B_a between limits defined by the positions of the coil sides.

$$\phi_a \Big|_{-\pi/2}^{+\pi/2} = \frac{\ell\lambda B_1}{\pi} \frac{2N_a I_a}{\pi^2 F_f} \sum_{n=odd}^{\infty} \frac{1}{n} \left\{ \frac{4b_o}{n} \cos(\omega t - \delta) + \frac{2nb_2}{n^2-4} \cos(\omega t + \delta) \right\}$$

$$\text{since} \sum_{n=\text{odd}}^{\infty} \left(\frac{1}{n^2}\right) = \frac{\pi^2}{8} \quad \text{and} \quad \sum_{n=\text{odd}}^{\infty} \left(\frac{1}{n^2-4}\right) = 0, \text{ see 8.9}$$

the fundamental armature reaction flux linking the reference coil is expressed by

$$C\ell\lambda B_1\, b_o \cos(\omega t - \delta) \quad \ldots\ldots\ldots\ldots\ldots\ldots\ldots (8)$$

With the simplification of $\overline{B}_a$ into B_a, C and b_o may be regrouped into more meaningful terms with reference to existing inductor-alternator conventions.

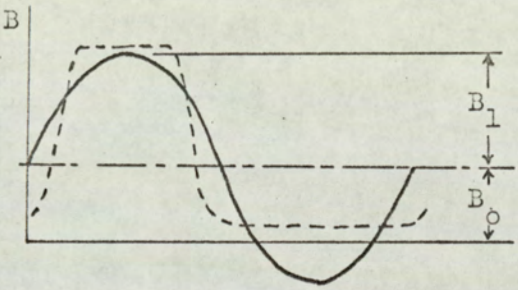

Fig 53: B_{oc} ——————
fund ——————
steady — — — —

In fig 53 the B_{oc} distribution is shown together with its steady and fundamental components. Thus

$$\varepsilon_2 = \left(\frac{2B_1}{\pi B_o}\right) = \left(\frac{2}{\pi b_o}\right)$$

$$\therefore \quad \phi_{a}\Big|_{-\pi/2}^{+\pi/2} = \frac{2C}{\varepsilon_2} . B_1 \frac{\ell\lambda}{\pi} \cos(\omega t - \delta)$$

Raby [36] defined a design parameter

$$'a' = \frac{\text{peak armature reaction ampere turns}}{\varepsilon \times \text{open circuit rated field ampere turns}}$$

This was specifically for Guy-type designs and was later modified to allow for the effects of damping circuits. Chapter 3 has investigated the undesired flux variations and their damping in Lorenz-type designs: these effects are very small compared to those experiences with Guy-type designs, since the Guy-slotting represents the 'ideal' geometry for producing the undesired second harmonic flux linkages with the field winding.

It is proposed to use 'a' for Lorenz-type designs such that at any operating condition

$$a = \frac{\text{mean armature reaction ampere turns}}{\varepsilon \times \text{field ampere turns}} = \frac{2N_a I_a}{\pi\varepsilon_2 . N_f I_f} = \frac{2C}{\varepsilon_2}$$

Hence, $\phi_{a}\Big|_{-\pi/2}^{+\pi/2} = aB_1 \frac{\ell\lambda}{\pi} \cos(\omega t - \delta)$ ....(9)

The r.m.s. fundamental e.m.f. due to $\overline{B}_a$ is derived by differentiating equation (9) with regard to time

$$E_a = \sqrt{2}\, N_a\, a\, B_1\, \ell\lambda f \sin(\omega t - \delta)$$
$$= a\, E_{oc} \cos(\omega t - \pi/2 - \delta)$$

where $-(\pi/2 + \delta)$ defines the phase angle between E_a and E_{oc}, see fig 54.

(a)

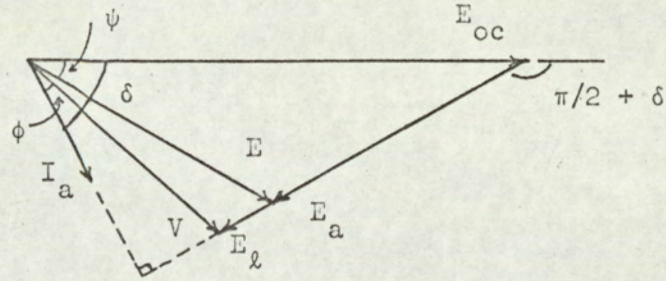

(b)

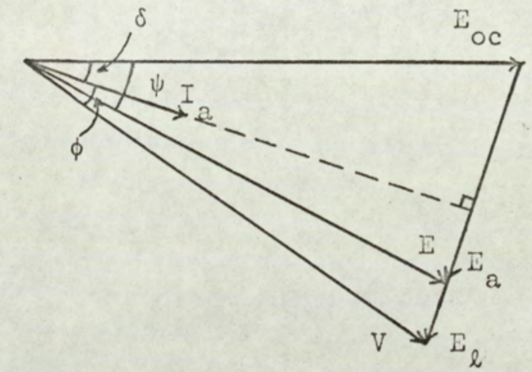

Fig 54: (a) lagging p.f. (b) leading p.f.

5.2.3 Theoretical derivation of the internal generated voltage on load, $\overline{E}$.

For the field setting which establishes B_1, combining $\overline{E}_{oc}$ and $\overline{E}_a$ gives an expression for the internal generated voltage on load, $\overline{E}$.

$$\overline{E} = \overline{E}_{oc} + \overline{E}_a$$

$$E = E_{oc} \{ (1 - a \sin \delta) \cos \omega t - a \cos \delta \sin \omega t \}$$

$$= E_{oc} A \cos (\omega t - \psi)$$

$$\text{where } A = \surd \{ (1 - a \sin \delta)^2 + (a \cos \delta)^2 \}$$

$$= \surd(1 - 2a \sin \delta + a^2)$$

$$\text{and } \cos \psi = (1 - a \sin \delta)/A$$

The time relationship of the peak values of (ϕ_f, ϕ_a) and (E_{oc}, E_a and E), the fluxes linking and the fundamental r.m.s. voltages induced in the stator reference coil, may be represented by the vector diagram of fig 52(a).

For a polyphase machine this diagram would also represent the space relationships of rotating field and armature m.m.f.s for one phase, leading to a combined on load m.m.f. generating $\overline{E}$. The angle between ϕ_E and ϕ_f, fig 52(b), in polyphase synchronous machine theory is known as the load angle. If this theory were applied to a polyphase inductor-alternator, the load angle would be given by ψ.

However, the machine being investigated is single phase. The two dominant components of the armature reaction flux are fundamental in space and contra-rotating at synchronous speed. Only the forward rotating component may appear on a synchronously rotating space diagram with the field flux which, because it depends on the rotor geometry, is itself rotating forward synchronously. More importantly, the combination of these two fields would lead to a value of load angle given by 'α' in fig 52(c) if the polyphase definition for load angle were accepted. This is the angle by which the position of the peak fundamental sinusoidal m.m.f. on load moves from the corresponding position on no load: it is a combination of real rotor movement and a shift of the resultant m.m.f. distribution. Since the concept of 'load angle' is employed to express the relative displacement of 'rotor' and stator field patterns with load, it is proposed to consider the angle 'ψ' as the load angle for this machine. It has been shown to be directly analogous with polyphase theory and is more simply expressed than 'α'. Further, 'ψ' gives the total effect of armature reaction rather than the partial effect represented by 'α'. This is discussed further in 6.3

5.2.4 The relationship between E_{oc}, E, and V leading to a general expression for the terminal voltage on-load

The generated voltage (E) supplies the terminal voltage (V) through the impedance of the armature windings. This depends upon the slot and end-winding leakage paths together with the resistance of the armature windings; the latter being usually negligible. The reactive voltage due to leakage fluxes (E_ℓ) will therefore depend on the leakage reactance X_ℓ and have the same direction as E_a,

$$E_\ell = \frac{I_a}{\sqrt{2}} X_\ell \cos(\omega t - \pi/2 - \delta)$$

Thus the terminal voltage is expressed by the solution of the vector triangle in fig 54

$$V = \sqrt{\left\{ (E_{oc}A)^2 + \left(\frac{I_a}{\sqrt{2}} X_\ell\right)^2 + 2E_{oc}A\frac{I_a}{\sqrt{2}} X_\ell \sin(\psi-\delta) \right\}}$$

at an angle $(-\delta \pm \phi)$ to E_{oc} (+ for lagging p.f.)
or, in terms of the load power factor rather than the load angle.

$$E = \sqrt{\left\{ V^2 + \left(\frac{I_a}{\sqrt{2}} X_\ell \right)^2 \pm 2V \frac{I_a}{\sqrt{2}} X_\ell \sin\phi \right\}} \text{ (+ve for lagging p.f.)}$$

The complexity of these expressions for the terminal voltage are due to the separate derivations of E_a and E_ℓ, with the intermediate expression for E. Whereas E_a stems directly from B_a, i.e. is resultant on the airgap flux distribution, E_ℓ is introduced to account for flux distributions on load which are not controlled by the airgap region. For the purposes of this analysis the well tried concepts of leakage reactance [35] which were used in the design of the experimental machine are employed.

E_a and E_ℓ may be combined as one reactive voltage due to armature reaction in the following manner.

$$E_a = a\, E_{oc} \qquad \text{from 5.2.2}$$

$$= (a_o\, i\, \frac{k}{k'}\, V_o)$$

$$\text{if } a_o = \frac{2N_a I_{ao}}{\varepsilon_2 \pi N_f I_{fo}} = a\,\frac{k'}{i}$$

$$E_\ell = \frac{I_a}{\sqrt{2}} X_\ell = i x_\ell V_o$$

if x_ℓ is the p.u. leakage reactance ($= X_\ell \frac{I_{ao}}{V_o\sqrt{2}}$)

The assumption is made that, similar to E_a, E_ℓ must be modified by the factor $k/_{k'}$, to allow for non-linear effects. (Walker [2] refers to a similar 'saturation factor').

$$\text{Hence} \qquad E_a + E_\ell = i\,\frac{k}{k'}\,(a_o + x_\ell)\, V_o$$

Using this combined voltage in the solution of the vector triangle in fig 54 leads to a complete expression for V in terms of E_{oc}.

$$(E_{oc})^2 = V^2 + (E_a + E_\ell)^2 \pm 2V(E_a + E_\ell) \sin \phi$$

$$(kV_o)^2 = V^2 + \{i\tfrac{k}{k'} (a_o + x_\ell)V_o\}^2 \pm 2V\, V_o\, i\tfrac{k}{k'} (a_o + x_\ell) \sin \phi$$

Dividing by $V_o^{\;2}$ and re-arranging into the quadratic solution form gives the p.u. expression, (since $V = vV_o$)

$$v = \mp i\tfrac{k}{k'} (a_o + x_\ell) \sin\phi \pm \surd\left[k^2 - \{i\tfrac{k}{k'} (a_o + x_\ell) \cos\phi\}^2\right] \quad \ldots (10)$$

In fig 55, equation (10) is represented by

$$OA = \mp AB \pm OB$$

Thus for positive OB, the negative value of AB represents a lagging power factor condition. With simplifications the p.u. r.m.s. terminal voltage on load is given by

$$v = \surd\{k^2 - (M\cos\phi)^2\} \mp M\sin\phi \qquad \text{(-ve:lagging p.f.)} \quad \ldots\ldots. (11)$$

where $M = i\frac{k}{k'} (a_o + x_\ell)$

Equation (11) has restricted applications as discussed in 5.2.5 since the following must be known -

a) open-circuit characteristic
b) load and field currents at the operating point
c) leakage reactance
d) load power factor

(a)

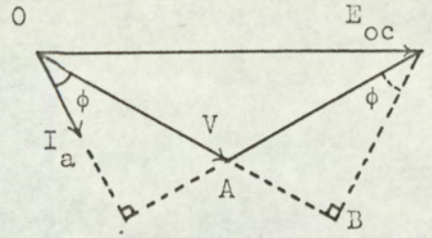

(b)

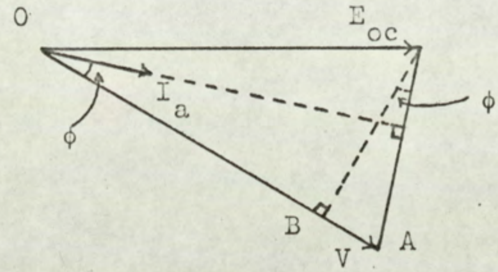

Fig 55: (a) lagging p.f. (b) leading p.f.

5.2.5 General analysis of the terminal voltage expression

The expression for terminal voltage on load given by equation (11) requires a knowledge of the particular relationship of load current to field current for the machine being studied. Thus it may be used for analysis of existing machines, to indicate the effect of a change in design or operating conditions, but not for new design calculations.

In 5.3.1 the experimental machine is analysed for two conditions of loading to compare the theoretical and actual results. It is fully recognised that far reaching assumptions are involved both in the series representation of flux density patterns, and in the superposition of fields required to establish this theory. The conditions peculiar to this machine which allow these assumptions are, respectively, that the b_o, b_1 and b_2 terms included in the theory form the major components of the space distribution and, that where the airgap is small, harmonic pole to pole leakage within the gap is negligible.

Because the theoretical derivation of armature reaction is based on open circuit conditions the terminal voltage is expressed in terms of the factors k and k'. Equation (11) may be re-arranged in the form

$$k' = f(i, v, \varepsilon_2, \phi, x_\ell \text{ and } k)$$

This normalised form may be presented graphically by plotting k' against k. Families of curves result; for a range of p.u. current while v, ϕ, ε_2 and x_ℓ are held constant; for a range of power factors while i, v, ε_2 and x_ℓ are held constant; etc, as shown in figs 60 and 61.

Of these parameters, i and v are p.u. values, ε_2 and x_ℓ are due to the 'geometry' of the design and will have particular values for a given machine while cos ϕ, the load circuit power factor, will have conventional values say unity or $\pm$ 0.9. Therefore, the five families of curves represent conditional relationships between k and k' for all possible loads and machine geometries (within the assumptions).

A second relationship between k' and k, peculiar to each machine, is obtained from the open circuit characteristic, fig 56. The intersection of any one curve from $k' = f(i, v, \varepsilon_2, \phi, x_\ell \text{ and } k)$ and the open circuit k'/k relationship represents a simultaneous satisfaction of the normalised load conditions and the open circuit non-linearity particular to that machine. This technique is possible because the field pattern due to load is expressed in terms of open circuit parameters. The use of this process to pre-determine machine characteristics depends upon the ability to pre-determine the open circuit characteristic: this is accepted practice.

Section 5.3.2 describes this process of building up the load characteristic point by point for level regulation. The result is a curve which accurately pre-determines the necessary field current for practical load currents at conventional power factors.

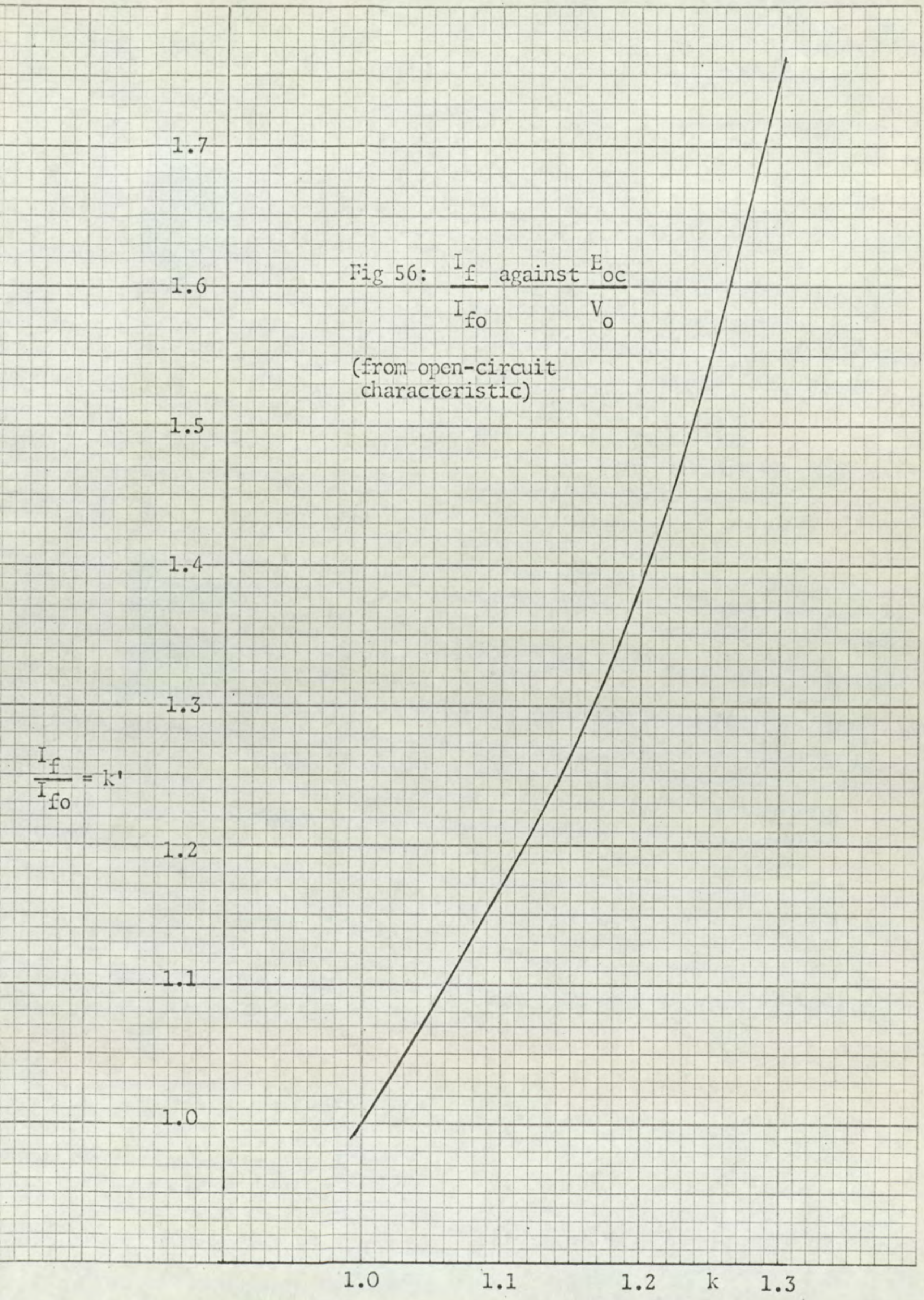

Fig 56: $\frac{I_f}{I_{fo}}$ against $\frac{E_{oc}}{V_o}$
(from open-circuit characteristic)
$\frac{I_f}{I_{fo}} = k'$
1.0
1.1
1.2
1.3
1.4
1.5
1.6
1.7
k

5.3 Application of the terminal voltage expressions to experimental and industrial machines

5.3.1 Two examples of comparisons between measured and calculated voltage characteristics

(1) Measurements of terminal voltage are taken when the alternator is supplying a constant impedance load; for a range of field current values, load current, terminal voltage and open circuit voltage are measured. These are given in Table 12 together with corresponding values for k, k' and k/k'.

Table 12: Test values with corresponding p.u. factors for constant impedance load.

V_o = 150V, I_{ao} = 314A, I_{fo} = 0.88A

I_f	k'	I_a	i	E_{oc}	k	k/k'	V
.25	.284	42.4	.135	46	.307	1.081	27
.5	.568	87.0	.277	90	.599	1.055	54
.75	.852	130.0	.414	131	.873	1.025	80
1.0	1.136	169.7	.540	162.5	1.083	.955	104
1.25	1.420	205.1	.653	184	1.226	.863	125
1.5	1.704	233.3	.743	199.5	1.330	.781	143
1.75	1.988	255.9	.815	209	1.396	.702	156
2.0	2.272	274.3	.873	215	1.433	.631	167

The remaining information required to calculate V at each of the measured points is as follows:

1) load circuit power factor = .973 lag (measured average of readings at each point)

2) p.u. leakage reactance = 0.32, by design, section 2.1

3) $a_o = \left(\frac{2}{\varepsilon_2 \pi} \quad \frac{N_a I_{ao}}{N_f I_{fo}} \right)$ or $\left(b_o \frac{N_a I_{ao}}{N_f I_{fo}} \right)$, these are theoretically equal, 5.2.2, but $\left(\frac{2}{\pi b_o} \right) = 0.89$ compared with the design value for ε_2 of 0.83. The comparison between calculations using both values is given in fig 57.

$$\frac{N_a I_{ao}}{N_f I_{fo}} = \frac{1 \times 314}{270 \times 0.88} = 1.322$$

using the 'design' value for ε_2, $a_o = 1.013$
using the 'theoretical' form, $a_o = 0.938$

calculations are presented in Table 13 using the 'theoretical' form i.e. $M = ik/_{k'} (a_o + x_\ell) = 1.258\ ik/_{k'}$

Table 13: Components of equation (11) leading to the calculated value of V for comparison with Table 12

I_f	M	$M^2\cos^2\phi$ a	k^2 b	(b-a)	$\sqrt{(b-a)}$ c	$M\sin\phi$ d	(c-d) v	V
.25	.184	.032	.094	.062	.249	.043	.206	30.9
.5	.368	.128	.359	.231	.481	.085	.396	59.4
.75	.534	.270	.762	.492	.701	.123	.578	86.7
1.0	.649	.399	1.173	.774	.880	.150	.730	109.5
1.25	.709	.476	1.503	1.027	1.013	.164	.849	127.4
1.5	.730	.505	1.769	1.264	1.124	.169	.955	143.3
1.75	.720	.491	1.949	1.458	1.207	.166	1.041	156.2
2.0	.693	.455	2.053	1.598	1.264	.160	1.104	165.6

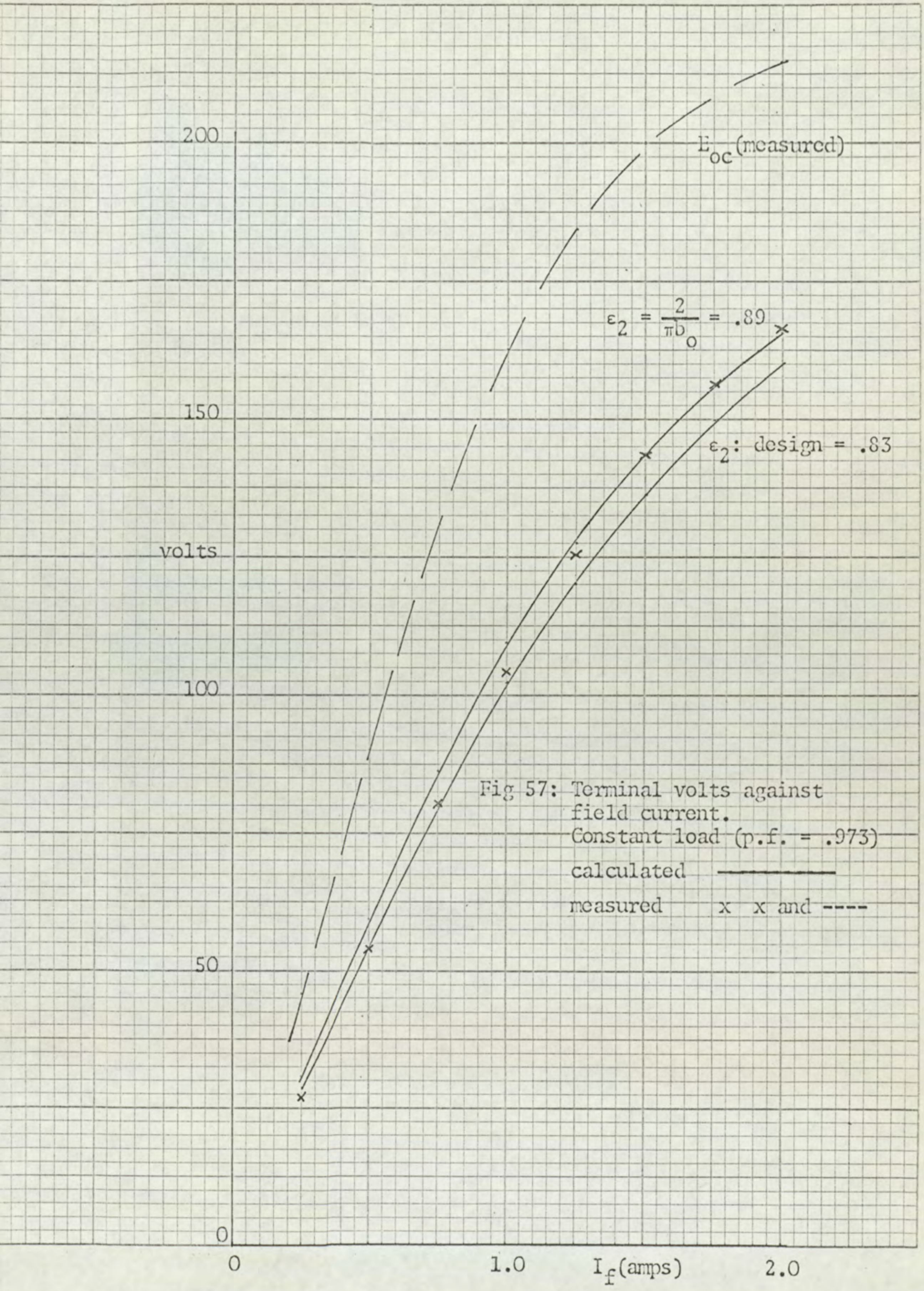

Fig 57: Terminal volts against field current. Constant load (p.f. = .973)

(2) In the second example, measurements of terminal characteristics are taken when the alternator is supplying a varying impedance load: the field current is held constant which results in k, k' and $k/_{k'}$, having constant values. Each point is associated with a different value of load power factor which is calculated from Table 14.

Table 14: Measurements of r.m.s. terminal load current, voltage and power together with calculated values for power factor. Field current = 1.0amp.

$Ia/\sqrt{2}$	V	Kw	cos ϕ
0	163	-	1.0
62.5	143.5	8.92	.995
104	121	12.46	.99
120	104	12.29	.985
155	62.6	9.51	.98
165	39.2	6.08	.94
168	24.5	3.58	.87

$$\text{Thus} \quad \left.\begin{aligned} k &= 163/150 = 1.087 \\ k' &= 1.0/0.88 = 1.136 \end{aligned}\right\} \; k/_{k'} = 0.957$$

and equation (11) simplifies to the form

$$v = \sqrt{\{1.181 - (1.204 \text{ i} \cos\phi)^2\}} - 1.204 \text{ i} \sin\phi$$

Table 15 gives the components of this equation leading to the calculated values of V using the 'theoretical' derivation of ε_2. Fig 58 shows the calculated values of V both from Table 15 and when using the 'design' value for ε_2, together with the measured values. Vector diagrams representing approximately the 60 amp and 160 amp points of fig 58 are given in fig 59.

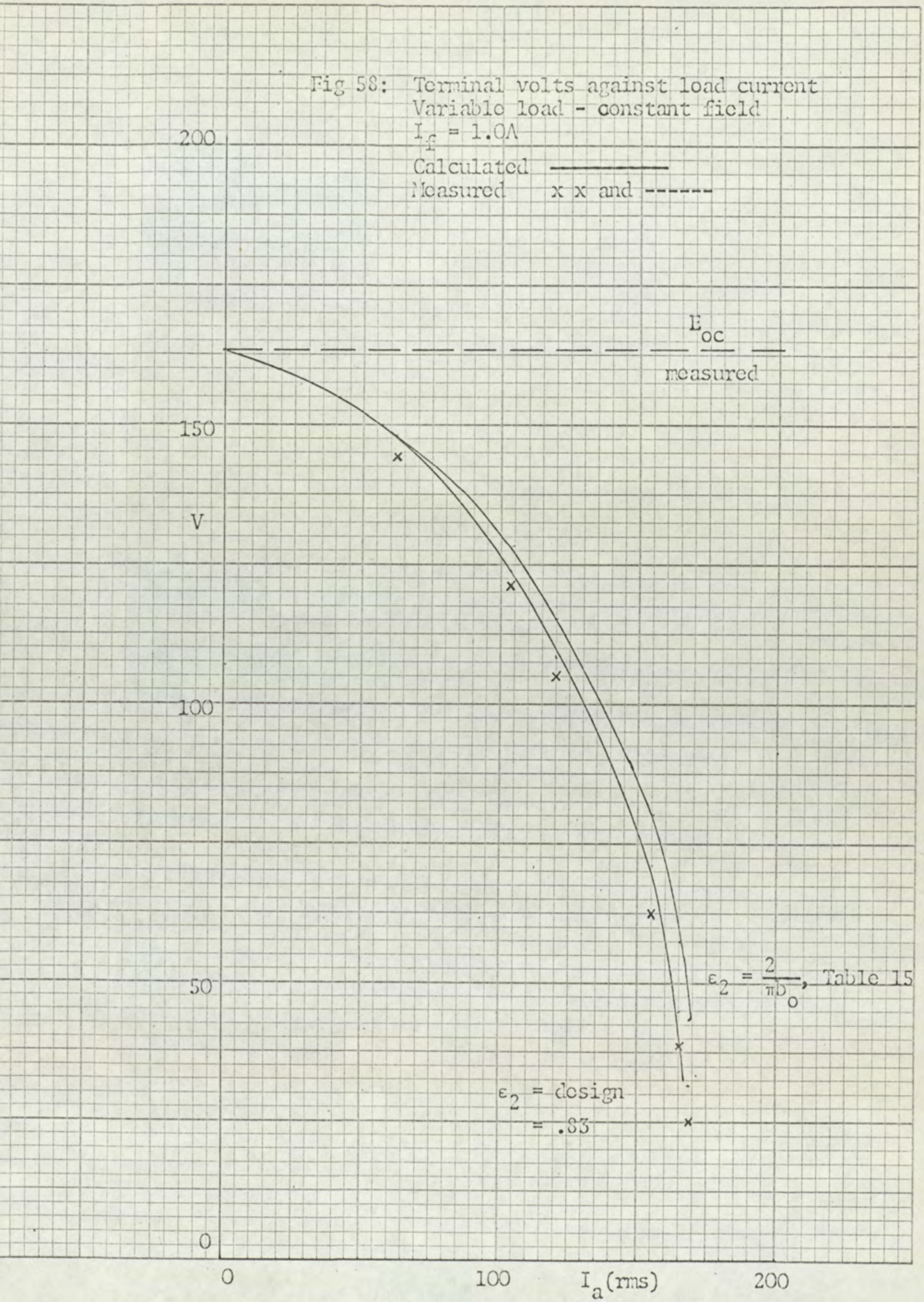
Fig 58: Terminal volts against load current
Variable load - constant field
I_f = 1.0A
Calculated
Measured x x and
E_{oc}
measured
$\varepsilon_2 = \frac{2}{\pi b_o}$, Table 15
ε_2 = design
= .83
V
200
150
100
50
0
0
100
200
I_a(rms)

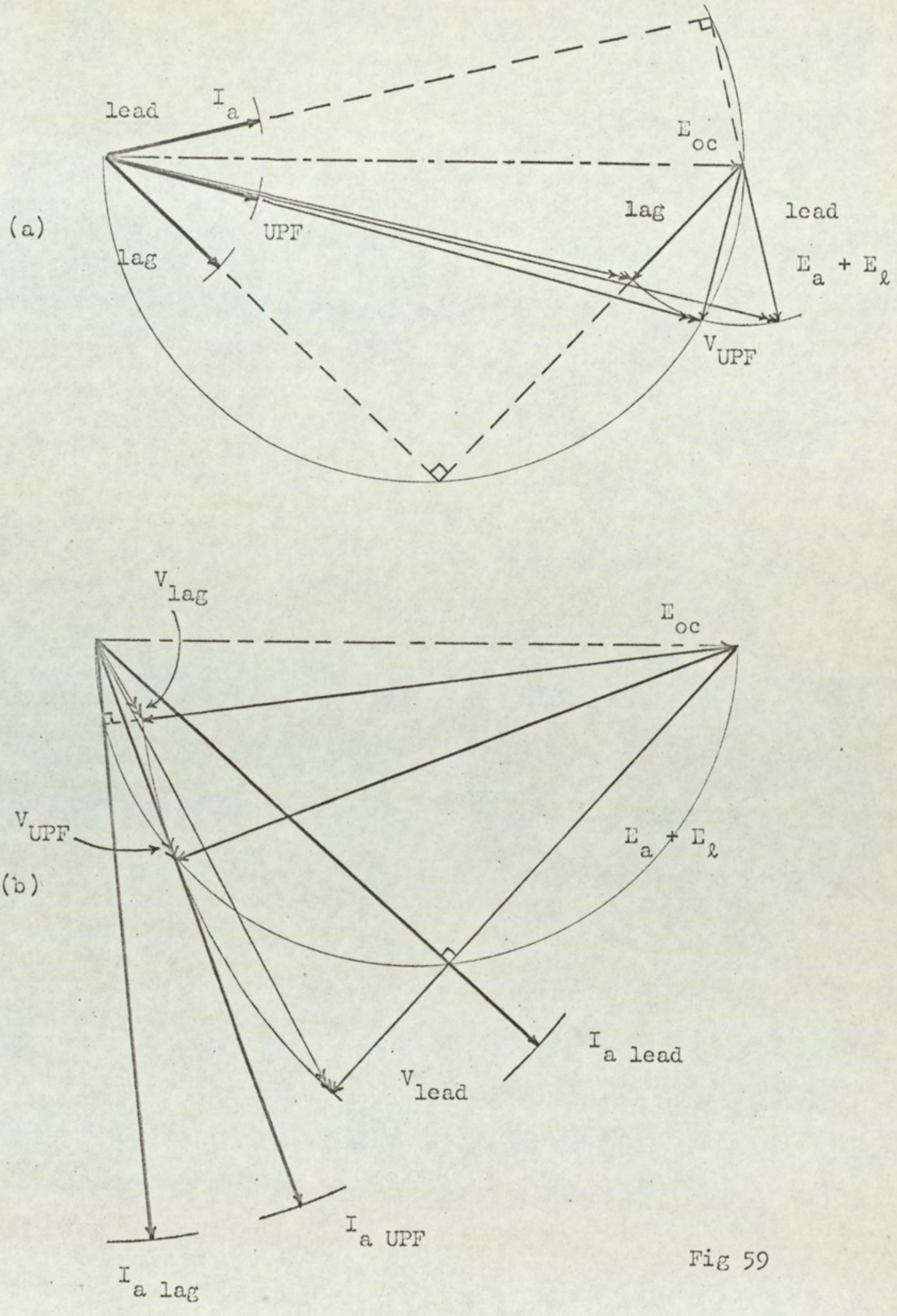

lead
I_a
E_{oc}
(a)
UPF
lag
lag
lead
$E_a + E_\ell$
V_{UPF}
V_{lag}
E_{oc}
V_{UPF}
(b)
$E_a + E_\ell$
$I_{a\ lead}$
V_{lead}
$I_{a\ UPF}$
$I_{a\ lag}$

Fig 59

Table 15: Components of equation (11) leading to the calculated value of V for comparison with Table 14

$Ia/\sqrt{2}$	i	M	$M^2\cos^2\phi$ a	(k^2-a) b	$\sqrt{b}$ c	$M\sin\phi$ d	$(c-d)$ v	V
0	-	-	-	1.182	1.089	-	1.089	163
62.5	.281	.338	.113	1.049	1.024	.034	.990	148
104	.468	.563	.311	.870	.933	.079	.854	128
120	.540	.650	.410	.771	.878	.112	.766	115
155	.698	.840	.678	.493	.702	.167	.535	80
165	.743	.895	.708	.473	.688	.305	.383	57
168	.756	.910	.627	.554	.744	.449	.295	44

5.3.2 The relationship between field current and terminal voltage

For lagging power factor equation (11), 5.2.4, may be rearranged in terms of $M = ik/_{k'}\,(a_o + x_\ell)$,

$$M^2 + 2v\sin\phi\, M + (v^2 - k^2) = 0$$

$$\text{or} \quad M = -v\sin\phi \pm \sqrt{\{v^2\sin^2\phi - (v^2 - k^2)\}}$$

taking the positive square root as previously, 5.2.4,

$$k' = \frac{ik\,(a_o + x_\ell)}{\sqrt{(k^2 - v^2\cos^2\phi)} - v\sin\phi} \qquad \text{................(12a)}$$

similarly for leading power factor conditions

$$k' = \frac{ik\,(a_o + x_\ell)}{\sqrt{(k^2 - v^2\cos^2\phi)} + v\sin\phi} \qquad \text{................(12b)}$$

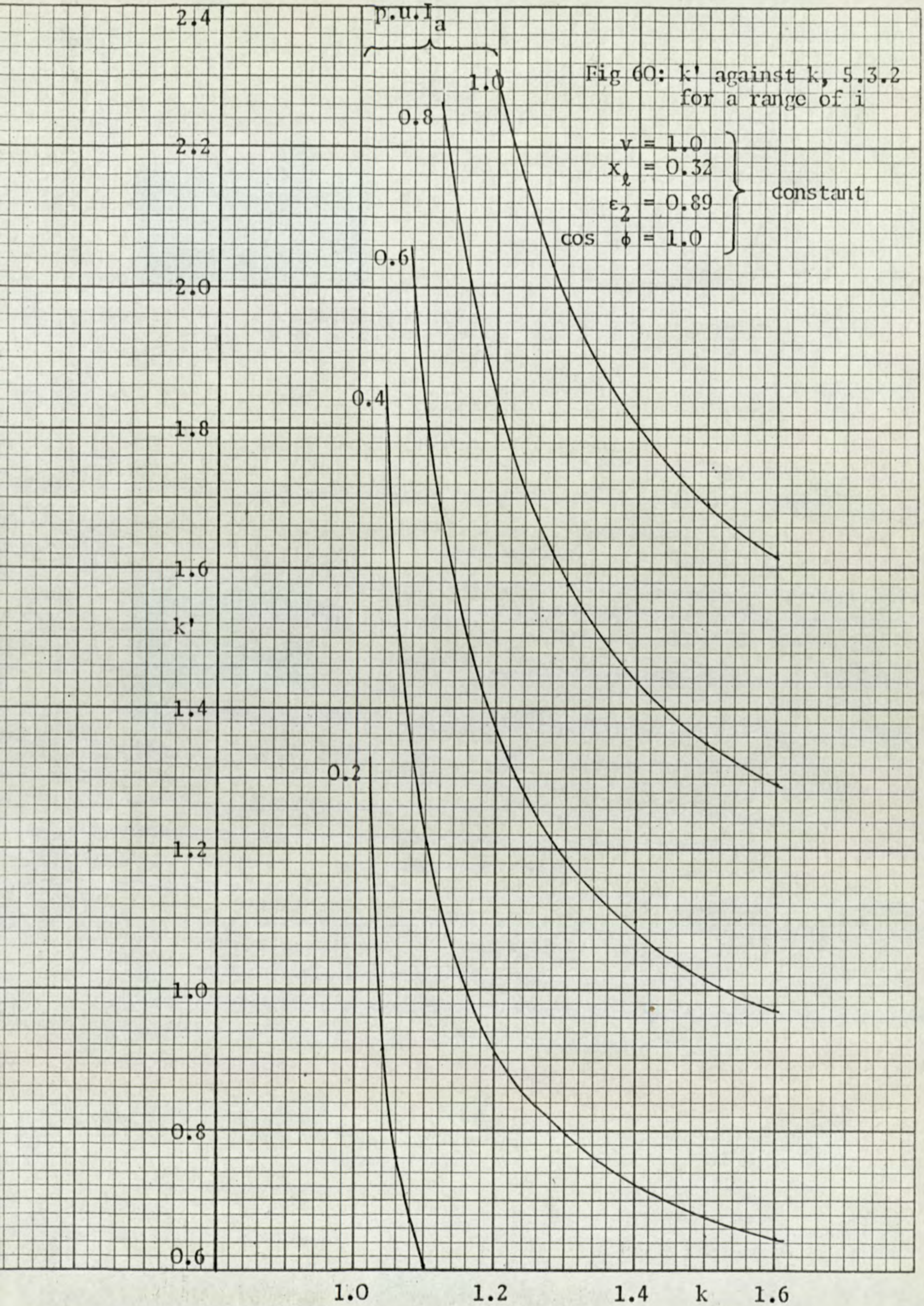
p.u. I_a
1.0
0.8
0.6
0.4
0.2
Fig 60: k' against k, 5.3.2
for a range of i
v = 1.0
x_ℓ = 0.32
ε_2 = 0.89
cos ϕ = 1.0
constant
k'
2.4
2.2
2.0
1.8
1.6
1.4
1.2
1.0
0.8
0.6
1.0
1.2
1.4
k
1.6

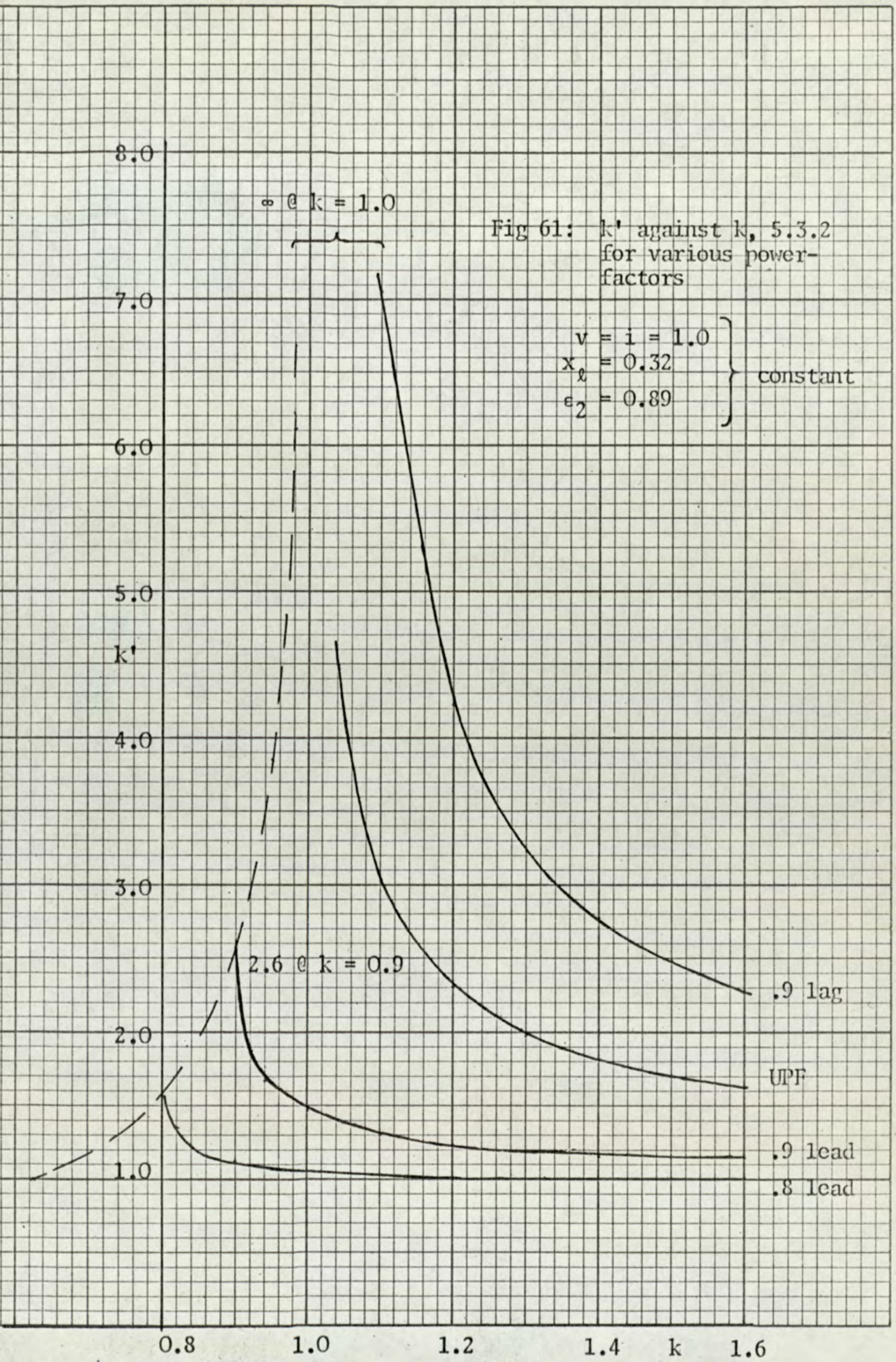

Fig 61: k' against k, 5.3.2 for various power-factors

Figs 60 and 61 are examples of families of curves for k' plotted against k, representing the effect of one parameter varying while the rest were held constant. Since k' is directly proportional to i, all the curves in fig 60 are in fact the same curve; each level of i sets a different scale to the axes. In fig 61 the variable is ϕ; each curve is unique and subject to limits dependent on the constant values chosen for the remaining parameters.

Measurements were made of load and field current on the experimental machine adjusted for level regulation at each load. Table 16 presents these readings with p.u. values for the load current and calculated values of the load power factor.

Table 16: Measurements of field current, load current and power together with calculated power factor; each setting adjusted for V = 150 volts.

$Ia/\sqrt{2}$	i	Kw	pf	I_f
62.5	.281	9.32	.994	1.03
88.8	.400	13.25	.995	1.14
99.4	.447	14.79	.992	1.18
104.8	.472	15.50	.986	1.21
127.8	.575	18.88	.985	1.32
138.2	.622	20.43	.985	1.49
202.3	.910	30.00	.988	1.78

Although some significance may be attached to the variation in calculated load power factor in that it tends to decrease as the load resistance decreases, consistent reading of the watt meter to this accuracy is not practical. Therefore the calculations are made for $\cos \phi = .995$ and $\cos \phi = .985$, representing the two extreme values.

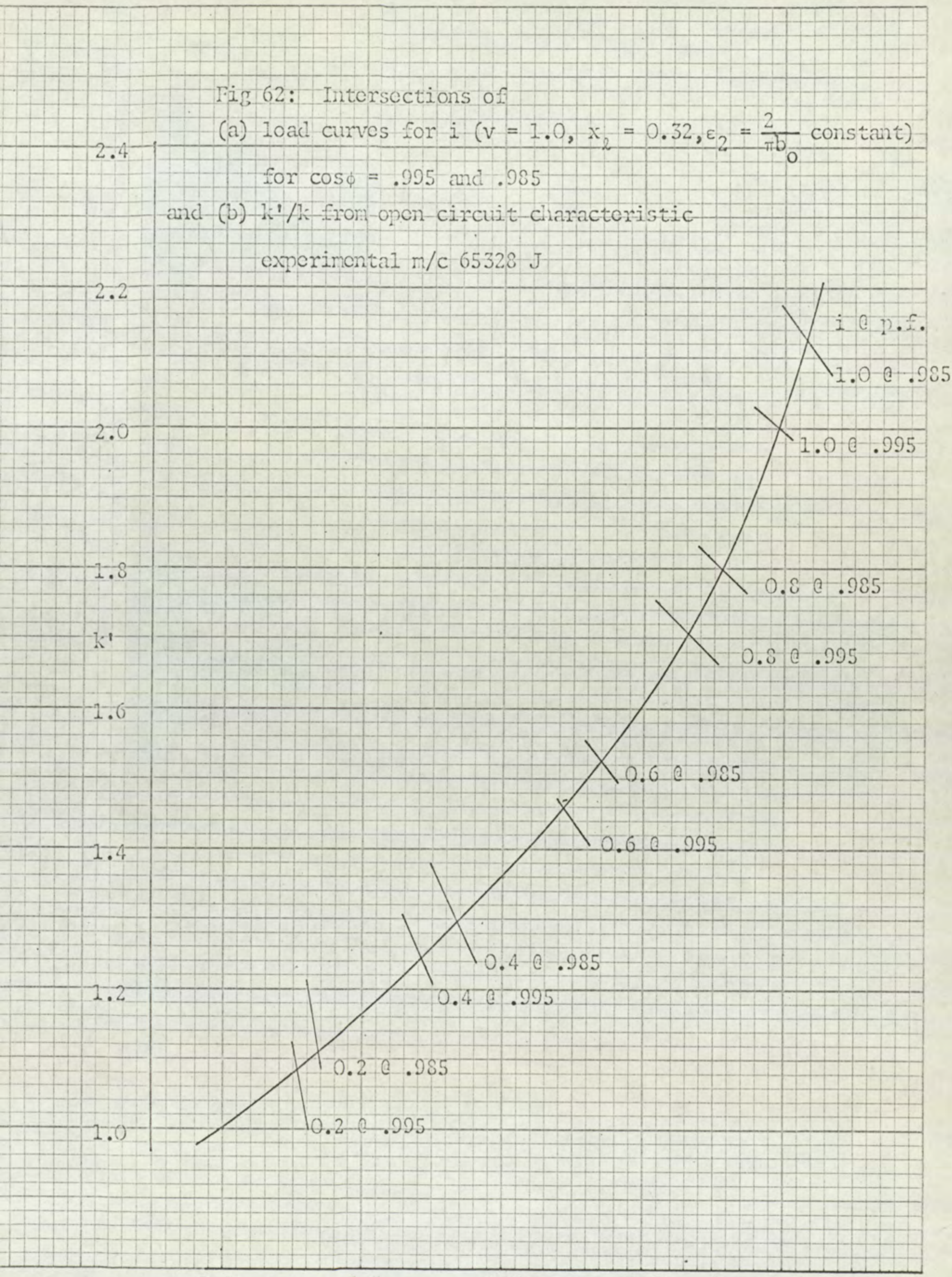

Fig 62: Intersections of
(a) load curves for i ($v = 1.0$, $x_\ell = 0.32$, $\epsilon_2 = \frac{2}{\pi b_o}$ constant) for $\cos\phi$ = .995 and .985
and (b) k'/k from open circuit characteristic
experimental m/c 65328 J

Fig 63: Field current against p.u. load current at .995 p.f. and .985 p.f.
Calculated for $(\varepsilon_2 = \frac{2}{\pi b_o})$ ————

Measured on experimental m/c 65328 J x x

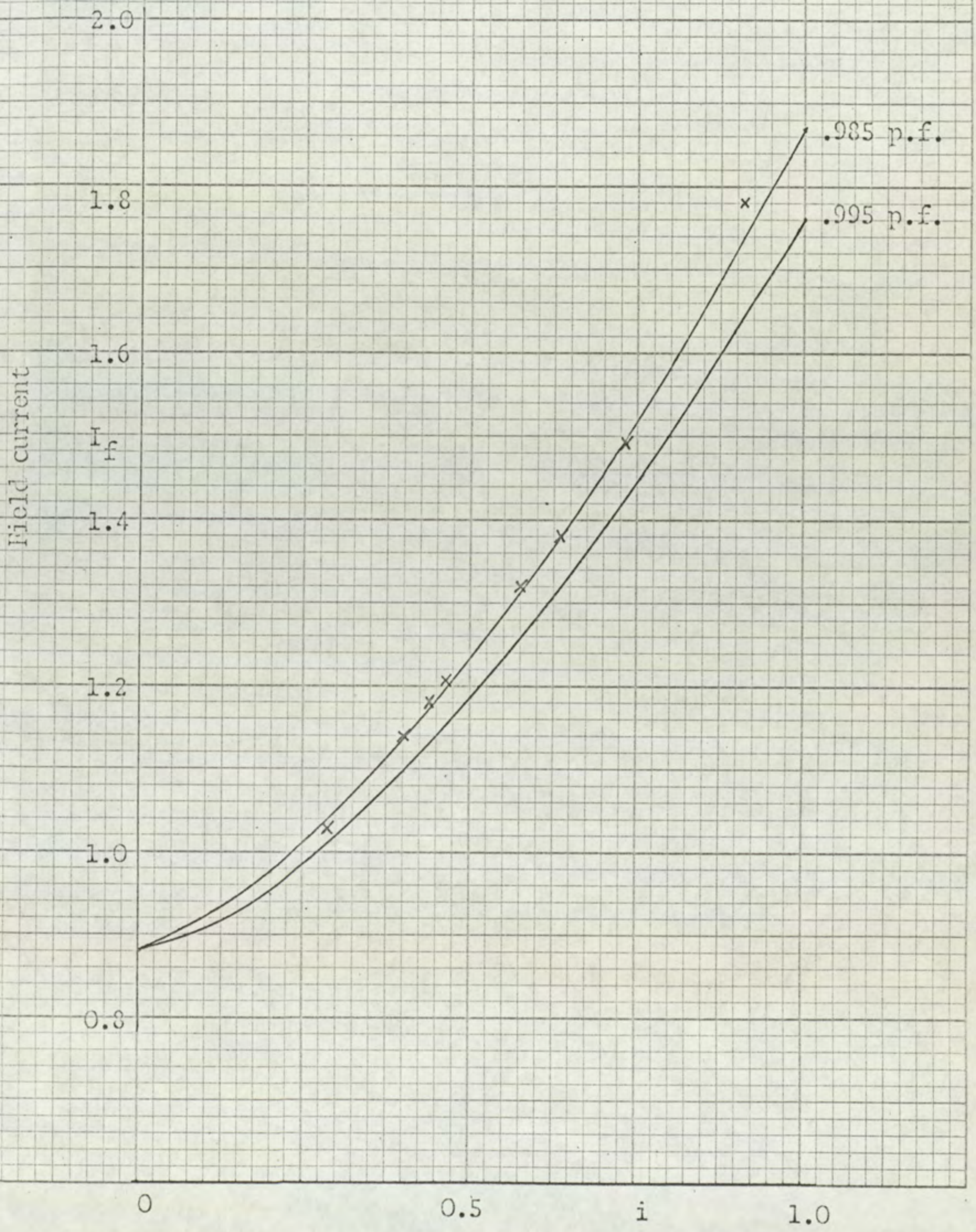

Fig 64: Field current against p.u. load current at .995 p.f. and .985 p.f.

Calculated for (ε_2: design = .83) ———

Measured on experimental m/c 65328 J x x

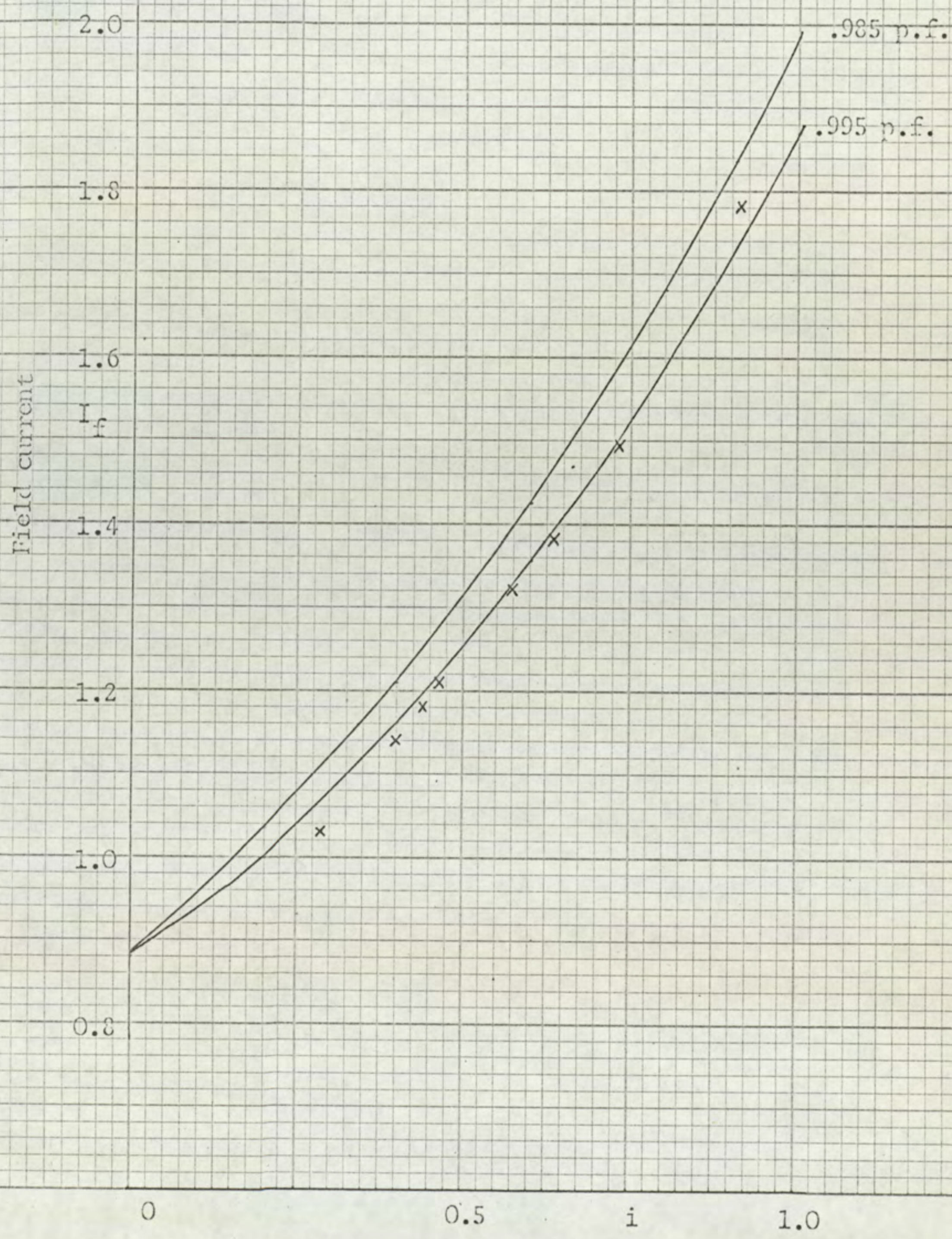

The procedure for calculating the curve representing I_f against I_a has two parts as follows,

(1) k' is plotted against k. The values are taken from a measured (or calculated) open circuit characteristic. On the same graph portions of a family of curves similar to fig 60 are plotted to establish the points of intersection.

(2) Each intersection describes the necessary p.u. field current (k') required to support the p.u. armature current associated with that particular curve of the family. Hence the values of k' and I_a at each intersection lead to a curve of I_f against I_a for a specific voltage and power factor.

Fig 62 represents part (1) above for the experimental machine and fig 63 the resulting calculations of the load characteristic for both .985 and .995 lag power factors. Measurements are marked by crosses for comparison with the theoretical curves, which used $\varepsilon_2 = \frac{2}{\pi b_o}$. Fig 64 shows the same measurements together with calculated curves using the 'design' value of ε_2.

The open circuit characteristic of the industrial machine (on which this experimental alternator is modelled), 2.1, is shown in fig 65 in the form of k' against k. The manufacturer's load measurements were made with a load power factor described as being '...... certainly between UPF and 0.98 lag and ... probably between 0.99 and unity'. Accordingly the variable i families were plotted for $\cos \phi = 1.0$ and 0.98 lag in the region of their intersection with the open circuit characteristic. Fig 66 shows these intersections converted into load characteristics and compared with the manufacturer's measurements. The theory suggests that the load power factor was 0.995 lag; this corroborates the manufacturer's expectations.

Thus, calculations based on the theory derived in this thesis, both for the experimental and for the industrial machine, have agreed closely with the experimental measurements and the manufacturer's tests respectively.

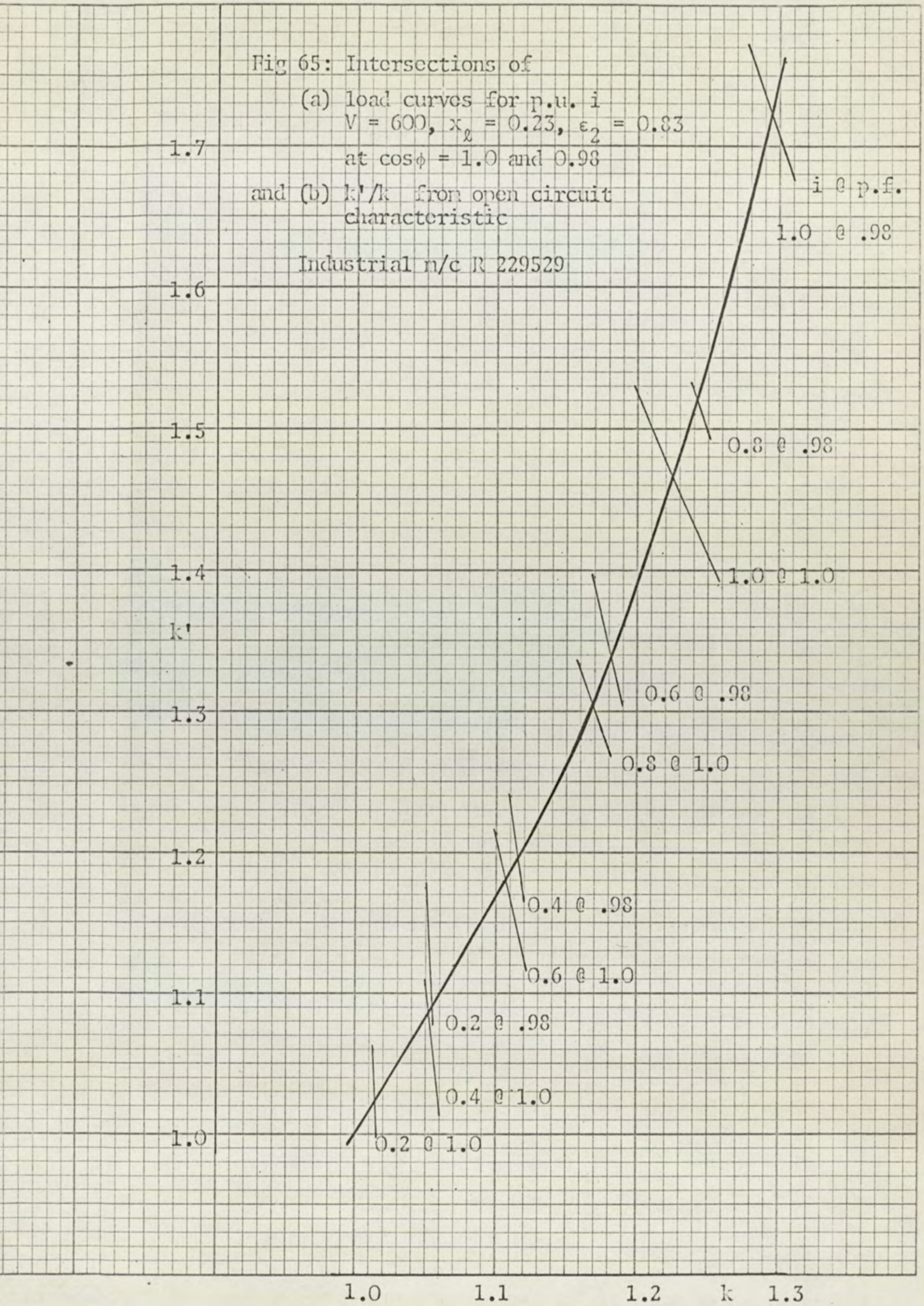

Fig 65: Intersections of
(a) load curves for p.u. i
V = 600, x_ℓ = 0.23, ε_2 = 0.83
at cosϕ = 1.0 and 0.98
and (b) k'/k from open circuit characteristic
Industrial m/c R 229529
i @ p.f.
1.0 @ .98
0.8 @ .98
1.0 @ 1.0
0.6 @ .98
0.8 @ 1.0
0.4 @ .98
0.6 @ 1.0
0.2 @ .98
0.4 @ 1.0
0.2 @ 1.0
k'
1.0
1.1
1.2
1.3
1.4
1.5
1.6
1.7
k

Fig 66: Industrial m/c R 229529
Field ampere-turns/pole against
load ampere-turns/pole
calculated at UPF and .98 p.f. ———
measured by manufacturers x x x

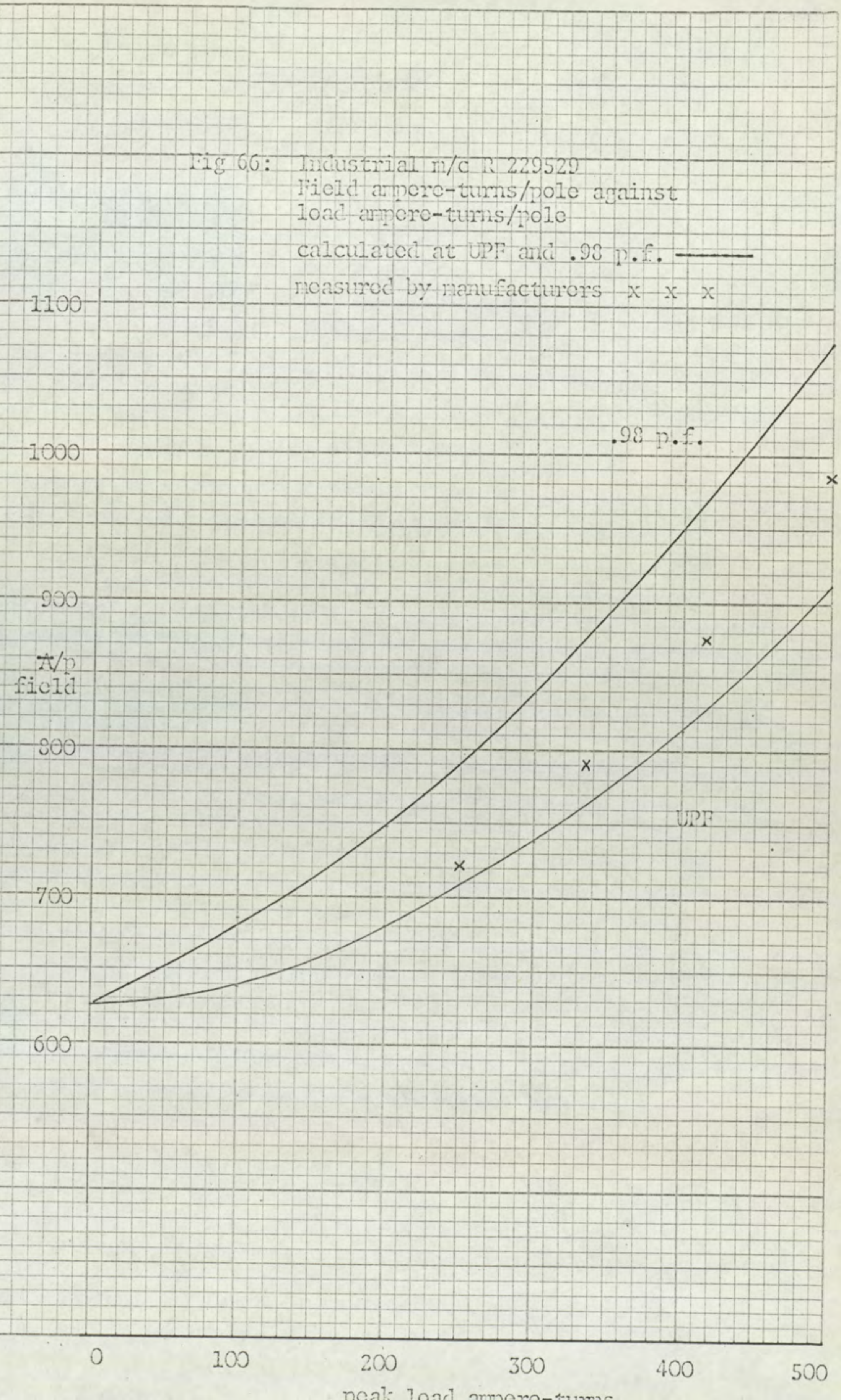

CHAPTER 6 <u>Future work - some thoughts on starting points suggested by this thesis</u>

Summary

This thesis presents an analysis of the distribution of flux throughout the stator and airgap of a Lorenz-type inductor-alternator. It is therefore a basis for investigations into many aspects of this class of machine which have not yet been studied in the limited literature.

The motive for extending the 'classical' theory has been fully discussed in Chapter 1 and subsequent chapters have demonstrated its capacity to usefully describe conditions in practice. Many of the techniques, both theoretical and practical, which have evolved during the derivation and corroboration of the theory, are by no means restricted to this particular class of machine.

This chapter discusses two recognised problems, losses and self-excitation, which have not been solved during the work but which, it is hoped, will now be more tractable. During the theoretical and experimental analysis two further areas of great interest have developed. The first concerns the concept of 'load-angle' which arose when considering the inductor-alternator's similarities to the synchronous machine. This leads to an expression for power output dependent on terms describing the electrical and magnetic balance of the design.

The second area which the analysis describes in new detail concerns the manner in which the output waveform is produced. Due to the square nature of the open circuit wave and the sinusoidal nature of the major components of armature reaction, the combination is clearly seen in a series of traces of open circuit and on-load terminal volts.

6.1 The calculation of iron losses

It has become accepted practice in the calculation of iron loss for inductor-alternators, to multiply the calculated value by an empirical factor (ranging between 2 and 3) to arrive at the value expected from tests.

The discovery that alternating fluxes exist in regions which previously were presumed to carry d.c. flux only, suggests a primary source of additional loss. The distribution of flux within the teeth, investigated with the conducting paper analogue, suggests a further loss mechanism associated with the harmonic pole to pole paths completed in the tooth surface.

Measurements of the flux density distribution along a slot centre line radius, fig 67, showed that the majority of the loss occurred close to the slots. Calculations of core loss with this distribution gave lower values than the existing practice of considering 'mean tooth flux density' filling a depth of core equal to half a tooth width. With the additional components passing behind the field slot, the total loss comes close to the design value, fig 19. Losses due to second-harmonic fluxes are calculated to add 6% to the fundamental frequency losses. On-load, the general distribution of components remains very similar to the open circuit pattern. The additional second harmonic components appear to be reduced below their theoretical value in the same manner that open circuit second harmonic components are affected by distortion. There is evidence, however, that the field pole to pole paths suggested by the extension of the open circuit theory in Chapter 3, are not the only possible paths. Only small values of second harmonic flux appear to leave a rotor tooth and complete a field pole to pole path through the rotor core. For values of load angle when the rotor tooth is opposite an armature slot i.e.opposite parts of two adjacent stator teeth, at the

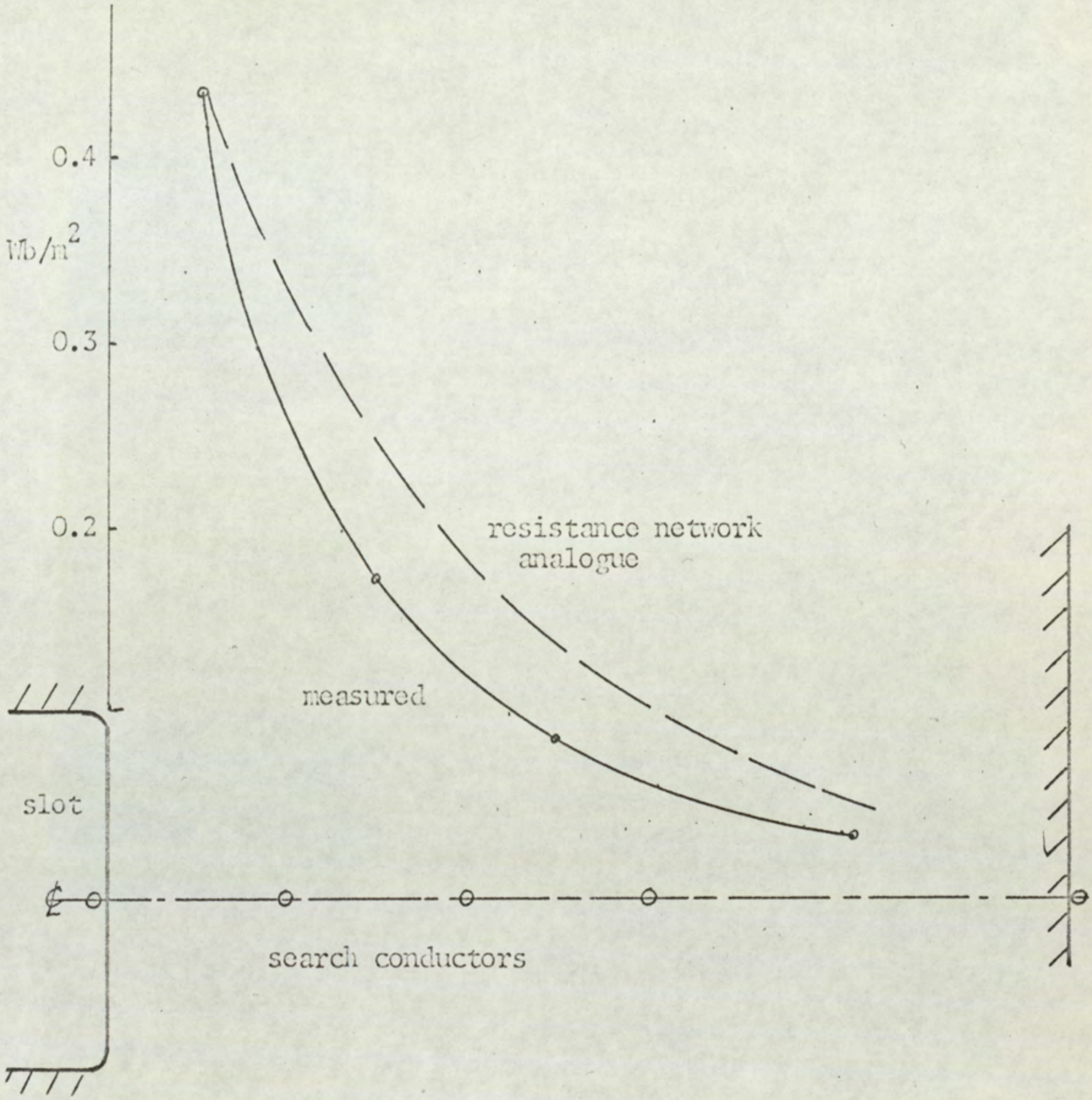

Fig 67: Density of fundamental flux passing behind armature slot, at open circuit rated volts undamped

instant of peak armature current, the armature reaction flux may pass through the rotor tooth surface, fig 68. In terms of the composite on-load airgap flux distribution, harmonic pole to pole paths exist in the rotor tooth surface.

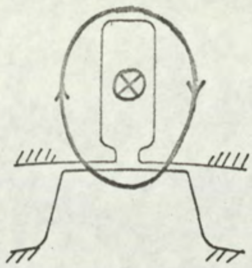

Fig 68: Rotor surface path for armature reaction flux

The losses resulting from these 'surface paths' are very similar to pole-shoe tooth-ripple losses which have been considered in some detail for salient pole alternators. Greig and Mukherji [41] have shown experimental verification of theories presented by Bondi and Mukherji [42] which show that two different modes of flux penetration exist in the surface of laminated pole-shoes. The first is in accordance with the 'classical' depth of penetration employed by Carter [43] and Gibbs [44]. The second involves a penetration of much greater depth of the order of a slot pitch. Measurements on the Lorenz experimental machine show that even harmonic fluxes complete surface paths within the first third of the stator tooth length (i.e. within a depth equal to the third harmonic wavelength). Further into the tooth the flux variations lose any 'space' distribution and are varying in time with magnitudes dictated by the tooth width at the airgap.

Following further experimentation, Greig and Sathirakul [45] conclude that the discrepancies between theory and practice for .016" laminations were not inconsistent with the phenomenon normally referred to as the 'loss anomaly'. In this connection it is interesting to note the findings of Boon and Thompson [40] who show, for polycrystalline 3% silicon-iron sheet at 50c/s, that the ratio of rotational to alternating loss is, approximately, two.

Analysis of the conducting paper analogue studies has demonstrated the rotational nature of flux densities in the surface regions of Lorenz stator teeth. A mathematical treatment (neglecting the 'classical' effects of eddy currents) has expressed this density in terms of radial and circumferential components of the form

$$\overline{B_x} = \exp\frac{-\pi y}{a} \sin\frac{\pi x}{a}$$

$$\overline{B_y} = \exp\frac{-\pi y}{a} \cos\frac{\pi x}{a}$$

and $$\overline{B} = \sqrt{B_x^2 + B_y^2} = \exp\frac{-\pi y}{a}$$

where x is measured circumferentially along the tooth surface and y, radially into the tooth iron.

These equations are very similar to those used by Freeman [46], although derived in a different manner. For any penetration y, as x takes values from 0 to 2a, $\overline{B}$ has the magnitude $\exp\frac{-\pi y}{a}$ and direction $\frac{\pi x}{a}$ radians from the y axis; this describes a complete cycle of rotation as the source of the harmonic space distribution, i.e. the rotor, moves a harmonic wavelength.

Chapter 3 demonstrated the simultaneous existence of 'sin ωt' and 'cos ωt' components of flux in the half teeth and core of the stator; i.e. their combination may also be considered as a rotational flux.

Therefore, a future study of loss mechanisms and their calculation must

1) consider qualifications to the pole-shoe theories to account for the effect of slots in the stator and rotor, perhaps by investigating in greater depth analogue studies which simulate the tooth boundaries.

2) consider the additional loss present when the flux density is rotational, and in which regions of the iron this is significant.

In the writer's opinion rotational surface losses will account for the present discrepancy between calculation and measurement. The stator iron is subjected to an extreme form of tooth ripple flux while the rotor experiences the negative sequence components of single phase armature reaction: both are, at present, neglected in the loss calculations and both contain rotational characteristics.

6.2 Self-excitation

Due to the comparatively high p.u. synchronous reactance $(a + x_\ell)$ inherent for inductor-alternators, the natural regulation characteristic is poor. Improvement both in regulation and the overall magnetic to electrical balance of a design is obtained by supplying the load through a series capacitor. This is known as compensation; the degree of compensation is defined as $\left(\frac{x_c}{(a + x_\ell)}\right)$ where x_c represents the p.u. capacitive reactance.

If x_c is made equal to $(a + x_\ell)$ i.e. 100% compensation, a short circuit fault in the load circuit would result in a resonance condition, theoretically reducing the load on the machine to the armature resistance alone. Naturally this disastrous possibility is avoided. If two or more machines are required to be paralleled, synchronous operation depends upon the paralleling circuit impedance having an inductive component. Thus over-compensation introduces a restriction on the design's application.

Two types of self excitation occur in under-compensated systems.

1) asynchronous self-excitation
2) self-excitation due to ferro-magnetic resonance.

Both depend upon the 'tuning' of the machine reactance with the capacitance of the load circuit.

1) Asynchronous self-excitation occurs during run up. It is dependent upon a frequency (less than rated frequency) at which the load capacitance tunes with the synchronous reactance. Characteristic signs are a low frequency induced in the field circuit and a mixing of this and the generated frequency in the output circuit.

This much is industrial experience. Given a tuned condition, the phenomenon would appear to depend on the mutual inductance of the armature and field coils. Chapter 3 has evolved techniques for studying the components of flux linking both coils expressed in terms of the combined field and armature m.m.f.s. These may well lead to a fuller understanding of the mechanism and suggest appropriate winding characteristics, or damping circuits, to limit the effects.

2) Whereas 'asynchronous self-excitation' is primarily a fault phenomenon, transient surge conditions may also stimulate self-excitation. One explanation suggests that momentary saturation of the iron circuit may reduce the effective machine reactance to a level at which it equals the load capacitance; the resulting resonance may be transient or sustained.

Since the expressions for terminal volts on-load, derived in Chapter 5, are dependent on a saturation factor $(k/_{k'})$, the conditions controlling a reduction in machine reactance as described above may be analysed theoretically. It is the writer's opinion that a solution to 'ferro-magnetic resonance' will form one part of a general transient analysis. The major application for inductor-alternators at present is to supplying coreless induction furnaces; these present a highly inductive load. The p.f. may be as low as 0.1, dependent upon frequency and lining thickness. By using shunt capacitors to compensate for the large wattless current, the necessary alternator size is very greatly reduced. Change in load p.f., as seen by the alternator, occurs during the melt; hence it is necessary to vary the value of the capacitors to limit this power factor variation.

A full transient analysis of such a system is necessary to establish operating criteria, without which present designs must contain substantial overload capacity.

6.3 An output expression for studying balanced designs

The Lorenz-type inductor-alternator has many of the characteristics of salient pole synchronous machines. Because adjacent direct axes have dissimilar permeance coefficients and the quadrature axis permeance is unsymmetrical, normal two axis theory is inapplicable. If a transform function with a period of 2π (electrical rad) is discovered a modified two-axis theory will follow. Until such a discovery continuous expressions for the composite field at any point in the airgap must be used.

In Chapter 5 it was shown that the fundamental vector diagram was very similar to that of a synchronous machine and that, for the single phase alternator, a parameter analogous to the conventional 'load-angle' might be expressed.

$$\text{i.e. } \cos\psi = (1 - a\sin\delta)/A$$

Continuing the analogy, assuming the peak energy stored in the gap to be $\frac{\mu_o}{2}\left(\frac{F_f A}{g}\right)^2$, a fictitious combination of F_f and F_a regardless of the contra-rotating nature of F_a, the load angle may be written into an expression for power of the form

$$\text{Power} = \frac{\text{poles}}{2}\ \frac{\pi}{2}\ \frac{2R\ell w_r}{gc}\ F_f^{\,2} A \sin\psi$$

Eliminating ψ and substituting $\frac{V_T}{V_f}\cos\phi$ for $\cos\delta$

$$\text{Power} = \text{poles} \times \frac{R\ell w_r}{g\varepsilon_2 c}\ F_f F_a\ \frac{V_T}{V_f}\cos\phi$$

Not surprisingly, the load circuit power factor ($\cos\phi$), the angular velocity (w_r) and the regulation ($\frac{V_T}{V_f}$) control the output power. The 'design for optimum magnetic to electric balance' may be studied by reference to the dimension term $\frac{R\ell}{g\varepsilon_2 C}$ governing flux densities in the iron, and the terms F_f and F_a representing the m.m.f.s resulting from the electrical loading.

6.4 Output waveform

The open circuit voltage waveform will be proportional to all the odd harmonic components of the open circuit airgap flux density pattern: consequently it is 'flat topped' as shown in fig 69(a). Since the major components of reactive voltage due to armature reaction, 5.2.4 and 8.7, are at fundamental frequency, the on-load voltage waveform is a combination of the open circuit pattern and a sinusoidal pattern due to the armature currents. The amplitude of the sine pattern is proportional to the load: further, the axis of the sine pattern moves relative to the open circuit pattern as the load-angle varies. The resulting change in waveform with load is shown in fig 69: this accounts for the industrial experience that on-load waveforms are in general closer to being sinusoidal than open circuit waveforms.

Two factors require further study:

1) The flux variations at the tooth surface contain substantial 3rd, 5th etc. harmonic components, while the flux variations at the tooth root are predominantly fundamental. The voltage waveform resembles the tooth surface flux pattern rather than a combination of the two extremes. Perhaps the waveform may be much improved, at the expense of increased leakage paths, by locating the armature conductors further from the airgap. This investigation would include another important study: the distribution of current between the conductors in a coil side.

2) If the airgap distribution controls the output waveform it would seem possible to design the full load conditions for optimum harmonic content. In Chapter 4 terms from the composite airgap flux density expression were chosen to describe the pattern moving with the rotor. By selecting terms linking the reference coil at each harmonic frequency and considering their simultaneous minimum values, criteria will appear

in terms of b_o b_2 b_3 etc. and δ. Thus correct airgap geometry and electrical to magnetic balance of design may remove the necessity to skew and stagger the rotor core, 1.2.2(18)

Fig 69: Output waveforms $I_f = 0.2A$

(a) $V_{oc} = 36$

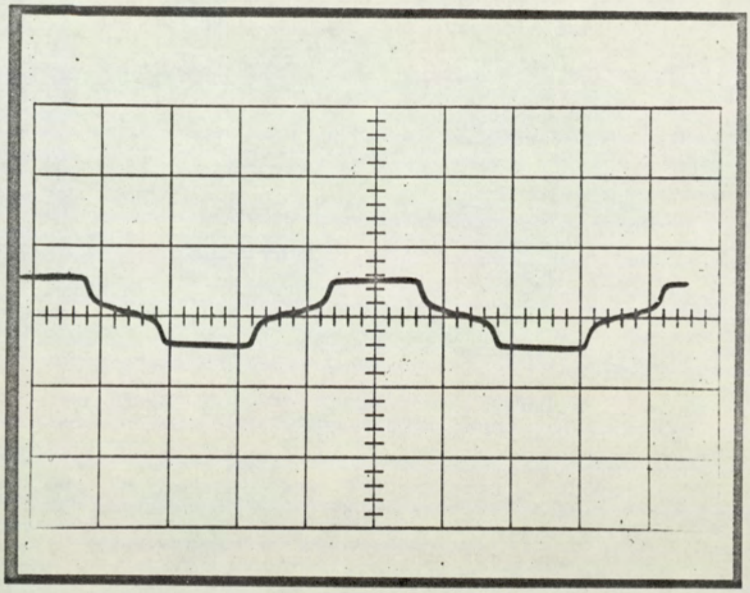

(b) $V_a = 34.5$
$I_a = 9.25$

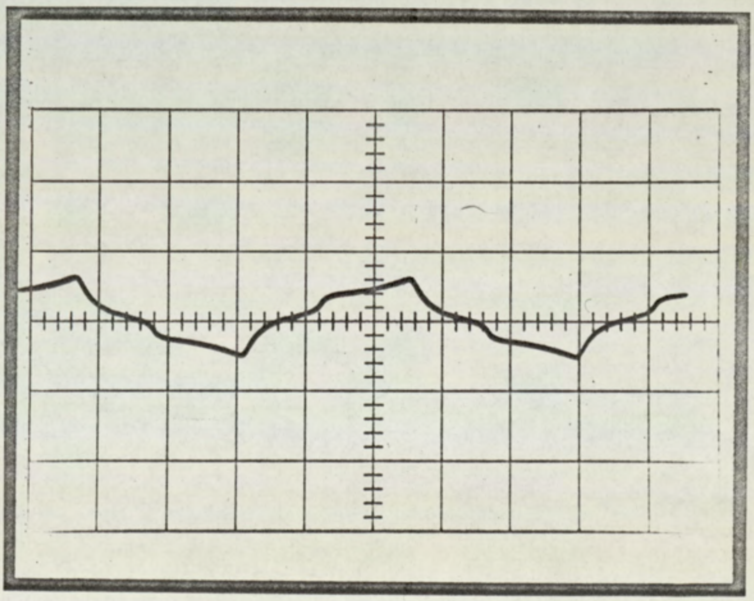

Fig 69: Output waveforms $I_f = 0.4A$

(c) $V_{oc} = 75$

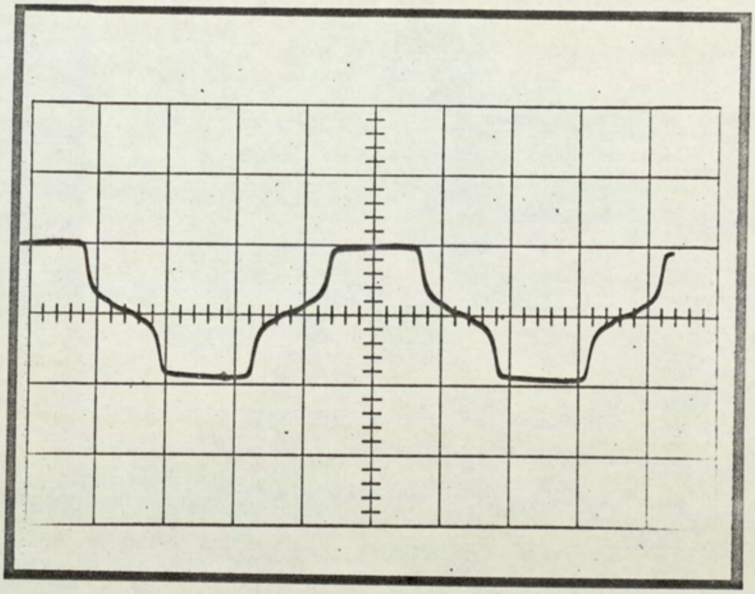

(d) $V_a = 69$

$I_a = 18.5$

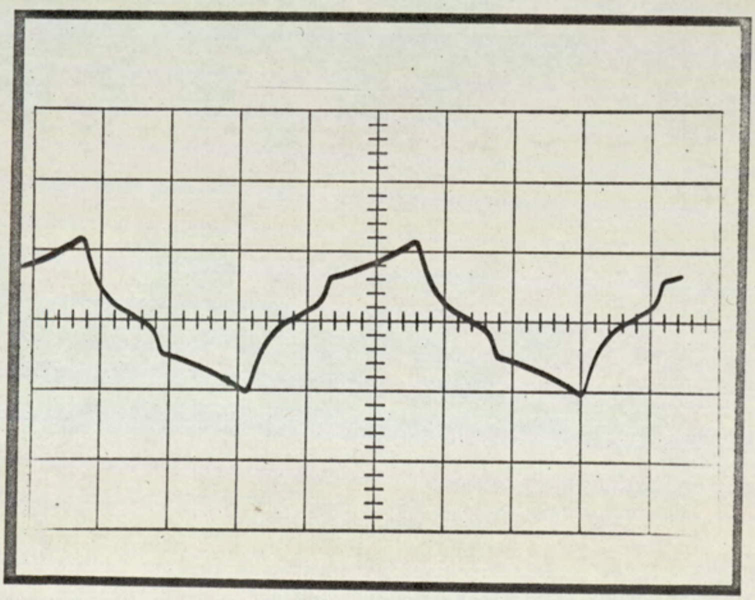

Fig 69: Output waveforms I_f = 0.6A

(e) V_{oc} = 110

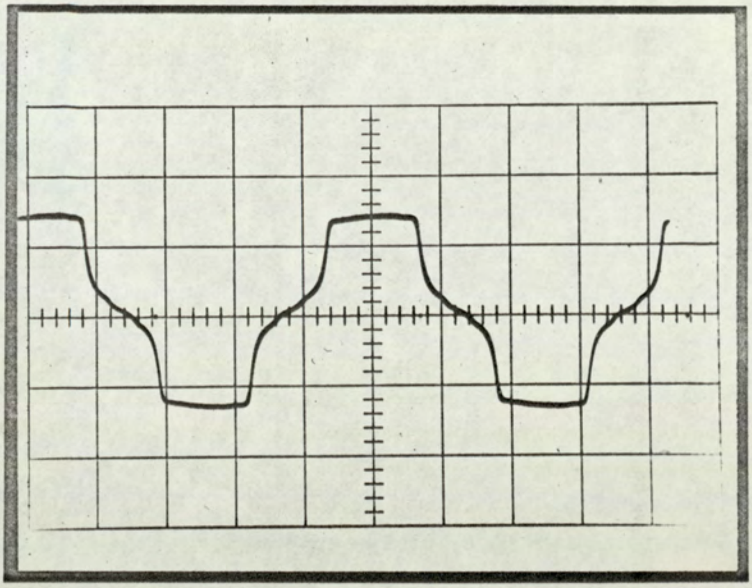

(f) V_a = 101.5
I_a = 28.2

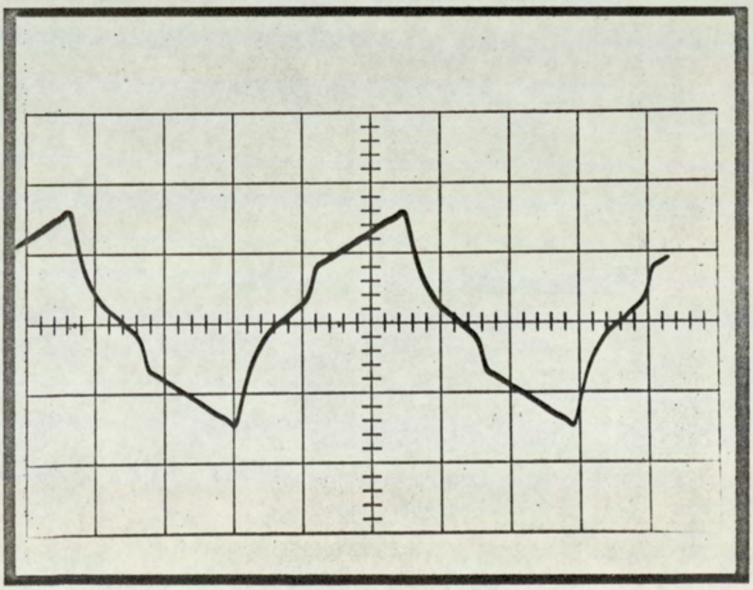

Fig 69: Output waveforms $I_f = 0.8A$

(g) $V_{oc} = 141.5$

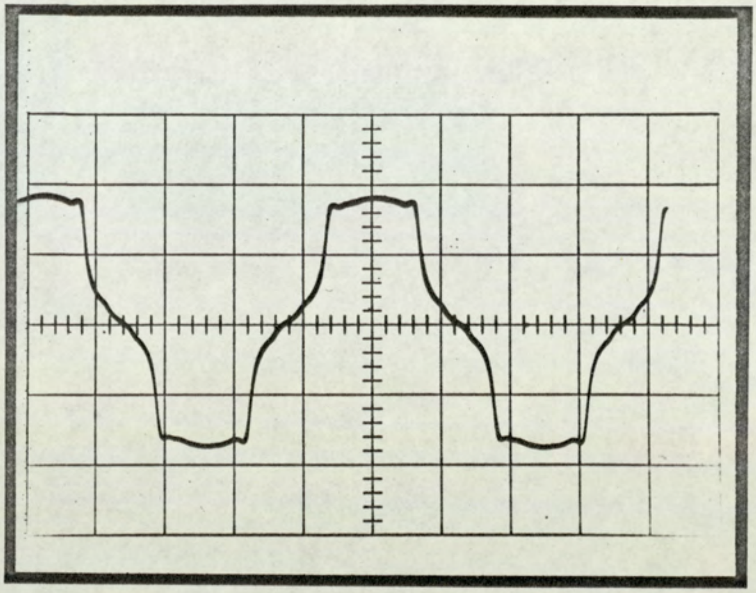

(h) $V_a = 128.5$
$I_a = 35.7$

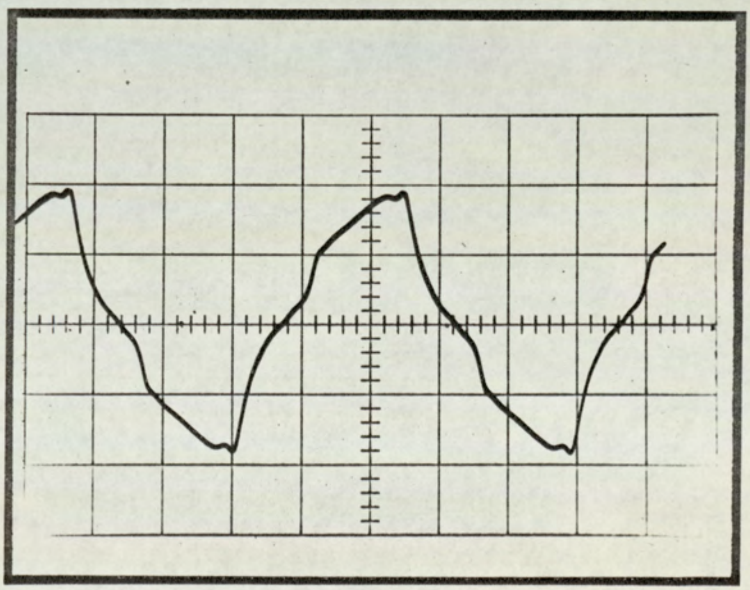

Fig 69: Output waveforms I_f = 1.0A

(i) V_{oc} = 165

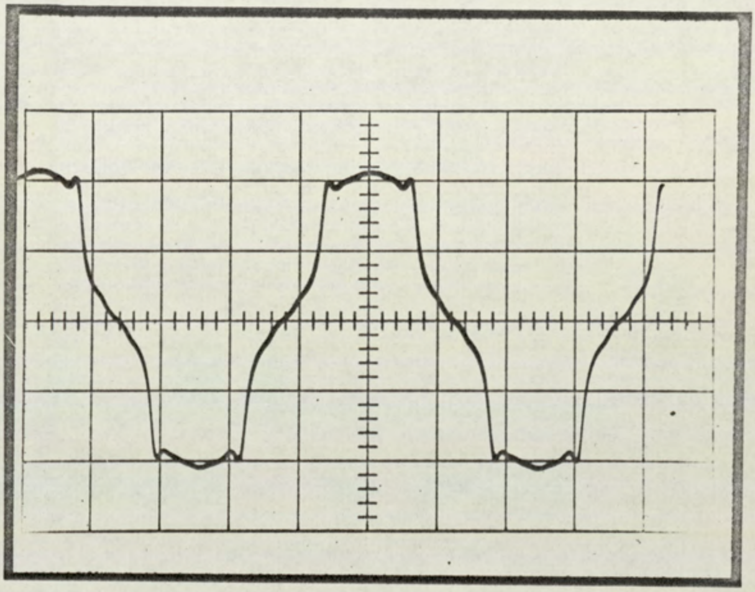

(j) V_a = 153.5
I_a = 42.9

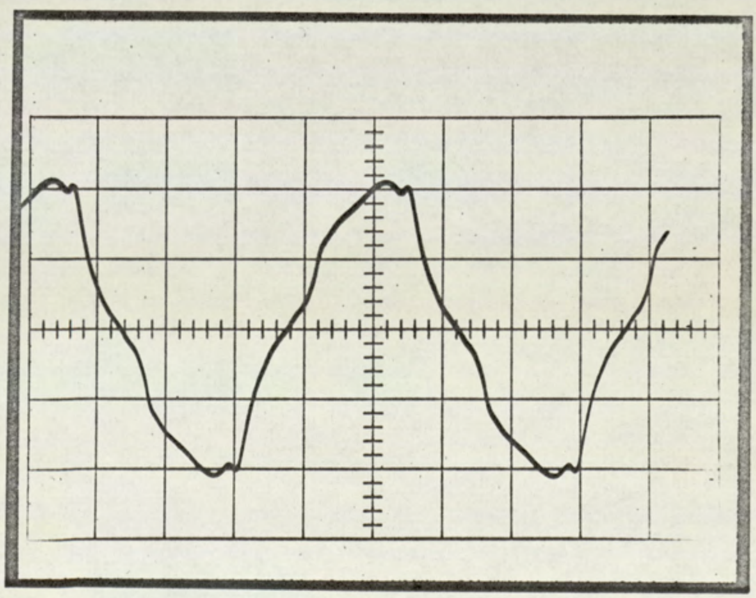

Fig 69: Output waveforms $I_f = 1.5A$

(k) $V_{oc} = 200$

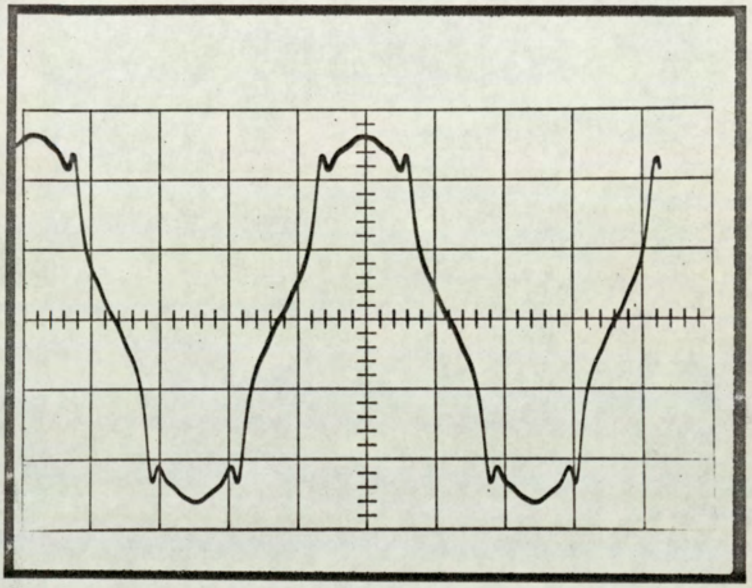

(1) $V_a = 191.5$
$I_a = 54.0$

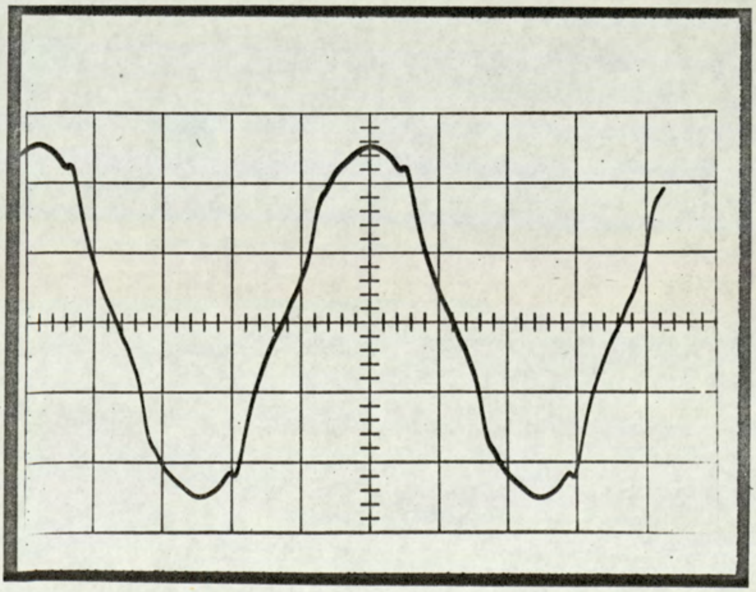

Fig 69: Output waveforms $I_f = 2.0A$

(m) $V_{oc} = 215.5$

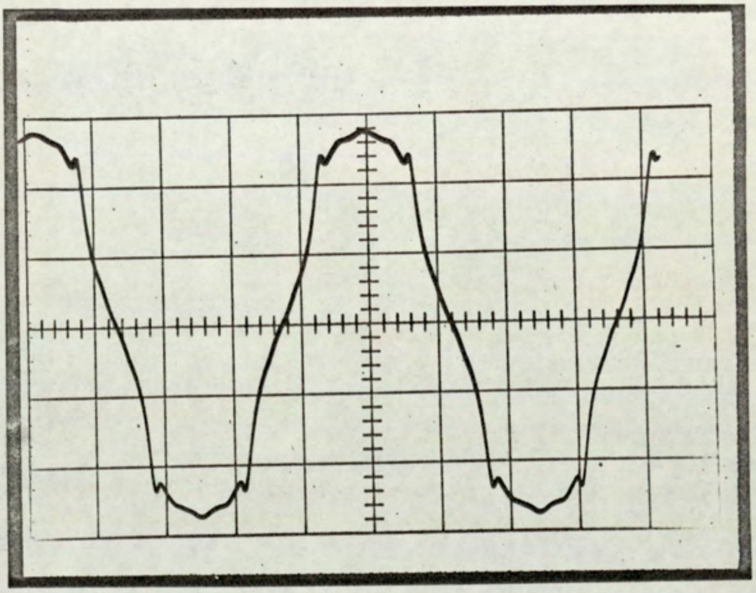

(n) $V_a = 208$
$I_a = 59$

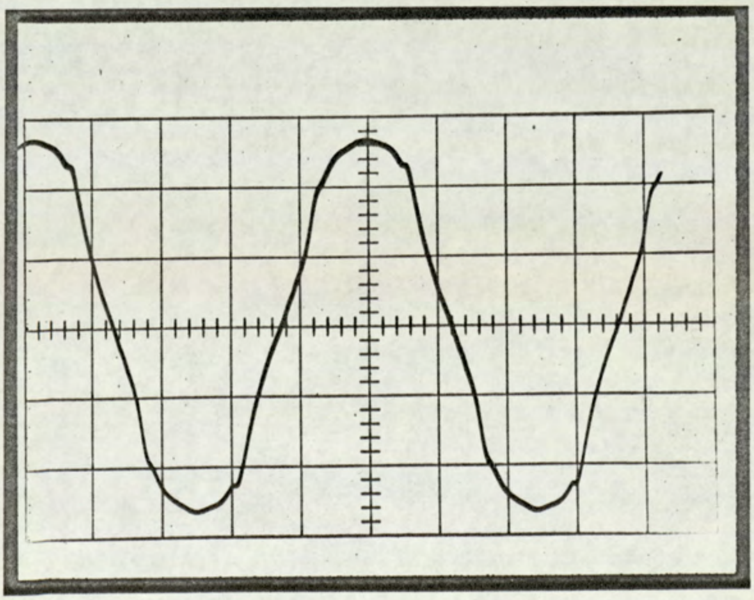

Fig 69: Typical ZPF lag output waveform

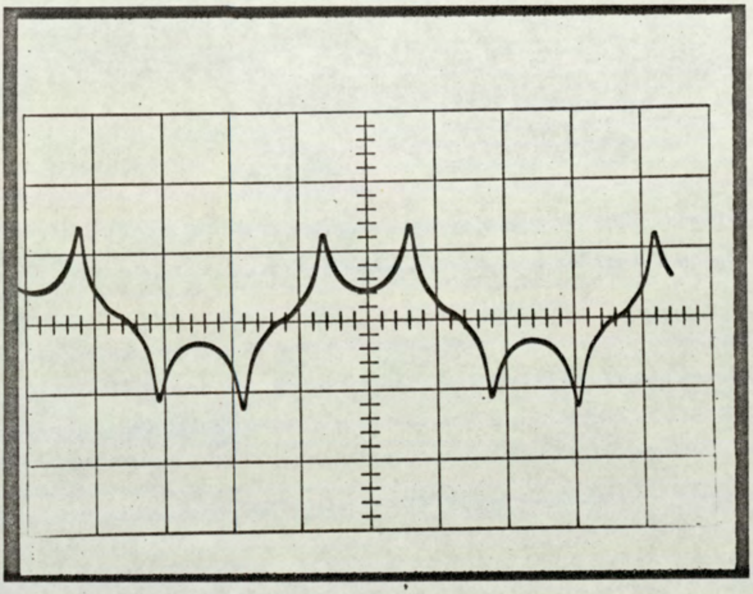

CHAPTER 7 References and Acknowledgments

Summary of References

General

Numerals e.g. 3.1.4, refer to chapter three, section one, subsection four. Exceptions occur (a) in 1.2.2 where further divisions are denoted by 1.2.2(1), 1.2.2(2) etc., and (b) in chapter eight section one which deals with instruments; 8.1 item 5 refers to the fifth instrument in that list.

Page references

Numerals in the top right hand corner of each page refer to the General section that starts or is continued on that page. Each page is also numbered sequentially; these figures appear bottom centre.

Bibliography

References to the Bibliography are given as superscript numerals, e.g. [20].

Equations

Bracketed numerals in the right hand margin or in the text refer to equations; these are listed in 7.3.

7.1 Symbols - in order of introduction

		section
B	flux density (Wb/m^2)	1.2.2(2)
s	width of rotor slot (m)	1.2.2(2)
t	width of rotor tooth (m)	1.2.2(2)
g	length of airgap over rotor tooth (mm)	1.2.2(2)
β	$(s/g)^2 + 2$ — section 1.2 only	1.2.2(2)
γ	$\pm \frac{s}{g} \sqrt{\{(\frac{s}{g})^2 + 4\}}$ — section 1.2 only	1.2.2(2)
δ	$\pm \dfrac{s/g}{\{\sqrt{(\frac{s}{g})^2 + 4}\}}$ — section 1.2 only	1.2.2(2)
K	parameter corresponding to values of x	1.2.2(2)
x	space co-ordinate measured along a rotor slot pitch from the axis of a slot ($0 \leqslant x \leqslant \frac{s+t}{2}$)	1.2.2(2)
f	frequency (c/s)	1.2.2(3)
λ	rotor slot pitch ($= t + s$) (m)	1.2.2(3)
ε_1 ε_2	flux utilisation coefficients	1.2.2(4)
ϕ_{ac}	peak fundamental component of alternating flux (Wb)	1.2.2(5)
B_{DC}	steady flux density (Wb/m^2)	1.2.2(6)
ϕ_t	flux in stator tooth opposite a rotor tooth (Wb)	1.2.2(7)
ϕ_s	flux in stator tooth opposite rotor slot (Wb)	1.2.2(7)
ϕ	flux passing into core ($= \phi_s + \phi_t$) (Wb)	1.2.2(7)
d	depth of rotor slot	1.2.2(8)
ω	2π x frequency	1.2.2(10)
N_a	effective turns per armature coil	1.2.2(10)
I_a	peak armature current	1.2.2(10)

θ	space measurement around airgap in electrical radians where $\lambda = 2\pi^{c}$	1.2.2(10)
t	time (sec)	1.2.2(10)
P_a	number of 'high frequency poles' (= 2 x rotor teeth)	1.2.2(10)
F_f	field ampere-turns per pole	1.2.2(11)
F_a	peak armature reaction ampere-turns/pole	1.2.2(11)
Λ	permeance coefficient	1.2.2(11)
μ	permeability	1.2.3
$\overline{H}$	magnetic field intensity	"
$\overline{B}_{oc}$	open circuit airgap flux density distribution relative to the stator	3.1.4
B_m	mth coefficient of the $\overline{B}_{oc}$ series (Wb)	3.1.4
m	order of space flux density distribution harmonic	"
ℓ	active length of core (m)	"
σ	stator-slot opening (electrical rad)	"
δ	time phase angle by which the peak o.c. volts lead the peak armature current	3.2.2
b_m	p.u. coefficient of B_{oc} series where base B_1 = 1 p.u.	3.2.2
$\overline{B}_a$	airgap flux density distribution due to F_a	"
C	$\frac{N_a I_a}{\pi F_f}$ $\propto$ ratio of armature and field m.m.f.s	"
$\overline{B}'_{oc}$	open circuit airgap flux density distribution relative to the rotor	4.1.1
$\cos\phi$	load circuit power factor	4.2.1
V_T	terminal voltage for a specific value of I_f and I_a	"

V_f	open circuit voltage for a specific value of I_f	4.2.1
$\overline{E}_{oc}$	complete series expression for open circuit voltage	5.1.1
E_{oc}	fundamental r.m.s. component of $\overline{E}_{oc}$	"
$\phi_{oc}{}_{-\pi/2}^{\pi/2}$	flux linking 'reference coil' on open circuit $f(\theta, t)$	"
ϕ_1	fundamental peak component of $\phi_{oc}{}_{-\pi/2}^{+\pi/2}$	"
c	Carter's coefficient for airgap fringing	"
$\overline{E}_a$	complete series expression for voltage due to armature reaction m.m.f.	5.2.1
E_a	fundamental r.m.s. component of $\overline{E}_a$	"
$\overline{E}$	complete series expression for the internal generated voltage on load	"
E	fundamental r.m.s. component of $\overline{E}$	"
I_{ao}	rated full load peak armature current	"
i	p.u. armature current	"
V_o	rated open circuit r.m.s. voltage	"
v	p.u. terminal voltage	"
I_{fo}	field current required to establish V_o	"
k,k'	p.u. system non-linear factors	"
a_o	$\frac{2N_a I_{ao}}{\pi \varepsilon_2 N_f I_{fo}}$	"
a	$(i/k')\, a_o$	"
ϕ_f	fundamental flux vector due to field m.m.f.	5.2.2
ϕ_E	fundamental flux vector associated with E	"

ψ	angle between ϕ_f and ϕ_E and/or E_{oc} and E	5.2.2
B_a	fundamental (in time) component of $\overline{B}_a$	"
$\phi_{a\,-\pi/2}^{\,+\pi/2}$	fundamental (in time) component of flux linking reference coil due to armature reaction m.m.f.	"
X_ℓ	leakage reactance (Ω)	5.2.3
$\overline{V}$	complete series expression for on-load terminal voltage	"
V	fundamental r.m.s. component of $\overline{V}$	"
E_ℓ	fundamental r.m.s. reactive voltage due to leakage fluxes	"
α	phase-shift between forward synchronously rotating open circuit and on-load m.m.f.s	"
A	$E/E_{oc} = \sqrt{(1 - 2a\sin\delta + a^2)}$	"
M	$i\,\frac{k}{k'}\,(a_o + x_\ell)$	"
x_c	reactance (p.u.) due to capacitive compensation	6.2
R	airgap radius dimension	6.3
w_r	rotor angular velocity	
D	$\frac{\ell\lambda B_m}{2m\pi}$	8.3.1
D'	$\frac{\ell\lambda N_a I_a B_1}{2\pi^2 F_f}$	8.3.2

7.2 Bibliography

1. WALKER J.H. : 'The theory of the inductor alternator', J.IEE, 1942, Pt. II, pp 227-241
2. WALKER J.H. : 'High frequency alternators', J.IEE, 1946, Pt II, p.67
3. SCHMIDT K. : 'Die Maschinen für drahtlöse Telegraphic', Elektrotech. Z., 1921, 42, p.245
4. SCHMIDT K. : 'Fortschritte im Bau von / ittel - und Hochfrequenzmaschinen', Elektrotech. Z., 1928, 49,p1565
5. ARNOLD E. : 'Die Wechselstromtechnik', 1913, 2nd ed., 4, p.35
6. ROSENBERG F. : 'Wirbelströme in massivem Eisen', Elektrotechnik und Maschinenbau, 41, p.317, 1923
7. POHL R. : 'Eine einfache Theorie der žusätzlichen Verluste im Nutenkupfer von Welchselstrommaschinen', Elektrotech, Z., 1920, 41, p.908
8. CARTER F.W. : 'The magnetic field of the Dynamo-Electric Machine', J.IEE, 1926, 64, p.1115
9. COE R.T., TAYLOR H.W. : 'Some problems in Electrical machine design involving elliptic functions', Philospphical Magazine, 1928, 6, p.120
10. TRUTT F.C., ERDELYI E.A., JACKSON R.F. : 'The non-linear potential equation and its numerical solution for highly saturated electrical machines', IEEE Trans. Aerospace, 1963, AS-1 No. 2, p. 430-39
11. TRUTT F.C., ERDELYI E.A. : 'No-load flux distribution in saturated high-speed homopolar inductor alternators', IEEE Trans. Aerospace, 1963, AS-1 No. 2, p.417-28
12. ERDELYI E.A., TRUTT F.C., HOPKINS R.E. : 'Flux distribution in saturated high-speed homopolar alternators with purely reactive loads', IEEE Trans. Aerospace, 1963, AS-1 No. 2, p. 407-11

13. LANDGRAFF R.W., ERDELYI E.A. : 'Influence of airgap curvature on the flux distribution in saturated homopolar alternators', IEEE Trans. Aerospace, 1964, AS-2, No. 2, p. 904-912

14. SURTI K.K., ERDELYI E.A. : 'The effects of slotting on the flux distribution in saturated high-speed homopolar inductor alternators', IEEE Trans. Aerospace, 1964, AS-2, No. 2, p. 937-47

15. ERDELYI E.A. : 'Influence of inverter loads on the airgap flux of Aerospace homopolar alternators', IEEE Trans. Aerospace, 1965, AS-3 No. 2, p. 7-12

16. HOPKINS R.E., ERDELYI E.A. : 'Optimization of rotor tooth shape of Aerospace homopolar alternators', IEEE Trans. Aerospace, 1965, AS-3 No. 2, p. 12-18

17. ERDELYI E.A., AHAMED S.V., JACKSON R.F., SHAH M.J. : 'Eddy current losses in the rotor teeth of Aerospace homopolar alternators', IEEE Trans. Aerospace, 1965, AS-3, No. 2, p. 24-32

18. AHAMED S.V., ERDELYI E.A., HOPKINS R.E. : 'Non-linear theory of heteropolar electrical machines' IEEE Trans. Aerospace, 1965, AS-3 No. 2, p. 32-39

19. ERDELYI E.A., HOPKINS R.E. : 'Saturated high speed homopolar alternators at balanced loads', IEEE Trans. Aerospace, 1964, AS-2 No. 2, p. 929-936

20. German patent DRP 303321 (30th October, 1914)

21. LAFFOON C.M. : 'H-F Alternator developments', Electrical Review 1929, 104, p.674

22. LAY R.K. : 'Inductor-alternator terminology' JIEE, 1966, 12, p.287

23. THOMPSON S.P. : 'Dynamo-electric machinery' (Spon, 1905, 7th edn. p. 121-122)

24. French patent 307264 (21st Jan. 1901, with additions 17th Jan.1902)

25. STEVENSON A.R., PARK R.H. : 'Graphical determination of magnetic fields', Trans. AIEE, 1927, 46, p. 112

26. WIESEMAN R.W. : 'Graphical determination of magnetic fields', Trans. AIEE, 1927, 46, p.141

27. GIBBS W.J. : 'Conformal transformation in electrical engineering', (Chapman and Hall, 1958)

28. BINNS K.J. : 'Calculation of some basic flux quantities in induction and other doubly-slotted electrical machines', Proc. IEE, 1964, III No. 11, p. 1847

29. LIEBMANN : 'Electrical Analogues', Brit.J.Appl.Physics, 1953, 4, p.193

30. DAVIES E.J., PEDERSEN N.P. : 'An experimental and theoretical study of the Lorenz-type inductor-alternator under load', IEEE Trans. Applic. Indust. 1963, No. 67, p.174

31. METZLER K. : 'Die Magnetisierungscharacteristik der Gleichpol-Induktortype', Archiv. für Elektrotechnik, 1927, 19, p.57

32. THOMSON J.J. ; 'On the heat produced by eddy currents in an iron plate exposed to an alternating magnetic field', The Electrician, 1892, p.599 - (also see Phil. Mag. Nov. 1891)

33. WILKINS F.J., DRAKE A.E. : 'Measurement and interpretation of power losses in electrical sheet steel', Proc. IEE, 1965, 112, No.4,p.771

34. BAFFREY A.R. : 'Rotating machines for generating medium frequencies', 1965, Nov., Revue General de l'ectricité

35. ALGER P.L. : 'The nature of Induction Machines' (Gordon and Breach, 1965, 1st edn.)

36. RABY K.F. : 'Inductor Alternators for 10Kc/s', Student's Quarterly Journal IEE, Sept. 1950, p.15

37. MAMAK R.S., LAITHWAITE E.R. : 'Numerical evaluations of inductance and A.C. resistance', Proc. IEE, 1960 Part C, 108, pp.240-246

38. AHAMED S.V., ERDELYI E.A. : 'Non-linear vector potential equations for highly saturated heteropolar electrical machines', IEEE Trans. Aerospace,1964, AS-2 No. 21, pp. 896-903

39. KING R.W.P. : 'Fundamental Electromagnetic Theory', (Dover Publiciations, 1963, 2nd edn., p.139)

40. BOON C.R., THOMPSON J.E. : 'Alternating and rotational power loss at 50c/s in 3% silicon-iron sheets', 1965, Proc.IEE, 112 No. 11, p. 2147-51

41. GREIG J., MUKHERJI K.C. : 'An experimental investigation of tooth-ripple flux pulsations in smooth laminated pole-shoes', 1957, IEE Monograph 223S

42. BONDI H., MUKHERJI K.C. : 'An analysis of tooth-ripple phenomena in smooth laminated pole-shoes', 1957, IEE Monograph 225S

43. CARTER F.W. : 'Pole-face losses', 1916, Journal IEE, 54, p.168

44. GIBBS W.J. : 'Tooth-ripple losses in unwound pole shoes', 1947, Journal IEE, 94 Pt. II, p.2

45. GREIG J., SATHIRAKUL K. : 'Pole-face losses in Alternators', 1960 IEE Monograph 404S

46. FREEMAN E. : 'A Study of Tooth-Ripple Eddy Current Losses in laminated pole-shoes', 1964, a thesis submitted to Kings College Faculty of Engineering, University of London

7.3 List of equations

Reference	Description	Section
1A 1B	Flux density distribution due to Carter	1.2.2(2)
2	Open circuit B distribution	3.1.4
3	Armature turns distribution	3.2.2
4	Armature reaction flux density in terms of the open circuit flux density	"
5	Equation (4) expanded	"
6	Combination of equations (2) and (5) to give complete on-load flux density expression relative to the stator	4.2.1
7	Equation (6) relative to the rotor	"
8	Expression of flux due to armature reaction fundamental component	5.2.2
9	Equation (8) rewritten to include 'a'	"
10	p.u. terminal volts	5.2.4
11	Equation (10) rewritten to include "M"	"
12A 12B	Equation (10) rewritten in terms of the non-linear factors k' and k	5.3.2

7.4 Acknowledgments

Firstly the writer wishes to acknowledge with gratitude the continuous advice and encouragement given by Professor E.John Davies, Professor in Electrical Engineering, the University of Aston in Birmingham, who has supervised the work from which this thesis is drawn.

The writer also wishes to thank the following:

Associated Electrical Industries Ltd. for manufacturing the experimental machine and Messrs. K.F. Raby and E. Beedham at A.E.I. (Rugby) both at the manufacturing stage, with test results (5.3.2), and discussion later.

Messrs. A.Stevenson and M.J. Ellett for invaluable work in connection with assembling and instrumenting the experimental machine: in particular for producing a system of search conductors probably more delicate and numerous than has previously been attempted on a machine of this size. Without the successful and continuous service of these search conductors the theories of this thesis must have remained untested.

Miss Sally Fitch and Mr. J.T. Whittle to whom the writer is indebted for the typing and reproduction of the manuscript.

The writer's colleagues in the departments of Electrical Engineering and Mathematics for many hours of helpful discussion.

CHAPTER 8 Appendices

8.1 Instruments

	Item	Manufacturer	Type	Serial No.
1	Oscilloscope	Tektronix	533A	100677
2	Operational amplifiers	Tektronix	O	003118
3	Dual trace amplifiers	Tektronix	CA	104363
4	Camera	Tektronix	C12	005207
5	Wave analyser	Muirhead	Parmetrada	D489 GM
6	Wave analyser	Marconi	TF 2330	52410/024
7	Frequency analyser	Venner	TSA 3336/2	L9519
8	Test Set	Cambridge	20-2000c/s	L386 768
9	Electronic Voltmeter	Bruel & Kjoer	2409	135726
10	Digital voltmeters	Digital Measurements	2003	15190 15654
11	Double element watt meter	Sangamo Weston	579.1.56	AP 63488
12	Ammeter (d.c.)	Sangamo Weston	AP.S82	AP 56386
13	Voltmeter (d.c.)	Sangamo Weston	S82	AP 31660
14	Micro ammeter (d.c.)	Sullivan	T2010	641379
15	D.C. supply	Farnell	L30	1373
16	Starter	Electrical Apparatus	20QODSD	L608872
17	Variable load	Educational Measurements (10 amps max)		
18	Decade resistors	Cambridge		L 397934 L 397885
19	Variable resistor	Bereostat	15Ω 4.7amp	447

8.2 Supply circuits for Alternator Field and Driving Motor

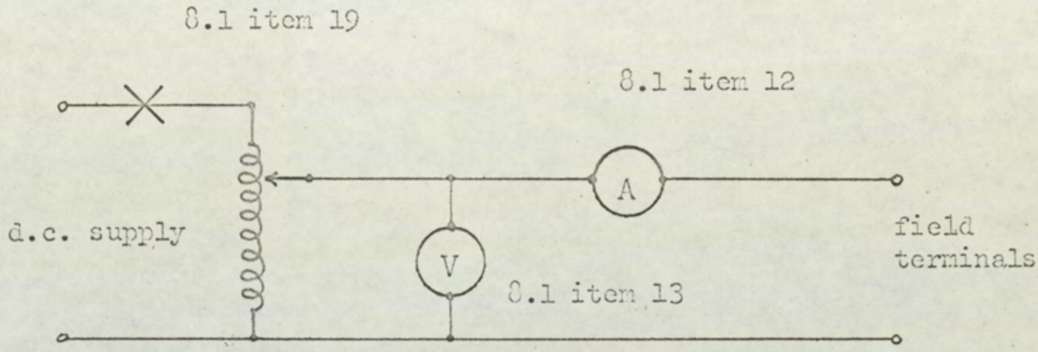

Field supply circuit

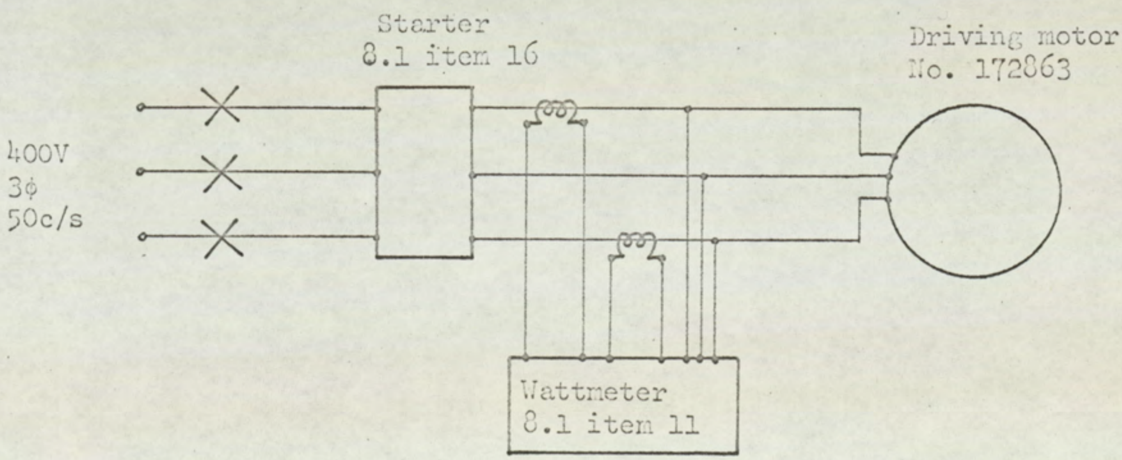

Driving motor supply circuit

8.3 Tooth contributions to core flux

8.3.1 Contributions to B_{oc}

In practice, the stator airgap surface between field slots is interrupted by a.c. slot openings of width σ electrical radians. Section 3.1.4 and fig 33(a) describe the teeth and their airgap peripheral limits as:

Tooth	1	$-\pi$	$\rightarrow$	$(\frac{\pi}{2} + \frac{\sigma}{2})$
	2	$-(\frac{\pi}{2} - \frac{\sigma}{2})$	$\rightarrow$	$(\frac{\pi}{2} - \frac{\sigma}{2})$
	3	$(\frac{\pi}{2} + \frac{\sigma}{2})$	$\rightarrow$	$(\frac{3\pi}{2} - \frac{\sigma}{2})$
	4	$(\frac{3\pi}{2} + \frac{\sigma}{2})$	$\rightarrow$	$(\frac{5\pi}{2} - \frac{\sigma}{2})$
	5	$(\frac{5\pi}{2} + \frac{\sigma}{2})$	$\rightarrow$	3π
	6	4π	$\rightarrow$	$(\frac{9\pi}{2} - \frac{\sigma}{2})$

The total net flux contributed to the core by tooth 1 due to B_{oc} is ϕ_{oc1}

$$\phi_{oc1} = \ell R \int_{-\pi}^{-(\frac{\pi}{2} - \frac{\sigma}{2})} B_{oc} d\theta = \sum_{m=0}^{\infty} \frac{\ell\lambda}{2\ \pi} \left[\frac{B_m}{m} \sin m(\theta - \omega t - \frac{\pi}{2}) \right]_{-\pi}^{-(\frac{\pi}{2} - \frac{\pi}{2})}$$

$$= \sum_{m=0}^{\infty} D \{\sin m(-\pi - \frac{\sigma}{2} - \omega t) - \sin m(- \frac{3\pi}{2} - \omega t)\}$$

$$\text{where } D = \frac{\ell\lambda B_m}{2m\pi}$$

$$= \sum_{m=0}^{\infty} D \{-\sin m \left(\frac{\sigma}{2} + \omega t\right) \cos m\pi + \sin \frac{3m\pi}{2} \cos m\, \omega t + \cos \frac{3m\pi}{2} \sin m\, \omega t\}$$

$$= \sum_{m=0}^{\infty} \{D\, f_1(\omega t)\}$$

Thus for each tooth, by integrating the B_{oc} wave between appropriate limits;

$$f_1(\omega t) = \{- \cos m\pi \sin m\left(\frac{\sigma}{2} + \omega t\right) + \sin \frac{3m\pi}{2} \cos m\, \omega t + \cos \frac{3m\pi}{2} \sin m\, \omega t\}$$

$$f_2(\omega t) = \{- \sin m\left(\frac{\sigma}{2} + \omega t\right) - \cos m\pi \sin m\left(\frac{\sigma}{2} - \omega t\right)\}$$

$$f_3(\omega t) = \{- \sin m\left(\frac{\sigma}{2} - \omega t\right) - \cos m\pi \sin m\left(\frac{\sigma}{2} + \omega t\right)\}$$

$$f_4(\omega t) = \{- \cos 2m\pi \sin m\left(\frac{\sigma}{2} + \omega t\right) - \cos m\pi \sin m\left(\frac{\sigma}{2} - \omega t\right)\}$$

$$f_5(\omega t) = \{- \cos 2m\pi \sin m\left(\frac{\sigma}{2} - \omega t\right) + \sin \frac{5m\pi}{2} \cos m\, \omega t - \cos \frac{5m\pi}{2} \sin m\, \omega t\}$$

$$f_6(\omega t) = \{- \cos 4m\pi \sin m\left(\frac{\sigma}{2} + \omega t\right) - \sin \frac{3m\pi}{2} \cos m\, \omega t + \cos \frac{3m\pi}{2} \sin m\, \omega t\}$$

When comparing the directions of these contributions at any instant in time, to establish the paths followed by the various components, allowance must be made for tooth six lying within a pole of opposite sense to that containing teeth 1 - 5. Therefore, when comparing contributions from teeth 5 and 6, the correct expressions are

$$\sum_{m=0}^{\infty} D\, f_5(\omega t) \quad \text{and} \quad - \sum_{m=0}^{\infty} D\, f_6(\omega t)$$

8.3.2 Tooth contributions to core flux due to B_a

$$B_a = \frac{F_a}{F_f} B_{oc}$$

for the fundamental components of F_a and B_a

$$= \frac{2N_a I_a B_1}{F_f} \{\cos(\theta + \omega t - \delta) + \cos(\theta - \omega t + \delta)\} \cos(\theta - \omega t - \frac{\pi}{2})$$

Hence ϕ_a between limits (1) and (2)

$$= \frac{N_a I_a B_1 \ell\lambda}{2\pi^2 F_f} \Big[- \tfrac{1}{2} \{ \sin(2\theta - \delta - \frac{\pi}{2}) + \sin(2\theta - 2\omega t + \delta - \frac{\pi}{2}) \} + \theta \{ \cos(2\omega t - \delta + \frac{\pi}{2}) + \cos(\delta + \frac{\pi}{2}) \} \Big]_{(2)}^{(1)}$$

where the limits are taken for each tooth with the same roation as in 8.3.1 for tooth 1, lying between $(-\pi)$ and $(- \frac{\pi}{2} - \frac{\sigma}{2})$

$$\phi_{a1} = D' \Big[- \tfrac{1}{2} \{ \sin(- \frac{3\pi}{2} - \sigma - \delta) - \sin(- \frac{5\pi}{2} - \delta) + \sin(- \frac{3\pi}{2} - \sigma - 2\omega t + \delta) - \sin(- \frac{5\pi}{2} - 2\omega t + \delta) \} + (\frac{\pi}{2} - \frac{\sigma}{2}) \{ \cos(2\omega t - \delta + \frac{\pi}{2}) + \cos (\delta + \frac{\pi}{2}) \} \Big]$$

where $D' = \dfrac{N_a I_a B_1 \ell\lambda}{2\pi^2 F_f}$

$$\phi_{a1} = D' \Big[- \tfrac{1}{2} \{ \cos(\sigma + \delta) + \cos\delta + \cos (\sigma + 2\omega t - \delta) + \cos (2\omega t - \delta) + (\frac{\pi}{=} - \frac{\sigma}{2}) - \sin(2\omega t - \delta) - \sin\delta \} \Big]$$

For lagging ZPF loads $\delta = \frac{\pi}{2}$, then

$$\phi_{a1}(ZPF) = D' \left[-\tfrac{1}{2} \{ -\sin\sigma + \sin(\sigma + 2\omega t) + \sin 2\omega t \} + \tfrac{1}{2} (\pi - \sigma)(\cos 2\omega t - 1) \right]$$

$$= \frac{D'}{2} \{ (\sin\sigma - \pi + \sigma)(1 - \cos 2\omega t) - (1 + \cos\sigma) \sin 2\omega t$$

For leading p.f. load $\delta = 0$, then

$$\phi_{a1}(\delta=0) = D' \left[-\tfrac{1}{2} \{ \cos\sigma + 1 + \cos\sigma \cos 2\omega t - \sin\sigma \sin 2\omega t + \cos 2\omega t \} + \tfrac{1}{2} (\pi - \sigma)(- \sin 2\omega t) \right]$$

$$= \frac{D'}{2} \{ (\sin\sigma - \pi + \sigma) \sin 2\omega t - (1 + \cos\sigma)(\cos 2\omega t + 1) \}$$

Thus for each tooth, by integrating the B_a wave between appropriate limits;

$$f_1(2\omega t)_{ZPF} = \tfrac{1}{2} \{ (\sin\sigma - \pi + \sigma)(1 - \cos 2\omega t) - (1 + \cos\sigma) \sin 2\omega t \}$$

$$f_2(2\omega t)_{ZPF} = (\sin\sigma - \pi + \sigma)(1 - \cos 2\omega t) = f_3(2\omega t)_{ZPF} = f_4(2\omega t)_{ZPF}$$

$$f_5(2\omega t)_{ZPF} = \tfrac{1}{2} \{ (\sin\sigma - \pi + \sigma)(1 - \cos 2\omega t) + (1 + \cos\sigma) \sin 2\omega t \}$$

$$f_1(2\omega t)_{\delta=0} = \tfrac{1}{2} \{ (\sin\sigma - \pi + \sigma) \sin 2\omega t - (1 + \cos\sigma)(\cos 2\omega t + 1) \}$$

$$f_2(2\omega t)_{\delta=0} = (\sin\sigma - \pi + \sigma) \sin 2\omega t = f_3(2\omega t)_{\delta=0} = f_4(2\omega t)_{\delta=0}$$

$$f_5(2\omega t)_{\delta=0} = \tfrac{1}{2} \{ (\sin\sigma - \pi + \sigma) \sin 2\omega t + (1 + \cos\sigma)(\cos 2\omega t + 1) \}$$

The combination of $m = n = 1$, therefore, produces twice line frequency components of flux. Each tooth contribution within a field pole has the same sign, i.e. these components must link the field winding.

Considering the general case (neglecting coefficients)

$$f_{n,m} = 4 \cos n\theta \cos(\omega t - \delta) \cos m(\theta - \omega t - \pi/2)$$

$$= \left[\begin{array}{ll} & \cos \{ (n+m)\theta + (1-m)\omega t - \delta - m\pi/2 \} \\ + & \cos \{ (n-m)\theta + (1+m)\omega t - \delta + m\pi/2 \} \\ + & \cos \{ (n+m)\theta - (1+m)\omega t + \delta - m\pi/2 \} \\ + & \cos \{ (n-m)\theta - (1-m)\omega t + \delta + m\pi/2 \} \end{array}\right]$$

$$\phi_{n,m}\Big|_{-\pi}^{3\pi} = \left[\begin{array}{ll} & \cos \{ \frac{\pi}{2}(6n+5m) + (1-m)\omega t - \delta \} \\ + & \cos \{ \frac{\pi}{2}(6n-5m) + (1+m)\omega t - \delta \} \\ + & \cos \{ \frac{\pi}{2}(6n+5m) - (1+m)\omega t + \delta \} \\ + & \cos \{ \frac{\pi}{2}(6n-5m) - (1-m)\omega t + \delta \} \\ - & \cos \{ \frac{\pi}{2}(-2n-3m) + (1-m)\omega t - \delta \} \\ - & \cos \{ \frac{\pi}{2}(-2n+3m) + (1+m)\omega t - \delta \} \\ - & \cos \{ \frac{\pi}{2}(-2n-3m) - (1+m)\omega t + \delta \} \\ - & \cos \{ \frac{\pi}{2}(-2n+3m) - (1-m)\omega t + \delta \} \end{array}\right]$$

for $n = 1$ and $m = 0$

$\phi_{1,0}$ per pole =

$$\left[\begin{array}{ll} & \cos(3\pi + \omega t - \delta) + \cos(3\pi + \omega t - \delta) \\ + & \cos(3\pi - \omega t + \delta) + \cos(3\pi - \omega t + \delta) \\ - & \cos(-\pi + \omega t - \delta) - \cos(-\pi + \omega t - \delta) \\ - & \cos(-\pi - \omega t + \delta) - \cos(-\pi - \omega t + \delta) \end{array}\right]$$

$$= 2 \{ -\cos(\omega t - \delta) - \cos(\omega t - \delta) + \cos(\omega t - \delta) + \cos(\omega t - \delta) \} = 0$$

Similarly $\phi_{1,2}$ per pole =

$$\begin{bmatrix} & \cos(8\pi - \omega t - \delta) + \cos(-2\pi + 3\omega t - \delta) \\ + & \cos(8\pi - 3\omega t + \delta) + \cos(-2\pi + \omega t + \delta) \\ - & \cos(-8\pi - \omega t - \delta) - \cos(2\pi + 3\omega t - \delta) \\ - & \cos(-8\pi - 3\omega t + \delta) - \cos(2\pi + \omega t + \delta) \end{bmatrix}$$

$$= 2\{\cos(\omega t + \delta) + \cos(3\omega t - \delta) - \cos(\omega t + \delta) - \cos(3\omega t - \delta)\} = 0$$

Thus, steady and second-harmonic components of the B_{oc} distribution combining with the fundamental of armature-reaction do not produce net linkages from field pole to pole. Linkages are produced only if $(n + m)$ is even.

8.4 Coefficients of B_{oc} from a conducting paper analogue

A model of the airgap over a rotor slot pitch for a smooth stator, fig 70, was cut from conducting paper. Although the model was symmetrical about a slot centre-line, i.e. all the available information might be gained from one half, the advantages of short electrodes dictated that the model be of a full slot pitch.

By passing current from one electrode to the other the potential at two points (marked as x x in fig 70) may be measured with a Wheatstone bridge. The resistance between these points is proportional to $\left(\frac{d\theta}{\ell}\right)$. Hence the orthogonal analogy between resistance and permeance coefficient per unit core-length, which is also proportional to $\left(\frac{d\theta}{\ell}\right)$. Thus, assuming the resistance of a unit square of the conducting paper is constant as is the permeability of a unit volume of the airgap, the resistance between 'x x' is analogous to the flux (the m.m.f. is assumed to be uniform across the rotor slot pitch). By taking a series of values of resistance for equal widths across the rotor slot pitch the analogy may be extended to equating the relative values of resistance to relative levels of flux density.

Fig 70 shows these relative values of resistance plotted to a scale such that the flux density at the rotor tooth centre-line is taken as 1.0 p.u. Points taken from this graph were Fourier analysed (by computer). Table 17 gives the first fifteen harmonic components in terms of a fundamental (100%) of rotor slot pitch wavelength. These are the values required for the coefficients of equation (2), 3.1.4, in terms of $B_1 = 1.0$ p.u., i.e. $B_m = b_m B_1$.

Fig 70: Half the conducting paper analogue with p.u.B_{oc} plot from orthogonal model

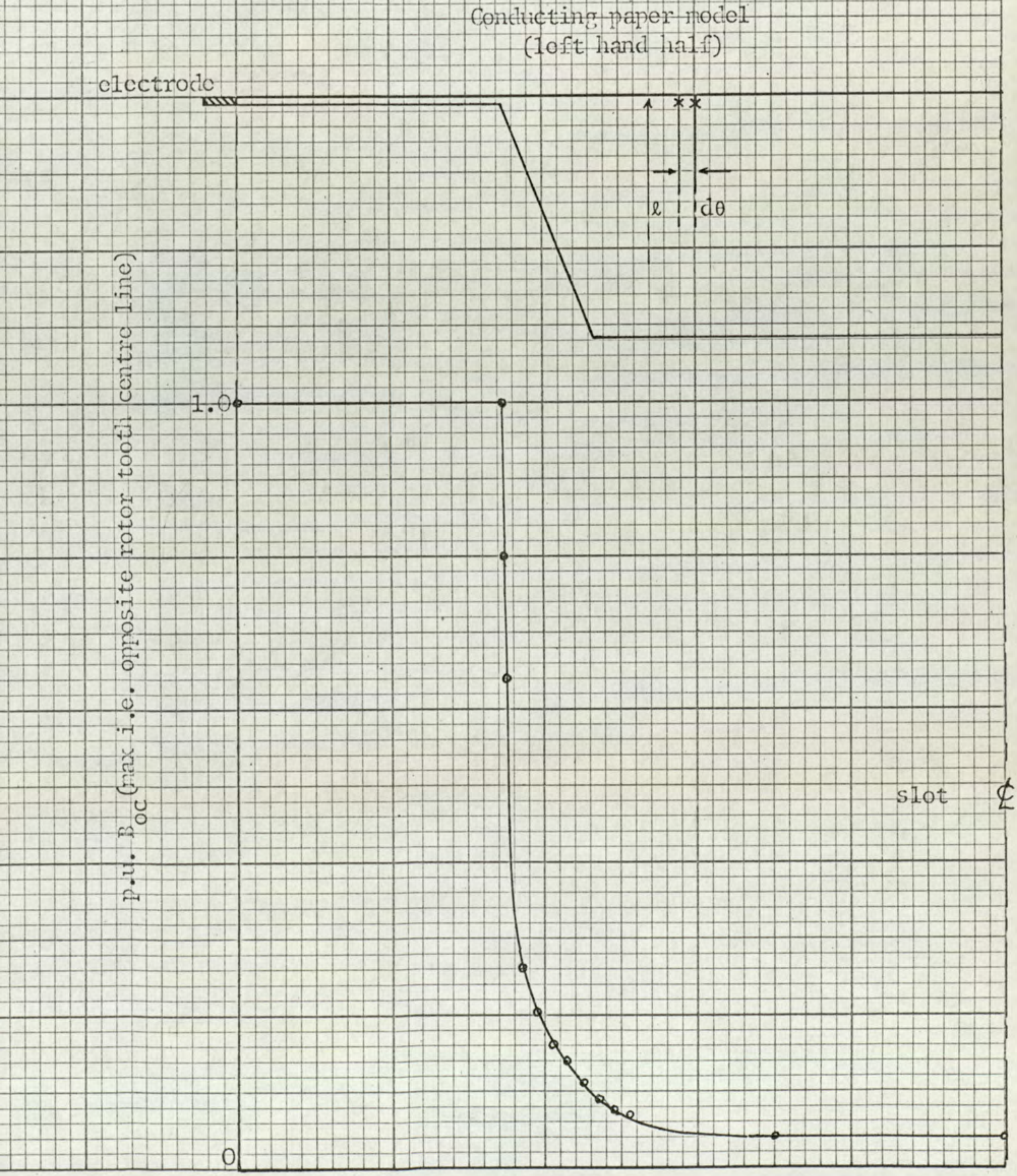

Table 17: Harmonic content of B wave, fig 70, plotted from conducting paper analogue and Fourier analysed

Harmonic component (m)	%	b_m	Harmonic component (m)	%	b_m
Steady (0)	71.3	.71	8	4.6	.05
1	100.0	1.0	9	6.0	.06
2	38.5	.39	10	8.3	.08
3	10.5	.11	11	2.1	.02
4	24.0	.24	12	5.0	.05
5	10.6	.11	13	6.0	.06
6	7.4	.07	14	0.8	.01
7	12.8	.13	15	4.5	.05

Computed open circuit points, B_1 = 1 p.u.
average across tooth surface 1.7906

SQ	
0.1430	
0.3959	
1.7899	1.7906
1.7569	
1.8444	
1.7520	
1.8444	
1.7569	
1.7899	
0.3959	
0.1430	
0.0641	
0.1006	
0.0381	
0.1021	
0.0380	
0.1021	
0.0381	
0.1006	
0.0642	

8.5 Variations of airgap flux density with time due to field slot leakage

Neglecting the a.c. slots, fig 71(a) shows the position of the rotor teeth relative to the d.c. pole at four points during a cycle.

Fig 71

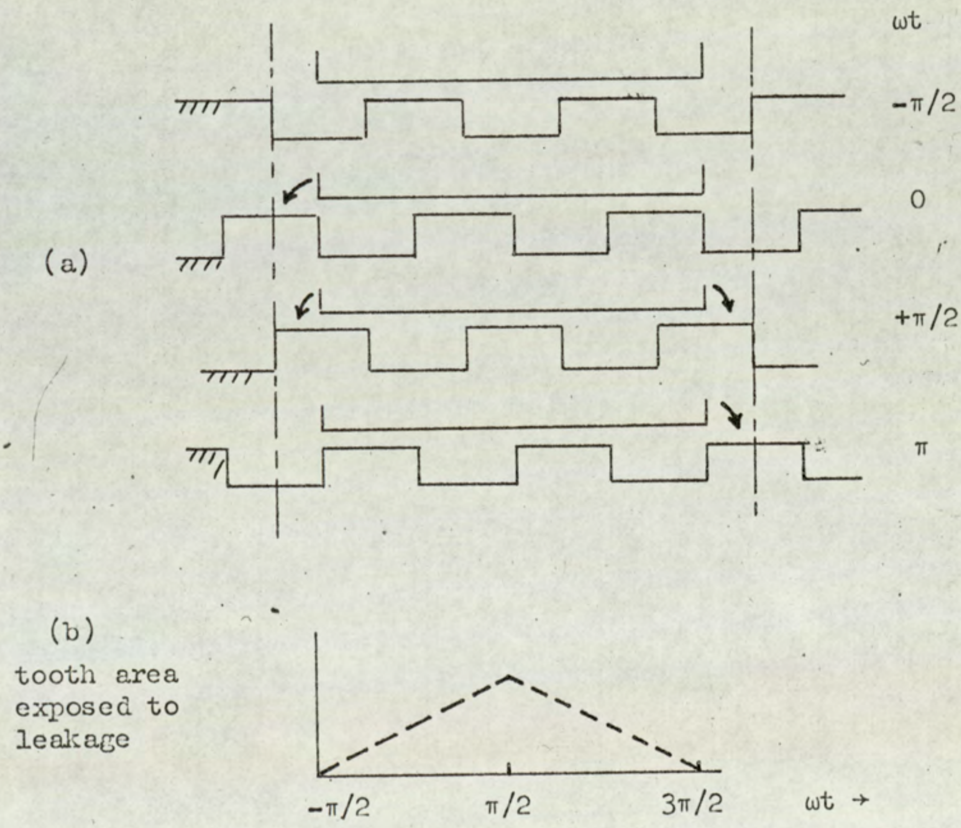

A permeance variation with time exists due to the leakage through the field slot opening, first at the leading edge and then at the trailing edge of the field pole arc. This appears always as an addition to the steady permeance. The area of rotor tooth exposed to leakage fluxes varies linearly between zero and maximum, fig 71(b).

Considering the simple case of circular leakage paths from the field slot side to the surface of the approaching tooth fig 72(a), at time t the leakage path permeance is expressed by

$$\Lambda_\ell \doteq \frac{2}{\pi} \ln \frac{\pi}{2(g+x)}$$

where $x = (\frac{\pi}{2} - \omega t)$

i.e. $\Lambda_\ell \doteq \frac{2}{\pi} \ln \frac{\pi}{2(g+\frac{\pi}{2}-\omega t)}$

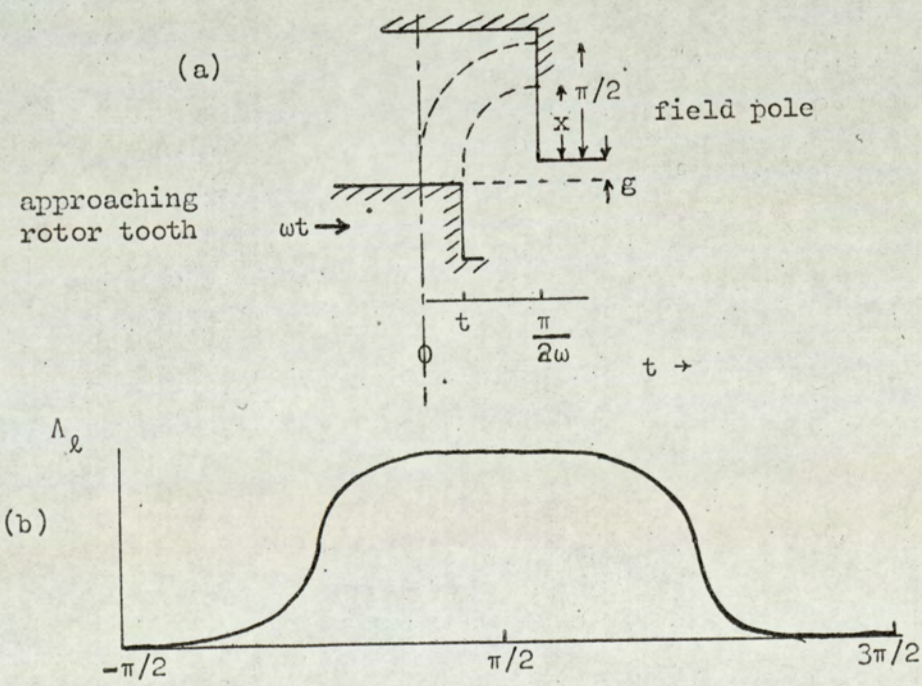

Fig 72

This leads to the logarithmic pattern of permeance shown in fig 72(b), which may be approximately expressed by

$$\frac{2}{\pi} \ln \frac{\pi}{2g} \left(1 + \frac{4}{\pi} \sum_{r=odd}^{\infty} \frac{1}{r} \sin r\omega t\right)$$

Consecutive poles of opposite sense experience leakage permeance variations π radians out of phase. Hence there can be no net linkage with the whole field winding although in each individual coil odd-harmonic voltages will be induced. These will be reduced by short circuited damping turns in the field coil plane.

8.6 Expansion and selection of terms from equation (5), section 3.2.2

$$B_a = \frac{N_a I_a B_1}{\pi F_f} \sum_{\substack{m=0.1.2.. \\ n=odd}}^{\infty} \frac{b_m}{n} \sin\frac{n\pi}{2} \left[\begin{array}{l} \cos\{(n+m)\theta - (m-1)\omega t - \frac{m\pi}{2} - \delta\} \\ +\cos\{(n+m)\theta - (m+1)\omega t - \frac{m\pi}{2} + \delta\} \\ +\cos\{(m-n)\theta - (m-1)\omega t - \frac{m\pi}{2} - \delta\} \\ +\cos\{(m-n)\theta - (m+1)\omega t - \frac{m\pi}{2} + \delta\} \end{array} \right]$$

For $m = 0$ and $n = 1$ $\quad B_a = \frac{N_a I_a B_1}{\pi F_f} \{ 2b_0 \cos(\theta - \omega t + \delta) \}$

For $m = 2$ and $n = 1$ $\quad B_a = \frac{N_a I_a B_1}{\pi F_f} \{ -b_2 \cos(\theta - \omega t - \delta) \}$

These are the only terms in $(\theta - \omega t)$ which are available, i.e. the forward rotating fundamental space components. To relate these stator terms to the rotor, the 'ωt' components are removed leaving

$$\frac{N_a I_a B_1}{\pi F_f} \{ 2b_0 \cos(\theta + \delta) - b_2 \cos(\theta - \delta) \}$$

These terms may also be found, relative to the rotor, in section 8.7.1 as (B01 + C01) and (C21)

8.7 Armature reaction flux density pattern relative to the rotor

8.7.1 Analysis of major components

Relative to the rotor, the armature turns distribution is moving backwards at synchronous speed and the open circuit flux density pattern B_{oc} is stationary. Thus, the armature reaction flux density pattern relative to the rotor, B_a', becomes

$$\frac{4N_aI_aB_1}{\pi F_f}\sum_{\substack{m=0.1.2\ldots\\n=\text{odd}}}^{\infty}\frac{b_m}{n}\sin\frac{n\pi}{2}\cos m\left(\theta+\frac{\pi}{2}\right)\cos n(\theta+\omega t)\cos(\omega t\pm\delta)$$

$$=\frac{N_aI_aB_1}{\pi F_f}\sum_{\substack{m=0,1,2\ldots\\n=\text{odd}}}^{\infty}\frac{b_m}{n}\sin\frac{n\pi}{2}\left[\begin{array}{ll}\cos\left\{(m+n)\theta+(n+1)\omega t-\frac{m\pi}{2}-\delta\right\} & \text{A}\\ +\cos\left\{(m+n)\theta+(n-1)\omega t-\frac{m\pi}{2}+\delta\right\} & \text{B}\\ +\cos\left\{(m-n)\theta-(n-1)\omega t-\frac{m\pi}{2}-\delta\right\} & \text{C}\\ +\cos\left\{(m-n)\theta-(n+1)\omega t-\frac{m\pi}{2}+\delta\right\} & \text{D}\end{array}\right]$$

Expanding each component gives Table 18 on the next page.

Terms with no 'ωt' component are those describing the constant (in time) distribution across the rotor tooth.

Terms with no 'θ' component are constant in space across rotor tooth but have magnitudes dependent on time.

All other combinations describe patterns moving relative to the rotor tooth either forward or backward.

	n \ m	0	1	2
A	1	$\cos(\theta + 2\omega t - \delta)$	$\cos(2\theta + 2\omega t - \frac{\pi}{2} - \delta)$	$\cos(3\theta + 2\omega t - \pi - \delta)$
	3	$\cos(3\theta + 4\omega t - \delta)$	$\cos(4\theta + 4\omega t - \frac{\pi}{2} - \delta)$	$\cos(5\theta + 4\omega t - \pi - \delta)$
	5	$\cos(5\theta + 6\omega t - \delta)$	$\cos(6\theta + 6\omega t - \frac{\pi}{2} - \delta)$	$\cos(7\theta + 6\omega t - \pi - \delta)$
B	1	$\cos(\theta + \delta)$	$\cos(2\theta - \frac{\pi}{2} + \delta)$	$\cos(3\theta - \pi + \delta)$
	3	$\cos(3\theta + 2\omega t + \delta)$	$\cos(4\theta + 2\omega t - \frac{\pi}{2} + \delta)$	$\cos(5\theta + 2\omega t - \pi + \delta)$
	5	$\cos(5\theta + 4\omega t + \delta)$	$\cos(6\theta + 4\omega t - \frac{\pi}{2} + \delta)$	$\cos(7\theta + 4\omega t - \pi + \delta)$
C	1	$\cos(\theta + \delta)$	$\cos(\frac{\pi}{2} + \delta)$	$\cos(\theta - \pi - \delta)$
	3	$\cos(3\theta + 2\omega t + \delta)$	$\cos(2\theta + 2\omega t + \frac{\pi}{2} + \delta)$	$\cos(\theta + 2\omega t + \pi + \delta)$
	5	$\cos(5\theta + 4\omega t + \delta)$	$\cos(4\theta + 4\omega t + \frac{\pi}{2} + \delta)$	$\cos(3\theta + 4\omega t + \pi + \delta)$
D	1	$\cos(\theta + 2\omega t - \delta)$	$\cos(2\omega t + \frac{\pi}{2} - \delta)$	$\cos(\theta - 2\omega t - \pi + \delta)$
	3	$\cos(3\theta + 4\omega t - \delta)$	$\cos(2\theta + 4\omega t + \frac{\pi}{2} - \delta)$	$\cos(\theta + 4\omega t + \pi - \delta)$
	5	$\cos(5\theta + 6\omega t - \delta)$	$\cos(4\theta + 6\omega t + \frac{\pi}{2} - \delta)$	$\cos(3\theta + 6\omega t + \pi - \delta)$

Table 18: 'm n' expressions of components A B C and D

Each term is subject to the factor $\left\{\frac{b_m}{n} \sin \frac{n\pi}{2}\right\}$. Each component of armature reaction flux density in Table 18 may be integrated ω.r.t. θ to provide corresponding expressions for flux (linking the area defined by the limits of integration) varying in time.

When integrating ω.r.t. θ, the factor qualifying each component of Table 18 must be divided by the relevant coefficient of θ. Table 19 shows the relative magnitudes and speeds (on a 1. p.u. base of synchronous speed) of each component for m = 0, 1 and 2 and n = 1, 3 and 5.

Table 19: Relative magnitudes and speeds (synchronous speed = 1. p.u., forward direction positive) for 'm, n' expressions of components A B C and D., when integrated ω.r.t. θ, i.e. ∝ flux.

	m	0		1		2	
	n	Magnitude K	Speed ($\times n_s$)	Magnitude K	Speed ($\times n_s$)	Magnitude K	Speed ($\times n_s$)
A	1	.71	-2	.50	-1	.13	-2/3
	3	.08	-4/3	.08	-1	.03	-4/5
	5	.03	-6/5	.03	-1	.01	-6/7
B	1	.71	0	.50	0	.13	0
	3	.08	-2/3	.08	-1/2	.03	-2/5
	5	.03	-4/5	.03	-2/3	.01	-4/7
C	1	.71	0	1.0	0*	.39	0
	3	.08	-2/3	.16	-1	.13	-2
	5	.03	-4/5	.05	-1	.02	-4/3
D	1	.71	-2	1.0	0†	.39	+2
	3	.08	-4/3	.16	-2	.13	-4
	5	.03	-6/5	.05	-3/2	.02	-2

K = magnitude $\frac{b_m}{n(m \pm n)}$ for $b_0 = .71$, $b_1 = 1.0$, $b_2 = .39$

* component C11 has no space nor time variation.

† component D11 is constant in space but varies with time.

Table19 shows those terms moving synchronously with the rotor to be: B01, B11, B21, C01 and C21. These combine to form the flux distribution travelling with the rotor which will lead to the flux density distribution across a rotor tooth surface.

Neglecting components with magnitudes < 0.1, Table19 shows the main flux distributions moving relative to the rotor to be from: A 01, A 11, A 21, C 13, C 23, D 01, D 21, D 13 and D 23, as underlined. In detail these are:

a) backward at 4 x synchronous speed:

$0.13 \sin (\theta + 4\omega t - \delta)$ D 23

b) backward at 2 x synchronous speed:

$1.42 \sin (\theta + 2\omega t - \delta)$ A 01 and D 01

$0.13 \sin (\theta + 2\omega t + \delta)$ C 23

$-0.16 \cos (2\theta + 4\omega t - \delta)$ D 13

c) backward at 1 x synchronous speed:

$-0.5 \cos (2\theta + 2\omega t - \delta)$ A 11

$-0.16 \cos (2\theta + 2\omega t + \delta)$ C 13

d) backward at 2/3 x synchronous speed:

$-0.13 \sin (3\theta + 2\omega t - \delta)$ A 21

e) forward at 2 x synchronous speed:

$-0.39 \sin (\theta - 2\omega t + \delta)$ D 21

Thus, the major contribution to the distributions moving relative to the rotor come from components A and D for m = 0 and n = 1. This contribution is fundamental in space moving at twice synchronous speed backward.

Components B and C for m = 0 and n = 1 are the major contributions to the distribution travelling synchronously with the rotor. These two patterns represent the fundamental contra-rotating components of the pulsating armature reaction flux.

8.7.2 Verification of sampling technique used in section 4.2.2

Integrating the armature reaction flux density distribution provides an expression for the flux, as a function of time, linking a general surface coil with sides at $\theta = \alpha$ and $\theta = \beta$

$$\phi'_a(t)_{\alpha\beta} = \frac{\ell d}{2\pi}\int_{\beta}^{\alpha} B'_a \, d\theta$$

For component A of the expression for B'_a (Section 8.1.1) the flux is:

$$\frac{\ell\lambda}{2\pi} \sum_{\substack{m = 0.1.2.. \\ n = \text{odd}}}^{\infty} \frac{b_m}{n(m+n)} \sin\frac{n\pi}{2} \{ P \sin (n+1)\omega t + Q \cos (n+1)\omega t\}$$

where $P = \cos \{(m+n)\alpha - \frac{m\pi}{2} - \delta\} - \cos \{ (m+n)\beta - \frac{m\pi}{2} - \delta\}$

$Q = \sin \{(m+n)\alpha - \frac{m\pi}{2} - \delta\} - \sin \{ (m+n \beta - \frac{m\pi}{2} - \delta\}$

Considering the time dependent terms,

at time $t = t_1$: $P \sin (n+1)\omega t_1 + Q \cos (n+1)\omega t_1$

$t = \left(\frac{\pi}{2\omega} - t_1\right)$ $\quad P \sin (n+1)\omega t_1 - Q \cos (n+1)\omega t_1$ $\quad$ n=1 and 5

$t = \left(\frac{\pi}{2\omega} + t_1\right)$ $\quad -P \sin (n+1)\omega t_1 + Q \cos (n+1)\omega t_1$ $\quad$ n=1 and 5

$t = \left(\frac{\pi}{2\omega} - t_1\right)$ $\quad -P \sin (n+1)\omega t_1 - Q \cos (n+1)\omega t_1$

Thus the sum of four measurements of flux taken at $t = t_1, \left(\frac{\pi}{2\omega} - t_1\right), \left(\frac{\pi}{2\omega} + t_1\right)$ and $\left(\frac{\pi}{\omega} - t_1\right)$ will be zero for component A when n=1, 5, 9 etc.

Similarly component D of the expression for B'_a leads to flux linking the general area between $\theta = \alpha$ and $\theta = \beta$:

$$\frac{\ell\lambda}{2\pi} \sum_{\substack{m=0.1.2..\\ n=odd}}^{\infty} \frac{b_m}{n(m-n)} \sin\frac{n\pi}{2} \left\{ R \sin (n+1)\omega t + S \cos (n+1)\omega t \right\}$$

where $R = \cos \{(m-n)\beta - \frac{m\pi}{2} + \delta\} - \cos \{(m-n)\alpha - \frac{m\pi}{2} + \delta\}$

$S = \sin \{(m-n)\alpha \quad \frac{m\pi}{2} + \delta\} - \sin \{(m-n)\beta - \frac{m\pi}{2} + \delta\}$

Hence the same conditions apply to flux resulting from component D. For $n = 1, 5, 9$ etc., the sum of four measurements at the above times is zero.

8.8 Solution of equation (6) using a computer

8.8.1 Components of the complete space distribution of airgap flux density on load relative to the rotor

Each component is p.u., where $B_1 = 1$ and the term $\frac{F_a}{\pi F_f}$ is represented by C.

Term	(B_{oc})		(B_a)	
Steady	bo		$- C \sin\delta$	
Fundamental		$\sin\theta$	$+ 2Cb_0 \cos(\theta + \delta)$	$- Cb_2 \cos(\theta - \delta)$
2nd	$-b_2$	$\cos 2\theta$	$+ C \sin(2\theta + \delta)$	$- Cb_3 \sin(2\theta - \delta)$
3rd	$-b_3$	$\sin 3\theta$	$- Cb_2 \cos(3\theta + \delta)$	$+ Cb_4 \cos(3\theta - \delta)$
4th	b_4	$\cos 4\theta$	$- Cb_3 \sin(4\theta + \delta)$	$+ Cb_5 \sin(4\theta - \delta)$
5th	b_5	$\sin 5\theta$	$+ Cb_4 \cos(5\theta + \delta)$	$- Cb_6 \cos(5\theta - \delta)$
6th	$-b_6$	$\cos 6\theta$	$+ Cb_5 \sin(6\theta + \delta)$	$- Cb_7 \sin(6\theta - \delta)$
7th	$-b_7$	$\sin 7\theta$	$- Cb_6 \cos(7\theta + \delta)$	$+ Cb_8 \cos(7\theta - \delta)$
8th	b_8	$\cos 8\theta$	$- Cb_7 \sin(8\theta + \delta)$	$+ Cb_9 \sin(8\theta - \delta)$
9th	b_9	$\sin 9\theta$	$+ Cb_8 \cos(9\theta + \delta)$	$- Cb_{10} \cos(9\theta - \delta)$
10th	$-b_{10}$	$\cos 10\theta$	$+ Cb_9 \sin(10\theta + \delta)$	$- Cb_{11} \sin(10\theta - \delta)$

8.8.2 <u>The computer programme</u>

```
AIR GAP FLUX DENSITY DISTRIBUTION RELATIVE TO ROTOR'

BEGIN REAL  B0, B2, B3, B4, B5, B6, B7, B8, B9, B10, B11,
            D0, D1, D2, D3, D4, D5, D6, D7, D8, D9, D10, D,
            D0D, D1D, D2D, D3D, D4D, D5D, D6D, D7D, D8D,
            D9D, D10D, DD, DDD,
            X,Y,
            NI,PI,FF,
            CX1, CX2, CX3, CX4, CX5, CX6, CX7, CX8, CX9, CX10,
            SX1, SX2, SX3, SX4, SX5, SX6, SX7, SX8, SX9, SX10,
            CY, SY'

            B0:=0.713' B2:=0.385' B3:=-0.105' B4:=-0.24'
            B5:=-0.106' B6:=0.074' B7:=0.128' B8:=0.046'
            B9:=-0.06'  B10:=-0.083'
            NI:=170.0' PI:=3.1416' FF:=270.0'

FOR   Y:=-3.1416 STEP 0.3927 UNTIL 2.7489 DO

      BEGIN PRINT ££L4?DELTA=?, ALIGNED (4,2),
            SAMELINE,Y*57.2956, £DEGS?, ££L2S4? SQ£S13??,
            Z£BA THETA£S10? B THETA?'

      FOR   X:=0 STEP 0.31416 UNTIL 5.96904 DO

            BEGIN  CX1:= COS(X)'
                   CX2:= COS(2*X)'
                   CX3:= COS(3*X)'
                   CX4:= COS(4*X)'
                   CX5:= COS(5*X)'
                   CX6:= COS(6*X)'
                   CX7:= COS(7*X)'
                   CX8:= COS(8*X)'
                   CX9:= COS(9*X)'
                   CX10:= COS(10*X)'

                   SX1:= SIN(X)'
                   SX2:= SIN(2*X)'
                   SX3:= SIN(3*X)'
                   SX4:= SIN(4*X)'
                   SX5:= SIN(5*X)'
                   SX6:= SIN(6*X)'
                   SX7:= SIN(7*X)'
                   SX8:= SIN(8*X)'
                   SX9:= SIN(9*X)'
                   SX10:= SIN(10*X)'

                   CY := COS(Y)'
                   SY := SIN(Y)'
```

```
D0 := B0
D0D:= - SY'

D1 := SX1'
D1D:=2*B0*(CX1*CY-SX1*SY)
              -B2*(CX1*CY+SX1*SY)'

D2 := -B2*CX2'
D2D:=(SX2*CY+CX2*SY)
             -B3*(SX2*CY-CX2*SY)'

D3 := -B3*SX3'
D3D:= - B2*(CX3*CY-SX3*SY)
                +B4*(CX3*CY+SX3*SY)'

D4 := B4*CX4'
D4D:= - B3*(SX4*CY+CX4*SY)
               +B5*(SX4*CY-CX4*SY)'

D5 := B5*SX5'
D5D:=B4*(CX5*CY-SX5*SY)
               -B6*(CX5*CY+SX5*SY)'

D6 := -B6*CX6'
D6D:=B5*(SX6*CY+CX6*SY)
                -B7*(SX6*CY-CX6*SY)'

D7 := -B7*SX7'
D7D:= - B6*(CX7*CY-SX7*SY)
                +B8*(CX7*CY+SX7*SY)'

D8 := B8*CX8'
D8D:= - B7*(SX8*CY+CX8*SY)
               +B9*(SX8*CY-CX8*SY)'

D9 := B9*SX9'
D9D:=B8*(CX9*CY+SX9*SY)
              -B10*(CX9*CY+SX9*SY)'

D10:= -B10*CX10'
D10D:=B9*(SX10*CY+CX10*SY)
                  -B11*(SX10*CY-CX10*SY)'

D   := D0+D1+D2+D3+D4+D5+D6+D7+D8+D9+D10'

DD  := (D0D+D1D+D2D+D3D+D4D+D5D+D6D+D7D+
           D8D+D9D+D10D )*(NI/(PI*FF))'
DDD:=D+DD'

PRINT ALIGNED (4,4),D, SAMELINE ,££S8??,
DD, ££S8??,DDD'

      END'

    END'

END OF PROGRAM'
```

8.9 Proof of identity $\sum_{n=\text{odd}}^{\infty} \left(\frac{1}{n^2-4}\right) = 0$

To sum $\left(\frac{1}{n^2-4}\right)$ for odd values of $n \to \infty$ is equivalent to summing $\left(\frac{1}{(2n-1)^2-4}\right)$ for all values of $n \to \infty$

$$S_\infty = \sum_{n=1}^{\infty} \left\{ \frac{1}{(2n-1)^2-4} \right\}$$

but $$\frac{1}{(2n-1)^2-4} = \tfrac{1}{4} \left\{ \frac{1}{(2n-1)-2} - \frac{1}{(2n-1)+2} \right\}$$

$$= \tfrac{1}{4} \left\{ \frac{1}{2n-3} - \frac{1}{2n+1} \right\}$$

Therefore $$S_\infty = \tfrac{1}{4} \left\{ \sum_{n=1}^{\infty} \frac{1}{2n-3} - \sum_{n=1}^{\infty} \frac{1}{2n+1} \right\}$$

Let $S_1 = \sum_{n=1}^{n=N} \frac{1}{2n-3}$ and $S_2 = \sum_{n=1}^{n=N} \frac{1}{2n+1}$

where N is a positive integer $\geqslant 2$

Then $S_\infty = \frac{1}{4} ({S_1}_{N=\infty} - {S_2}_{N=\infty})$

If S_1 and S_2 are expanded;

$$S_1 = \frac{1}{2-3} + \frac{1}{4-3} + \frac{1}{6-3} + \frac{1}{8-3} + \cdots\cdots + \frac{1}{2R-3}$$

$$S_2 = \frac{1}{2+1} + \frac{1}{4+1} + \cdots\cdots + \frac{1}{2R-3} + \frac{1}{2R-1} + \frac{1}{2R+1}$$

Since the 'central block' of terms are identical, the difference $S_1 - S_2$ is simply the first two terms of S_1 less the last two terms of S_2

$$\text{i.e.}\quad S_1 - S_2 = \left\{\frac{1}{(2-3)} + \frac{1}{(4-3)} - \frac{1}{(2R-1)} - \frac{1}{(2R+1)}\right\}$$

$$= \quad - \left\{\frac{1}{(2N-1)} + \frac{1}{(2N+1)}\right\}$$

As N tends to ∞ clearly $S_1 - S_2$ tends to zero and therefore S_∞ with $N = \infty$ is also zero.

The writer is grateful to N.R. Tomlinson, Associate Research Fellow in the Department of Mathematics, University of Aston in Birmingham, for this proof.

8.10 General test curves for experimental machine 65328 J

a)	Open circuit characteristic	Fig 57
b)	Short circuit characteristic	Fig 73
c)	sin ψ (sine of 'load-angle', 5.2.3) against output	Fig 74
d)	Efficiency against output	Fig 75
e)	Load current (U.P.F.) against field current	Fig 76
f)	Total losses against output	Fig 77

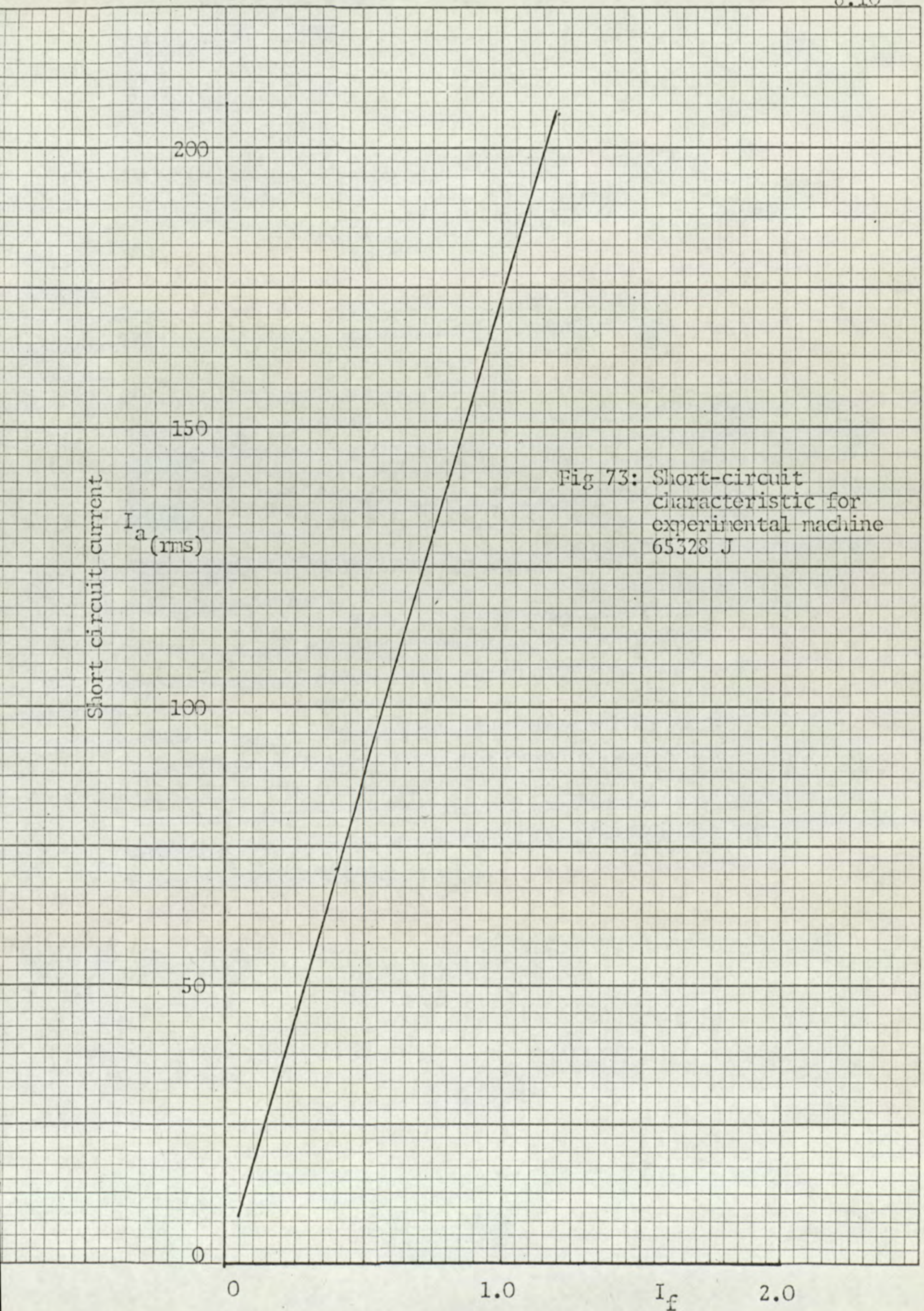

Fig 73: Short-circuit characteristic for experimental machine 65328 J

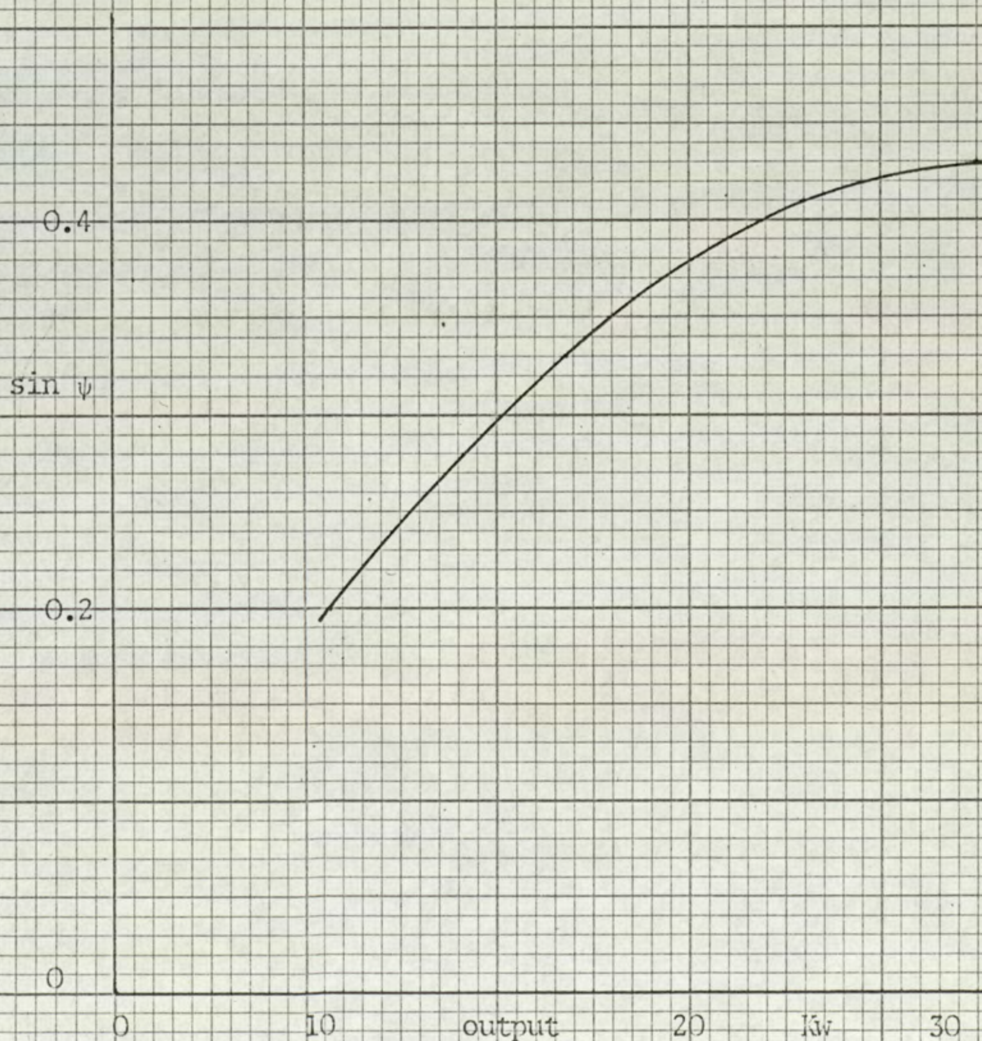

Fig 74: sin ψ (sine 'load-angle') against output at UPF for experimental machine 65328 J

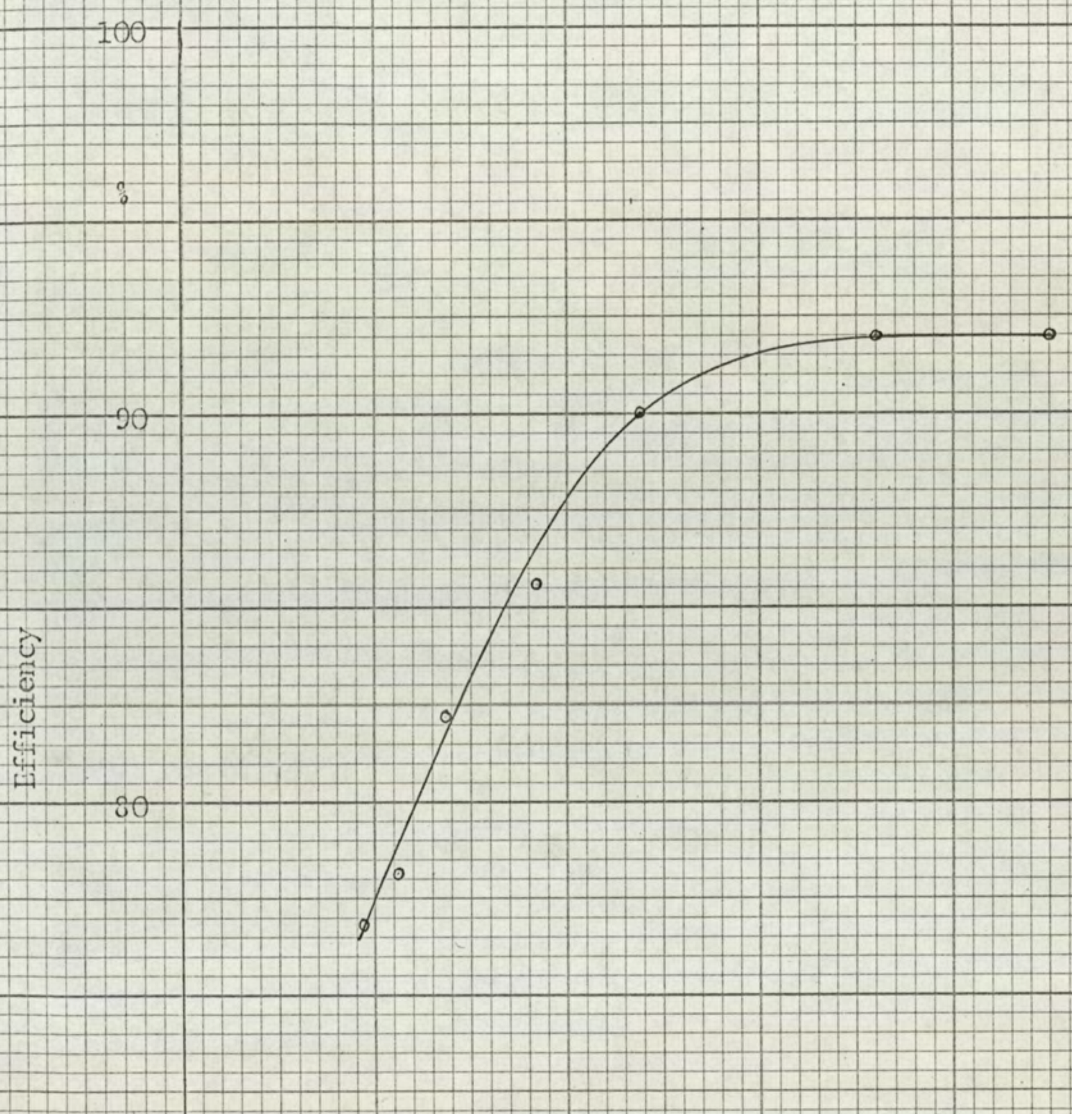

Fig 75: Efficiency against output for experimental machine 65328 J

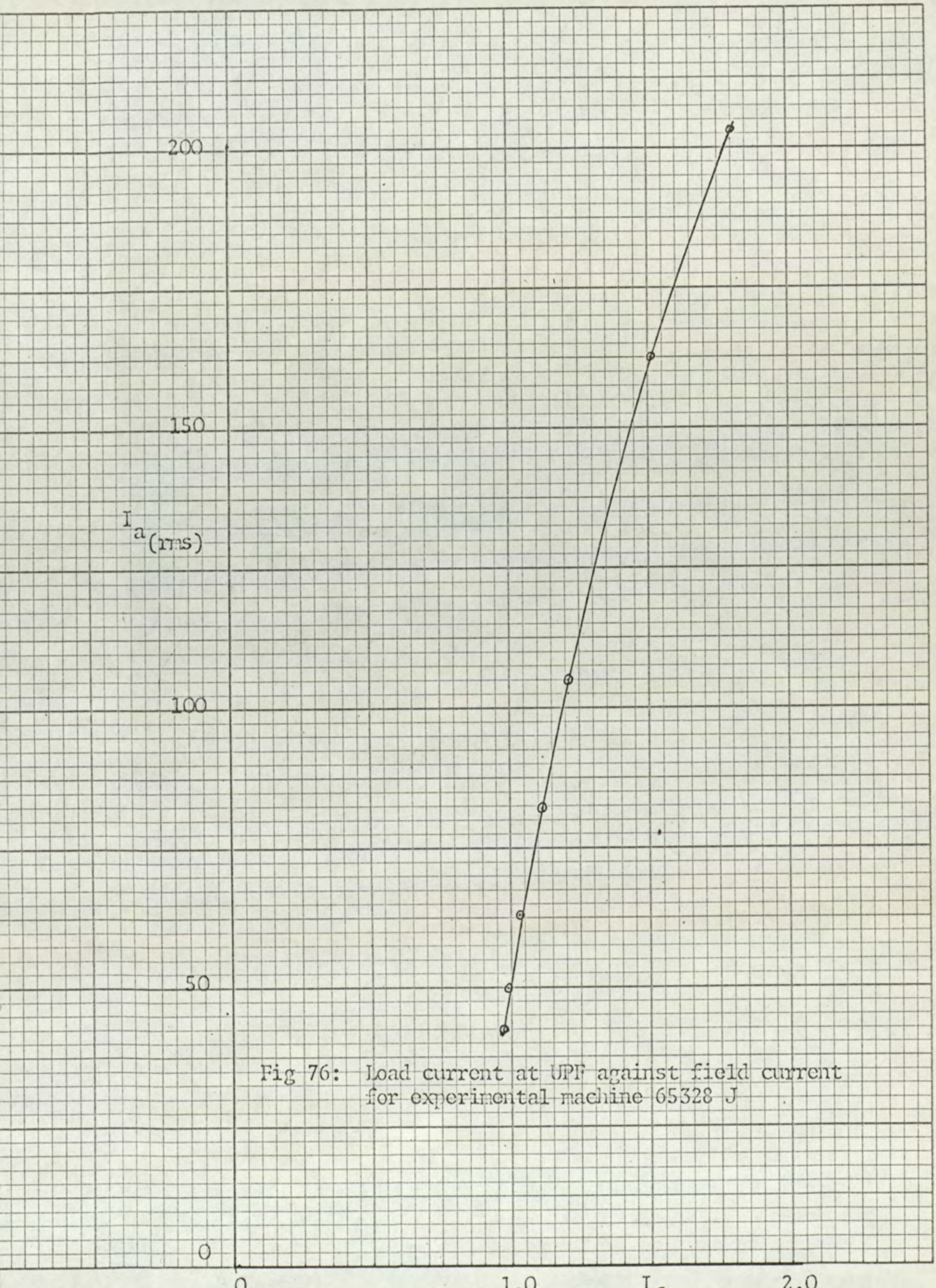

Fig 76: Load current at UPF against field current for experimental machine 65328 J

Fig 77: Total losses against output for experimental machine 65328 J

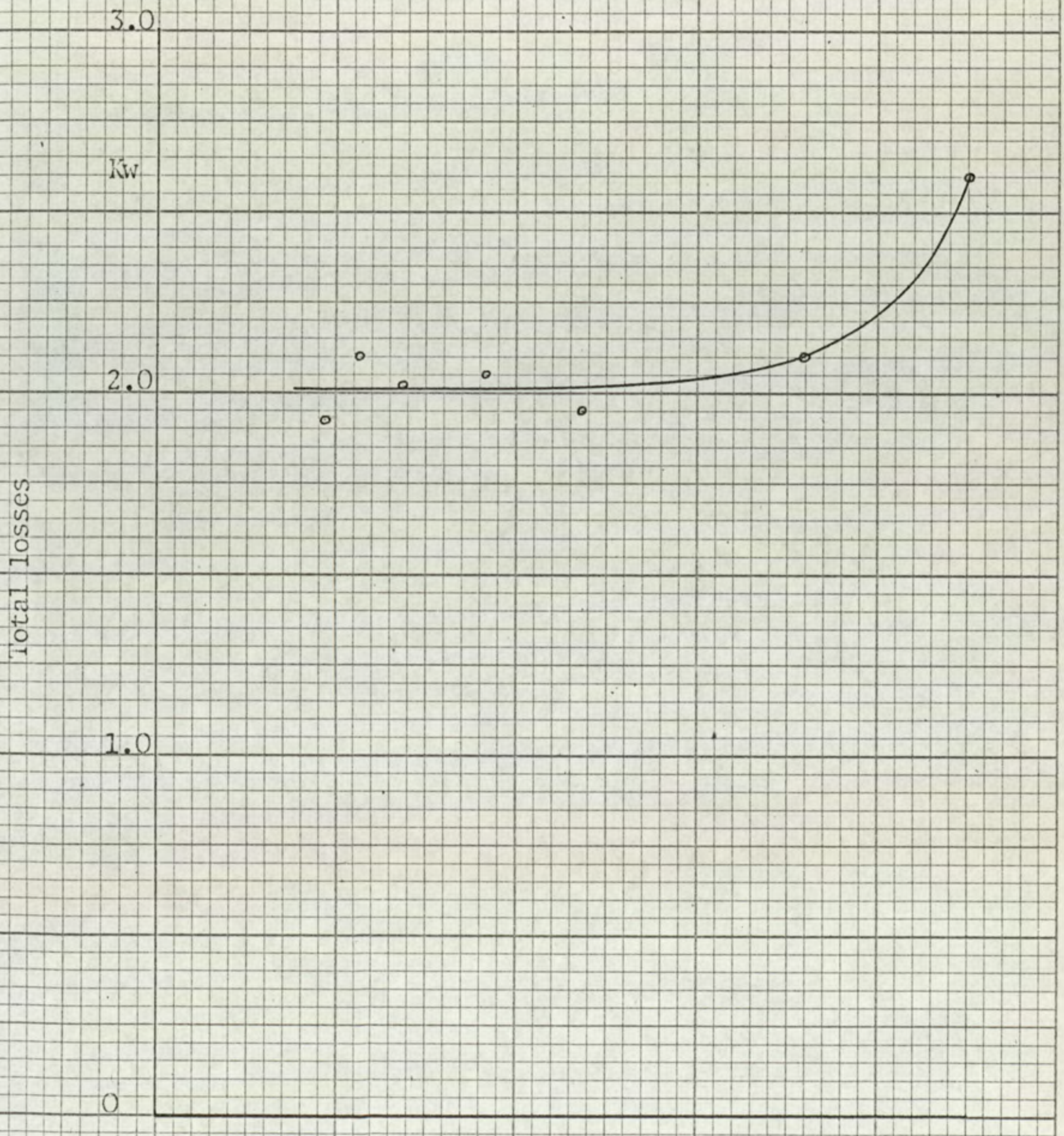

8.11 Supporting papers

a) 'Stator Flux distributions in Lorenz-type medium-frequency inductor-alternators'

E.J. Davies and R.K.Lay, 1966, Proc. IEE, Vol 113 No. 12, p.2023

b) 'Rotor surface flux distributions in Lorenz-type medium-frequency inductor-alternators'

E.J. Davies and R.K.Lay, accepted for publication in the Proceedings IEE, 16th March, 1967

c) 'The History and Changing Fortunes of the inductor-alternator'

R.K.Lay, read before the South Midland, the Mersey and North Wales, and the Sheffield Graduate and Student Sections of the I.E.E. 1966/67

Stator flux distributions in Lorenz-type medium-frequency inductor alternators

E. J. Davies, B.Sc., Ph.D., Sen.Mem.I.E.E.E., C.Eng., M.I.E.E., and R. K. Lay, B.Sc.(Eng.), Mem.I.E.E.E., Graduate I.E.E.

Synopsis

This theoretical and experimental analysis of the magnitudes and distribution of stator-flux harmonic components in a Lorenz-type inductor alternator is part of a broad investigation into this class of machine. The test alternator is a specially designed 30kW model of the standard 300kW industrial unit. Current designs employ field damping to reduce second-harmonic flux modulations expected by analogy with the Guy-type inductor alternator on load. The paper shows that no modulation of the field flux could exist in an ideal Lorenz-type alternator. However, the practical machine, with a.c.-slot openings interrupting the stator surface between field slots, will have harmonic components of flux, both on open circuit and on load, whose magnitudes depend on the width of the a.c.-slot opening. Damping is shown to be sucessful in reducing second- (and other even-) harmonic components, whilst being totally ineffective against fundamental variations in field flux and odd-order-harmonic fluxes. A theory is given that explains these effects. Measurements on the experimental model verify this theory. The paper introduces a technique for relating fluxes to the geometry of the airgap surfaces, and has shown the distribution for inductor alternators to be somewhat more complex than was presumed. It is expected that this analysis will solve the problem of accurate loss calculation in these machines.

List of symbols

B_{oc} = open-circuit airgap flux-density wave, Wb/m^2
B_m = peak value of mth harmonic component of B_{oc} wave, Wb/m^2
l = effective core length, m
λ = rotor-pole pitch, m
λ_s = stator-slot pitch, m
σ = a.c.-slot opening, electrical rad.
t_w = rotor-tooth width at the airgap surface, m
ϕ_{kn} = peak kth-harmonic magnetic flux contributed to the core by tooth n, Wb
ω = fundamental angular frequency of B_{oc} wave, rad/s
t = time
E = voltage induced in field
N = number of turns
f = frequency, c/s
ϕ = magnetic flux, Wb
t_r = rotor tooth width, m

1 Introduction

Inductor generators are used at frequencies that are physically impossible for conventional wound-pole machines, because the rotor-pole pitch would be too small and the rotor windings difficult to retain. As the frequency rises to 1000c/s, say, the rotor windings are omitted and the flux-density variation at the stator surface is produced by modulations of the airgap permeance with rotor teeth. If the machine is homopolar,[1] the stator windings in the polyphase case will be similar to the conventional machine, although they are usually wound 1 slot/pole per phase, single phase in practice. The heteropolar[1] version of this machine is the subject of this paper. It was invented by Schmidt,[2] patented[3] and manufactured, and is described in Section 2.1. Still higher frequencies are required for surface-heating applications (8–10kc/s at 3000rev/min). The rotor-pole pitch is now only about 5mm for a 30cm rotor diameter and the 1 slot/pole per phase stator winding becomes impracticable. At these frequencies, Guy[4] slotting is used with unwound teeth to modulate the pole flux on both stator and rotor. This machine has been described in detail by Raby,[5] including a discussion of the interaction of the armature-reaction m.m.f. with the airgap permeance in producing second-harmonic effects in the field windings.

This paper is concerned with stator harmonics in the Lorenz machine, as part of a general investigation. It has been the practice to fit damping windings in the field slots, by analogy with the Guy machine, whereas our calculations showed that there would be no second harmonic in the ideal Lorenz machine. Tests showed that even-harmonic voltages were present both on load and on open circuit, and were amenable to damping. Also, substantial odd-order-harmonic fluxes were present, again on load and on open-circuit; these were not eliminated by a field-damping winding. The paper gives experimental and calculated results, and shows that these harmonic fluxes and voltages are due to the a.c. slotting interrupting the natural flux paths. The redistribution explains the inability of the damping windings to reduce the odd-order-harmonic fluxes and relates the magnitude of tooth and core fluxes to the width of the stator tooth at the airgap surface.

2 Lorenz machine

2.1 Description of machine

The upper limit for salient-pole, wound-field generators is set by the minimum practicable pole pitch, say 2–3cm, combined with the mechanical difficulties of retaining windings at 2-pole synchronous speed. This limit is not precise, but falls in the 400–800c/s region. Melting furnaces are usually supplied at 1kc/s. Generators for this frequency use the inductor principle; the rotor has unwound teeth, and the flux variations at the stator surface are caused by the modulation of a constant m.m.f. with a variable-reluctance pattern. Fig. 1b shows the rotor of such a machine. If constant excitation is applied to the airgap, and stator slotting is neglected, the flux-density pattern shown in Fig. 1c will result; this pattern is found by flux-plotting or analogue methods. It can be analysed into a steady flux density on which is superimposed a fundamental, of wavelength equal to the rotor-slot pitch, and its harmonics. The stator slotting can be single phase or polyphase, but a 1 slot/pole per phase, single-phase winding is usual, resulting in two stator slots per rotor slot. A 1kc/s, 3000rev/min generator with 30cm

Paper 5139 P, first received 13th July and in revised form 25th August 1966

Mr. Davies and Mr. Lay are with the Department of Electrical Engineering, The University of Aston in Birmingham, Birmingham 4, England

rotor diameter has 20 rotor slots, 40 stator slots and a stator-slot pitch λ_s of 2·36cm. If the machine were homopolar (Fig. 2*a*), it would be exactly analogous to the normal synchronous machine, except that the armature reaction will act on the slotted rotor instead of an array of poles.[6] In modern practice, the transient behaviour of the homopolar machine is too slow, because of the solid iron in the magnetic circuit, and the fully laminated heteropolar construction (Fig. 2*b*) is used. This is also cheaper. Figs. 2*c* and 2*d* show two possible arrangements of pole slotting in a heteropolar machine. These will be discussed in detail later.

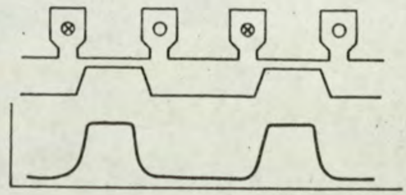

Fig. 1
Basic inductor alternator airgap geometry showing resulting flux-density pattern

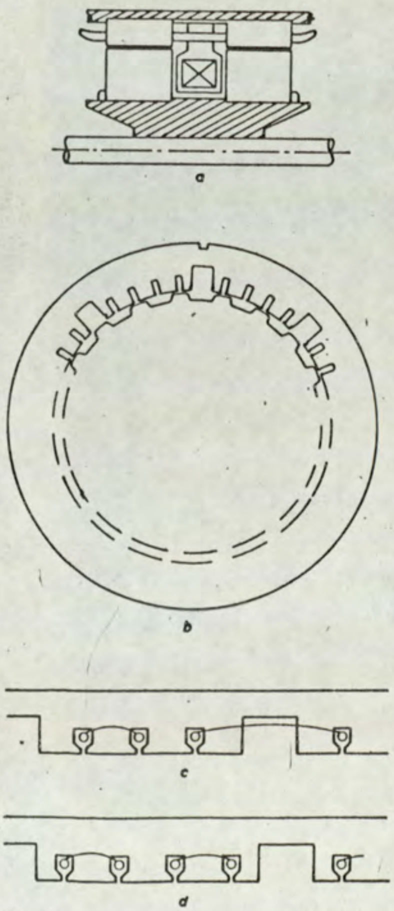

Fig. 2
Alternative field and armature windings
a Homopolar machine, slotting similar to Fig. 1
b Heteropolar slotting
c Heteropolar Lorenz slotting—odd a.c. slots per d.c. pole
d Heteropolar Lorenz slotting—even a.c. slots per d.c. pole

2.2 Operation of machine

The flux-density wave shown in Fig. 1*c* moves with the rotor. Motion relative to the stator changes the flux linkages with the stator windings; if these have the winding directions shown in Fig. 1*a*, the induced voltages will be cumulative. The armature-reaction m.m.f. caused by the load current flowing in the stator windings will be pulsating, not rotating. Fig. 3 shows the B_{oc} wave in more detail to define the co-ordinate system and the position of the rotor

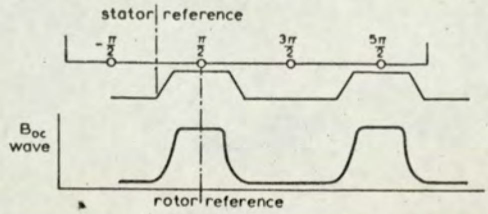

Fig. 3
Reference axes showing position of rotor reference relative to stator reference at time $t = 0$

relative to the stator at any instant. If the stator slots were negligibly small and the active pole width an exact number of rotor pitches, it will be seen that the total flux entering the pole on open circuit would be constant, irrespective of rotor position. There is no change of flux linkages with the field. There will be flux-density variations in the iron at all the frequencies present in this original flux-density wave.

3 Experimental machine

3.1 General

The work described in this paper is part of a broader investigation of this type of machine. The smallest standard commercial generator in regular production is 300kW; this is much too big for university-laboratory use. Our machine is a 30kW, 1000c/s, 0·9 power-factor alternator, and is a specially built scaled model of the normal machine. Details of the model are as follows:

Stator o.d.	= 40·0cm
Stator i.d.	= 29·85cm
Airgap	= 0·28mm
Rotor teeth	= 20
D.C. poles	= 8
Stator-teeth/pole	= $(3 + 2 \times \frac{1}{2})$
Speed	= 3000rev/min
Core length	= 13·97cm

This model is exactly equivalent to the larger machines of the same type, except that its armature resistance is 0·017 p.u., against 0·008p.u. for the normal machine.

3.2 Windings

3.2.1 A.C. windings

The a.c. coils are made as push-through hairpin coils. Because the machine was to be used for experimental work, special links were devised to complete the coils at the connection end. These allow the machine to be dismantled without difficulty. 32 a.c. slots each contain four rectangular conductors (6·1mm × 2·3mm). Two parallel circuits are wound in alternate pairs of poles, i.e. poles 1, 2, 5 and 6 and poles 3, 4, 7 and 8, giving 32 effective turns in series.

3.2.2 Field windings

Each of the eight field coils comprises 270 turns of 0·71mm-diameter wire. The coils are series connected and wound with consecutive coils having opposite directions. The internal connection between coils 1 and 2 is tapped and brought out to enable measurements to be made on one field coil alone.

3.3 Search coils

Fig. 4*a* shows the search conductors incorporated into the machine. A special stator-core packet, 1·27cm long, was fastened together using rivets situated away from the varying fluxes. This was then drilled as shown, with 0·025 cm-diameter holes. The packet was securely clamped to minimise burrs.

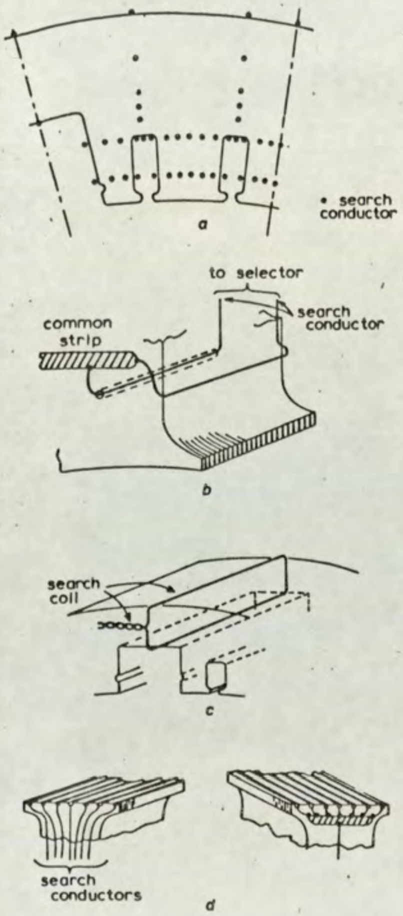

Fig. 4

Details of search conductors
a Position of search conductors in a test stack punching
b Test stack with search conductors showing common strip
c Search coil for sensing flux passing behind field slot
d Surface search conductors on stator teeth seen from both ends of the core

It was not possible to anneal after drilling, because the punchings were already varnished, but it was felt that the error from this source would be small. The laminations on either side of the packet were cut away to allow the introduction of the 0·02 cm-diameter search wires. These were brought in radially (Fig. 4*b*), passed through their respective holes, and connected to a common strip at the other end. Thus any two search wires may be chosen externally to form a search coil. These search coils are supplemented by bigger coils

(*a*) around the stator core behind the field coil (Fig. 4*c*)
(*b*) in the surface of the stator teeth (Fig. 4*d*).

These coils run the whole length of the stator and so embrace the total machine flux passing through that section. Since the airgap was designed to be as short as possible consistent with economic manufacture, it was necessary to let the surface search wires into the iron. Channels 0·025 cm wide and 0·02 cm deep were machined using a slotting saw. The search wires were connected to a common strip at one end, set into their channels with Araldite and led, suitably twisted, from the other end of the stator to the selector switches.

3.4 Damping windings

These are in the form of a cage of copper strips lying at the bottom of each field slot. At one end, all the strips were connected to a common endring. From the other ends individual leads, all of the same length, were brought out to a special terminal block at which any number could be connected together.

4 The machine on open circuit

4.1 Preliminary tests

Tests using the search coils described in Section 3.3 showed that second-harmonic voltages are induced in the field under load conditions. In addition to these, the whole spectrum of odd and even harmonics was present (Fig. 5). It was also found that all the harmonics were relatively insensitive to load-current variations. Next, the flux passing behind a d.c. slot was measured. This was assumed to be the flux linking the field winding, although later this was shown to be incorrect. When the measured flux behind the field slot was checked against the measured voltage induced in the field, using $E = 4{\cdot}44\phi Nf$, the even harmonics agreed fairly well, but the odd harmonics showed no agreement. The conclusions from these preliminary tests were

(*a*) odd-harmonic fluxes were present which had been assumed not to exist
(*b*) these odd harmonics showed a peculiar flux/voltage relationship
(*c*) even harmonics were present on both no load and load
(*d*) both odd and even harmonics appeared to be independent of load current.

To explain these facts, it was decided to investigate open-circuit conditions fully before continuing the load analysis.

4.2 Open-circuit tests

Fig. 5 shows the harmonic analysis of the voltages induced in a single field coil. The open-circuit and short-circuit measurements were taken at rated voltage and current, respectively. The voltages induced on open circuit are little changed by loading the machine, suggesting that these harmonics are not load phenomena, as is usually claimed, but are associated with the open-circuit flux patterns. The

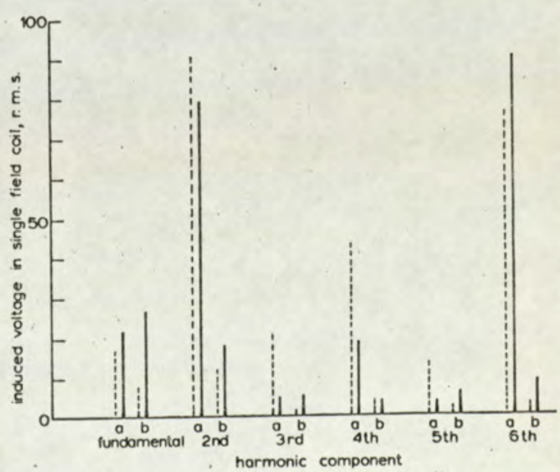

Fig. 5

Harmonic voltage modulations present in a single field pole winding (fundamental frequency, 1000 c/s)
---- open circuit
—— short circuit
a Undamped
b Damped

numerous coils described in Section 3.3 were used to investigate these, and Fig. 6 shows the flux levels linking the various coils for several harmonic frequencies. The damping winding, described in Section 3.4, would not previously have been expected to be effective under open-circuit conditions, but, in view of the flux variations shown in the preliminary tests, it was decided to measure all fluxes with and without the damping circuit connected. This immediately produced a further anomaly; not all the fluxes apparently linking the field coil were reduced when the damping coil was connected. Table 1 shows the fluxes present behind the field slot for each harmonic, damped and undamped, together with the flux that would necessarily link the field coil to induce the voltages given in Fig. 5.

Table 1 shows clearly that:

(*a*) The even-harmonic fluxes agree reasonably well with the voltages they induce. They are all substantially reduced by damping.

(*b*) The odd-harmonic fluxes have much greater magnitudes than are required to induce the voltages found in the field coil. The fundamental and third harmonics are almost unaffected by damping, suggesting that the vector sum of the two fluxes behind adjacent field slots does not vary in time within the damping winding of that pole.

Table 1

COMPARISON OF HARMONIC FLUXES MEASURED BEHIND THE FIELD SLOT WITH THOSE CALCULATED FROM THE VOLTAGES INDUCED IN THE FIELD COIL

Harmonic	Damped/ undamped	Open-circuit flux measured	Open-circuit flux required to induce measured voltage
		μWb	μWb
1	undamped	191	7·8
	damped	189	3·1
2	undamped	15	19
	damped	2·6	2·5
3	undamped	20	2·9
	damped	19	0·3
4	undamped	7·7	4·6
	damped	0·7	0·4
5	undamped	4·6	1·2
	damped	2·3	0·2
6	undamped	4·4	3·9
	damped	0·3	0·2

4.3 Open-circuit flux linkages with the field winding

4.3.1 Effect of slot openings

For ideal conditions of the stator airgap surface (Section 2.2), i.e. continuous between field slots; Appendix 8.1

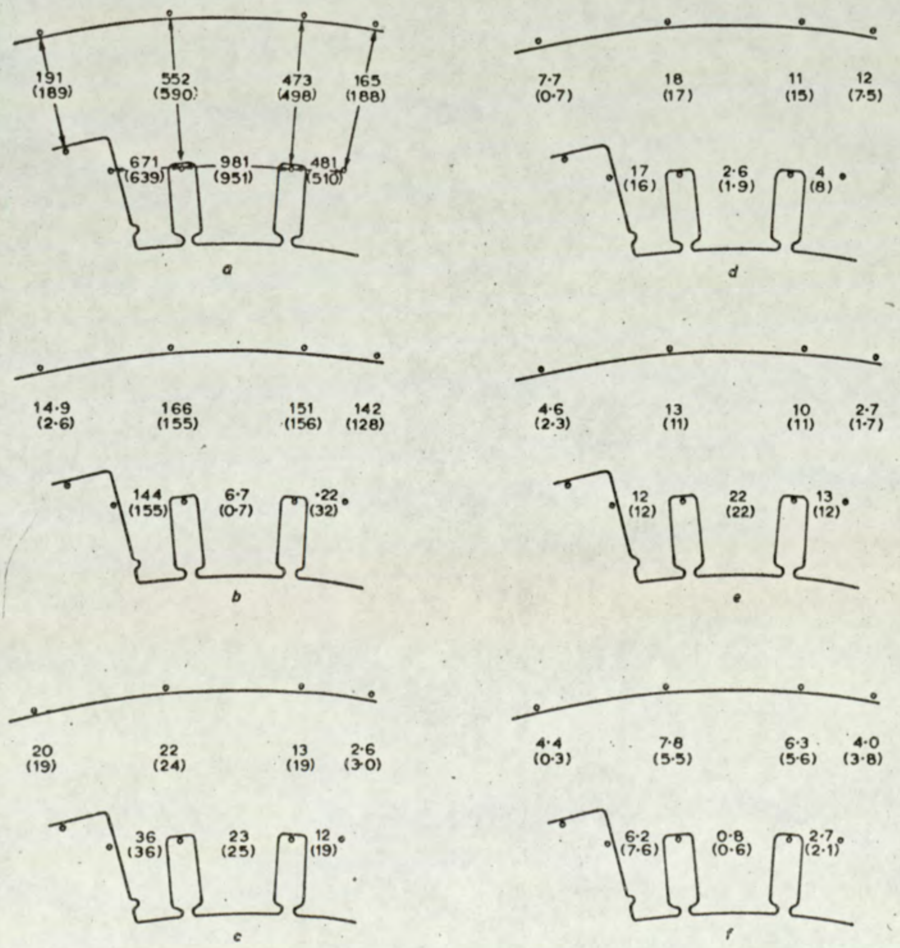

Fig. 6

Harmonic components of peak flux, in μWb, in core and teeth at rated open-circuit voltage

Bracketed values refer to damped conditions
a Fundamental *b* Second harmonic *c* Third harmonic *d* Fourth harmonic *e* Fifth harmonic *f* Sixth harmonic

establishes that no time-varying flux linkages exist to induce a voltage in the field. In the practical machine, the stator a.c. slotting is a major divergence from this ideal. This interrupts the stator surface between field slots and forces the fundamental and harmonic pole fluxes to close by different paths from the natural ones. This is especially true of the odd harmonics, which would have to take different paths even if the a.c. slots were very narrow. It also applies to the even harmonics, since normal tooth widths are less than an integral number of harmonic pole pitches. Tables 2 and 3 summarize the contributions of the individual teeth to the core flux at fundamental and second-harmonic frequencies, respectively, in terms of the stator-slot opening σ (electrical rad). The tooth numbering is shown in Fig. 7*a* and the expressions are derived in detail in Appendix 8.2. These Tables lead to explanations of the anomalies and to methods for calculating the various components of flux that exist.

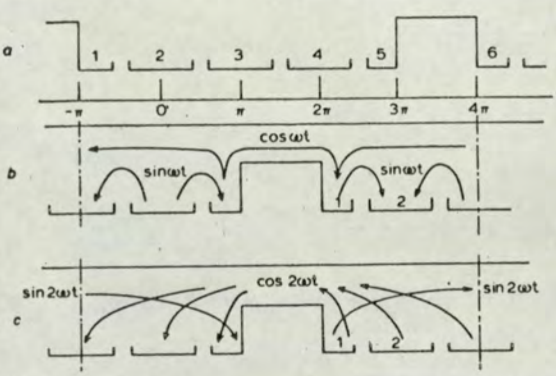

Fig. 7

Distribution of open-circuit flux variations (even a.c. slots per d.c. pole)

a Numbering system
b Paths of fundamental components
c Paths of second-harmonic components

Table 2

SUMMARY OF FUNDAMENTAL-FREQUENCY CONTRIBUTIONS TO CORE FLUX

Tooth	Fundamental-frequency contribution in units of $l\lambda B_1/2\pi$
Tooth 1	$\cos\sigma/2 \sin\omega t - (1 - \sin\sigma/2)\cos\omega t$
2	$-2\cos\sigma/2 \sin\omega t$
3	$2\cos\sigma/2 \sin\omega t$
4	$-2\cos\sigma/2 \sin\omega t$
5	$\cos\sigma/2 \sin\omega t + (1 - \sin\sigma/2)\cos\omega t$
6	$\cos\sigma/2 \sin\omega t - (1 - \sin\sigma/2)\cos\omega t$

Table 3

SUMMARY OF SECOND-HARMONIC-FREQUENCY CONTRIBUTIONS TO CORE FLUX

Tooth	Second-harmonic contribution in units of $l\lambda B_2/4\pi$
Tooth 1	$-\sin\sigma\cos 2\omega t - (1 + \cos\sigma)\sin 2\omega t$
2	$-2\sin\sigma\cos 2\omega t$
3	$-2\sin\sigma\cos 2\omega t$
4	$-2\sin\sigma\cos 2\omega t$
5	$-\sin\sigma\cos 2\omega t + (1 + \cos\sigma)\sin 2\omega t$
6	$\sin\sigma\cos 2\omega t + (1 + \cos\sigma)\sin 2\omega t$

4.3.2 Fundamental frequency

The sum of the terms in $\sin\omega t$ (Table 2) over one d.c. pole pitch, i.e. teeth 1–5, is zero. The second term, $\cos\omega t$, for tooth 5 can be balanced by contributions from either tooth 1 (passing across the d.c. pole) or tooth 6 (passing behind the field slot) (Fig. 7*b*). The relative flux levels depend upon path reluctances, but, as there is symmetry in successive poles, the net flux entering a pole is zero. This explains how there can be fundamental flux passing behind the field slot with the machine on open circuit without voltages being induced, either in the damping winding or in the field coil, by these fluxes. These remarks are true even if σ is very small; only the complete elimination of slotting gives the conditions described in Appendix 8.1.

4.3.3 Second-harmonic frequency

Table 3 shows that the terms in $\cos 2\omega t$ are additive; their paths from pole to pole can only be completed by passing behind the field slot (Fig. 7*c*). This explains the correct relationships between measured fluxes and voltages and the reduction in this flux due to damping (Table 1). These terms are critically dependent on the angle σ, tending to zero as σ itself goes to zero. Table 3 also shows that the $\sin 2\omega t$ terms of teeth 1–5 sum to zero, and that those of teeth 5 and 6 are of the same sign. Hence, these second-harmonic fluxes must close inside a d.c. pole, and cannot pass from pole to pole. They are not eliminated by making σ small; only complete removal of slotting will eliminate them. These fluxes cause core losses, but do not induce voltages in the field or damper windings.

4.4 Calculation of tooth-flux contributions to the core

Table 2 shows the fundamental contributions from teeth 2, 3 and 4 to have magnitude $\dfrac{l\lambda B_1}{\pi}\cos\dfrac{\sigma}{2}\sin\omega t$.

For the experimental machine

$$B_1 = 0{\cdot}55\,\text{Wb/m}^2$$
$$l = 12{\cdot}22\,\text{cm}$$
$$\lambda = 4{\cdot}69\,\text{cm}$$
$$\sigma = 0{\cdot}46 \text{ electrical rad } (26{\cdot}35 \text{ electrical deg}).$$

Then

$$\phi_{12} = -\phi_{13} = \phi_{14} = 977\,\mu\text{Wb}$$

$$\phi_{11} = \frac{l\lambda B_1}{2\pi}\left\{\cos\frac{\sigma}{2}\sin\omega t - \left(1 - \sin\frac{\sigma}{2}\right)\cos\omega t\right\}$$

$$= \text{vector sum of } 488 \sin\omega t \text{ and } 387 \cos\omega t$$

$$= 623\,\mu\text{Wb}$$

Assuming that the $\cos\omega t$ component of ϕ_{11} is split equally between the two possible circuits (Fig. 8), then flux behind field slot = flux across pole pitch = $193\,\mu$Wb maximum.

The permeances of the two paths 'behind field slot' and 'across pole pitch' are not in fact equal, nor does their ratio vary linearly with flux. Since the path behind the field slot carries the d.c. field flux, the components of ϕ_{11} modulate about a high mean level. The path across the pole pitch is comparatively lightly loaded magnetically; at the pole centre line the ϕ_{11} component is the only flux present. Thus the path behind the field slot will experience a reduction in incremental permeance as the overall flux level increases. The agreement

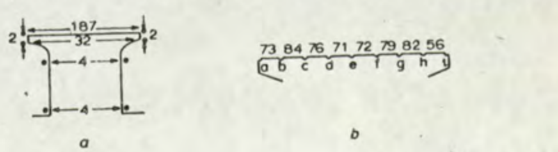

Fig. 8

Detail of fluxes measured in tooth 2

a Second-harmonic fluxes, in μWb, at various tooth cross-sections
b Lettering system used with second-harmonic fluxes, in μWb, measured by surface coils

in Table 4 is due to the two ϕ_{11} components being approximately equal for the rated open-circuit-voltage field.

Table 3 shows the second-harmonic contributions from teeth 2, 3 and 4 to have magnitude

$$\frac{l\lambda B_2}{2\pi}\sin\sigma\cos 2\omega t$$

$$B_2 = 0{\cdot}36B_1 = 0{\cdot}2\,\text{Wb/m}^2$$

and $$-\phi_{22} = -\phi_{23} = -\phi_{24} = 80\,\mu\text{Wb}$$

$$-\phi_{21} = \frac{l\lambda B_2}{4\pi}\{\sin\sigma\cos 2\omega t + (\cos\sigma + 1)\sin 2\omega t\}$$

$$= \text{vector sum of } 40\cos 2\omega t \text{ and } 171\sin 2\omega t$$

$$= 176\,\mu\text{Wb}$$

Table 4

CORE FLUX: FIELD SET FOR RATED OPEN-CIRCUIT VOLTAGE

	Fundamental		Second harmonic	
	calculated	measured	calculated	measured
	μWb	μWb	μWb	μWb
From tooth 1	623	645	171	152
From tooth 2	977	990	80	4
Behind field slot	193	189	160	10
Across pole pitch	193	186	176	159

The comparison of measured and calculated values for the fundamental components shows good agreement, suggesting that the distributions discussed in Section 4.3.2 are soundly based. Equally, the comparison of second-harmonic fluxes suggests that Section 4.3.3 is not the complete description. The $\sin 2\omega t$ component from tooth 1 gives calculations of the right size (Table 4), but those for tooth 2 are clearly affected by another mechanism. Since the flux measured behind the field slot is approximately twice that contributed by tooth 2, the flux paths suggested in Fig. 7*c* seem correct; so it is the magnitude of the flux in tooth 2 which must be investigated.

The measured values of flux in Table 4 and Fig. 6 were derived from analysis of the search coil e.m.f.s at fundamental and second-harmonic frequencies. These were converted to values of peak flux using the standard expression

$$\phi = \left(\frac{E}{4{\cdot}44Nf}\right)$$

4.5 Second-harmonic flux in tooth 2

Fig. 8*a* shows measured flux levels in tooth 2 and Fig. 8*b* the flux which linked an array of search coils along the airgap surface of tooth 2, at rated open-circuit voltage. The average surface search-coil flux was $74\,\mu$Wb. Correcting for pitch this establishes the presence of $187\,\mu$Wb of second-harmonic flux in the airgap. (This agrees with the theory of Section 4.3, since for $\sigma = \pi/2$, i.e. a tooth width equal to half a second-harmonic wavelength, $\phi_{22} = 181\,\mu$Wb.) However, for the experimental machine the theory leads to a value of $80\,\mu$Wb (Table 4) where only $32\,\mu$Wb (Fig. 8*a*) is measured. Further, the assumption that whatever flux penetrates the tooth surface will be contributed to the core without loss is shown to be unacceptable; only $4\,\mu$Wb is in fact contributed. The theory of Section 4.3 depends upon the basic assumption that sinusoidal time variations of flux density in the stator teeth are the result of the uniform motion of the rotor with its associated sinusoidal space distribution of flux density. Since we know the second-harmonic flux per pole and the pitch of the tooth-surface coils, measurement of second-harmonic voltage in these coils can be compared with calculated values, using the known flux, to show any flux distortion that is present. Table 5 shows the actual pitch and the expected voltage, together with the measured voltage and the pitch that would correspond to those measurements. This shows that there is distortion at the tooth tips causing more flux to link those coils than expected.

Thus more of the second-harmonic flux distribution is able to complete its path within the tooth surface than was expected, reducing the contribution to the tooth proper from $80\,\mu$Wb to $32\,\mu$Wb. The flux not finding a path from one harmonic pole to the next within a tooth width is proportional to the armature-slot opening (Section 4.3). The distortion of flux distribution has effectively reduced the slot opening to a quarter its actual dimension (coil *ai*, 0·95 instead of 0·8). Fig. 9*a* shows the spatial distortion of the second-harmonic

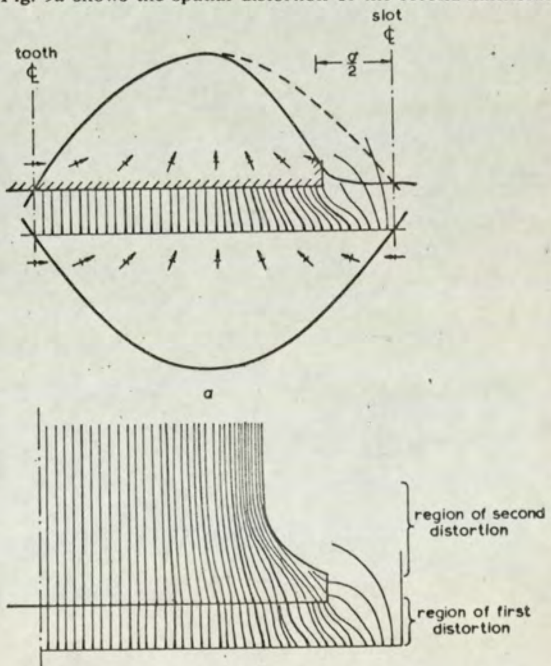

Fig. 9
Postulated distortion of second-harmonic flux in tooth 2
a Flux entering tooth surface
---- undistorted flux
—— distorted flux
Lower curve is spatial second-harmonic component of airgap flux
b Assumed distribution of flux within tooth

Table 5

CALCULATED AND MEASURED SECOND-HARMONIC VOLTAGES WITH CORRESPONDING VALUES OF PITCH FOR THE TOOTH-SURFACE SEARCH COILS (FIG. 8*b*)

	de	*df*	*ae*	*af*	*ag*	*bh*	*ah*	*ai*
Calculated voltage, V	0·49	0·95	1·53	1·61	1·53	1·53	1·30	0·95
Actual pitch	0·1	0·2	0·4	0·5	0·6	0·6	0·7	0·8
Measured voltage, V	0·5	0·95	1·62	1·48	1·05	0·95	0·55	0·25
Corresponding pitch	0·1	0·2	0·5	0·63	0·77	0·8	0·89	0·95

component of airgap flux density at the tooth surface, with the associated redistribution of time-varying flux denoted by the vector arrows. The constriction of the teeth, due to the slotting, distorts the flux pattern at the sides of the teeth even further (Fig. 9*b*). The combination of the distortions at the gap surface and in the tooth makes the assumed linearity invalid and allows the flux within the tooth to complete more of its pole-to-pole path, reducing the contribution to the core below that expected from theory (Table 4). Note that the second harmonic in the B_{oc} wave depends upon t_r/λ, decreasing as this ratio approaches $0 \cdot 5$.

4.6 Application of distribution theory to designs having odd a.c. slots per d.c. pole

Since the theory of Section 4.3 was substantiated by the agreement between measured and calculated values in Section 4.4, the theory is now extended to describe the distributions of flux for the design of Fig. 2*c*. Designs for odd a.c. slots per d.c. pole are produced by removing one or more stator teeth after the armature slots have been notched around the complete periphery. This fixes the field slot opening at $(n\pi + \sigma)$. If $n = 2$ (corresponding to two teeth removed), application of the technique of Appendix 8.2 to discover the core-flux contributions leads to Fig. 10*a*. The fundamental

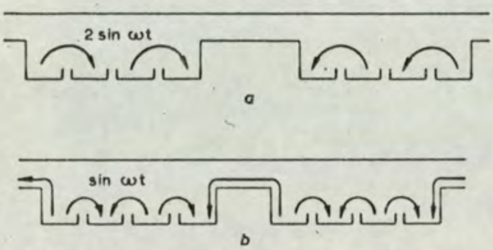

Fig. 10

Distribution of fundamental open-circuit flux variations (odd a.c. slots per d.c. pole)

a Paths of fundamental components if two stator teeth are removed to form a field slot
b Paths of fundamental components if one stator tooth is removed to form a field slot

contributions find satisfactory paths from tooth to tooth, no flux being required to pass behind the d.c. slot. The second-harmonic contributions, however, are all of the same sign within each pole pitch; thus their only path for completion is from pole to pole passing behind the field slot. If $n = 1$, the contributions from teeth on either side of a field slot, taking the sense of each pole into consideration, are of opposite sign. Thus the fluxes from these teeth will divide in the ratio of the permeances of the paths, both behind the field slot and into the adjacent tooth of their own pole (Fig. 10*b*). The second-harmonic distribution for $n = 1$ is identical to that of $n = 2$; all second-harmonic contributions must pass behind the field slot.

5 Conclusions

It has been shown both by experiment and from theory that the Lorenz machine will have harmonic-flux components that link the field winding caused by the presence of the stator a.c. slotting. The fundamental components in the teeth can be calculated, but the exact route that will be chosen is nebulous, and dependent on the relative permeances of the paths behind the field slot and across the pole face. In either event the damper winding is ineffective. The second-harmonic fluxes do link the field coil, but distortion in the airgap reduces their effect. Measurements on open circuit and on load show that the harmonics are present in roughly the same amounts, suggesting that the mechanisms we have discussed apply to both conditions. We hope to deal with performance on load and losses in a later paper.

6 Acknowledgments

We gratefully acknowledge the help of Associated Electrical Industries Ltd., in manufacturing the experimental machine described in this paper, and of Messrs. K. F. Raby and E. Beadham at A.E.I. (Rugby) both at the manufacturing stage and with discussions and encouragement later.

7 References

1 LAY, R. K.: 'Inductor alternator terminology', *Electronics & Power*, 1966, 12, p. 287
2 SCHMIDT, K.: 'Die Maschinen für Drahtlone Telegraphie', *Electrotech. Z.*, 1921, 42, p. 245
3 German Patent, DRP 303321, 1914
4 French Patent 307264, 1901
5 RABY, K. F.: 'Inductor alternators at 10kc/s', *Students' Quart. J. IEE*, 1950, 21, p. 15
6 DAVIES, E. J., and PEDERSEN, N. P.: 'An experimental and theoretical study of the Lorenz-type inductor alternator under load', *IEEE Trans. Applic. Industr.*, 1963, 82, p. 174

8 Appendix

The net flux linkages with the field winding due to the open-circuit airgap flux-density distribution are calculated for ideal and practical machines.

8.1 Ideal machine

Assume ideal conditions, i.e. continuous stator airgap surface between field slots.

The open-circuit airgap flux-density distribution relative to the stator reference axis (Fig. 3) is given by

$$B_{oc} = \sum_{m=0}^{\infty} B_m \cos m(\theta - \omega t - \pi/2)$$

The total flux linked by a coil having conductors at θ_1 and θ_2 of active length l will be

$$\phi_{\theta_1}^{\theta_2} = \frac{l\lambda}{2\pi} \int_{\theta_1}^{\theta_2} B_{oc} d\theta$$

Integrating between $-\pi$ and 3π gives the net flux that will link the field winding, ignoring field-slot leakage:

$$\phi\Big|_{-\pi}^{+3\pi} = \frac{l\lambda}{2\pi}\int_{-\pi}^{+3\pi} B_{oc} d\theta = \sum_{m=0}^{\infty} \frac{l\lambda}{2\pi}\left\{\frac{B_m}{m}\sin m(\theta - \omega t - \pi/2)\right\}_{-\pi}^{+3\pi}$$

$$= \sum_{m=0}^{\infty} \frac{l\lambda}{2\pi}\frac{B_m}{m}\{\cos m\,\omega t(2\sin 2m\pi \cos m\pi/2) + \sin m\omega t\,(2\sin 2m\pi \sin m\pi/2)\}$$

$$= 0 \text{ for } m \text{ odd or even}$$

For $m = 0$, B_{oc} is constant. Therefore no time-varying flux linkages with the field coil can exist if

(*a*) the stator-airgap surface between field slots is smooth and continuous
(*b*) the field-pole pitch at the airgap is an even multiple of π electrical rad.

8.2 Practical machine with slots

In practice, the stator airgap surface between field slots is interrupted by a.c. slot openings of width σ electrical rad.

Section 4.3 and Fig. 7*a* describe the teeth and their airgap peripheral limits as:

Tooth 1	$-\pi \rightarrow -(\pi/2 + \sigma/2)$
2	$-(\pi/2 - \sigma/2) \rightarrow (\pi/2 - \sigma/2)$
3	$(\pi/2 + \sigma/2) \rightarrow (3\pi/2 - \sigma/2)$
4	$(3\pi/2 + \sigma/2) \rightarrow (5\pi/2 - \sigma/2)$
5	$(5\pi/2 + \sigma/2) \rightarrow 3\pi$
6	$4\pi \rightarrow (9\pi/2 - \sigma/2)$

The total net flux contributed to the core by tooth 1 due to B_{oc} is

$$lR\int_{-\pi}^{-(\pi/2+\sigma/2)} B_{oc}d\theta = \sum_{m=0}^{\infty} \frac{l\lambda}{2\pi}\left\{\frac{B_m}{m}\sin m\left(\theta - \omega t - \frac{\pi}{2}\right)\right\}_{-\pi}^{-(\pi/2+\sigma/2)}$$

$$= \sum_{m=0}^{\infty} C\left\{\sin m\left(-\pi - \frac{\sigma}{2} - \omega t\right) - \sin m\left(-\frac{3\pi}{2} - \omega t\right)\right\}$$

where $C = \frac{l\lambda}{2\pi}\frac{B_m}{m}$

$$= \sum_{m=0}^{\infty} C\left\{-\sin m\left(\frac{\sigma}{2} + \omega t\right)\cos m\pi + \sin\frac{3m\pi}{2}\cos m\omega t + \cos\frac{3m\pi}{2}\sin m\omega t\right\}$$

$$= \sum_{m=0}^{\infty}\{Cf_1(\omega t)\}$$

Thus for each tooth, by integrating the B_{oc} wave between appropriate limits:

$$f_1(\omega t) = \left\{-\cos m\pi \sin m\left(\frac{\sigma}{2} + \omega t\right) + \sin\frac{3m\pi}{2}\cos m\omega t + \cos\frac{3m\pi}{2}\sin m\omega t\right\}$$

$$f_2(\omega t) = \left\{-\sin m\left(\frac{\sigma}{2} + \omega t\right) - \cos m\pi \sin m\left(\frac{\sigma}{2} - \omega t\right)\right\}$$

$$f_3(\omega t) = \left\{-\sin m\left(\frac{\sigma}{2} - \omega t\right) - \cos m\pi \sin m\left(\frac{\sigma}{2} + \omega t\right)\right\}$$

$$f_4(\omega t) = \left\{-\cos 2m\pi \sin m\left(\frac{\sigma}{2} + \omega t\right) - \cos m\pi \sin m\left(\frac{\sigma}{2} - \omega t\right)\right\}$$

$$f_5(\omega t) = \left\{-\cos 2m\pi \sin m\left(\frac{\sigma}{2} - \omega t\right) + \sin\frac{5m\pi}{2}\cos m\omega t - \cos\frac{5m\pi}{2}\sin m\omega t\right\}$$

$$f_6(\omega t) = \left\{-\cos 4m\pi \sin m\left(\frac{\sigma}{2} + \omega t\right) - \sin\frac{3m\pi}{2}\cos m\omega t + \cos\frac{3m\pi}{2}\sin m\omega t\right\}$$

When comparing the directions of these contributions at any instant in time, to establish the paths followed by the various components, allowance must be made for tooth 6 lying within a pole of opposite sense to that containing teeth 1–5. Therefore, when comparing contributions from teeth 5 and 6, the correct expressions are $\sum_{m=0}^{\infty} Cf_5(\omega t)$ and $-\sum_{m=0}^{\infty} Cf_6(\omega t)$.

ROTOR SURFACE FLUX DISTRIBUTIONS IN LORENZ-TYPE MEDIUM-FREQUENCY INDUCTOR ALTERNATORS

by

E.J. Davies, B.Sc., Ph.D., Sen.Mem.I.E.E.E., C.Eng., F.I.E.E., and
R.K. Lay, B.Sc.,(Eng.), Mem.I.E.E.E., Associate Member I.E.E.

Dr. Davies and Mr. Lay are with the
Department of Electrical Engineering,
The University of Aston in Birmingham,
Birmingham 4, England.

Synopsis

The paper considers the fluxes existing in the airgap of a single-phase Lorenz-type inductor alternator under load conditions. From the interaction of the field and armature reaction m.m.f.s with the rotor permeance, expressions are derived from the airgap flux density waves. These can be separated into a) components stationary with respect to the rotor, resulting in distortion of the no-load waveform, which can be used to calculate voltage and load waveforms and b) components moving with respect to the rotor, of varying wavelength, which produce surface losses in the rotor. Experimental verification is given for the flux density distribution under load, using search coils attached to the rotor surface of a 30kW model, making use of the heteropolar nature of the machine. The measurements of the load flux density distribution are complicated by the presence of the non-synchronous waves, which also generate signals in the rotor search coils. A novel method of interpretation of the search coil signals is given that substantially eliminates the unwanted components. A computer program was used to synthesise the load flux density curve from the no-load waveform using an angle δ, which can be derived from a simple phasor diagram. It is shown to predict the load waveform under various conditions.

Diagram Captions

FIG. 1 Stator and rotor slotting (armature slots reduced to zero for 'ideal machine)
a) open-circuit airgap flux-density wave
b) flux linking rotor surface coil for ideal machine

FIG. 2 Armature reaction m.m.f. a) theoretical
b) actual

FIG. 3 Example of computed rotor tooth-surface flux-density distributions

FIG. 4 Vector diagram relating the open-circuit and terminal voltages with the load current, load power factor and δ. See section 3.2

FIG. 5 Rotor tooth-surface search conductors
a) general view from each end of the core
b) numbering system (seen from 'switch' end)

FIG. 6 Integrated search coil signals, alternator open-circuit (α flux)
a) conductors 1 - 8, = heteropolar flux
b) conductors 4 - 5, = tooth flux

FIG. 7 Integrating and measuring circuit

FIG. 8 Rotor tooth-surface flux-density distribution on open-circuit

FIG. 9 Search coil signals ($\frac{d\phi}{dt}$)
a) open-circuit b) on-load

FIG.10 Integrated search coil signals, alternator on load
a) period for rotor to pass three field poles
b) period for rotor to pass central tooth of one field pole

FIG.11 Rotor tooth-surface flux-density distribution on load, computed and measured

Symbols:

B_{oc}	Airgap flux density distribution on open-circuit relative to the stator.
B_1	Fundamental coefficient of B_{oc} series and base for the flux density p.u. system. (Wb/m^2).
b_m	p.u. mth order coefficient of B_{oc} series.
θ	Measurement of peripheral airgap distance : (electrical rad)
F_f	Field m.m.f. (ampere-turns)
ω	Angular velocity of rotor movement. (rad/sec)
t	Time. (sec)
δ	Angle by which the peak armature current leads or lags the peak open-circuit voltage. (E^*) .
N_a	Effective armature turns in series per phase
I_a	Peak fundamental armature current. (amps)
F_a	Armature reaction m.m.f. (ampere turns)
B_a	Airgap flux density distribution due to armature reaction relative to the stator
Λ	Permeance coefficient
C	Factor : $\frac{(F_a)}{(^*F_f)}$
I_f	Field current. (amps)
ϕ_{oc}	Open-circuit flux, per pole (Wb)
V_T	Terminal volts for field F_f. (volts)
ϕ	Power factor
V_f	Open-circuit volts for field F_f. (volts)
n_s	Synchronous speed
K	Factor : $\frac{b_m}{N(m\pm n)}$
A,B,C,D	Components of the airgap flux density distribution relative to the rotor
B'_a	Airgap flux density distribution due to armature reaction relative to rotor
B'_{oc}	ditto on open-circuit
α, β	Arbitrary values of θ
$\phi'_a(t)_{\alpha\beta}$	Flux due to armature reaction (as a function of time) which links the area between points α and β on the rotor

Cont'd.......

P,Q,R,S Factors in section 8.1.3

B_α, B_β } General flux density terms

F_α, F_β } " m.m.f. terms

m, n } Harmonic order subscripts

1. Introduction

An earlier paper [1] discussed the flux distributions in the stator of a Lorenz-type 1000 c/s inductor alternator. Fig. 1. shows the stator and rotor slotting of such a machine with the slots containing the a.c. winding reduced to zero size. In such an ideal machine the problems discussed in the earlier paper disappear and the machine reduces to a smooth stator facing a slotted rotor. Fig. 1a shows the flux-density pattern in the airgap on open-circuit; this pattern moves with the rotor and results from the field excitation acting on the airgap permeance.

In this paper we are concerned with the fluxes that exist in the airgap under load conditions. These can be used to calculate voltages, waveforms and losses, so this understanding is important. As in other machines, the problem of load behaviour is concerned with the interaction of the armature-reaction m.m.f. (produced by the stator windings) and the airgap permeance, superimposed on existing a.c. conditions. In the Lorenz machine the problem is complicated by the use of a single phase, 1 slot/pole/phase stator winding, so that the armature reaction m.m.f. produced by an ideal winding concentrated at discrete points, ignoring slots, will be a square wave fixed in space with magnitude varying sinusoidally in time phase with the variation of the load current [2]. In a practical machine, the armature reaction wave is not square but trapezoidal, because the windings are spread over the width of a stator a.c. slot.

The interactions of the armature reaction, the field excitation and the airgap permeance are considered mathematically and expressions given for the distortion of the main flux density wave, which can be used to calculate voltages and load waveforms, and for the harmonics that are moving with respect to the rotor, which result in harmonic frequency losses in the stator and rotor iron at the airgap surface. To prove that the theory is soundly based, emphasis is placed on the experimental verification. This is especially important as the mathematics for the interaction of armature reaction and rotor permeance is not strictly correct, but is shown to give results of good engineering accuracy. Direct methods of flux measurement, such as Hall crystals, cannot be used in the restricted airgaps so indirect methods, using search coils, are employed. These bring considerable problems of interpretation, which are described in detail in Section 3.4.

The complications in the theory come from the high harmonic content of the m.m.f. and permeance waves and can be eliminated by assuming an armature reaction wave sinusoidally distributed in space and varying sinusoidally in magnitude with time. Such a wave can be resolved into two contra-rotating sinusoidal waves: one will move forward at synchronous speed and will be stationary with respect to the rotor, the other will move at twice synchronous speed backwards with respect to the rotor.

The forward component will distort the open-circuit flux density pattern, producing a new airgap space distribution. The power factor of the load will determine the angular displacement between the wave and the rotor. At zero p.f. lag, the effect will be wholly demagnetizing; at normal working power factors, approaching unity, the distortion will demagnetize the loading edge and magnetize the trailing edge. This distorted waveform is the new flux-density wave travelling with the rotor and generating voltage in the stator winding.

The negative sequence component of m.m.f. will interact with the rotor permeance. Losses will be induced in the rotor iron and this component also contributes to the reactive volt-drop seen by the stator winding.

Both these effects could easily be measured in an ideal heteropolar Lorenz machine by an array of conductors running axially along the rotor surface (see Fig. 5), brought out to slip rings and capable of being connected in pairs to form search coils. The stator would be smooth between field slots and advantage could then be taken of the heteropolar nature to say that whatever happens across one pole reverses sign across the next pole. The "constant" distortion produced by the forward component of armature reaction will therefore reverse from pole to pole at the d.c. frequency, giving a measurable signal in the search coils at this frequency. The negative sequence component will induce voltages at twice rated frequency (modified by the 'heterodyne' effect of the d.c. poles). These could easily be separated. It will be shown later that these techniques are still valid in the presence of the whole spectrum of m.m.f.'s, but that careful interpretation is needed.

In the following sections, we shall be looking for these two fundamental wavelength effects, but in both theory and experiment we shall have to allow for the presence of the other harmonics in the armature reaction and for the effects of stator slotting.

2. Theoretical Analysis of airgap flux density distribution on load.

2.1 Introduction.

In this section, the equations for the interaction of the field, the armature reaction and the rotor permeance will be summarized. Starting with the open-circuity flux density distribution and the armature reaction m.m.f. expressed in series form, the latter is impressed on the rotor permeance to give load flux.

It must be emphasized that this theory is used in a manner that does not strictly satisfy the conditions, as discussed in (2.4), but nevertheless, the answers it gives agree sufficiently to justify the use of the method. This class of machine always has an airgap that is very short compared with a rotor tooth pitch, so that the airgap in the regions of high flux density is short compared with all the harmonic pole pitches of any consequence that exist in the airgap. For this reason the harmonic poles cannot produce pole to pole leakage in the airgap itself and the approximation we have used becomes valid.

2.2 Series representation of density and m.m.f. patterns.

The open-circuit flux density distribution around the airgap (B_{oc}) as in Fig. 1(a) may be described by the series:

$$B_1 \sum_{m=0,1,2\ldots}^{\infty} b_m \cos m\theta \quad \text{relative to a stationary rotor}$$

where:-

B_1 = peak value of the fundamental component of B_{oc} associated with 1 p.u. field m.m.f. (F_f) Wb/m^2

b_m = p.u. value of the mth coefficient of the B_{oc} series for B_1 = 1 p.u.

θ = peripheral angular distance around the airgap measured from the rotor tooth centre-line (electrical rad)

If the rotor moves with angular velocity ωt and if a rotor tooth centre-line coincides with a stator a.c. slot at time $t = 0$, (i.e. $+\pi/2$ relative to an armature coil axis), the B_{oc} pattern becomes

$$B_1 \sum_{m=0,1,2}^{\infty} b_m \cos m\left(\theta - \frac{\pi}{2} - \omega t\right) \qquad (1)$$

relative to the stator.

Similarly, with θ measured from the coil axis, the distribution of armature turns is expressed by:

$$\frac{4}{\pi}\sum_{n\ \mathrm{odd}}^{\infty} \frac{1}{n} \sin\frac{n\pi}{2} \cdot \cos n\theta$$ per turn, being a unit rectangular full-pitch pattern.

If the armature current reaches its peak value at time $t = (\delta/\omega)$, the m.m.f. due to armature reaction (F_a) is expressed by:

$$\frac{4N_aI_a}{\pi}\sum_{n\ \mathrm{odd}}^{\infty} \frac{1}{n} \sin\frac{n\pi}{2} \cos n\theta \cos(\omega t-\delta) \qquad (2)$$

where,

N_a = effective armature turns in series per phase;

I_a = peak fundamental armature current;

F_a may be thought of in one of two ways;

(1) A pulsating rectangular pattern, stationary relative to the stator varying in magnitude with time.

(2) The combination of contra-rotating space harmonics i.e. terms in $(n\theta \pm \omega t)$. Each harmonic is constant in magnitude (equal to half the peak value of the corresponding harmonic component for the 'pulsating' representation) travelling at $\frac{1}{n}$ th synchronous speed.

Note that all the forward rotating harmonics, except the fundamental, are moving backwards relative to the rotor. The (2n+1) harmonic moving forward with respect to the stator at $n_s/(2n+1)$ is moving backward at $n_s(2n/2n+1)$ w.r.t. the rotor. This, combined with its (2n+1) pole pairs induces a rotor frequency of $2nf_1$. Similarly, the (2n+1) harmonic moving backwards with respect to the stator at $n_s/(2n+1)$ is moving backward at $n_s(2n+2)/(2n+1)$ with respect to the rotor and induces a frequency of $(2n+2)f_1$. All the stator odd harmonics (except the forward fundamental) tend to produce even harmonics in the rotor and their waves are moving backwards w.r.t. the rotor. We shall see (8.1.1.) that this is further complicated by the interaction of these waves with the rotor permeance.

2.3 Armature reaction flux density distribution in terms of the open-circuit flux density distribution

When an m.m.f. F_α is applied to the airgap of a rotating electrical machine, the distribution of the resulting flux density may be

expressed as B_α. Both F_α and B_α may be functions of (θ, t) where t is time and peripheral airgap distance is measured by θ. A second m.m.f. F_β will produce a flux density wave B_β. F_α and F_β may have different magnitudes and time-dependence but providing they have identical space distributions acting on the same permeance:

$$\frac{F_\alpha}{F_\beta} = \frac{B_\alpha}{B_\beta}$$

Thus, if B_{oc} results from F_f and B_a from F_a, then from section 2.2 equation (1) and (2)

$$B_a = \frac{F_a}{F_f} \cdot B_{oc} \quad \ldots\ldots\ldots\ldots\ldots\ldots\ldots\ldots\ldots\ldots\ldots\ldots (3)$$

$$= \frac{4N_aI_aB_1}{\pi F_f}\sum_{\substack{m=0,1,2\ldots \\ n=\mathrm{odd}}}^{\infty} \frac{b_m}{n} \sin\frac{n\pi}{2} \cos n\theta \cos \omega t-\delta \cos m\left(\theta-\frac{\pi}{2}-\omega t\right) \quad \ldots\ldots (4)$$

The complete airgap flux density distribution is expressed by: $B_{oc}\left[1+\frac{F_a}{F_f}\right]$ —(5)

This makes the normal assumptions of linearity and superposition.

2.4 Justification for equation (3) applied to several armature coils

F_a is constant at any instant in time across an armature coil pitch (Fig. 2). The rectangular representation (section 3.2) assumes an instantaneous change in the sense of F_a at slot centre lines, which if applied rigorously, leads to incompatible field boundaries for consecutive coil pitches. Fortunately, the real distribution of $F_a x \Lambda$ at the stator airgap surface more closely resembles a trapezoid since the armature slot openings interrupt the field, allowing the transition from peak values under one coil to the opposite peak values to occupy a finite time, as distinct from occurring instantaneously.

A trapezoidal distribution of F_a allows equation (3) to be applied to several armature coil pitches since no boundary incompatabilities exist.

The terms providing the 'instantaneous change of sense' in the rectangular series are small and of very high harmonic order. In any quantitative work using the series they would probably be neglected. The time field pattern in the slot opening region is not completely described by the theory, however, due to the low density of this region (itself the result of the slot opening permeance) any discrepancies are small.

2.5 Expression for rotor tooth flux distribution

Equation (4) represents the complete flux density pattern due to armature reaction. To select the terms which describe the density distribution relative to the rotor will require two operations.

1) Select terms in $n(\theta - \omega t)$ only.
2) Remove from this expression all 'ωt' components. This refers the expression to the rotor, giving the space distribution relative to the rotor.

Section 8.2 expands equation (4), and gives the forward rotating fundamental component of the flux density distribution across the rotor tooth surface due to armature reaction:

$$\frac{N_a I_a B_1}{\pi F_f} \left\{ 2b_o \cos(\theta + \delta) - b_2 \cos(\theta - \delta) \right\}$$

To obtain the complete distribution this must be superimposed on the fundamental of the B_{oc} wave relative to the rotor: $B_1 \sin\theta$

i.e.
$$B_1 \left[\sin\theta + \frac{N_a I_a}{\pi F_f} \left\{ 2b_o \cos(\theta + \delta) - b_2 \cos(\theta - \delta) \right\} \right]$$

2.6 The computer programme

The selected components of section 2.5 from equation (4) superimposed on the open-circuit wave are given to the 10th harmonic in section 8.3. Using these, the distribution was computed for a range of δ.

Values of b_m for $m = 0 \rightarrow 11$ were obtained by Fourier analysis of the open-circuit wave, which in turn was derived from flux plots.

The value of the ratio of armature and field m.m.f. ($C = \frac{F_a}{\pi F_f}$) only affects the B_a distribution, so the print-out was arranged to supply both open-circuit and armature reaction components before combining them. The armature reaction component could thus be scaled to suit any value of C and curves derived without the need to compute every condition of load and field. Thus the computed figures for one value of C become a 'standard' set. Each point for the standard set was plotted against δ. This allowed any value of δ to be used rather than only the discrete values covered by the computed range. Therefore from the 'standard' figures the distribution of flux density across a rotor tooth surface may be plotted for any value of C and δ. These points will be in p.u. with B_1 as base. With the knowledge of B_1/I_f from tests or calculations, the distributions may be plotted directly in Wb/m^2.

Fig. 6. shows examples of distributions plotted in this manner.

2.7 Derivation of values for δ

In section 2.2, δ/ω was defined as the time at which the armature current reached its peak value. At time $t = 0$ the rotor position was chosen such that the voltage induced by ϕ_{oc} was at its peak value. Hence the angle δ describes the phase shift by which the armature current lags or leads the open-circuit voltage for the chosen field conditions.

Thus δ is dependent on the power factor and the load angle associated with the load. By reference to Fig. 4, with the assumption that the vector difference between open-circuit volts and terminal volts lies perpendicular to a vector describing the armature current, a simple technique for discovering the value of δ at any load is obtained.

$$\cos\delta = \frac{V_T \cos\phi}{V_f}$$

where:

V_T = terminal volts for field F_f

ϕ = power factor

V_f = open-circuit volts for field F_f

3. Measurements

3.1 The Experimental Machine

Measurements to confirm the theory were taken on a specially built scale model of an industrial machine. This machine has been described in some detail in a previous paper.[1]

To investigate the rotor tooth surface flux distribution, search conductors of 0.18 m.m. (.007") diameter wire were set in shallow slots 0.25 m.m. (.01") wide and 0.18 m.m. (.007") deep, Fig. 5(a). At one end of the rotor core all the search conductors were connected to a common strip, while the other ends were led out to a slipring assembly mounted on a shaft extension. Thus any two search conductors could be combined to sense the flux linking various areas of the rotor tooth surface.

3.2 Search coil outputs: Comparison of stationary and rotating tests

Ideally, the rotor flux distribution would be measured with an array of devices reading flux density directly e.g. Hall crystals. This is not practical in a small high speed machine, therefore an indirect way of measuring B has to be found.

Taking the conductors in adjacent pairs to form seven search coils, each coil was calibrated using a flux meter during a stationary test.

Use was made of the heteropolar nature of this machine to compare rotating and stationary tests. A rotor search coil experiences a reversal of field under successive poles during rotation. Integration of the search coil signals when displayed, Fig. 6(a), clearly shows the alternate sense of the flux under consecutive poles. Fig. 6(b), the integration of signals from a coil which is small in comparison with the armature slot opening, shows the fluxes associated with individual stator teeth. The depression in the peak region as the rotor coil passes each stator tooth is associated with the change in overall permeance due to a rotor tooth passing across a stator slot opening.

Measurements of these displays from peak to peak for field current I_f are calibrated against readings of flux during a stationary test for a reversal of field current from $+I_f$ to $-I_f$. This calibration was linear over the range of I_f. Each coil, however, required a correction for area; this came from the gradient of the airgap line. Assuming the airgap to be uniform and working at flux densities such that the distribution across the rotor tooth was uniform, the gradient of flux plotted against field current is proportional to the area of each coil. Thus each coil could be corrected to one seventh of the total tooth surface area. Peak to peak measurements of the integrated signals during rotating tests also led to correction factors. The integrating and measuring circuit is shown in Fig. 7. The d.c. voltage required to bias the display across the oscilloscope graticule is measured by a digital voltmeter. Using the oscilloscope amplifiers to magnify the display and a three decimal place digital voltmeter enabled considerable accuracy to be achieved in these measurements.

Table 1 shows the correction factors obtained from each method. The second places of the stationary factors are due to readings of parts of a division on the flux meter scale whilst the digital voltmeter reading has been rounded to two decimal places.

Table 1: Area Correction for rotor surface coils from Stationary and Rotating tests.

	5-6	6-7	7-8	8-9	9-10	10-11	11-12
Stationary (fluxmeter)	.88	1.09	.97	1.0	.97	.98	.89
Rotating (peak to peak)	.88	1.02	.98	1.00	1.00	.98	.89

The similarity between these test results is taken as further proof of the accurate response of the integrating circuit to the search coil signal.

As a further comparison between stationary and rotating conditions, the signal from search coil (4-5) Fig. 5(b) was analysed at heteropolar frequency. This r.m.s. voltage was divided by the search coil pitch factor and the resulting fundamental-pitch-voltage led to the peak a.c. fundamental flux. This peak value was converted into the rectangular wave from which flux per tooth and thus flux per coil, during rotation, was calculated. Table 2 shows the comparison between flux measured with a flux meter during a stationary test and the calculated value of flux from the coil signal during rotation.

Table 2: Stationary (fluxmeter) and Rotating (calculated from coil signal) measurements of heteropolar flux linking coil (4-5): μWb

I_f	0.2	0.4	0.6	0.8	1.0
Heteropolar flux					
Fluxmeter	71	149	220	288	350
Calculated	73	148	219	285	336

3.3 Open-circuit flux density distribution

Whereas the analysis of the search coil signal is a more fundamental approach to meauring flux than calibrating the integrated signal, greater consistent accuracy is possible with the second technique. The search coil pitch-factor is 0.0297. Small changes in pitch factors of this size greatly affect the value of calculated flux. Wave analysers must be calibrated for the signal level since typical accuracies are not better than ± 1 db.

Hence the open-circuit flux density distributions for a range of I_f from 0.2 to 2.0 amps, given in Fig. 8, are derived from calibrated measurements. Coil (4-5) has been analysed at field currents from 0.2 to 1.0 amp. These values of flux are given as a check.

3.4 On-load flux density distributions

Fig. 9 compares the signal from a rotor search coil on open-circuit and on-load. On open-circuit, the effect of armature slot openings is symmetrical, allowing analysis of the heteropolar frequency. On load, the unequal flux density either side of an armature slot opening produces a signal whose fundamental is not solely due to the heteropolar characteristics. Thus, unfortunately, the direct approach to measuring flux, using signal volts and a harmonic analyser, is impracticable.

It is therefore necessary to examine carefully the actual nature of the flux that links a rotor search coil under load conditions and to use this knowledge to approximate to the steady load flux. There are four main components of the total flux linking a rotor search coil:-

i) The "steady" component caused by field excitation. This is constant across a d.c. pole but reverses at each pole, so that a signal of heteropolar frequency appears in the search coil.

ii) The "steady" component caused by the forward synchronous component of armature reaction. This also varies at heteropolar frequency.

(i and ii) are the required signals.

iii) Dips in the steady components which occur at the stator a.c. slot openings. These occur regularly at easily recognised intervals and can be used as timing marks to define the instantaneous position of the search coil.

iv) All the non-synchronous components of armature reaction which form harmonic poles of various wavelengths moving at different speeds with respect to the rotor search coil. The coil has a definite pitch with respect to each of the harmonics, being very short-pitched for the backward rotating fundamental. It has already been shown (2.2) that all these harmonics induce even harmonics in the rotor. Section 8.1.2 shows that these major components result from the fundamental of the armature reaction m.m.f. i.e. when n=1.

The output signal from each rotor search coil is the time rate-of-change of the total flux linking the coil from all four sources. If integrated, using an operational amplifier, and displayed on an oscilloscope, a waveform similar to Fig. 10a will be obtained. This corresponds to Fig. 9b. From this, we want to extract components i) and ii) above, taking account of the existence of iii) and iv). Fig. 10b is an enlargement of Fig. 10a during the time taken for the coil to pass from the centre line of one stator a.c. slot to the next and the instants of passing these two centre-lines can be arbitrarily defined as $t=0$ and $t=\pi/\omega$. The time at which the search coil links maximum flux, having moved across the slot opening and come fully under the influence of the stator tooth, is taken as t_1, as shown; the corresponding time when the coil leaves the same stator tooth is $(\pi/\omega - t_1)$. Similarly we can define $(\pi/2\omega \pm t_1)$ as t_1 on either side of the tooth centre line.

In Section 8.1.3, it is shown that the general term for time varying flux through a search coil, when sampled at the four points t_1; $(\pi/2\omega - t_1)$; $(\pi/2\omega + t_1)$ and $(\pi/\omega - t_1)$, sum to zero for the 2nd, 6th, 10th etc. time harmonics, which includes the most important

terms. This is an extension of the identity

$$\sin n(\theta + \alpha) + \sin n(\theta + \pi - \alpha) + \sin n(\theta + \tfrac{\pi}{2} + \alpha) + \sin n(\theta + \tfrac{\pi}{2} - \alpha) = 0$$

for $n = 2, 6, 10$ etc.

To eliminate the major terms of type iv) above, four readings were taken at the points shown on Fig. 10b and averaged. As each pole flux, indeed each tooth flux, is not identical due to manufacturing and material tolerances, the readings were taken consistently on certain teeth on certain poles; these were chosen because the measurements were found to agree closely with the average of all the peak to peak readings between all possible combinations, for selected examples.

4. Comparison of measured flux density distributions and computed curves

The average of the four 'peak to peak' readings at chosen times for each search coil is converted to flux density and corrected for coil area.

Table 3: Measured values of load current, voltage, p.f. and field current, together with derived values of δ (see 2.2). Flux density distributions at these load conditions are given in Fig. 11.

Load	Ia	Va	p.f.	I_f	δ
Resistive	104	122	1.0	1.0	45^o
Impedance	165	39	0.94	1.0	77^o
Short-Circuit	100	6	0	0.58	90^o

Armature current, voltage and watts were measured on a test set accurate at 1,000 c/s. The load was resistive; for high currents however the load resistor had to be reduced to a level where lead reactance affected the impedance presented to the machine. Knowing the open-circuit voltage at each value of field current δ was calculated using the expression of section 3.7

The computed values of equation (5) Section 2.3 (expanded in Section 8.3) for values of C and δ from Table 3, are presented in Fig. 11, the points being the values derived from measurements.

5. Conclusions

The close agreement between test and calculated flux densities under load conditions give confidence both in the assumptions involved in using the product of m.m.f. and permeance in the short airgaps of these machines and in the method employed to measure the flux density distribution under load. A companion paper is being prepared that uses these results to calculate the load excitation of this type of machine.

6. Acknowledgements

We gratefully acknowledge the help of Associated Electrical Industries Limited in manufacturing the experimental machine described in this paper.

7. References

1. DAVIES E.J., LAY R.K. : 'Stator flux distributions in Lorenz-type medium frequency inductor alternators'. Proc. IEE 1966, 113 No. 12, p. 2023

2. WALKER J.H. : 'The theory of the inductor alternator'. J.IEE 1942, 89, Pt.II, p. 227

8. Appendices

8.1 Armature reaction flux density pattern relative to the rotor

8.1.1 In Sections 3.2 and 3.3 an expression is derived (4) for the armature reaction flux density relative to the stator. Relative to the rotor, the armature turns distribution is moving backwards at synchronous speed and the open-circuit flux density pattern B_{oc} is stationary. Thus, relative to the rotor, the armature reaction flux density pattern B_a becomes:

$$\frac{4N_aI_aB_1}{\pi F_f}\sum_{\substack{m=0.1.2...\\ n=odd}}^{\infty} \frac{b_m}{n} \sin\frac{n\pi}{2} \cos m\left(\theta + \frac{\pi}{2}\right) \cos n(\theta + \omega t) \cos(\omega t \pm \delta)$$

$$= \frac{N_aI_aB_1}{\pi F_f}\sum_{\substack{m=0,1,2\cdots\\ n=odd}}^{\infty} \frac{b_m}{n} \sin\frac{n\pi}{2}\left[\begin{array}{ll} \cos\left\{(m+n)\theta + (n+1)\omega t - \frac{m\pi}{2} - \delta\right\} & A\\ +\cos\left\{(m+n)\theta + (n-1)\omega t - \frac{m\pi}{2} + \delta\right\} & B\\ +\cos\left\{(m-n)\theta - (n-1)\omega t - \frac{m\pi}{2} - \delta\right\} & C\\ +\cos\left\{(m-n)\theta - (n+1)\omega t - \frac{m\pi}{2} + \delta\right\} & D \end{array}\right]$$

Expanding each component gives Table 4.

Table 4: 'm' expressions of components A B C. and D.

	n \ m	0	1	2
A	1	$\cos(\theta + 2\omega t - \delta)$	$\cos(2\theta + 2\omega t - \frac{\pi}{2} - \delta)$	$\cos(3\theta + 2\omega t - \pi - \delta)$
	3	$\cos(3\theta + 4\omega t - \delta)$	$\cos(4\theta + 4\omega t - \frac{\pi}{2} - \delta)$	$\cos(5\theta + 4\omega t - \pi - \delta)$
	5	$\cos(5\theta + 6\omega t - \delta)$	$\cos(6\theta + 6\omega t - \frac{\pi}{2} - \delta)$	$\cos(7\theta + 6\omega t - \pi - \delta)$
B	1	$\cos(\theta + \delta)$	$\cos(2\theta + \ - \frac{\pi}{2} + \delta)$	$\cos(3\theta - \pi + \delta)$
	3	$\cos(3\theta + 2\omega t + \delta)$	$\cos(4\theta + 2\omega t - \frac{\pi}{2} + \delta)$	$\cos(5\theta + 2\omega t - \pi + \delta)$
	5	$\cos(5\theta + 4\omega t + \delta)$	$\cos(6\theta + 4\omega t - \frac{\pi}{2} + \delta)$	$\cos(7\theta + 4\omega t - \pi + \delta)$
C	1	$\cos(\theta + \delta)$	$\cos(\ . \ \frac{\pi}{2} + \delta)$	$\cos(\theta - \pi - \delta)$
	3	$\cos(3\theta + 2\omega t + \delta)$	$\cos(2\theta + 2\omega t + \frac{\pi}{2} + \delta)$	$\cos(\theta + 2\omega t + \pi + \delta)$
	5	$\cos(5\theta + 4\omega t + \delta)$	$\cos(4\theta + 4\omega t + \frac{\pi}{2} + \delta)$	$\cos(3\theta + 4\omega t + \pi + \delta)$
D	1	$\cos(\theta + 2\omega t - \delta)$	$\cos(\ 2\omega t + \frac{\pi}{2} - \delta)$	$\cos(\theta - 2\omega t - \pi + \delta)$
	3	$\cos(3\theta + 4\omega t - \delta)$	$\cos(2\theta + 4\omega t + \frac{\pi}{2} - \delta)$	$\cos(\theta + 4\omega t + \pi - \delta)$
	5	$\cos(5\theta + 6\omega t - \delta)$	$\cos(4\theta + 6\omega t + \frac{\pi}{2} - \delta)$	$\cos(3\theta + 6\omega t + \pi - \delta)$

Terms with no 'ωt' component are those describing the constant (in time) distribution across the rotor tooth.

Terms with no 'θ' component are constant in space across rotor tooth but have magnitudes dependent on time.

All other combinations describe patterns moving relative to the rotor

tooth, either forward or backward.

Each term is subject to the factor $\left\{\frac{b_m}{n} \sin\frac{n\pi}{2}\right\}$. Each component of armature reaction flux density in Table 4 may be integrated w.r.t. θ to provide corresponding expressions for flux (linking the area defined by the limits of integration) varying in time.

8.1.2 When integrating w.r.t. θ, the factor qualifying each component of Table 4 must be divided by the relevant coefficient of θ. Table 5 shows the relative magnitudes and speeds (on a 1. p.u. base of synchronous speed) of each component for m = 0, 1 and 2 and n = 1, 3 and 5.

Table 5: Relative magnitudes and speeds (synchronous speed = 1. p.u., forward direction positive) for 'm, n' expressions of components A B C and D., when integrated w.r.t. θ, i.e. $\propto$ flux.

	m:	0		1		2	
	n	Magnitude K	Speed ($\times n_s$)	Magnitude K	Speed ($\times n_s$)	Magnitude K	Speed ($\times n_s$)
A	1	$\underline{.71}$	$\underline{-2}$	$\underline{.50}$	$\underline{-1}$	$\underline{.13}$	$\underline{-2/3}$
	3	.08	-4/3	.08	-1	.03	-4/5
	5	.03	-6/5	.03	-1	.01	-6/7
B	1	.71	0	.50	0	.13	0
	3	.08	-2/3	.08	-1/2	.03	-2/5
	5	.03	-4/5	.03	-2/3	.01	-4/7
C	1	.71	0	1.0	0*	.39	0
	3	.08	-2/3	$\underline{.16}$	$\underline{-1}$	$\underline{.13}$	$\underline{-2}$
	5	.03	-4/5	.05	-1	.02	-4/3
D	1	$\underline{.71}$	$\underline{-2}$	1.0	0+	$\underline{.39}$	$\underline{+2}$
	3	.08	-4/3	$\underline{.16}$	$\underline{-2}$	$\underline{.13}$	$\underline{-4}$
	5	.03	-6/5	.05	-3/2	.02	-2

K = magnitude $\frac{b_m}{n(m\pm n)}$ for $b_0 = .71$, $b_1 = 1.0$, $b_2 = .39$

* component C11 has no space nor time variation.

+ component D11 is constant in space but varies with time.

Table 5 shows those terms moving synchronously with the rotor to be: B01, B11, B21, C01 and C21. These combine to form the flux distribution travelling with the rotor which will lead to the flux density distribution across a rotor tooth surface.

Neglecting components with magnitudes < 0.1, Table 5 shows the main flux distributions moving relative to the rotor to be from: A 01, A 11, A 21, C 13, C 23, D 01, D 21, D 13 and D 23, as underlined. In detail these are:

a) backward at 4 x synchronous speed:

$0.13 \sin (\theta + 4\omega t - \delta)$	D 23

b) backward at 2 x synchronous speed:

$1.42 \sin (\theta + 2\omega t - \delta)$	A 01 and D 01
$0.13 \sin (\theta + 2\omega t + \delta)$	C 23
$-0.16 \cos (2\theta + 4\omega t - \delta)$	D 13

c) backward at 1 x synchronous speed:

$-0.5 \cos (2\theta + 2\omega t - \delta)$	A 11
$-0.16 \cos (2\theta + 2\omega t + \delta)$	C 13

d) backward at 2/3 x synchronous speed:

$-0.13 \sin (3\theta + 2\omega t - \delta)$	A 21

e) forward at 2 x synchronous speed:

$-0.39 \sin (\theta - 2\omega t + \delta)$	D 21

Thus, the major contribution to the distributions moving relative to the rotor come from components A and D for $m = 0$ and $n = 1$. This contribution is fundamental in space moving at twice synchronous speed backward.

Components B and C for $m = 0$ and $n = 1$ are the major contributions to the distribution travelling synchronously with the rotor. These two patterns represent the fundamental contra-rotating components of the pulsating armature reaction flux.

8.1.3 Verification of sampling technique used in section 3.4

Integrating the armature reaction flux density distribution provides an expression for the flux, as a function of time, linking a general surface coil with sides at $\theta = \alpha$ and $\theta = \beta$

$$\phi'_a(t)_{\alpha\beta} = \frac{\ell d}{2\pi}\int_{\beta}^{\alpha} B'_a \, d\theta$$

For component A of the expression for B'_a (Section 8.1.1) the flux is:

$$\frac{\ell d}{2\pi} \sum_{\substack{m = 0.1.2.. \\ n = odd}}^{\infty} \frac{b_m}{n(m+n)} \sin\frac{n\pi}{2} \{ P \sin (n+1)\omega t + Q \cos (n+1)\omega t \} \quad (6)$$

where $P = \cos \{(m+n)\alpha - \frac{m\pi}{2} - \delta\} - \cos \{(m+n)\beta - \frac{m\pi}{2} - \delta\}$

$Q = \sin \{(m+n)\alpha - \frac{m\pi}{2} - \delta\} - \sin \{(m+n)\beta - \frac{m\pi}{2} - \delta\}$

Considering the time dependent terms in (6);

at time $t = t_1$: $P \sin (n+1)\omega t_1 + Q \cos (n+1)\omega t_1$

at $t = \left(\frac{\pi}{2\omega} - t_1\right)$	$P \sin (n+1)\omega t_1 - Q \cos (n+1)\omega t_1$	$n=1$ and 5
$t = \left(\frac{\pi}{2\omega} + t_1\right)$	$-P \sin (n+1)\omega t_1 + Q \cos (n+1)\omega t_1$	$n=1$ and 5
$t = \left(\frac{\pi}{2\omega} - t_1\right)$	$-P \sin (n+1)\omega t_1 - Q \cos (n+1)\omega t_1$	

Thus the sum of four measurements of flux taken at $t = t_1, \left(\frac{\pi}{2\omega} - t_1\right), \left(\frac{\pi}{2\omega} + t_1\right)$ and $\left(\frac{\pi}{\omega} - t_1\right)$ will be zero for component A when $n=1, 5, 9$ etc.

Similarly component D of the expression for B'_a leads to flux linking the general area between $\theta = \alpha$ and $\theta = \beta$:

$$\frac{\ell d}{2\pi} \sum_{\substack{m=0.1.2.. \\ n=odd}}^{\infty} \frac{b_m}{n(m-n)} \sin\frac{n\pi}{2} \left\{ R \sin (n+1)\omega t + S \cos (n+1)\omega t \right\}$$

where $R = \cos \{(m-n)\beta - \frac{m\pi}{2} + \delta\} - \cos \{(m-n)\alpha - \frac{m\pi}{2} + \delta\}$

$S = \sin \{(m-n)\alpha - \frac{m\pi}{2} + \delta\} - \sin \{(m-n)\beta - \frac{m\pi}{2} + \delta\}$

Hence the same conditions apply to flux resulting from component D. For $n = 1, 5, 9$ etc., the sum of four measurements at the above times is zero.

8.2 Expansion and selection of terms from equation (4) (Section 2.5)

$$B_a = \frac{N_a I_a B_1}{\pi F_f} \sum_{\substack{m=0.1.2.. \\ n=odd}}^{\infty} \frac{b_m}{n} \sin\frac{n\pi}{2} \begin{bmatrix} \cos\{(n+m)\theta - (m-1)\omega t - \frac{m\pi}{2} - \delta\} \\ +\cos\{(n+m)\theta - (m+1)\omega t - \frac{m\pi}{2} + \delta\} \\ +\cos\{(m-n)\theta - (m-1)\omega t - \frac{m\pi}{2} - \delta\} \\ +\cos\{(m-n)\theta - (m+1)\omega t - \frac{m\pi}{2} + \delta\} \end{bmatrix}$$

For $m = 0$ and $n = 1$ $\quad B_a = \frac{N_a I_a B_1}{\pi F_f} \{ 2b_0 \cos (\theta - \omega t + \delta) \}$

For $m = 2$ and $n = 1$ $\quad B_a = \frac{N_a I_a B_1}{\pi F_f} \{ -b_2 \cos (\theta - \omega t - \delta) \}$

These are the only terms in $(\theta - \omega t)$ which are available, i.e. the forward rotating fundamental space components. To relate these stator terms to the rotor, the 'ωt' components are removed leaving

$$\frac{N_a I_a B_1}{\pi F_f} \{ 2b_0 \cos (\theta + \delta) - b_2 \cos (\theta - \delta) \}$$

(These terms may also be found relative to the rotor in section 8.1 as (B01 + C01) and (C21)).

8.3 <u>Components of the complete space distribution of airgap flux density on load relative to the rotor.</u>

Each component is p.u., where $B_1 = 1$ (section 2.2) and the term $\left(\frac{N_a I_a}{\pi F_f}\right)$ is represented by C.

Term	(B_{oc})	(B_a)
Steady	bo	$- C \sin \delta$
Fundamental	$\sin\theta$	$+ 2Cb_0 \cos(\theta + \delta) - Cb_2 \cos(\theta - \delta)$
2nd	$-b_2 \cos 2\theta$	$+ C \sin(2\theta + \delta) - Cb_3 \sin(2\theta - \delta)$
3rd	$-b_3 \sin 3\theta$	$- Cb_2 \cos(3\theta + \delta) + Cb_4 \cos(3\theta - \delta)$
4th	$b_4 \cos 4\theta$	$- Cb_3 \sin(4\theta + \delta) + Cb_5 \sin(4\theta - \delta)$
5th	$b_5 \sin 5\theta$	$+ Cb_4 \cos(5\theta + \delta) - Cb_6 \cos(5\theta - \delta)$
6th	$-b_6 \cos 6\theta$	$+ Cb_5 \sin(6\theta + \delta) - Cb_7 \sin(6\theta - \delta)$
7th	$-b_7 \sin 7\theta$	$- Cb_6 \cos(7\theta + \delta) + Cb_8 \cos(7\theta - \delta)$
8th	$b_8 \cos 8\theta$	$- Cb_7 \sin(8\theta + \delta) + Cb_9 \sin(8\theta - \delta)$
9th	$b_9 \sin 9\theta$	$+ Cb_8 \cos(9\theta + \delta) - Cb_{10} \cos(9\theta - \delta)$
10th	$-b_{10} \cos 10\theta$	$+ Cb_9 \sin(10\theta + \delta) - Cb_{11} \sin(10\theta - \delta)$

FIG 1

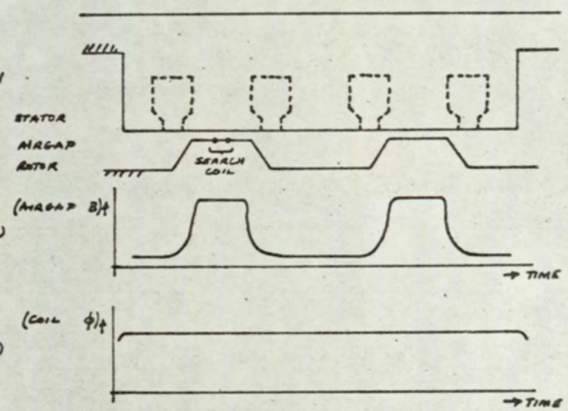

FIG 2

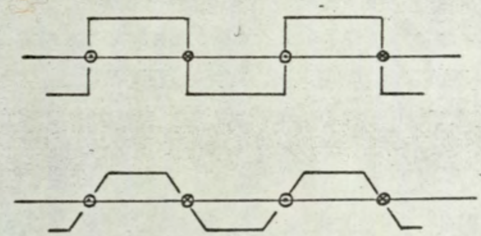

FIG 3

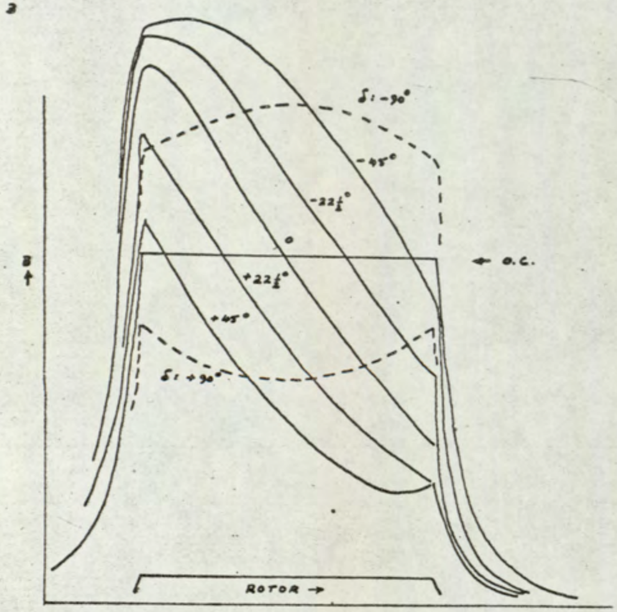

I_a AND I_f CONSTANT EXCEPT FOR $\delta = \pm 90°$ WHEN I_a IS REDUCED TO HALF VALUE.

FIG 4

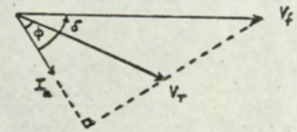

FIG 5

(a)

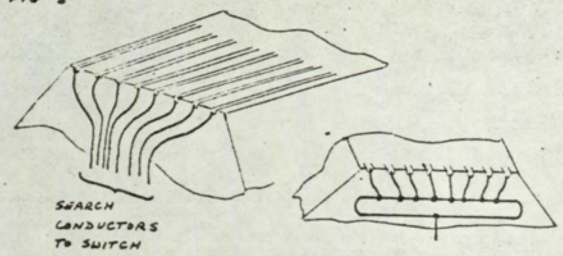

(b)

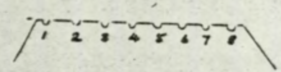

FIG 7

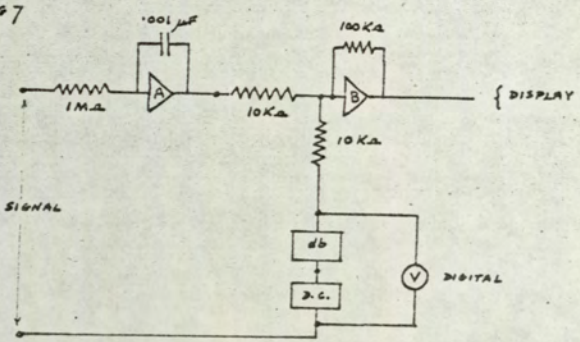

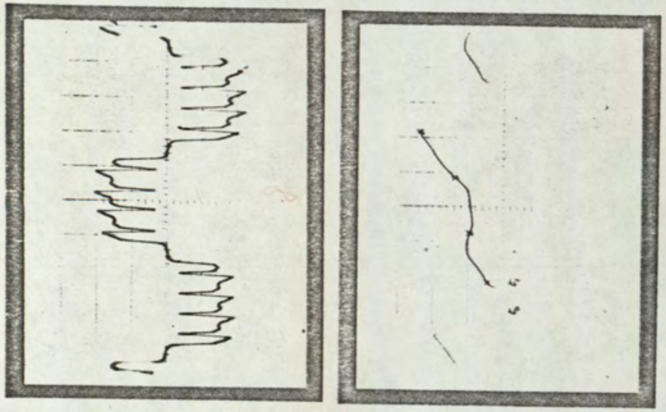

10 (a) 10 (b)

FIG 10

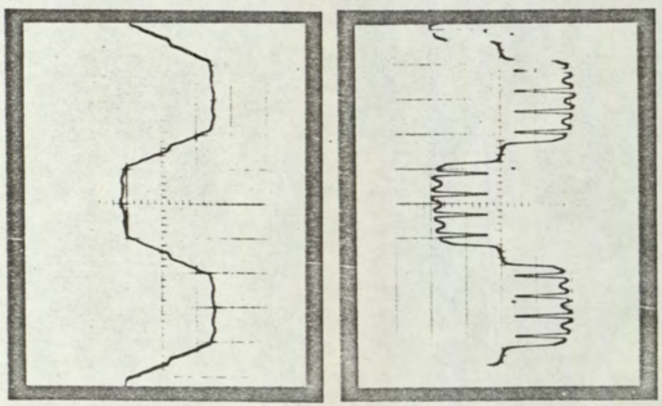

6(a) 6(b)

FIG 6

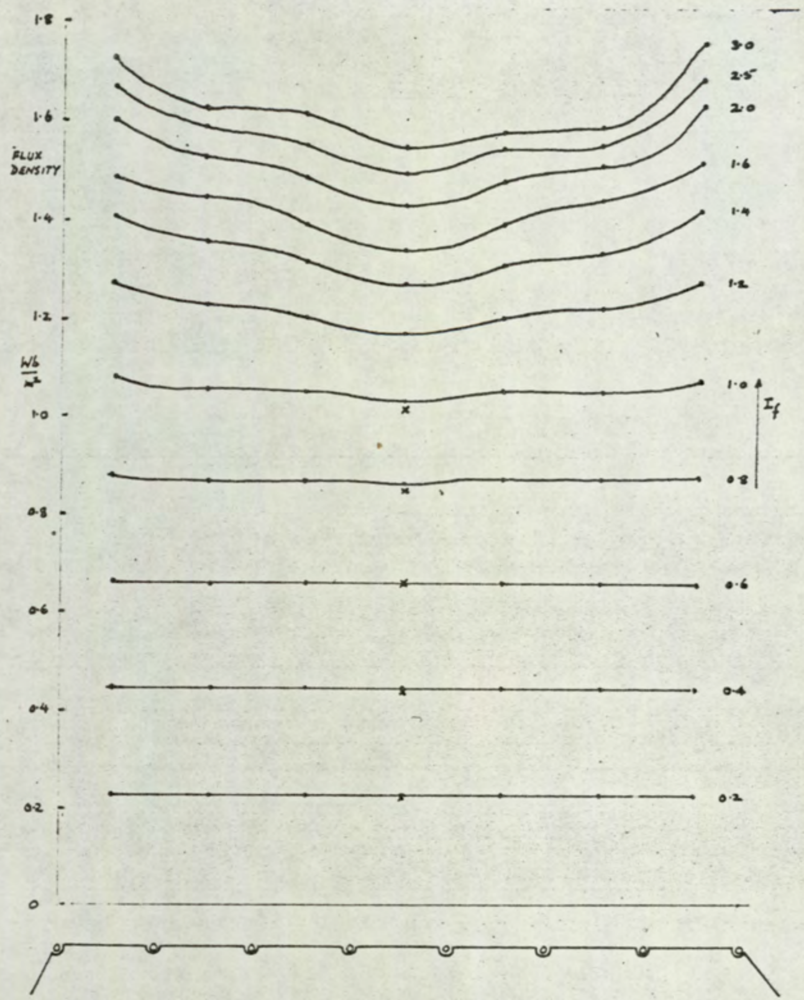

FIG 8

—•— MEASURED   x CALCULATED

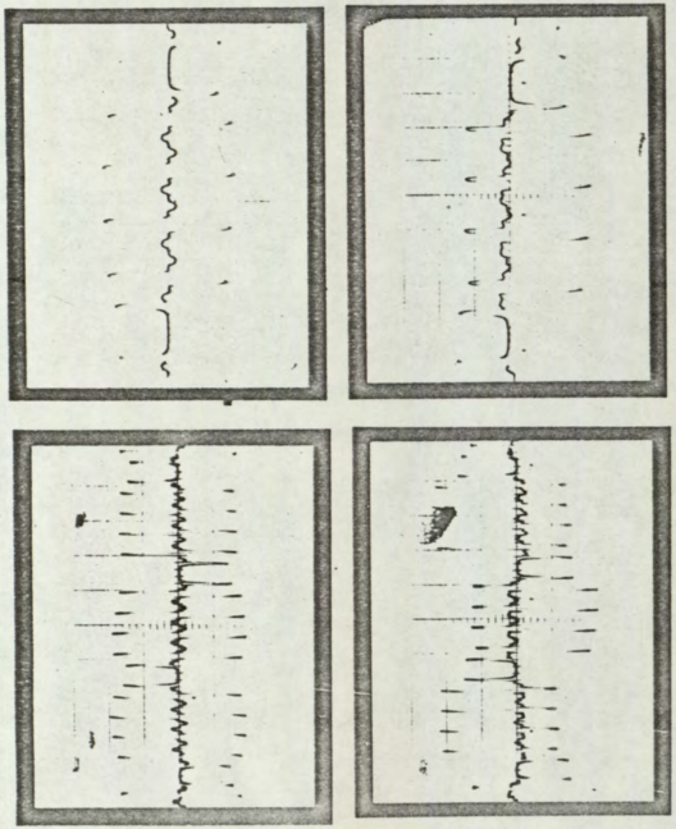
(a)
(b)

FIG 9

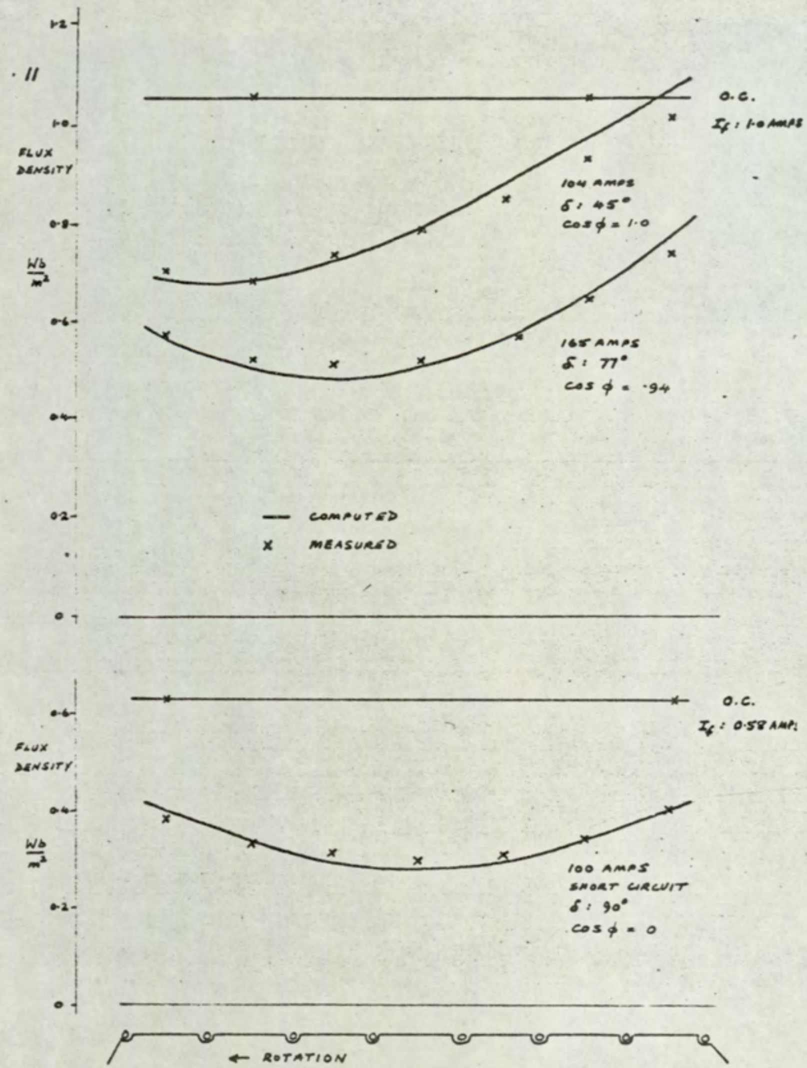
FLUX DENSITY
Wb/m²
1·2
1·0
0·8
0·6
0·4
0·2
0
O.C.
I_f : 1·0 AMPS
104 AMPS
δ : 45°
cos φ = 1·0
165 AMPS
δ : 77°
cos φ = ·94
COMPUTED
X MEASURED
O.C.
I_f : 0·58 AMP.
100 AMPS
SHORT CIRCUIT
δ : 90°
cos φ = 0
← ROTATION

FIG 11

CONTENTS:

Superscript numbers in brackets refer to diagrams.

THE HISTORY AND CHANGING FORTUNES OF THE INDUCTOR ALTERNATOR

By

R.K. LAY

Summary:

The Inductor Alternator has some unusual properties. This paper is a record of the manner in which electrical engineering has advanced on widely differing fronts with the help of this machine. The range of frequencies involved has been from 40c/s to 100,000c/s. The range of power has been from less than a kilowatt to more than a megawatt.

First the milestones in the development of generating machinery are given. These set the stage for the introduction of an alternator which enjoyed a remarkably speedy rise to popularity. The subsequent history, however, is one of widely changing fortunes. As soon as new techniques undermine the Inductor Alternator's superiority in one application, it is to be found at the development stage in a completely different field.

The subject of one rather special type of alternator is a restricted one. However, as an example of flexibility in design and application, this history is felt to be of wide significance.

1 History and Heredity

The inductor alternator, as a type, evolved in the late 1880s. This species of alternator enjoyed rapid recognition and, to quote Professor Sylvanus P. Thompson, "seemed likely in the nineties to supersede all other kinds".

Certain properties of design and behaviour set these alternators apart from machines in general. To understand the motives leading to their introduction, it is necessary to recount the major developments in generating machinery.

Faraday first published the findings of his famous experiments of 1831 by letter to a French journal. Before the year was over an Italian, Pixii, who was Ampere's instrument maker, had developed what may be called the first dynamo. It is important to note that the experimenters of the day, who were battery or cell orientated, had no use for periodic currents. Consequently Pixii's multi-turn iron cored bobbin was designed to supply direct current through a pivoted switch operated by the shaft carrying the magnet. In the following year, 1832, Ampere suggested the switch be replaced by a split cylindrical contact carried on the shaft. Thus the commutator was born. However Ampere firmly places the credit on Pixii for realising Faraday's findings in "Machine" form.

The first claim to multipolar construction was by Emil Stohrer of Leipzig. Three horseshoe magnets were grouped so that six bobbins rotated past the pole pieces. By switching the spring metal brushes to bear upon one of three commutators, series and parallel connections of the bobbin turns offered variable voltage direct current outputs. This was in 1843.

A year later in Birmingham, probably the first commercial machine was designed by Woolrich for the Elkington works. Plating by electrolytic deposition had been discovered by Jacoby in 1838. Woorich's machine rotated bobbins between the pole pieces of horseshoe magnets and a compound commutator similar to Stohrer's enable one, two, three or four plating baths to be supplied.

By 1857 Professor F. H. Holmes was trying to arouse interest in the use of alternating current for a.c. arc lamps in lighthouses. His design is the first to resemble present day machines since the bobbins were mounted on the shaft with their axes radial. Two sliprings led out the single phase alternating current. Eventually Professor Holmes took his

ideas to France where the Compagnie de L'Alliance manufactured several successful lighthouse generating sets.

The next real contribution came from Pancinotti in 1860. His ring armature was a great improvement upon the previous bobbin or shuttle windings. Pancinotti's papers make it plain that he was aware that the distributed armature could be both motor and generator. However the concept was not fully accepted until the Belgian, Gramme, reintroduced the idea ten years later.

The merits of a.c. over d.c. for arc lamps was marginal until Jablochkoff introduced his famous 'candles' in 1876. These were much smaller and more efficient, really turning the experiments in public lighting systems into commercial propositions. In 1878 there were several hundred Gramme machines in service, the latest type supplying alternating current, which was found more suitable for the Jablochkoff candles. In that year London (some three years behind Paris) saw its first electric illuminations. The Gaiety Theatre was lit by six Lontin lamps, Billingsgate Fish Market, the Holborn Viaduct and the Thames embankment between Waterloo and Westminster bridges, soon followed.

This skeleton history shows the situation at the beginning of the 1880s. The generation of electrical power had emerged from the laboratories and shed its experimental status. It is true that plating can claim an earlier commercial success; however, the universal interest in electric lighting really forced the art into maturity. The demand was for a machine both economic to manufacture and operate.

The sequence of discoveries and developments had evolved a technique for inducing voltages in coils by changing the linking flux in direction and magnitude. This is clearly traced from the inevitable use of permanent magnets with North and South pole pieces. Stohrer's multipolar machine set the fashion for increased numbers of "pairs of poles". Since the induction of electromotive-forces depends upon the rate at which linking magnetic flux is changing (not necessarily on a change in flux direction) it is possible to design field magnet systems in which the flux linking any given part of the armature simply alters its magnitude.

A magnet system which presents similar poles to its armature is known as homopolar as distinct from the alternate pole system of a heteropolar field. The substitution of such a magnet in alternators is due to Mordey.

The Mordey homopolar field alternator employed the advantage that only one exciting coil is required to establish the field system. (SLIDE 1) A stationary thin disc armature containing no iron was positioned in the axial airgap between the pole pieces of the branches of the single magnetic circuit.[1]

This design enabled the supply to the field system to be simplified. Indeed there is no reason that the field coil need rotate, although for mechanical reasons it was considered preferable to wind it actually on the magnet core.

The homopolar magnet was ideally suited to the available casting techniques. It was simple and robust. Maintenance to the armature was easy.. This was a machine both cheap to operate and manufacture, and a contribution to the evolution of power generating equipment in its own right. However for the purposes of this paper its greatest significance lies in the fact that it led naturally to the development of the inductor alternator.

2 THE INDUCTOR ALTERNATOR AND THE SUPPLY INDUSTRY

This type of machine is characterised by having no moving conductors. The only moving parts are iron. These are arranged so as to set up variations of magnetic flux.

Professor Thompson suggests that "several early workers" had put forward the concept and that he revived the idea in a patent in 1883 which eventually led to a design by Kingdon[2], reported in 1888. (SLIDE 2)

However, the first name of commercial significance appears to be that of Mordey. In 1886 he introduced the homopolar type of Inductor Alternator. (SLIDE 3) In 1888 he patented the "Mordey Inductor Alternator"[4] (SLIDE 4) which the Brush Electrical Engineering Company successfully manufactured for a decade. (SLIDE 5)

It would seem that the rugged simplicity of this design, coupled with its ability to meet the demands for greater outputs, formed the basis for its wide acceptance. Acceptance, that is, amongst converts to the concept of central stations generating a.c. A bitter battle was joined between the alternator designers, Mordey, Ferranti and Gordon, and the equally outstanding names of Crompton, Hopkinson and Kennedy, supporters of the continuous current system.

The main advantage of the a.c. system, that of transmission, was not realised because of the parochial 1882 Electric Lighting Act. This presumed that each small district would naturally be served best by its own power station. Continuous currents at a suitable voltage could be sent over the mile or so involved without undue loss. The use of standby batteries for periods of light load made the continuous current stations more reliable and economic. Any failure at an a.c. station was liable to cause a sudden and total extinction of all the consumers' lamps. Such accidents were far from uncommon. Alternating current was no better for incandescent lighting and could not be used for driving motors, since no single phase motors were yet suitable.

If the business of electricity supply had been destined to continue in the limited manner originally adopted, there is little doubt that continuous current systems would have prevailed.

The expansion of a.c. power station outputs was held up for some years by the early difficulties of paralleling two or more machines. Ironically it had been Hopkinson (who favoured d.c.) who had shown that parallel working was theoretically possible in 1884. By 1887 parallel running was a matter of routine in the United States, incoming machines being brought in by a lamp.

However, no less a prophet of a.c. supremacy than J.E.H. Gordon commented in 1888 upon the "three or four minutes jumping in the big machines .... taking a month's life off 20,000 lamps .... the practice being, to say the least, inadvisable".

In many cases, the real problem was the uneven torque of the prime movers, although Thompson reports the e.m.f. waves of some alternators as having not the slightest resemblance to a sine curve!

In 1891, Mordey arranged a demonstration at which two of his alternators were paralleled by means of a transformer and lamp with perfect success. One set was then caused to drive the other as a motor, which still did not impress one stubborn critic. This prominent engineer claimed that the tests were not conclusive because the machines could be pulled out of step when paralleled through a resistance capable of absorbing half their combined output!

By 1894 parallel running was common. This year also marked the height of the battle. In greater London, 373,000 lamps were served by continuous current, while 320,000 were served by a.c. Professor Thompson, also in 1894, read a paper in which he drew attention to the recently invented Scott system of 2/3 phase transformer connections. The increase in demand and the advance in transformer technology began to make the advantages of a.c. transmission too obvious to be denied. The introduction of polyphase motors and generators further added to the desirability of a.c. supplies. With E.H.T. d.c. coming to the fore, it is interesting to note Lord Rayleigh's prophecy that direct current would have its revenge in the final encounter.

Mordey and Ferranti alternators had no iron in their armatures. They were termed "copper type" as distinct from Gordon's "iron type". Remembering the difficulties Gordon reported on paralleling, and the comparative successes of Mordey, a reason may be discovered for the apparent lack of successful British "iron type" designs. Continental companies were prolific in "iron type" machines, notable Oerlikon,[5] Kloben,[6] Allgemeine[7] and Ganz. These were both single and three phase, homopolar and heteropolar in construction. (SLIDES 6, 7, 8, 9)

Throughout the '90s the steam turbine had steadily established its claim to be the most satisfactory prime mover. The inductor type of construction seemed at first to offer special advantages for turbine work. In 1901 Oerlikon designed a 4-pole 3-phase 1,000kv machine. However, the simplicity of slow speed inductor rotors was lost at turbine speeds. Ventilation and balancing problems became excessive. By 1907 all thought of using Inductor Alternators had been given up, primarily because of the disproportionate amount of material involved.

"These were years," to quote R. H. Parsons, "When every enterprise was largely of a pioneering nature". The pattern of the future Supply Industry was dictated by a series of meteoric developments, not least of which was that of the Inductor Alternator.

3 THE EARLY DAYS OF WIRELESS

Between 1895 and 1899 Marconi carried out his experiments with Hertzian waves, which culminated in a cross-Channel link by radio-telegraphy in 1899. This early equipment used a spark coil as a transmitter and a Coherer as the receiver.

The next significant contribution was due to Professor Fessenden. As early as 1900 he argued the merits of transmitting a continuous wave instead of the pulses obtained from a spark transmitter. Instead therefore, of damped waves of 2×10^6 c/s, he suggested that an alternator should supply 100,000c/s directly to the aerials.

While Fessenden was specifying what would be a suitable supply, others were already beginning to investigate the potential of the inductor alternator for generating higher frequencies. The noted French engineer M. Leblanc, whilst in America, asked Mr. Westinghouse for a 10,000c/s alternator for certain experimental work. The machine was designed by B.G. Lamme in 1902, and reported to the A.I.E.E. in 1904.[3] (SLIDE 9) The alternator generated 10,000c/s at 150V, developing 2kW power when driven at 3,000 rpm. Before this machine all high frequency designs were without iron in the alternator. It was well understood that high frequency would lead to very severe losses. Lamme however, built his alternator of individually varnished laminations .003" thick, enabling this to be the first high frequency alternator with an iron core.

In 1921 the Electric Journal reporting on the state of high frequency designs, commented that little change had been made since this early machine. Other than for the introduction of new materials, this lack of change afforded "striking evidence of the clear insight into the correct principles which govern the original design". (Lamme by this time was editing the Electric Journal!) The article recalls that in 1904 a few experiments were made in forming an arc with current at this high frequency, suggesting that Leblanc may have been investigating the radiation powers of a continuous spark. The Lamme machine was a homopolar construction and may be considered as falling within the class characterised as cylindrical. Cylindrical, that is, as distinguished from disc.

C. M. Laffoon, writing in the Electric Journal three years later, lists the relative merits of the cylindrical and disc designs of inductor alternator. Laffoon quotes the Lamme machine as an example of the cylindrical rotor, and

the Alexanderson machine as an example of the disc type.[8] This latter, was the machine designed specially to Professor Fessenden's specifications for continuous supply direct to aerials and was delivered in 1906. (SLIDE 10) The undoubted superiority of the continuous supply technique was immediately evident, and for the higher frequencies, say 100,000c/s, the disc machine was the only answer.[9] (SLIDE 11)

The main disadvantage of the disc machine lay in the diameter to the bottom of a rotor slot being fixed if frequency and rpm were specified. The output could only be increased by increasing the external diameter. The nature of the disc also introduced problems of accurate positioning in the air gap and accurate allowances for any expansion or end play which might be involved. Further, the interpolar space on the inductor needed to be filled with non-magnetic material to prevent whipping, friction and noise. This was not an easy mechanical task.

Where the cylindrical design was feasible it had the following advantages. (a) The output could be increased by the simpler technique of increasing the core length and (b) the mass of the rotor, giving it high inertia, produced good speed regulation.

The problem of attaching laminations to the peripheral surface of the cylindrical rotor placed a peripheral speed limitation on this design. Thus the majority of cylindrical rotor machines were direct driven at 3,000rpm by two pole induction motors. The disc rotor however, being much lighter and homogeneous in construction, may be rotated at much higher speeds with certain precautions. For instance, Alexanderson's original machine was driven at 20,000 rpm. At such speeds, it was not practicable to use a rigid shaft on account of the vibration which would be set up by small out of balance forces. A hollow flexible shaft, which allowed the disc to revolve around its exact mass centre was therefore adopted, thus avoiding any centrifugal stresses on the bearings. The rotor and shaft were carried on two sets of bearings, the outer pair of which supported the weight of the rotating parts. The inner pair of bearings did not touch the shaft in normal operation and were bored out to give 1/64" clearance. Their function was to prevent excessive vibration of the shaft when it passed through mechanical resonances.[10] (SLIDE 12)

High frequency alternators of a similar type but having outputs up to 200kW were subsequently designed by Alexanderson, and employed in numerous high power stations in America and Europe. Thus, from around 1910 until the mid 1920's, the standard transmitter for long range high power telegraphy consisted of a high frequency inductor alternator feeding a Poulson arc.

In 1921 the Electric Journal commented that the "high frequency alternator/Poulson arc transmitters capable of 2 to 1000kW input capacity is used in a majority of the continuous wave stations of the world at the present time, although it will probably be superseded in the future by the vacuum tube oscillator". The oscillatory properties of a feed back circuit had been discovered in 1912 by Armstrong. By 1921 radio telephone transmission over short distances had been developed universally employing the so called self-heterodyne principles. Eventually the high power transoceanic stations were equipped with vacuum tube oscillators, and the inductor alternator had lost another application.

4 THE CORELESS INDUCTION FURNACE

In this application we meet the first use of h.f. alternators which continues to be of great importance. As yet no serious contenders have emerged, except perhaps, voltage triplers for low frequencies. Dr. Robiette in his book entitled "Electric melting and smelting practice" describes the introduction of the coreless furnace as ... "undoubtedly representing one of the major advances in melting practice ...". The h.f. power is delivered to a water-cooled copper coil surrounding a refractory crucible. An intense alternating magnetic field is generated within the coil causing eddy currents to be induced in the charge. These currents heat the charge and, in the case of magnetic materials, there is an additional heating effect due to hysteresis.

Early experiments with this type of furnace employed static Tesla spark-gap converters. These suffered from the disadvantage of having restricted outputs.- i.e. only small quantity furnaces were feasible. The introduction and much of the development in this field was due to Dr. Northrup in researches at Princeton University.

It was soon realised that the 10 - 20 Kc/s delivered by Tesla spark-gap converters was not necessary for industrial furnaces. Motor alternator sets producing 500 - 3000c/s, and later up to 10Kc/s were designed, and the first industrial plant at Waterbury for the American Brass Co. started in 1925. The melting of tool steel and other ferrous materials was first exploited in this country by Edgar Allen and Co. Ltd. of Sheffield about a year later.

The immediate economy and advantage was one of furnace operation. With the crucible technique, as distinct from the channel type, no stand-by charges of molten metal are required. This allows the plant to be completely shut down between melts and further, it allows greater flexibility in mixture changes.

Thus the design problems for inductor alternators in this field of application were those of increasing outputs. The solutions were those common to all rotating electrical machinery. Improvements in insulation technology allowed more copper to carry more amps in each slot. Fan and water cooling improved the methods of extracting the heat due to the losses. High frequency magnetic materials improved with the addition of silicon.

Robiette comments that ".. employing electric furnaces produced results which are not attainable by other existing processes .. notably ferro-silicon.." which is to say that the new capacity for smelting accurate mixtures of ferro-alloys, given to steel makers by the development of electric furnaces, was fed back to the alternator designers, who were then able to produce bigger and better furnace supplies.

A further problem peculiar to this application was concerned with matching the alternator characteristics to the changing power factor of an induction furnace coil on load. Because of the high internal reactance of inductor alternators, large changes in terminal voltage occur with changing load. Automatic voltage control is employed, operating on the field current of the alternator. This establishes the preference for heteropolar machines with short field time constants, rather than homopolar machines whose magnetic circuits are mainly solid iron.

The induction furnace presents a highly inductive load. The p.f. may be as low as 0.1, dependent upon frequency and lining thickness. By using capacitors to compensate for the large wattless current, the alternator size may be reduced to a tenth. Originally, capacitor costs were prohibitive. The rise in popularity of this system has been closely linked to the ability of capacitor manufacturers to reduce costs.

Change in load p.f., as seen by the alternator, occurs during the melt. A steel charge when cold presents a high p.f. As the temperature rises and the material loses its magnetism, the p.f. drops. Even for non-magnetic materials, fusion of components reduces the resistivity of the charge also causing the p.f. to deteriorate. Hence it is necessary to vary the value of the capacitors during the melt.

The technique which has been established between alternator and furnace designers allows for a series capacitor to be permanently in circuit. This is specified by the alternator designer who guarantees that the machine will deliver its rated output providing the load p.f. is kept between ± 0.9 say, with this capacitor permanently in series. The furnace designer provides the operator or control system with variable banks of capacitors in order to meet this specification under all conditions of melting.(11) (12) (SLIDES 13,14)

Alternators for 1 and 3 Kc/s tend to be designed in units of the 300Kw to 500Kw range and paralleled if necessary, or single units of between 1 and 2 MW. World production approaches 300 MW per year.

5 ELECTRONIC EQUIPMENT

Many systems of electronic equipment require stable d.c. supplies. The choice between electronic supplies and rotating machine supplies will be dictated by the nature of the particular system.

At first sight electronic supplies might be thought to have a weight advantage. This however is not usually very great because of the size of transformers for normal frequencies (50/60 c/s). Solid state devices to carry substantial currents have been prohibitively costly, thus for a time favouring rotating machines. Costs however are rapidly being reduced.

High ambient temperatures may embarrass semi-conductors somewhat more than machines. The use of refrigeration may solve this problem but will further reduce any weight advantage electronics may have offered.

Corrosive or otherwise unfriendly atmospheres may be excluded from electronics. If machines are to be used in such conditions it is desirable that they be brushless. Further advantages are to be gained, when frequencies higher than normal 50/60 c/s are considered. These requirements lead to the choice of Inductor Alternators.

High power radar systems for fighting ships and aircraft are examples of equipment supplied by Inductor Alternators. The Klystron output valve for such a system will require E.H.T. d.c., possible of the order of 50Kv. The alternator output voltage must be suitable transformed before full wave rectification and smoothing is carried out. The equipment for these operations; transformers, rectifiers and capacitors all have power/size capacities proportional to frequency. Thus the additional weight of the inductor alternator is offset by the reduction in weight of the transformers etc. With one clear advantage. The transformers must be close the the valve and aerial which will be placed, in the instance of a ship, as high as possible, thus adding to the 'superstructure' weight. The Alternator at least can be located below decks, adding to the ballast. Moving to higher frequencies then, allows a more convenient distribution of weight.

The choice of frequency is controlled by two factors:

1) Transformer iron losses being proportional to frequency, an upper limit exists from weight or heating considerations: approximately 2Kc/s.

2) Even after smoothing, ripple will exist at 6x fundamental frequency (for full wave rectification). For Doppler tracking radar the target region

of the frequency range may fall to 6Kc/s. It is necessary for there to be a safe margin between frequencies radiated due to the d.c. supply equipment and the target region, placing a second upper limit on the choice of alternator frequency.

In general the problems of design for ship duty are those of reducing overall size and yet withstanding considerable shock duties. Aircraft also demand small overall sizes and extreme lightness. The nature of aircraft operations requires designing for comparatively short but extremely arduous life expectancy.

A further field of application in electronics is that of Data Links. The accepted standard for position control servo systems is 400c/s. A homopolar machine with a permanent magnet field is widely used for supplying such systems. With voltage and frequency proportional to speed and no field supply required, this type also finds application in monitoring turbines and other large machine sets.

Alexanderson would probably have been pleased that electronics should sometimes be dependent on inductor alternators, remembering the eclipse of his designs by vacuum valves. Crompton, Hopkinson and Kennedy might not have been so happy to find inductor alternators powering d.c. supplies!

---

6 SPACE CRAFT GENERATORS

The latest and most exciting application of inductor alternators is in the field of space craft generators. Present day space flights of light unmanned loads or short durations are satisfactorily powered by fuel or solar cells. Projected programmes for comparatively permanent laboratories in space and long journeys to planets such as Mars, require much more substantial power units. Life support, propulsion, control systems, communications as well as a host of uses which have been, or will be conceived, lift the demand from kW to MW.:

Electromagnetic generators are presently the only demonstrated source, although other devices are being investigated. The problems of space environmental conditions and the high speed of available prime movers, have led to the selection of solid rotor homopolar inductor alternators.

Equivalent rated wound rotor generators may be smaller for a given speed. However solid rotor machines can be designed for much higher speeds, and the alternator of such a high speed system will be smaller and lighter.

The heat exchange between nuclear reactor and turbine employs liquid metals. This system works at temperatures between 700°C and 300°C. Two design problems for the alternator immediately arise: it must run at temperatures close to the Curie point for common magnetic circuit materials and must also have an insulation system capable of protecting the conductors from the highly corrosive metal vapours.

The working temperatures demand the use of cobalt steels. These have high Curie points and also may be operated at higher flux density levels. The rotor material being subjected to high stress as well as temperature, will be liable to creep. This plastic deformation occurs over relatively long periods (10^3 - 10^4 hours) and must seriously affect safety factors.

High temperature insulation systems are inorganic, using glass and other ceramics or mica. An attempt may be made to check the vapours at the bearing between turbine and alternator. So far (1963) this is only partially successful. Ceramic coefficients of expansion do not match surrounding materials and conventional conductor and slot insulations crack, forming voids. This leads to investigations into core seals in the airgap, separating the windings into a compartment free of vapours.

First thoughts of increasing the airgap length to include a seal seem totally disadvantageous, since the alternator size must increase to keep its rating. However, a solid rotor has been chosen to make full use of the potential for high speed operation. Pole face losses in such a solid rotor due to airgap permeance fluctuations and harmonics in the armature m.m.f. lead to high rotor temperatures. Increasing the airgap length greatly reduces these pole face losses. Thus a suitable balance between allowable rotor temperature and output to weight ratio may be calculated.

Further environmental factors peculiar to space are vacuum and nuclear radiation. Windage losses for high speed rotors would be prohibitive in any medium other than a vacuum. However a crack of only .001" is a thermal barrier except for the small heat transfer potential of radiation. Thus rotor heat may only be withdrawn through the bearings. Indeed the cooling system of the alternator is a most important and difficult field of development.

Nuclear radiation adversely affects organic materials (insulations, lubricants) and even the physical nature of inorganic insulations, structural materials and conductors. Shielding is an unfortunate addition to the overall weight.

The problems, as with all operations in space, are extremely complex. The inductor alternator as a unit of electrical engineering is possibly the oldest concept to be involved in this new technology.

7 CONCLUSIONS

New materials and manufacturing techniques have naturally produced remarkable developments during the Electrical Engineering Industry's short history. In many instances new materials and techniques have been responsible for whole new technologies. The art of designing machines must be greatly involved in utilizing all such improvements.

The designer must also develop the flexibility and inventiveness shown so clearly by the men in this history. A wealth of ideas was thrown up in the highly competitive period at the end of the nineteenth centruy. Even if they remain of little specific use, their investigation offers a salutary experience.

The pioneering days are remote now and the young designer in a large office may not be called upon to consider the origins and fundamentals of his work. He is often too preoccupied in maintaining the situation he has been presented with. It may be presumed that Inductor Alternators will also be superseded as spacecraft generators. Whatever new concept does challenge; it will be the result of the same flexibility and inventiveness, applied by a new generation.

ACKNOWLEDGMENTS:

The author wishes to gratefully acknowledge the advice and assistance of the following people:

Miss M. K. Weston	Science Museum, London.
Dr. A.G.E. Robiette	for permission to reproduce Figs. 11 and 12.
Mr. J.H.R. Nixon	Historian to the Brush Co. Ltd.

Colleagues at A.E.I. (Rugby, Leicester and Blackheath) Ltd.

Colleagues at the University of Aston in Birmingham especially Dr. E.J. Davies who read the proofs.

REFERENCES:

1 "Dynamo - Electric Machinery" S.P. Thompson, seventh edition, E and F.N. Spon Ltd., 1905

2 Mr. Kingdon's Dynamo - Fig. 2 - Electrical Review, Vol. 22, p.178, 1888.

3 "The Early Days of the Power Station Industry". R.H. Parsons, University Press, 1939.

4 "The Foundations of Modern Radio", L. W. Chubb, C.T. Allcott, Electric Journal. Vol. 18 p. 120 1921

5 "Data and Tests on a 10,000c/s Alternator" B.G. Lamme, Trans. A.I.E.E., Vol. 23, p.417, 1904.

6 "Alternator for 100,000 cycles" E.F.W. Alexanderson. Trans. A.I.E.E. Vol.28, pt. I p.399, 1909

7 "High Frequency Alternators" C.M. Laffoon. Electric Journal. Vol. 21, p.416, 1924.

8 "H-F Alternator developments" C.M. Laffoon Electrical Review. Vol. 104, p. 674, 1929

9 "Electric Melting and Smelting practice" A.G.E. Robiette. Charles Griffin and Co. Ltd. 1955

FIG. 1 MORDEY-VICTORIA ALTERNATOR

(SKETCHED FROM REF. 1)

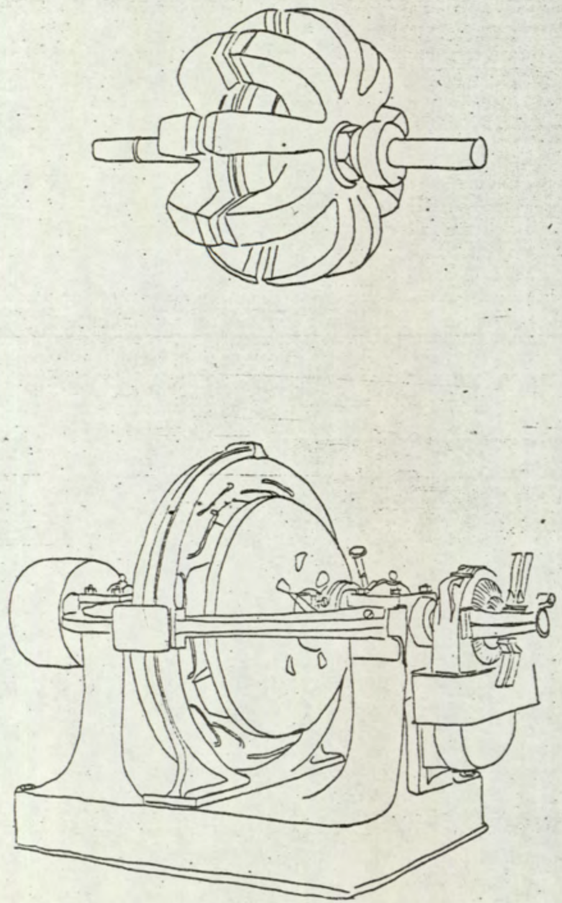

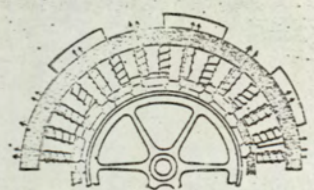

FIG 2 —KINGDON'S DYNAMO.

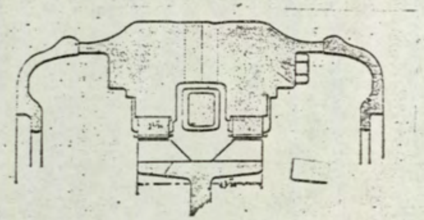

FIG. 3 LAMME'S 10,000 ~/S ALTERNATOR.

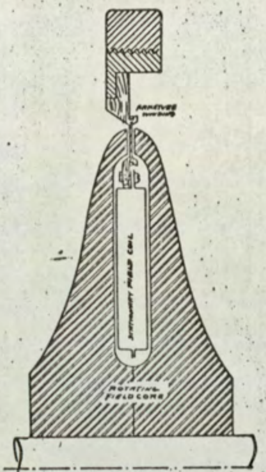

FIG. 8.

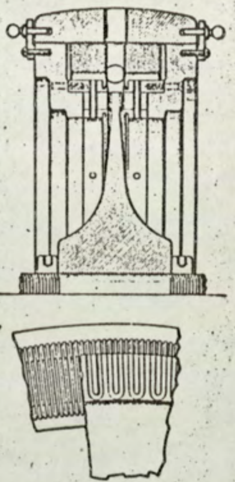

FIG. 9.

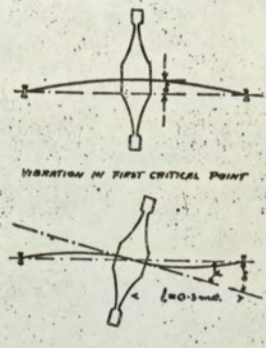

FIG. 10.

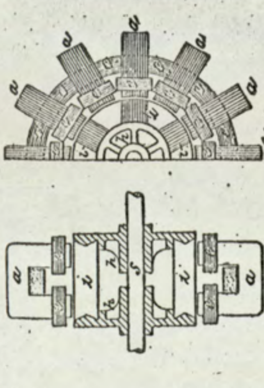

FIG. 4.—MORDEY'S INDUCTOR ALTERNATOR.

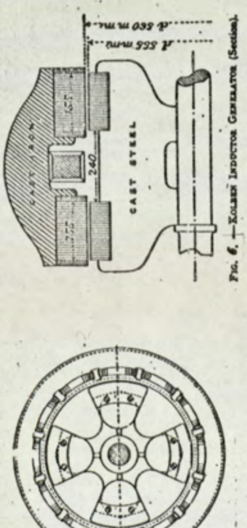

FIG. 6.—KOLBEN INDUCTOR GENERATOR (Section).

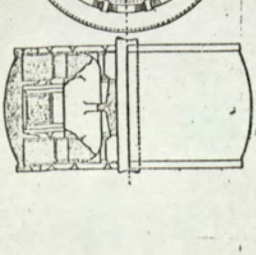

FIG. 5.—HOMOPOLAR INDUCTOR ALTERNATOR (OERLIKON CO.).

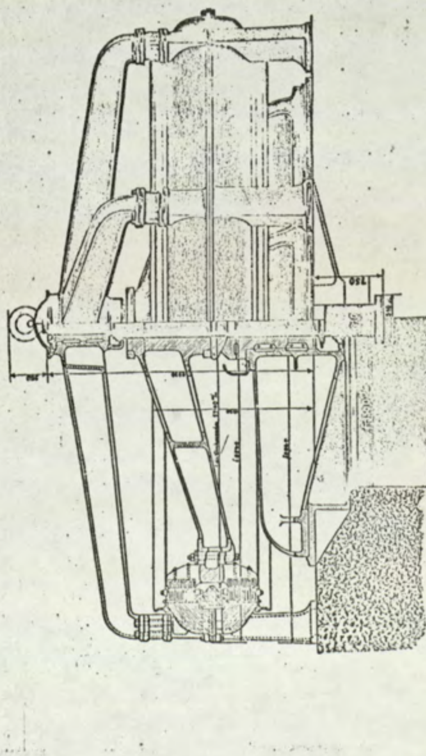

FIG. 7.—VERTICAL SHAFT INDUCTOR GENERATOR, BUILT FOR RHEINFELDEN TRANSMISSION PLANT.

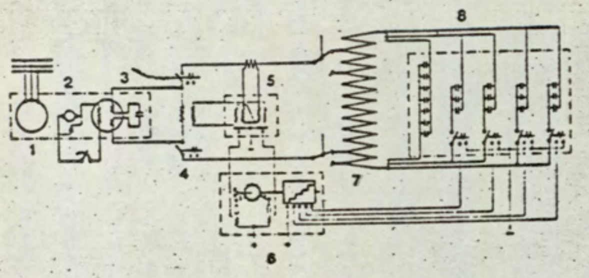

Fig. 11.—Circuit diagram for an automatic high-frequency furnace installation

1 Motor
2 Excitor
3 Generator with series capacitor
4 Main circuit-breaker
5 Balanced relay
6 Automatic controller
7 Furnace coil
8 Capacitor battery with contactors

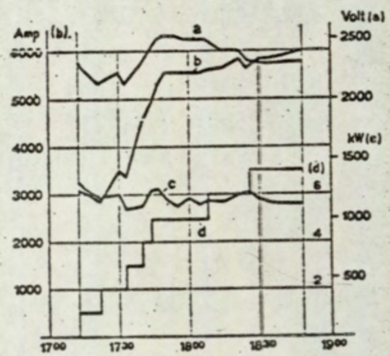

Fig. 12.—Load diagram for a 4·3-ton charge of stainless steel during re-melting. Melting time 1 hr 35 min. Specific furnace consumption 530 kWh per ton (measured in the three-phase network)

(*a*) Furnace voltage (*b*) Furnace current (*c*) Power consumption
(*d*) Number of capacitors in the coil circuit